Electron identification with the CMS detector and applications for Higgs and W boson searches

A dissertation submitted to

ETH Zürich

for the degree of

Doctor of Sciences

presented by

Wieland Hintz

Dipl.-Phys. ETH Zürich
born November 18, 1980
citizen of Germany

accepted on the recommendation of

Prof. F. Pauss examiner
Prof. G. Dissertori co-examiner

- **2010** -

Abstract

The efficient identification of high energy electrons at the Large Hadron Collider (LHC) is of primary importance for the study of many physics processes, like the search for the Higgs boson and other Standard Model and beyond Standard Model processes.

For the measurement of the electron energy, the CMS experiment uses a high precision Electromagnetic Calorimeter (ECAL). It is divided into a barrel and two end-caps composed of lead tungstate crystals, which are read by photo detectors. The integration of the ECAL readout electronics into the structure of the ECAL, the testing strategy, and the current performance of the ECAL electronics are presented in detail. In February 2010, 99.6% of the 75 848 ECAL readout channels were found to be fully operational.

The identification of isolated electrons with the CMS detector is discussed, focusing on the reduction of the fake rate, i.e. the rate of jets or photons that are miss-identified as electrons. Tools for the electron selection are introduced, and a simple and effective electron selection for isolated high energy electrons in the ECAL barrel is presented. The study of the electron selection based on Monte Carlo simulations results in a fake rate of only 10^{-4} and an efficiency to select genuine electrons of 70%.

The electron selection is applied to a study of the search of the Higgs boson in the channel $Higgs \rightarrow W^+W^- \rightarrow e^+\nu e^-\bar{\nu}$ and for a Higgs mass in the range 155-180 GeV. In particular, the background process $W^{\pm}X \rightarrow e^{\pm}\nu X$ is investigated in detail, where X is a jet or a photon that is miss-identified as an electron. Using the proposed electron selection, this background can be reduced well below the irreducible backgrounds.

Finally, the developed electron selection is used in a study of the selection of $W^{\pm} \rightarrow e^{\pm}\nu$ events with low background contributions. In addition, a new method to measure the transverse momentum spectrum of the selected W bosons is proposed. The measurement of this spectrum can constrain the gluon distribution functions of the proton at the LHC energies.

Zusammenfassung

Die effiziente Bestimmung hochenergetischer Elektronen ist eine der wichtigsten Voraussetzungen für die Untersuchung verschiedener physikalischer Prozesse am Large Hadron Collider (LHC); zum Beispiel für die Suche nach dem Higgs Boson und die Untersuchung anderer Standard Model Prozesse und Prozesse jenseits des Standard Models.

Am CMS Experiment wird ein hochpräzises elektromagnetisches Kalorimeter (ECAL) für die Messung der Energien von Elektronen eingesetzt. Es besteht aus Bleiwolframatkristallen und ist in den so genannten Barrel und in zwei Endkappen unterteilt. Der Einbau der Komponenten der ECAL Ausleseelektronik in die Struktur des ECALs, die Teststrategie für die Elektronik und ihre gegenwärtige Leistungsfähigkeit werden ausführlich beschrieben. Im Februar 2010 waren 99.6% der 75 848 ECAL Auslesekanäle voll funktionsfähig.

Des Weiteren wird die Bestimmung isolierter Elektronen mit dem CMS Experiment beschrieben, wobei der Schwerpunkt auf einer möglichst kleinen Rate von Jets und Photonen, die als Elektronen fehlinterpretiert werden, liegt. Verschiedene Auswahlkriterien werden definiert und eine einfache und effiziente Elektronenselektion für den Barrel des ECALs wird eingeführt. Bei der Untersuchung der Elektronenselektion mit Monte Carlo Simulationen, ergibt sich eine Wahrscheinlichkeit von 10^{-4}, Jets und Photonen als Elektronen zu messen. Die Effizienz, echte Elektronen zu selektieren, liegt bei 70%.

Die Elektronenselektion wird bei einer Studie der Higgs Boson Suche im Zerfallskanal $Higgs \rightarrow W^+W^- \rightarrow e^+\nu e^-\bar{\nu}$ und für eine Higgsmasse im Bereich von $155 - 180\,\mathrm{GeV}$ angewendet. Hierbei wird insbesondere der Untergrundprozess $W^{\pm}X \rightarrow e^{\pm}\nu X$ im Detail untersucht, wobei X Jets oder Photonen sind, die als Elektronen fehlinterpretiert werden. Unter Verwendung der eingeführten Elektronenselektion ergibt sich, dass der Beitrag dieses Untergrunds deutlich unter das Niveau der irreduziblen Untergründe gesenkt werden kann.

Schliesslich wird die Elektronenselektion angewandt, um simulierte $W^{\pm} \rightarrow e^{\pm}\nu$ Ereignisse mit sehr niedrigen Untergrundbeiträgen zu selektieren. Ausserdem wird eine neue Methode vorgestellt, das Spektrum der transversalen Impulse der selektierten W Bosonen zu messen. Die Messung dieses Spektrums kann dazu dienen, die Partonverteilungsfunktionen der Gluonen im Proton bei die Energien am LHC zu bestimmen.

Contents

Chapter 1.

Introduction

Throughout the last century, the knowledge of the fundamental constituents of matter experienced a tremendous progress. This progress was only possible thanks to ambitious and especially curious physicists, whose enduring work shed light on many of the former mysteries of nature. Their ultimate aim was (and is) the formulation of laws that can describe and predict the observed phenomena of nature. Thereby, the scientists make use of theory and experiment, where the results of either have fruitful influence on the development of the other.

The idea that matter consists of indivisible particles, called atoms, was firstly brought up by the Greek philosopher Democritus in the 5th century BC. Scientists of the 19th century scientists picked up the idea of a fundamental indivisible constituent of matter to explain chemical reactions. The discovery of the electron in 1897 by Thomson proved a substructure of the atoms, and the first atomic model described the atoms as a conglomerate of negatively charged electrons and positively charged protons. The famous experiments of Rutherford, however, showed that the atomic structure consists of a nucleus and an electron shell surrounding it. The first (effective) description of the electron shell of small atoms was the atomic model of Bohr. This partial successful model had several shortcomings and was therefore replaced by the invention of quantum mechanics. Quantum mechanics, which is based on the work of de Broglie, Heisenberg, Schrödinger and Dirac, is since then considered the ultimate description of (non-relativistic) microscopic particles in general, and the atomic electron shell in particular.

After that, research focused of the structure of the atomic nucleus. The theory, in which the nucleus consists of protons and neutrons, was confirmed with the discovery of the neutron by Chadwick in 1932. Since the known electromagnetic force could not explain the binding of the two particles inside the nucleus, the theory of an additional "strong" interaction between protons and neutrons was introduced. In the same year,

the anti-particle of the electron, the positron, was found by Anderson. This was the first discovery of an particle that is not a constituent of atoms.

In the 50s and 60s of the last century, the use of particle accelerators allowed the discovery of many new strongly interacting particles (*hadrons*). Due to some regularities in the properties of these particles, it was assumed that hadrons were not fundamental and have a substructure. The model that was built up to describe the nature of the hadrons' constituents, called the quark model, could be verified with the discovery of the substructure of protons in 1969, and the discovery of the J/ψ particle in 1974. Until now, six different quarks were discovered. In the experiments to date, they were found to be point like and are thus considered as fundamental particles. A second type of fundamental particles observed are the six leptons, like the electron.

In parallel to the discoveries of the fundamental particles that constitute matter, the forces that act on these particles were an important subject of the particle physics research. Three fundamental particle forces are observed. The first force, which was found to act on (charged) particles, was the electromagnetic interaction. The phenomenology of this force had already been described by the effective theory of the electromagnetism introduced by Maxwell in 1865. Together with the knowledge of quantum dynamics and Einstein's special relativity, however, the electromagnetic interaction is nowadays described by the *Quantum Electrodynamics*, which was introduced by Feynman, Schwinger and Tomonaga. Two further fundamental particle interactions, which were discovered, are the *weak* and the *strong interaction*. A prominent manifestation of the weak interaction is the nuclear decay. The strong interaction is responsible for the formation of hadrons and atomic nuclei.

The *Standard Model of Particle Physics* is the theory that describes the interaction of quarks and leptons through the three fundamental interactions. It is based on so-called *quantum field theories*. Within the picture of quantum field theories, particles interact via the exchange of massless *gauge bosons*. The discoveries of the different *gauge bosons* of all three interactions could confirm this theoretical picture. The bosons, which carry the electromagnetic and the strong interaction were indeed found to be massless. In contrast, the gauge bosons of the weak interaction, called W and Z bosons, have masses of about 100 times the proton mass. Together with the framework of the Standard Model, a theoretical mechanism was invented by Higgs, Brout and Englert in 1964 to introduce these masses. However, this so-called *Higgs mechanism* requires the introduction of a further particle, the *Higgs boson*.

Including the Higgs boson, the Standard Model is able to describe the observed phenomena of particle physics. The last piece missing to approve the Standard Model entirely, is however the discovery of the Higgs boson.

For its observation, the Higgs boson has to be produced in the collision of two particles. Due to energy conservation, the collision energy has to be high enough to produce the heavy Higgs boson. Accordingly, the collision energy of the former particle accelerators was too low in this respect. The search for the Higgs at the experiments at the Large Electron Positron Collider (LEP) at the European Laboratory for Particle Physics (CERN) could exclude the Higgs for a Higgs mass below $114\,\mathrm{GeV/c^2}$. Currently, the Large Hadron Collider (LHC) is under operation to search for the Higgs at higher masses. LHC is a proton-proton collider, which is designed to collide protons with a center-of-mass energy of $14\,\mathrm{TeV}$.

In order to discover the Higgs after its production in such particle collisions, it is necessary to identify the products of its instantaneous decay and to measure their kinematic parameters. This is achieved by particle detectors, like the Compact Muon Solenoid (CMS) at the LHC. The special challenge for CMS, and for the other experiments at the LHC, is the overwhelming rate of unwanted processes (background), which complicates the search for the comparably rarely produced Higgs bosons and other interesting processes. However, an important signature that helps to distinguish Higgs boson events from background, are electrons and their anti-particles, positrons, which appear as stable particles in certain decay chains of the Higgs. For simplicity, both will be denoted as electrons throughout this theses. The energy measurement of electrons is performed by the *Electromagnetic Calorimeter* (ECAL) of the CMS detector.

This thesis focuses on the development of a clean identification of electrons with the CMS detector. To verify the performance of this electron identification, it is applied to a study of the Higgs boson search. In addition, based on the electron identification, a new method to detect W bosons and the method for the worldwide first measurement of its transverse momentum with the CMS detector was developed.

The thesis is divided in ten chapters. The Chapters 2 and 3 give an overview of the Standard Model, the LHC and the CMS detector. The functionality of the ECAL is described in Chapter 4, and the integration and testing of its readout electronics in Chapter 5. The performance of the ECAL is summarized in Chapter 6. Chapter 7 explains the development of electron identification tools. Chapter 8 summarizes the reconstruction of *jets* and *missing transverse energy*. The search for the Higgs with mass around $165\,\mathrm{GeV}$ is presented in Chapter 9. The focus of this study is the determination of the background rate from W bosons that decay to an electron and a neutrino. A

study of the detection of W bosons and the measurement of its transverse momentum spectrum are presented in Chapter 10. Finally, conclusions and future perspectives are given in Chapter 11.

Chapter 2.

Standard Model of particle physics

The particles that constitute the known matter of the universe and the particle interactions are described by the *Standard Model of Particle Physics*. This chapter summarizes the Standard Model and describes, how interactions arise from local gauge symmetries. The electroweak interaction is introduced, the Higgs mechanism is explained, and the *strong interaction* and its implications on the *parton distribution functions* are discussed. Finally, tests and limitations of the Standard Model are summarized.

2.1. Overview

The observed fundamental particles are fermions (spin 1/2 particles), the quarks and leptons. Currently, six quarks and six leptons are known, which are considered as point-like (diameter $< 10^{-18}$ m). They are divided into three families each, and the members of one family are arranged in doublets. In addition, fundamental bosons (spin 1 particles) are observed, which mediate the interactions between the fermions. The three fundamental interactions are the *electromagnetic interaction*, the *weak interaction*, which is responsible for the neutron decay, and the *strong interaction*, which forms hadrons and atomic nuclei.

The leptons and their main parameters are summarized in Table 2.1. Each family includes a charged lepton (electron, muon, and tau) and a neutral lepton (neutrinos). The charged leptons have measurable masses. The masses of the neutrinos are unknown, only upper limits for their masses could be obtained from experiments. However, their non vanishing masses can be implied from the observed mixing in the neutrino sector, i.e. the transition from one neutrino to another.

The quarks of the Standard Model are shown in Table 2.2. Each of the three families consists of one *up-type* quark with charge $+2/3\,e$ (up, charm, and top quark) and one *down-type* quark with charge $-1/3\,e$ (down, strange, and bottom quark).

	1st family		2nd family		3rd family	
Flavor	Electron	Electron-Neutrino	Muon	Muon Neutrino	Tau	Tau-Neutrino
Mass [MeV/c^2]	0.511	$< 2 \times 10^{-6}$	105.7	< 0.19	1777 ± 0.17	< 18.2
Electric Charge [e]	-1	0	-1	0	-1	0

Table 2.1.: Leptons of the Standard Model of particle physics and their main parameters [1].

	1st family		2nd family		3rd family	
Flavor	up	down	charm	strange	top	bottom
Mass [MeV/c^2]	$1.5 - 3.3$	$3.5 - 6$	1270^{+70}_{-110}	104^{+26}_{-34}	171200 ± 2100	4200^{+170}_{-70}
Electric Charge [e]	$+2/3$	$-1/3$	$+2/3$	$-1/3$	$+2/3$	$-1/3$

Table 2.2.: Quarks of the Standard Model of particle physics and their main parameters [1].

For each quark or lepton an anti-particle with the same mass, spin, and lifetime, but opposite charge exists. In contrast to leptons, quarks interact via the *strong interaction* (Section 2.4). This is due to an additional quantum number of the quarks, called *color charge*. The color charge exists in three states usually described as red, blue, and green. Quarks appear in one of the three color states, whereas leptons are colorless.

As a result of the strong force, quarks are not observed as isolated particles. Instead, they are confined inside bound states called *hadrons*. To date, quarks could only be observed in quark-antiquark states called *mesons*, and states of three quarks or three antiquarks, called *baryons*. The two lightest baryons, the neutron and the proton, are the constituents of atomic nuclei. Together with the electron they form ordinary matter.

The three fundamental particle interactions are successfully described within the framework of *relativistic quantum field theories* based on the three local symmetry groups $SU(3) \times SU(2) \times U(1)$. In this theory, the interaction between two particles is described by the exchange of so-called *gauge bosons*. The bosons are considered as the quanta of the *gauge fields* that establish these interactions. The gauge bosons of the electromagnetic, the weak and the strong interactions are the photon (γ), the W$^\pm$ and Z^0 bosons, and 8 gluons, respectively. A comparison of the three interactions is given in Table 2.3.

Interaction	Electromagnetic	Weak	Strong
Coupling strength $(Q^2 \approx 1\,\text{GeV}^2)$	10^{-2}	10^{-6}	1
Range	∞	$\frac{1}{M_W} \approx 10^{-18}\,\text{m}$	$\approx 10^{-15}\,\text{m}$
Gauge boson	Photon	$W^{\pm}$ and Z^0 bosons	8 gluons
Mass (GeV/c^2)	0	$m_W = 80.4,\ m_Z = 91.2$	0

Table 2.3.: Parameters of the interactions of the Standard Model of particle physics [1].

For a detailed introduction of the Standard Model of particle physics see [2]. An overview of its historical development is given in [3]. A detailed discussions on quantum field theories can be found in [4].

2.2. Symmetry and interaction

Relativistic fermions and bosons that propagate in vacuum, can be described by the Dirac and Klein-Gordan equations, respectively. The Dirac equation results from the Euler-Lagrange equation using the following Lagrangian

$$L_{free} = i\bar{\psi}\gamma^{\mu}\partial_{\mu}\psi - m\bar{\psi}\psi, \tag{2.1}$$

where ψ is a 4-component complex field (Dirac spinor) representing a free fermion field with mass m, e.g. an electron. The expression $|\psi(x)|^2$ is the probability, that the electron is found in a volume d^3x around the point x in space. γ_{μ} are the Dirac-matrices.

According to Noether's Theorem, invariances of a Lagrangian under space transformations or time translations lead to conservation laws. An example for such transformations is the family of $U(1)$ phase rotations

$$\psi(x) \rightarrow e^{i\alpha}\psi(x). \tag{2.2}$$

$U(1)$ forms an abelian unitary group. Equation (2.1) is invariant under $U(1)$ transformations for a constant rotation phase α, i.e. the Lagrangian possesses a global gauge symmetry. According to Noether's Theorem, this implies the existence of a conserved quantity, here the electric charge.

For an arbitrary function of space and time, $\alpha(x)$, Equation (2.1) is not invariant under $U(1)$ phase rotations. To impose local invariance of the Lagrangian, one has to

modify the derivative ∂_μ. The *covariant derivative* D_μ is formed by introducing a vector field A_μ

$$D_\mu \equiv \partial - ieA_\mu. \tag{2.3}$$

A_μ is an arbitrary function of space and time called *gauge field*, and e is an arbitrary constant. Replacing ∂_μ with D_μ in Equation (2.1) gives

$$\mathcal{L} = \bar{\psi}(i\gamma^\mu\partial_\mu - m)\psi + e\bar{\psi}\gamma^\mu\psi A_\mu = \mathcal{L}_{free} + e\bar{\psi}\gamma^\mu\psi A_\mu. \tag{2.4}$$

This modified Lagrangian is invariant under local phase rotations, if A_μ transforms as

$$A_\mu \rightarrow A_\mu + \frac{1}{e}\partial_\mu A_\mu. \tag{2.5}$$

The first term is the Lagrangian of the free fermion, and the second term is interpreted as the coupling of the Dirac particle to the gauge field A_μ. This coupling can be considered as the coupling of an electron with charge $-e$ to a photon field A_μ. However, to identify the new field as the photon field, a kinetic term for the field A_μ has to be constructed to give dynamics to the photon. This additional term is $-\frac{1}{4}F_{\mu\nu}F^{\mu\nu}$, where $F_{\mu\nu} = \partial_\mu A_\nu - \partial_\nu A_\mu$ is the electromagnetic field strength tensor. It depends only on A_μ and derivatives of it and is invariant under local phase rotations. The Lagrangian of *Quantum Electrodynamics* (QED) is then

$$\mathcal{L} = \bar{\psi}(i\gamma^\mu\partial_\mu - m)\psi + e\bar{\psi}\gamma^\mu A_\mu\psi - \frac{1}{4}F_{\mu\nu}F^{\mu\nu}. \tag{2.6}$$

It describes the interaction of electrically charged fermions via the photon field, the electromagnetic interaction. A mass term for the gauge field, such as $\frac{1}{2}m^2 A_\mu A^\mu$, is forbidden by the local gauge symmetry, i.e. the photons must be massless to preserve the symmetry.

The effective coupling strength of the photon field to an electrically charged particle is expressed by the fine structure constant

$$\alpha = \frac{e^2}{4\pi} \approx 1/137. \tag{2.7}$$

In fact, the coupling is only constant at the limit of low momentum transfers Q^2 between the interaction particles. For high momentum transfers, the coupling becomes stronger.

This so-called running of the coupling constant, $\alpha(Q^2)$, was measured for example at the Large Electron-Positron Collider (LEP) experiments [5, 6, 7].

In summary, by imposing the "natural" requirement of local phase invariance on the Lagrangian of the free fermion, the interacting field theory of QED is obtained.

This procedure can be repeated to derive the interacting field theories that describe the weak and the strong interactions. They are derived from a $SU(2)$ and a $SU(3)$ symmetry group, respectively (Sections 2.3 and 2.4). In general, the theoretical procedure is the following: Starting from the Lagrangian of free Dirac particles, one requires a local symmetry G. To obtain the invariance of the Lagrangian, the derivative D_μ is introduced, which generalizes the derivative ∂_μ. This is done by introducing a set of real vector fields A_μ^a, such that $D_\mu = \partial_\mu - igA_\mu^a t^a$, where g is the gauge coupling, and t^a are the operators that generate the group G. To give a dynamic to these gauge fields, a gauge tensor $F_{\mu\nu}$ is introduced, which must be antisymmetric in its two spacial indices. It is common to define it as $igF_{\mu\nu}^a t^a = [D_\mu, D_\nu]$, which is the commutator of the covariant derivative.

If the group G is non-abelian (like $SU(2)$ and $SU(3)$) one finds a fundamental difference between the obtained Lagrangians and the Lagrangian of QED, which was constructed using the abelian group $U(1)$. In the QED case, the only interaction terms (terms with at least three fields) are the ones between the fermion fields and the gauge fields. In the non-abelian cases there are terms with three and even four gauge fields. This indicates, how the gauge fields (and thus their quanta, the gauge bosons) interact with each other through three- and four gauge field vertices.

2.3. Glashow-Salam-Weinberg model

The unification of the electromagnetic and the weak interactions to the *electroweak interaction*, is described by the Glashow-Salam-Weinberg model. It is based on a spontaneously broken local $SU(2) \times U(1)$ gauge field theory. To break the symmetry, an additional scalar field is introduced, the *Higgs field*.

2.3.1. Higgs mechanism and gauge boson masses

Following the procedure explained in the previous section, a local $SU(2) \times U(1)$ symmetry of Equation (2.1) is required. The covariant derivative is

$$D_\mu \equiv \partial_\mu - i\frac{g}{2}A_\mu^a t^a - i\frac{Yg'}{2}B_\mu, \tag{2.8}$$

where the weak isospin operators t^a generate the group $SU(2)$ and the *hypercharge Y* generates the group $U(1)$. A^a and B_μ are the gauge fields that correspond to the $SU(2)$ and the $U(1)$ symmetry, respectively. g and g' are the gauge couplings.

The corresponding Lagrangian then includes the terms, which describe the kinematics and the self-interaction of the gauge fields as described above

$$-\frac{1}{4}F^a_{\mu\nu}F^{\mu\nu}_a - \frac{1}{4}G_{\mu\nu}G^{\mu\nu}, \tag{2.9}$$

where

$$F^a_{\mu\nu} = \partial_\mu A^a_\nu - \partial_\nu A^a_\mu - g\epsilon_{abc}A^b_\mu A^c_\nu \quad \text{and} \quad G_{\mu\nu} = \partial_\mu B_\nu - \partial_\nu B_\mu \tag{2.10}$$

are the field strength tensors. ϵ_{abc} is the total antisymmetric tensor. The thus obtained Lagrangian of the electroweak interaction forbids the introduction of mass terms to maintain its local gauge invariance. However, the observed masses of the bosons are non-vanishing and they have to be introduced in a gauge invariant way. At the same time, the photon has to remain massless. This is achieved by *spontaneous symmetry breaking* of the $SU(2)$ symmetry. In the Standard Model, the symmetry is broken by introducing an additional complex field, the Higgs field

$$\Phi \equiv \begin{pmatrix} \Phi^+ \\ \Phi^0 \end{pmatrix}. \tag{2.11}$$

Using the gauge symmetry freedom to restrict the non-vanishing part to the lower entry, the *Higgs field* can be parametrized as

$$\Phi = \frac{1}{\sqrt{2}}\begin{pmatrix} 0 \\ \eta + h(x) \end{pmatrix}, \tag{2.12}$$

where η is a real constant representing the non-vanishing vacuum expectation value of Φ. The real scalar field $h(x)$ refers to fluctuations of Φ around the vacuum expectation value. The Lagrangian of the Higgs field is

$$\mathcal{L}_\Phi = (D_\mu\Phi)^\dagger(D_\mu\Phi) + \mu^2\Phi^\dagger\Phi - \lambda(\Phi^\dagger\Phi)^2 \tag{2.13}$$

where D_μ is the covariant derivative of Equation (2.8), μ is a mass parameter, and λ is the strength of the Higgs self interaction. For $\mu^2 > 0$, the Higgs potential $V(\Phi) = \mu^2\Phi^\dagger\Phi - \lambda(\Phi^\dagger\Phi)^2$ has a global minimum at $\Phi = 0$, which does not break the electroweak

gauge symmetry. For $\mu^2 < 0$, however, it has a minimum at

$$\eta = \sqrt{\frac{\mu^2}{\lambda}} \neq 0. \tag{2.14}$$

Using linear combinations of the gauge fields A^a and B, the mass eigenstates of the gauge fields are defined as

$$\begin{aligned}
W_\mu^\pm &= \tfrac{1}{\sqrt{2}}(A_\mu^1 \mp iA_\mu^2), \\
Z_\mu &= \frac{1}{\sqrt{g^2+g'^2}}(gA_\mu^3 - g'B_\mu), \text{ and} \\
A_\mu &= \frac{1}{\sqrt{g^2+g'^2}}(g'A_\mu^3 + gB).
\end{aligned} \tag{2.15}$$

These definitions are substituted in the Lagrangian of Equation (2.13) and the mass eigenstates acquire the following masses:

$$m_{W^\pm} = \frac{g\eta}{2}, \quad m_Z = \frac{\eta}{2}\sqrt{g^2 + g'^2}, \quad \text{and} \quad m_A = 0. \tag{2.16}$$

Thus, the spontaneous breaking of the gauge symmetry, called the Higgs mechanism, gives masses to the gauge bosons $W^\pm$ and Z. Since the $U(1)$ symmetry remains unbroken, the photon stays massless.

Since the field A_μ is identified as the electromagnetic potential, its coupling should be the electromagnetic coupling e. Thus, the following relation of the gauge couplings is found

$$e = \frac{gg'}{\sqrt{g^2 + g'^2}}. \tag{2.17}$$

The mixing of the field A^3 and B can also be parametrized using the weak mixing or Weinberg angle θ_W. θ_W defines the rotation in the neutral sector of the electroweak interaction

$$\begin{pmatrix} Z \\ A \end{pmatrix} = \begin{pmatrix} \cos\theta_W & -\sin\theta_W \\ \sin\theta_W & \cos\theta_W \end{pmatrix} \begin{pmatrix} A^3 \\ B \end{pmatrix}, \tag{2.18}$$

where

$$\cos\theta_W = \frac{g}{\sqrt{g^2 + g'^2}} \quad \text{and} \quad \sin\theta_W = \frac{g'}{\sqrt{g^2 + g'^2}}. \tag{2.19}$$

Together with Equation (2.16), the ratio of the $W^\pm$ and Z masses is

$$\frac{m_W}{m_Z} = \cos\theta_W. \tag{2.20}$$

The resent values for the measurements of the boson masses are [1]

$$m_W = 80.398 \pm 0.025\,\text{GeV} \text{ and } m_Z = 91.1876 \pm 0.0021\,\text{GeV}. \tag{2.21}$$

The weak mixing angle could e.g. be extracted from Z resonance observables and was measured to be $\sin^2\theta_W = 0.22331 \pm 0.00062$ by the LEP experiments [6]. The measurement agrees well with the ratio of the measured boson masses. The values of g and g' can be derived from Equations (2.17) and (2.19).

The relative strength of the weak interaction is expressed by the effective coupling constant of the weak interaction, the Fermi constant

$$G_F = \frac{\sqrt{2}}{8}\frac{g^2}{m_W^2} \approx 1.166 \times 10^{-5}\,\text{GeV}^{-2}. \tag{2.22}$$

η can be then determined from G_F

$$\eta = (\sqrt{2}G_F)^{-1/2} = 246\,\text{GeV}. \tag{2.23}$$

This non vanishing vacuum expectation value of the Higgs allows the Higgs mechanism to work.

In conclusion, the Higgs mechanism provides a handy tool to introduce the masses of the heavy bosons in the quantum field theory of the electroweak interaction. The mass of the Higgs boson is given by

$$m_H = \sqrt{2\lambda\eta}. \tag{2.24}$$

Unfortunately, the Higgs mass cannot be predicted, since the strength of the self-coupling of the Higgs field, λ, is a free parameter.

2.3.2. Generation of fermion masses

Experiments have shown that the weak interaction violates C and P-parity [8]. In particular, the $W^\pm$ bosons couple only to left-handed fermions and right-handed anti-fermions. Within the theory of the electroweak interaction, this fact is respected by

separating the fermion field ψ into left and right handed components,

$$\psi = \begin{pmatrix} \psi_L \\ \psi_R \end{pmatrix}. \tag{2.25}$$

The left handed projections of the fermion fields form $SU(2)$ doublets

$$\psi_L = \begin{pmatrix} \nu_e \\ e^- \end{pmatrix}_L, \begin{pmatrix} \nu_\mu \\ \mu^- \end{pmatrix}_L, \begin{pmatrix} \nu_\tau \\ \tau^- \end{pmatrix}_L, \begin{pmatrix} u \\ d \end{pmatrix}_L, \begin{pmatrix} c \\ s \end{pmatrix}_L, \begin{pmatrix} t \\ b \end{pmatrix}_L, \tag{2.26}$$

and the right handed projections are singlets

$$\psi_R = e_R^-, \mu_R^-, \tau_R^-, u_R, d_R, c_R, s_r, t_R, b_R. \tag{2.27}$$

The corresponding two representations are then treated separately by the theory. Using the Dirac theory, anti-fermions can be defined as adjoint spinors,

$$\bar\psi \equiv \psi^\dagger \gamma^0 = (\bar\psi_R, \bar\psi_L), \tag{2.28}$$

where the matrix γ^0 interchanges the left and right handed components. The Dirac Lagrangian (Equation (2.1)) can now be written as

$$\mathcal{L} = i\bar\psi_L \gamma^\mu \partial_\mu \psi_L + i\bar\psi_R \gamma^\mu \partial_\mu \psi_R - m(\bar\psi_L \psi_R + \bar\psi_R \psi_L). \tag{2.29}$$

The kinematic term of the Lagrangian separates the left- and right-handed components, whereas the mass term mixes them. Since ψ_L transforms as a doublet under $SU(2)$ and ψ_R as a singlet, the mass term is not invariant under $SU(2)$ transformations. Therefore the fermion mass term cannot simply be added to the electroweak Lagrangian.

However, one finds that it is possible to use the fermion interactions with Higgs field to generate the fermion masses. The electron mass for example is defined as:

$$m_e = \frac{1}{\sqrt{2}}\lambda_e \eta. \tag{2.30}$$

In a similar manner, all massive fermion fields can be introduced. Since the neutrinos mixing and subsequently the neutrino masses were discovered only very recently, the neutrinos stay massless by construction. The coupling λ_e describes the coupling of the Higgs field to the electron. The strength of this so-called Yukawa coupling constant depends linearly on the fermion mass.

2.4. Quantum Chromo Dynamics

Quantum chromodynamics (QCD) successfully describes the experimental observations of the strong interaction using the symmetry group $SU(3)$. According to observations, the strong interaction acts on quarks, anti-quarks and gluons. The corresponding quantum number that is assigned to the quarks, is called color charge. It appears in the states red, blue and green for quarks (q), and anti-red, anti-blue and anti-green for anti-quarks $(\bar{q})$.

QCD postulates that physical particles are colorless. Colorlessness can be achieved by either combining a color with its anti-color or by combining all three (anti-) colors. Thus, quarks appear only in bound states called hadrons, which exist in the following combinations

$$\bar{q}^i q_i, \quad \epsilon^{ijk} q_i q_j q_k \quad , \text{and} \quad \epsilon_{ijk} \bar{q}^i \bar{q}^j \bar{q}^k. \tag{2.31}$$

ϵ^{ijk} is the total anti-symmetric tensor. These combination are known as *mesons* $(\bar{q}^i q_i)$, *baryons* $(\epsilon^{ijk} q_i q_j q_k)$ and *anti-baryons* $(\epsilon_{ijk} \bar{q}^i \bar{q}^j \bar{q}^k)$. The Lagrangian of the strong interaction can be derived from the concepts presented in Section 2.2, now using the $SU(3)$ symmetry group. For a quark q in one quark flavor, the Lagrangian is

$$\mathcal{L}_{QCD} = \bar{q}(i\gamma^\mu D_\mu - m)q - \frac{1}{4}F^a_{\mu\nu}F^{\mu\nu}_a, \tag{2.32}$$

where the covariant derivative is defined as

$$D_\mu = \partial_\mu + ig_s T_a G^a_\mu. \tag{2.33}$$

T_a are eight linearly independent traceless 3×3 matrices. They represent the generators of the $SU(3)$ group. G^a_μ are eight gauge fields, the *gluons*. Due to the local gauge invariance, the gluons are required to be massless. g_s is the quark-gluon gauge coupling constant. The kinetic terms of the gluons are defined using the field strength tensor

$$F^a_{\mu\nu} = \partial_\mu F^a_\nu - \partial_\nu F^a_\mu - g_s f_{abc} G^b_\mu G^c_\nu, \tag{2.34}$$

where f_{abc} is the structure constant of the $SU(3)$ group, which is defined using the commutation relation of the generators

$$[T_a, T_b] = if_{abc}T_c. \tag{2.35}$$
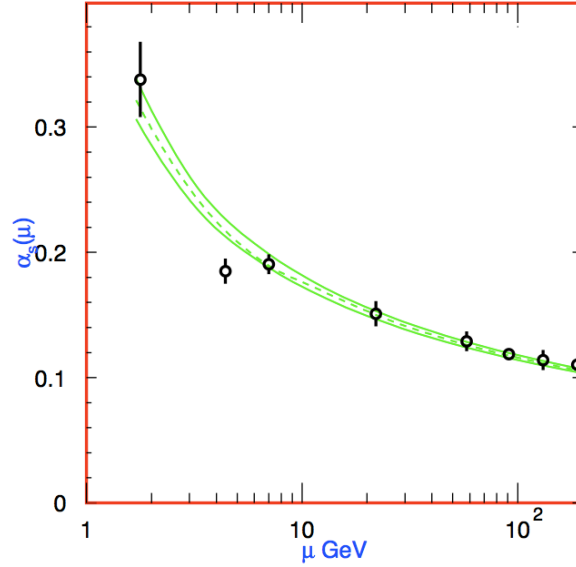
Figure 2.1.: Measured values of the QCD coupling strength α_s as a function of the energy
scale μ. The dashed line represents the mean value and the solid lines the $\pm 1\sigma$
limits of the QCD prediction [9].

The non-abelian nature of the $SU(3)$ group leads to self-interactions between the gauge
bosons, which are expressed by the last term in Equation (2.34). This leads to vertices
of three and four gluons, which do no appear in QED.

An observable consequence of this self coupling is the *asymptotic freedom* of strongly
interacting particles, which is expressed by the behavior of the effective coupling of QCD

$$\alpha_S = \frac{g_s^2}{4\pi}. \tag{2.36}$$

In particular, the asymptotic freedom results from the dependance of α_S on the mo-
mentum transfer Q^2 of an interaction, as shown in Figure 2.1 (where μ refers to Q^2).
Since α_S is small at high Q^2, the strong interaction is small at small distances and vice
versa: In the limit of low Q^2 (large distances), α_S becomes very large. Thus, quarks
form bound states and have never been observed as physical particles [9]. This behavior
is also known as *confinement*. If for example a quark-anti-quark (meson) pair is pulled
apart, the strong coupling between the quarks can get so large that it is energetically
more favorable to form a new quark-anti-quark pair. A manifestation of this effect is
the hadronization of quarks to so-called jets.

The asymptotic freedom of the quarks allows to calculate QCD processes at high mo-
mentum transfers perturbativly. The so-called *perturbative* QCD was tested successfully
in collision experiments [10].
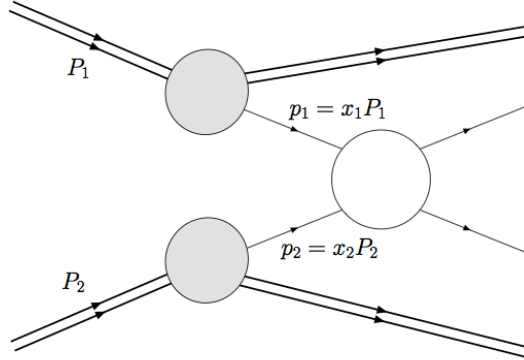
Figure 2.2.: A hadron-hadron collision. The incoming hadrons carry the momenta $P_{1,2}$ and the colliding partons the momenta $p_{1,2}$.

2.5. Parton distribution functions

As stated before, hadrons are bound states of quarks. Since the quarks in the proton are quasi-free, they can be considered as a loose cloud of non-interacting quarks and gluons, called partons. In high energy collisions of hadrons, these partons each carry a fraction x of the hadron's momentum [11]. According to this so-called *parton model*, the momenta of the partons are collinear with the hadron's momentum. The components of the parton's momentum, which are transverse to the hadron's momentum, are small due the asymptotic freedom of the partons.

Thus, hadron-hadron collision are in fact parton-parton collisions, where the partons are either quarks, anti-quarks, or gluons. The square of the center-of-mass energy of such collisions in a proton-proton collider is defined as

$$E_{CM}^2 = (x_1 P_1 + x_2 P_2)^2, \tag{2.37}$$

where $P_{1,2}$ are the momenta of the incoming protons, and $x_{1,2}$ are the fractions of the proton momentum carried by the colliding partons (Figure 2.2). According to the parton model, the other partons do not participate in the interaction (*spectator quarks*).

The distribution of the hadron momentum among the partons is described by the so-called *parton distribution functions* $f_f(x)$ (PDFs). Here, $f_f(x)dx$ gives the probability that a parton of type f carries a fraction within $[x, x+dx]$ of the hadron's momentum. Together, all partons of a hadron carry the total momentum of the hadron, i.e.

$$\sum_f \int_0^1 x f_f(x)dx = 1. \tag{2.38}$$
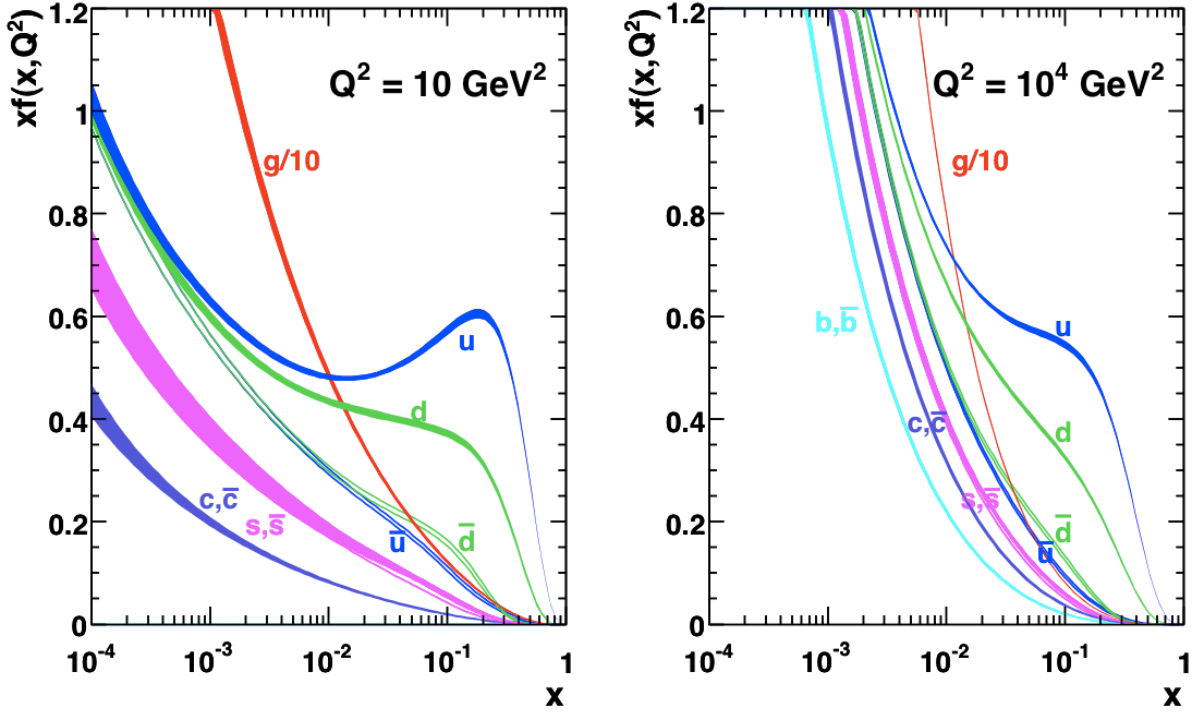
Figure 2.3.: PDFs of the proton at $Q^2 = 10\,\mathrm{GeV}^2$ and $Q^2 = 10^4\,\mathrm{GeV}^2$ for the quarks and gluons [12].

The partons of a hadron are the three quarks that constitute the hadron itself (*valence quarks*), the gluons, and the *sea quarks*. Protons, for example, have two *up* and one *down* valence quarks. Sea quarks are virtual quark-anti-quark pairs that are formed when a gluon splits. The reverse process is the annihilation of two sea quarks to a gluon. The result is a constant flux of gluon creations and splittings, called *the sea*. The probability to create such a quark-anti-quark pair decreases with the mass of the involved quarks. Thus, at low Q^2, the contributions of the three lightest quarks (*up*, *down*, and *strange*) to the sea are dominant.

The PDFs of protons are measured in deep inelastic scattering experiments, for example at the HERA accelerator [13]. Figure 2.3 shows the PDFs of the quarks and gluons inside the proton at the scales $Q^2 = 10\,\mathrm{GeV}^2$ and $Q^2 = 10^4\,\mathrm{GeV}^2$ [12]. As shown in the plots, the valence quarks carry a higher fraction of the proton's momentum compared to the sea quarks and gluons. However, for higher Q^2, the momentum fraction carried by the sea quarks becomes more important.

The cross-section of a hadronic process like $pp \rightarrow X$ is

$$\sigma(pp \rightarrow X) = \sum_{ff'} \int_0^1 dx_1 dx_2 f_f(x_1) f_{f'}(x_2) \hat{\sigma}, \qquad (2.39)$$

where the sum runs over all types of parton pairs ff' that may contribute to the process. $\hat{\sigma}$ is the cross-section of the hard scattering. It is constrained by the kinematics of the collision event (namely x_1, x_2 and E_{CM}), by the involved interaction, and by the type of the incoming particles. Detailed derivations of cross-section calculations can be found in [4].

2.6. Tests and limitations of the Standard Model

The Standard Model of particle physics, which was described in the previous sections, was tested in many experiments over the last decades. Thereby, the predictions of the electroweak and QCD quantum field theories could be confirmed. Table 2.4 shows the Standard Model predictions and measurements of some important quantities: m_t, m_W, and m_Z are the masses of the top quark, the W boson and Z boson, respectively. Γ_Z, $\Gamma_Z(\text{hadronic})$, $\Gamma_Z(\text{invisible})$, and $\Gamma_Z(\ell^+\ell^-)$, are the decay widths of the Z boson in decays to all particles, to hadrons, to neutrinos, and to charged leptons, respectively. The decay width of a particle is defined as the reciprocal of its lifetime τ. σ_{hadronic} is the total hadronic cross-section in electron-positron annihilations at a center-of-mass energy corresponding to m_Z. In all cases, the agreement between measurements and predictions is excellent.

Despite the success of the Standard Model, the Higgs boson, which was introduced to break the electroweak symmetry, was not yet discovered. In the Standard Model, the Higgs is introduced as spin- and charge-less, whereas its mass is a free parameter of the theory. Searches for the Higgs at the LEP experiments, however, established a lower limit on the Higgs mass of $m_H > 114.4\,\text{GeV}$ at 95 % CL [14]. An upper limit can be estimated from the dependancies of the Higgs mass on measurable quantities, like the masses of the W boson and the top quark. The upper limit quoted in [15] is $m_H \leq 157\,\text{GeV}$ at 95 % CL. When the exclusion of the Higgs for a mass lower than $114\,\text{GeV}$ from the LEP experiments is included, this limit moves up to $186\,\text{GeV}$. It is important to note, that with $150\,\text{GeV} \leq m_H \leq 180\,\text{GeV}$ the Standard Model stays consistent up to the Planck scale. The search for the Higgs at the Large Hadron Collider [16] is addressed in Chapter 9.

However, even with the discovery of the Higgs boson and the determination of its mass, the Standard Model leaves some unanswered questions:

- **Dark matter:** The observations of the rotational movement of galaxies deviate significantly from the theoretical predictions of the gravitational theory. An expla-

Quantity	Measurement	Standard Model best fit
m_t [GeV]	$170.9 \pm 1.8 \pm 0.6$	171.1 ± 1.9
m_W [GeV]	80.428 ± 0.039	80.375 ± 0.015
m_Z [GeV]	91.1876 ± 0.0021	91.1874 ± 0.0021
Γ_Z [GeV]	2.4952 ± 0.0023	2.4968 ± 0.0010
Γ_Z(hadronic) [GeV]	1.7444 ± 0.0020	1.7434 ± 0.0010
Γ_Z(invisible) [MeV]	499.0 ± 1.5	501.59 ± 0.08
$\Gamma_Z(\ell^+\ell^-)$ [MeV]	83.984 ± 0.086	83.988 ± 0.016
σ_{hadronic} [nb]	41.541 ± 0.037	41.466 ± 0.009

Table 2.4.: Comparison of the measured values and Standard Model predictions of important quantities of the Standard Model. Three masses and four decay widths of the Z boson are shown. σ_{hadronic} is the hadronic cross-section in electron-positron annihilations at a center-of-mass energy corresponding to m_Z [1].

nation for this phenomenology could be the so-called *dark matter*. So far, a possible candidate particle that could form the dark matter has not been found.

- **Hierarchy problem:** The Standard Model favors a Higgs mass of the order of $m_H \sim 100\,\text{GeV}$. The Higgs mass is affected by *quantum corrections* by virtual effects of every particle that couples to the Higgs. These radiative corrections lead to divergencies of the Higgs mass that have to be cancelled very precisely by nature. However, in theory there are no mechanisms at hand to provide this cancellation, since one assumes, that there is no new physics between the electroweak and the Planck scale. Thus, an extreme fine-tuning up to the masses of the Planck scale is required to keep the mass of the Higgs small.

- **Grand unification** The *grand unification theory* (GUT) tries to extend the electroweak unification described in Section 2.3 to the strong interaction. The idea behind this theory is, that the three observed interactions can be merged to a single, more fundamental interaction at a higher energy scale (GUT scale). This implies, that the couplings of the three interactions unify at this scale, which they do not within the frame of the Standard Model.

These questions are addressed by a variety of proposed *beyond Standard Model* theories. The most popular one is *Super-Symmetry*, where a super-symmetric partner for every Standard Model particle is introduced. An introduction to Super-Symmetry can be found in [17]. Other approaches use extra space dimensions or additional symmetries like *technicolor*. However, up to date, no experimental evidence for these or other extensions

of the Standard Model has been found. An exception are the observed neutrino masses, which are zero within the frame of the Standard Model.

The search for the Higgs boson and phenomena beyond the Standard Model is addressed in upcoming collider experiments, such as the Compact Muon Solenoid at the Large Hadron Collider.

Chapter 3.

Compact Muon Solenoid experiment at the Large Hadron Collider

This chapter introduces high energy physics experiments in general and describes in particular the Large Hadron Collider (LHC) and the Compact Muon Solenoid experiment (CMS) used for this thesis.

3.1. High energy physics at colliders

Particle physics research at colliders uses accelerated particles to convert their energy into matter according to Einstein's equation $E = mc^2$. Since the 1950s, scientists have discovered hundreds of particles in experiments using collisions induced by high energy particle beams. The results of these experiments have contributed significantly to the development and the validation of the Standard Model of particle physics (Chapter 2).

Particle accelerators are classified according to the kind of particles they accelerate. Electrons, positrons, protons, anti-protons, and heavy ion beams are used to study a variety of physics topics. In inelastic collisions of hadron beams, the "hard" interaction happens between the constituents of the hadrons, the quarks and gluons. Since the quarks and gluons carry a fraction of the hadron's momentum, according to the parton distribution function described in Section 2.5, the collision energy is a function of the parton distribution functions of the colliding hadrons. Thus, the resulting collision energies cover a wide range of particle masses, which can be produced in the collisions. This allows to discover particles with an unknown mass without changing the beam energy. In 1983 for example, the experiments UA1 and UA2 discovered the W and Z bosons using a proton anti-proton collider [18, 19]. The disadvantage of hadron collisions is the high rate of unwanted "soft" collisions that accompany the "hard" process and

therefore all interesting events. These "soft" collisions can be considered as a kind of noise that disturbs the measurement.

In lepton colliders, however, the energy of the colliding particles is precisely known, since leptons are point-like particles. Accordingly, the kinematics of these collision events is entirely constrained. Therefore, lepton accelerators are preferably used to perform high precision measurements of known or precisely predicted effects and particles. For example the masses of the W and Z bosons and the Z's decay width were measured with high precision at LEP [6, 7] at CERN.

One also distinguishes between linear accelerators and circular, so-called synchrotron accelerators. The main advantage of synchrotrons is the continuous beam acceleration, since the particles pass the same acceleration elements many times to achieve their nominal energy. The possibility to establish several collision points along the synchrotron ring allows to run several experiments in parallel. The disadvantage of a synchrotron accelerator is the continuos loss of beam energy due to synchrotron radiation. For a particle with mass m and energy E the energy loss per circulation is

$$\Delta E = \frac{4\pi\alpha}{2R}\beta^3\gamma^4, \text{with } \beta = \frac{v}{c} \text{ and } \gamma = \frac{E}{mc^2}, \tag{3.1}$$

where α is the fine structure constant, and R is the radius of the accelerator.

The experiments performed with particle beams are either fixed-target experiments, where incoming particles are scattered on a fixed, typically solid, liquid, or gaseous block of target matter, or collider experiments, where two incoming particle-beams are colliding head-on. The two parameters typically characterizing both experiments are the center-of-mass energy E_{CM} of the colliding particles and the luminosity. The luminosity of a fixed target experiment is defined as

$$\mathcal{L} = \Phi \times N, \tag{3.2}$$

where Φ is the flux of the incoming particle beam, and N the number of target particles. The luminosity of a collider experiment is defined as:

$$\mathcal{L} = \frac{N_a N_b n f}{A}, \tag{3.3}$$

with N_a (N_b) the number of particles per bunch in beam a (beam b), n the number of particle bunches per beam-type, f the frequency of the circulations, and $A = 4\pi\sigma_x\sigma_y$ the beam area at the interaction point (σ_x and σ_y are the width of the Gaussian shaped transverse beam profile). For the same beam parameters, the luminosity of fix target

experiments is much higher than that of colliders, since the particle density in the fixed targets is generally higher than in a second beam. At a given beam energy, however, the center-of-mass energy of colliders is much higher than of fixed target experiments, as can bee seen from the corresponding formulae

$$E_{CM}^{fixed-target} = \sqrt{2E_{beam} \cdot mc^2} \tag{3.4}$$

and

$$E_{CM}^{collider} = 2E_{beam}, \tag{3.5}$$

where E_{beam} is the beam energy and mc^2 the rest mass of a single target atom.

The number of processes $X \rightarrow Y$ which are expected to occur in an experiment during the time-interval $t_2 - t_1$, is computed as

$$N = \sigma(X \rightarrow Y) \times \mathcal{L}_{int}, \tag{3.6}$$

where $\mathcal{L}_{int}$ is the luminosity integrated over the time-interval $t_2 - t_1$. $\sigma(X \rightarrow Y)$ is the time independent cross-section of the process $X \rightarrow Y$ predicted by theory or already measured in another experiment. The cross-section of a process is determined by the kinematics of the collision event, and by the particles and interactions involved in the reaction (Section 2.5).

3.2. Large Hadron Collider

The Large Hadron Collider (LHC) is a proton-proton synchrotron located at CERN near Geneva, Switzerland [16, 20]. LHC has a nominal center-of-mass energy of 14 TeV and a design luminosity of $10^{34}\,\mathrm{cm}^{-2}\mathrm{s}^{-1}$. The LHC was installed in the LEP tunnel ring, which has a circumference of 26.7 km and is situated underground at an average depth of 100 m.

To keep proton beams on a circular orbit, a magnetic field is required. LHC uses 1232 superconducting dipole magnets that provide a maximal magnetic field strength of 8.33 T. They have a length of 14.3 m each and operate at a temperature of 1.9 K. The corresponding maximal energy of the proton beams is 7 TeV. Additionally, 400 quadrupole-magnets are installed to focus the proton beams.

The accelerator chain of LHC is displayed in Figure 3.1. Protons are accelerated by the linear accelerator (LINAC), the Booster, the proton synchrotron (PS), and the
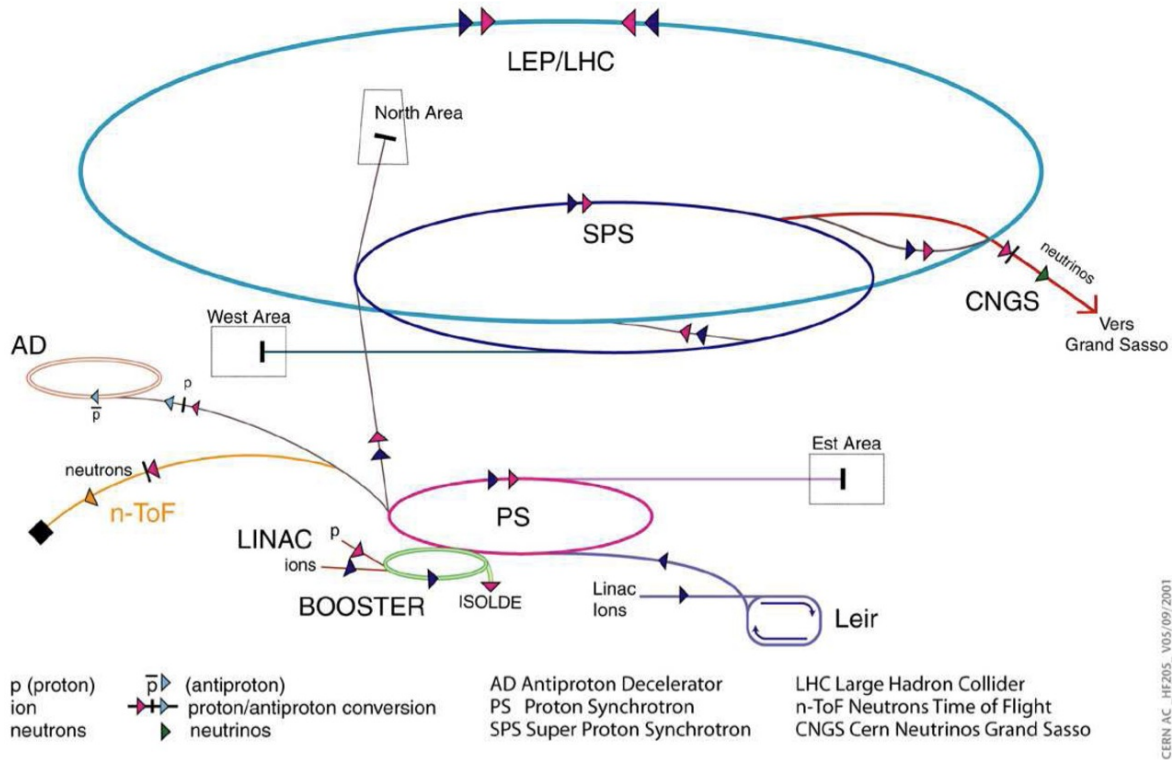
Figure 3.1.: The acceleration chain at CERN.

super proton synchrotron (SPS) up to an energy of 450 GeV before being fed into the LHC ring. LHC uses radio-frequency cavities to accelerate the particles to their maximal energy of 7 TeV. At design luminosity, each of the two beams is foreseen to contain up to 2 808 bunches, each bunch consisting of $\sim 1.5 \times 10^{11}$ protons. The expected minimal diameter of the beams is 16 μm at the four interaction points along the beam line. Under perfect conditions, the total fill- and ramping-time is predicted to be in the order of one hour. After having reached the nominal energy, the beams can be used for head-on collision reactions. The nominal bunch crossing rate at the interaction points is 40 MHz. The physics-time for one fill, i.e. the time until the luminosity drops below some useful value, is estimated to be around 20 hours. The reasons for the degradation of LHC's luminosity are the high cross-section of $\sigma_{tot} = 100$ mb [21] at the interaction points, intra-beam scattering[1], and collision of the beam with beam-gas particles[2].

The first proton beams with an energy of 450 GeV circulated on 10 September 2008. Due to a serious defect on 19 September 2008 in one interconnection between two of the accelerator's superconducting dipole magnets, the operation had to be stopped. The repairs lasted more than one year. On 20 November 2009, the proton beams were again

---

[1] Intra-beam scattering is the multiple Coulomb scattering between charged particles in a beam.

[2] Beam gas are leftover particles in the vacuum beam lines.

successfully circulated with an energy of $450 \, \text{GeV}$. The first proton-proton collisions at $E_{CM} = 900 \, \text{GeV}$ were recorded on 23 November 2009 and the first collisions at $E_{CM} = 2.36 \, \text{TeV}$ on 8 December 2009. The beam parameters of LHC reached in 2009 were:

- Proton energy $= 1.18 \, \text{TeV}$ per beam,

- number of protons per bunch $\sim 10^{10}$,

- number of bunches per beam $= 16$ at $450 \, \text{GeV}$ and 2 at $1.18 \, \text{TeV}$,

- beam diameter $= 250 \, \mu m$ at $450 \, \text{GeV}$ and $120 \, \mu m$ at $1.18 \, \text{TeV}$.

The integrated luminosities collected by each experiment were about $30 \, \mu b^{-1}$ at $900 \, \text{GeV}$ and $1 \, \mu b^{-1}$ at $2.36 \, \text{TeV}$. On 30 March 2010, LHC achieved for the first time collisions with center-of-mass energies of $7 \, \text{TeV}$, which is the highest energy reached at a particle collider to date.

In addition to the proton-proton program, LHC can also accelerate heavy ion beams, e.g. lead ions. Herby, the design center-of-mass energy of the nucleon-nucleon collisions is $5.5 \, \text{TeV}$, with a nominal luminosity of $10^{27} \, \text{cm}^{-2}\text{s}^{-1}$. The first lead ion collisions are planned for end of 2010.

Four experimental sites are situated along the accelerator at the interaction points: ATLAS (**A T**oroidal **LHC A**pperatu**S**) [22] and CMS (**C**omact **M**uon **Solenoid**) are general purpose detectors designed to fully exploit the physics potential offered by LHC. LHC-b (**L**arge **H**adron **C**ollider **B**eauty Experiment) is specialized in the investigation of b-quark physics and CP-violation [23]. ALICE (**A L**arge **I**on **C**ollider **E**xperiment) is dedicated to investigate lead ion collisions and the so-called quark-gluon plasma [24].

Additionally, there are the two smaller experiments. TOTEM (**TOT**tal Cross-Section, **E**lastic Scattering and Diffraction Dissociation at the LHC) is situated near the CMS experiment, and LHCf (**L**arge **H**adron **C**ollider **f**orward) near Atlas [25, 26].

3.3. The Compact Muon Solenoid detector

The CMS experiment is designed to the study proton-proton as well as heavy ion collisions at the LHC [21, 27, 28]. The aim of the experiments is to investigate and measure the following research topics:

- The study of Standard Model processes like electroweak, QCD, and top physics.

- The detection of the Higgs boson in the mass range of $100 \, \text{GeV}$ to $1 \, \text{TeV}$.

- The search for phenomena that reach beyond the Standard Model (e.g. supersymmetry or extra dimensions).

To meet the goals of this physics program, CMS must provide an accurate energy and momentum measurement for electrons, photons, and muons. Additionally, CMS provides good measurements of hadron jets and missing transverse energy (Section 8.2).

The CMS detector has a cylindric shape with the symmetry axis, the z-axis, given by the beam pipe. The detector consists of a barrel part, which is sealed with two end-caps installed perpendicularly to the beam axis. This geometry covers almost the complete solid angle around the proton-proton interaction point, which is the center of the CMS coordinate system. The y-axis points vertically upward, and the x-axis points radially inward toward the center of the LHC. The azimuthal angle ϕ is measured from the x-axis in the $x - y$ plane (the *transverse* plane) and the radial coordinate in this plane is denoted by r. The segmentation of the detector in the $r - z$ plane is characterized by the rapidity. For a particle with energy E and momentum p_z in the direction of the beam axis, the rapidity is defined as

$$Y = 0.5 \ln \left(\frac{E + p_z}{E - p_z} \right). \tag{3.7}$$

If the mass of the particle can be neglected with respect to its energy, the rapidity is approximated by the pseudorapidity which is defined as

$$\eta = - \ln \left(tan \, \frac{\theta}{2} \right), \tag{3.8}$$

where θ is the particle's angle along the beam axis. The CMS barrel covers a pseudorapidity range of $|\eta| < 1.5$ and the end-caps a range of $1.5 < |\eta| < 3$. Additionally, a forward detector is installed, which reaches up to $|\eta| = 5.3$.

The detector has a length of $21.6 \, \mathrm{m}$, a diameter of $14.6 \, \mathrm{m}$, and a total weight of $\sim 12 \, 500 \, \mathrm{t}$. The CMS experiment is divided into several sub-systems as displayed in Figure 3.2. Starting from the beam axis, the systems are: a tracker, an electromagnetic calorimeter, a hadronic calorimeter, a $3.8 \, \mathrm{T}$ super-conducting solenoid, and an outer muon system. Figure 3.3 shows the details of these subsystems in a $r - z$ cut of one quadrant of CMS. In the following sections, these CMS components and the trigger system, which performs the online event selection, are described.
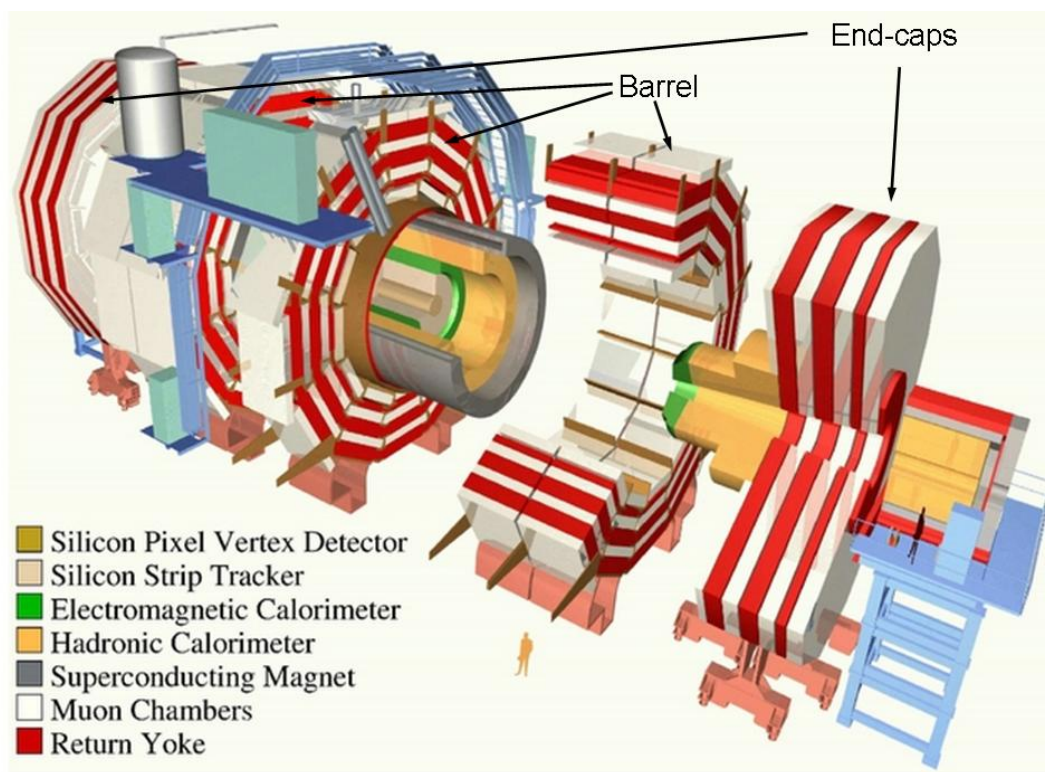
Figure 3.2.: Overview of the CMS detector and its major components.
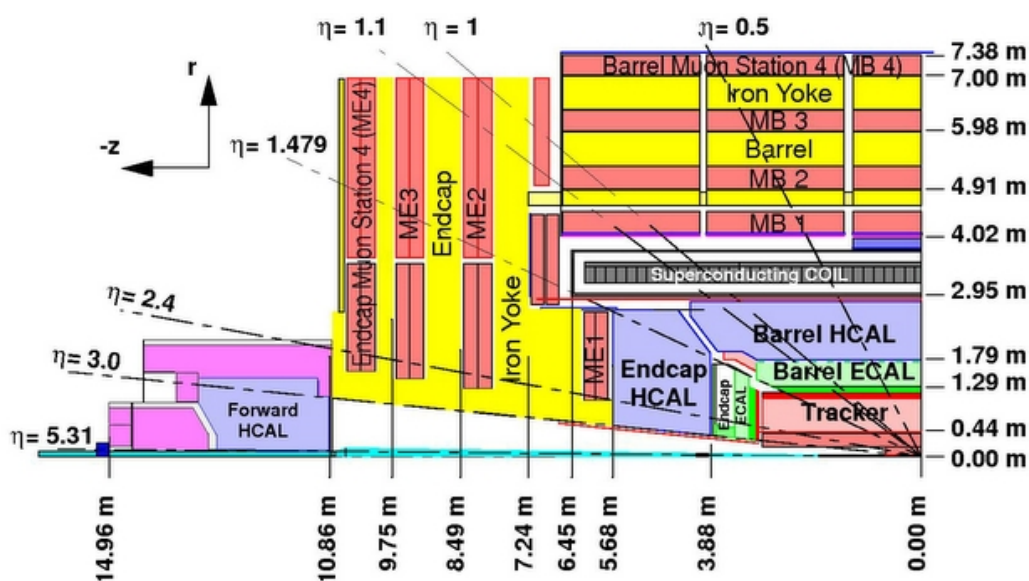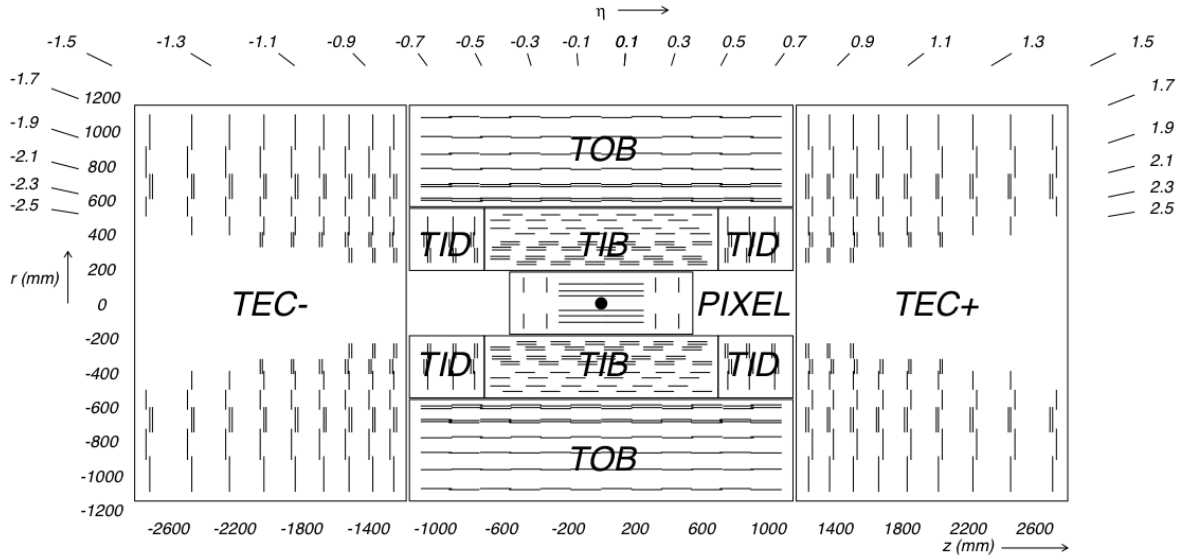

Figure 3.3.: One quadrant of the CMS detector from the side. The segmentation of the detector in the $r - z$ is characterized by the pseudorapidity $\eta = -ln \ (tan \ \frac{\theta}{2})$, where θ is the angle along the beam axis.

Figure 3.4.: Schematic transverse view of the tracker systems. PIXEL is the pixel detector. The TIB and TOB are the tracker inner and outer barrel; TID denotes the tracker inner discs, and TEC± the tracker end-caps.

3.3.1. Tracker

The tracking system, located around the interaction point in the center of CMS [29], consists of a silicon pixel detector and a silicon microstrip detector. The tracker provides precise measurements of tracks, impact parameters, and secondary vertices of charged particles. It has a high granularity and a fast response, such that the trajectories can be identified reliably and attributed to the correct bunch crossing.

The pixel detector will allow a precise vertex reconstruction and measure data points for the track reconstruction. It spans a radius range of 40-200 mm from the interaction point and consists of three layers in the barrel and two discs in each end-cap. The pixel detector contains 66 million pixels in total. One pixel cell has a surface of $100 \times 150 \, \mu\text{m}^2$.

The silicon microstrip detector spans the outer tracker region up to a radius of 1 160 mm. In the barrel it consists of four inner and six outer layers. On each side of the inner layers three inner discs are installed. The end-cap silicon-strips consists of nine additional discs (Figure 3.4). In total, the tracker is built up of a total of 15 148 silicon microstrip modules with an active silicon area of about 198 m². The silicon detectors are expected to develop an increased leakage current, which increases their electronic noise due to the high radiation flux. To limit this aging effect, the tracker is operated at a temperature of $-10°$C, which is provided by a dedicated cooling system.

The track reconstruction efficiency is estimated to be 95%. The expected transverse momentum resolution of the tracker Δp_T for muons as a function of p_T is shown in
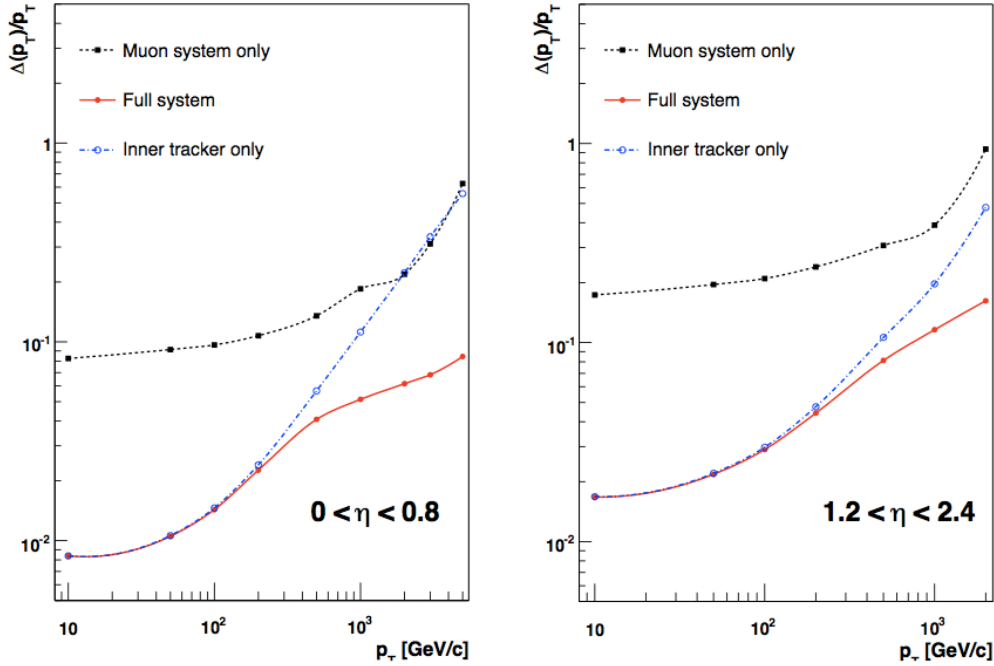
Figure 3.5.: The muon transverse momentum resolution as a function of the transverse momentum using the muon system only, the inner tracking only, and combining both systems for $|\eta| < 0.8$ (left side) and for $1.2 < |\eta| < 2.4$ (right side) [21].

Figure 3.5 for the central region ($|\eta| < 0.8$), and for $1.2 < |\eta| < 2.4$ using Monte Carlo simulations.

3.3.2. Calorimeter systems

The Electromagnetic Calorimeter (ECAL) and the Hadron Calorimeter (HCAL) are located between the tracker and the magnet coil [30, 31]. The ECAL detects electrons and photons. It is a homogeneous calorimeter made of scintillating lead tungstate ($PbWO_4$) crystals, which are installed in the barrel and the end-caps. The crystals are read out by photo detectors. A pre-shower detector precedes the ECAL end-caps. Chapters 4, 5 and 6 will describe the ECAL and its performance in detail.

The HCAL measures the energy and position of hadrons and particle jets. It is is a sampling calorimeter composed of $50\,mm$ thick brass absorber plates interleaved with $4\,mm$ thick plastic scintillators. The scintillation light of showering particles is converted by wavelength-shifting fibers, embedded in the scintillator tiles and channeled to photodetectors via optical fibers. The photodetectors used are hybrid photo-diodes, which amplify signals and operate in high axial magnetic fields. The HCAL barrel and end-caps cover a pseudorapidity range up to $|\eta| = 3$. The barrel has an inner radius

of 1.79 m, a length of 9 m, and a thickness of 1.16 m. The disk shaped HCAL end-caps are 1.8 m thick. Additionally, a forward iron/quartz-fibre calorimeter reconstructs jets up to $|\eta| = 5$. It is situated outside the muon system near the beam axis. The HCAL thickness, in interaction lengths, varies in the range 7-11 λ_I, depending on η.

3.3.3. Magnet

In CMS, a superconducting solenoid magnet [32] provides a homogeneous magnetic field of B = 3.8 T. It is used to measure the transverse momentum p_T of charged particles with the tracker (Section 3.3.1) using the relation $p_T = 0.3 \cdot q \cdot B \cdot R$, where q is the charge of the particle and R the radius of the circular trajectory in the magnetic field of strength B. The solenoid coil has a weight of 220 t, a length of 12.48 m, a thickness of 0.31 m and an inner diameter of 6.3 m, which was chosen large enough to install all calorimeters system inside the solenoid. This setup avoids scattering, absorption, and showering of particles in the solenoid material before entering in the calorimeters, which would degrade the resolution of the electromagnetic and hardronic energy measurements. The exception is the so-called tail-catcher of the HCAL, which is installed centrally to ensure the measurement of high transverse momentum jets.

The magnetic flux is returned trough saturated iron, the so-called return yoke. The yoke splits into three rings in the barrel and two discs in each end-cap. The outer diameter of the yoke is 15.0 m across flats, and its axial length including end-caps is 21.5 m. The yoke has a total weight of about 11 400 tons.

3.3.4. Muon system

The CMS muon system is the outermost part of the detector and inter-leafs the rings and disks of the iron return yoke [33]. It identifies muons and performs a second measurement of their transverse momenta. The muon system consists of tracking detectors and magnetized iron, the return yoke of the magnetic field (Figure 3.6). The tracking detectors of the muon system are: large drift chambers in the barrel region ($|\eta| < 1.2$) called drift tubes (DT), fine segmented cathode strip chambers (CSC) in the end-caps ($0.9 < |\eta| < 2.4$), and resistive plate chambers (RCP) in both barrel and end-caps, which are used to provide the muon trigger because of their fast response. The efficiency of the muon track reconstruction is expected to be above 95% for muons with energies above 1 GeV and $|\eta| < 2$. The expected transverse momentum resolution Δp_T for muons using the muon system, the tracker and both together as a function of p_T is shown in Figure 3.5 for the central region ($|\eta| < 0.8$) and for $1.2 < |\eta| < 2.4$.
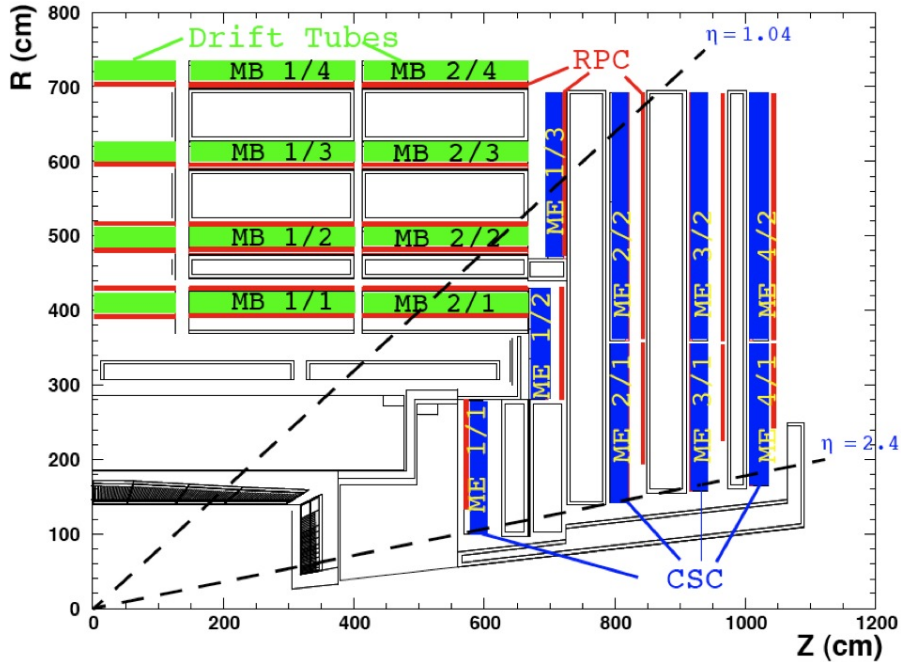
Figure 3.6.: R-z cut view of one quadrant of CMS muon system.

3.3.5. Trigger

At the design luminosity of $10^{34}\,\mathrm{cm^{-2}s^{-1}}$, 25 inelastic proton-proton collisions are on average expected per bunch crossing. The resulting rate of inelastic collisions is expected to be about $1\,\mathrm{GHz}$, which corresponds to a data flow of about $1000\,\mathrm{TB/s}$. However, the maximal rate that can be processed by CMS Data Acquisition System (DAQ) is $\sim\!100\,\mathrm{MB}$ per second. The necessary reduction is performed by the CMS trigger system, which reduces this rate down to $100\,\mathrm{Hz}$ by preselecting only interesting physics events [34]. The on-line reduction is achieved in two steps: the level 1 trigger (L1) and the high level trigger (HLT). Both are digital triggers. L1 is purely based on the measurements of the calorimeters and muon systems. In particular, the identification of muons, electrons, photons, jets, and missing transverse energy is used. The design output rate limit of the L1 trigger is $100\,\mathrm{kHz}$, which is translated in practice to a calculated maximal output rate of $30\,\mathrm{kHz}$. The HLT is divided into the level 2 and 3 (L2 and L3) trigger steps. Due to the rate reduction of the L1 trigger, more information can be processed for this trigger selection. L2 takes into account a finer granularity of the calorimeter and muon systems, together with precise tracking data, event kinematics and topology. The resulting L2 rate is designed to be $10^3\,\mathrm{Hz}$. The final reduction to a rate of $100\,\mathrm{Hz}$ (L3 trigger) is achieved with the on-line analysis and event reconstruction. The final data are stored on tape for later analysis.

Chapter 4.

Electromagnetic calorimeter

The measurement of the energy of electrons and photons with very high accuracy is of primary importance for the study of many physics processes with the CMS experiment. In particular, the searches for the Higgs boson is strongly based on decays with leptonic and photonic final states (Chapter 9). The choice of an high-resolution and high-granularity crystal calorimeter increases the ability to observe single electrons and photons above background. The fast response of the crystals, with respect to the LHC collision rate, avoids pileup of events from different bunch crossings. This chapter describes the structure of the ECAL, the scintillating crystals, and the photo detectors used to measure electron and photon energies. The functionality of the on-detector and off-detector readout chains, and the light monitoring and the detector control systems are summarized. The chapter is completed by a description of the ECAL resolution parameters. A more detailed description of the ECAL can for example be found in [35].

4.1. Layout and mechanics

The barrel part of the ECAL contains 61 200 lead tungstate ($PbWO_4$) crystals, which cover a pseudorapidity of $|\eta| < 1.479$ (Figure 4.1). The crystals are mounted in an off-pointing geometry, with a $\sim 3°$ tilt in both ϕ and η with respect to the interaction point. This avoids, that particles pass undetected through the gaps between the crystals. The granularity is 360-fold in ϕ and 170-fold in η. The design of the ECAL barrel is based on modularity (Figure 4.2). Arrays of 2×5 crystals grouped in a $200\,\mu$m thick glass fiber support (the so-called alveolar structure) form a sub-module. The sub-modules are assembled together on four different types of aluminum grids, the modules. Modules of type 2, 3 and 4 carry 20×20 crystals, and modules of type 1 20×25 crystals in $\phi\times\eta$. Four modules, one of every type, are mounted together into an aluminum support structure, the super-module. In total, one super-module consists of 20×85 crystals in $\phi \times \eta$. All
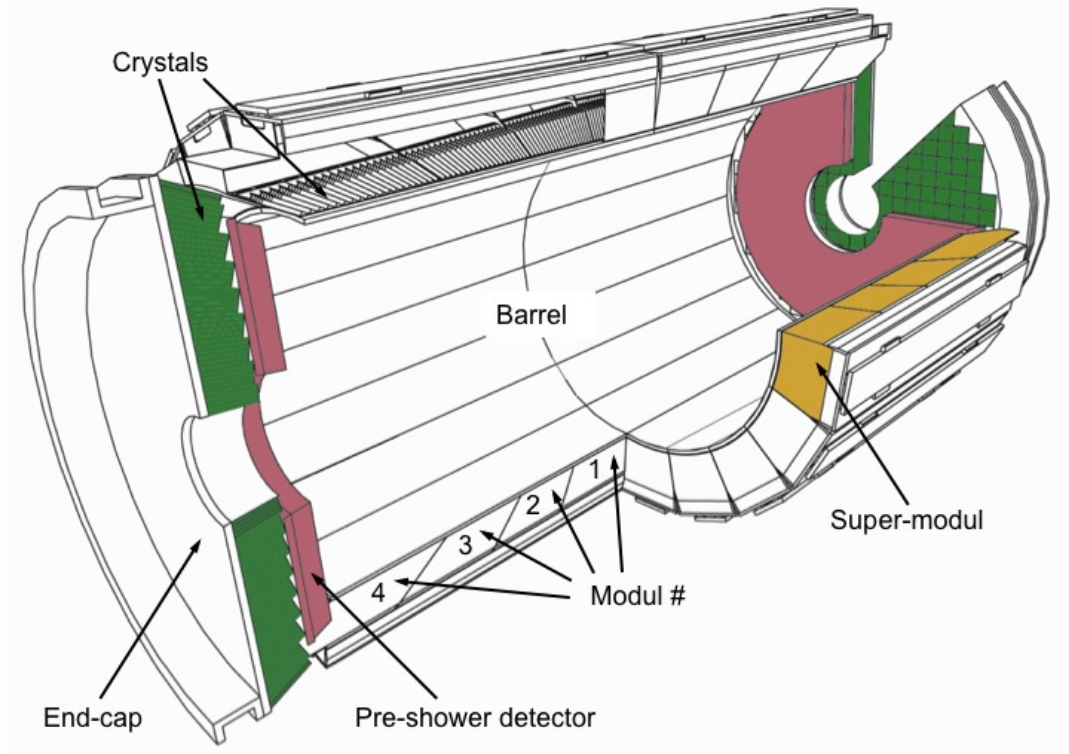
Figure 4.1.: The electromagnetic calorimeter.

services, cooling manifolds and cables converge to a patch panel at the external end of the super-module. Eighteen super-modules, each covering $20°$ in ϕ, form one of the two half barrels. One super-module has a total weight of ~ 3.5 tons, and the total weight of the ECAL barrel is about 125 tons.

The nominal ECAL operation temperature is $18 \pm 0.05°$C. Since the overall response of the ECAL to incoming electrons and photons varies by $-3.8 \pm 0.4\%/°$C, a dedicated cooling system assures a tight ambient temperature spread of $\pm 0.05°$C. Sections 4.2 and 4.3 describe the temperature dependances of the crystal light yield and the gain of the avalanche photo-diodes (APDs). Each super-module carries an autonomous cooling system that works with demineralized water at ~ 7 bar and consists of two parts. First, the cooling water of $18°$C enters a thermal shield that decouples the crystal arrays and the APDs from the silicon tracker and keeps their operating temperature stable. Secondly, the cooling water flows through the cooling blocks and evacuates the heat of ~ 4.6 kW generated by the electronics of the super-module.

The ECAL end-caps cover a pseudorapidity range of $1.48 < |\eta| < 3.0$ and consist of 14 648 crystals in total. High resolution energy measurements, however, are expected to be only possible for $|\eta| < 2.5$ due to the high flux of particles in the forward direction
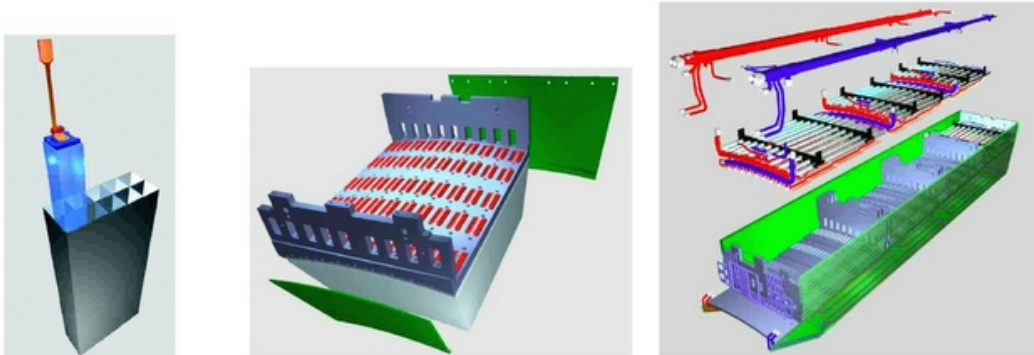
Figure 4.2.: The ECAL modularity from left to right: sub-module, module, super-module with cooling circuits.

of the detector. The crystals between the pseudorapidities 2.6 and 3 are installed to upgrade the energy-flow measurement. The crystal orientation is also off-pointing to ensure hermeticity. Each end-cap is divided into two halves or dees (due to their D-like shape) consisting of mechanical groups of 5×5 crystals assembled together into a carbon-fibre alveolar structure (super-crystals). The 3 662 crystals of one dee are contained in 138 standard super-crystals and 18 special partial super-crystals at the inner and outer circumference of the dee. The cooling system of a dee is similar to the one of a super-module. In front of each end-cap, a pre-shower detector is installed to improve π^0/γ separation. It covers a pseudorapidity range of $1.653 < |\eta| < 2.6$. The detector contains two layers of lead absorbers with a thickness of about three radiation lengths, followed by two orthogonal detector planes of silicon strip detectors with a pitch of $1.9\,\mu$m.

4.2. Lead tungstate crystals

The ECAL uses lead tungstate ($PbWO_4$) crystals as detector and scintillator material (Figure 4.3). The most important characteristics of the crystals used in barrel and end-caps are summarized in Table 4.1. $PbWO_4$ is a very fast scintillator with respect to the LHC collision rate: 80% of the scintillation light is emitted in $\sim$25 ns. It has a high density of $8.28\,$g/cm^3, a small Moliere radius of $2.19\,$cm, and an electromagnetic radiation length X_0 of $0.89\,$cm. The crystals of the barrel are truncated pyramidal shaped. The cross-section of $22{\times}22\,$mm^2 at the front face matches the Moliere radius. The cross-section at the rear face is $26{\times}26\,$mm^2. They have a total length of $230\,$mm corresponding to $25.8\,X_0$, which limits the longitudinal shower leakage of high-energy electrons and photons to less than $1\,\%$. The exact dimensions of each of the 17 types of
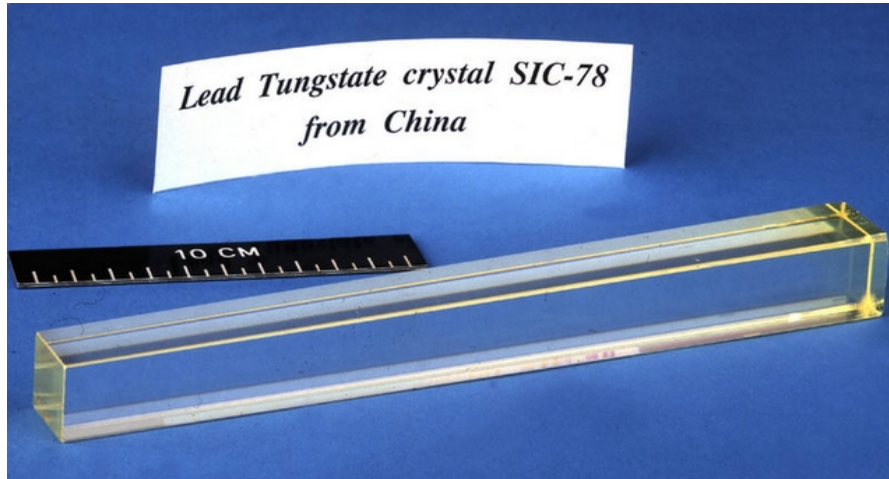
Figure 4.3.: Lead tungstate crystal.

Parameter	ECAL barrel	ECAL end-caps
Geometrical coverage	$|\eta| \leq 1.44$	$1.44 < |\eta| < 3$
Number of crystals	61 200	14 648
Geometrical length	230 mm	220 mm
Geometrical cross-section (front)	$22{\times}22\,\mathrm{mm}^2$	$28.62{\times}28.62\,\mathrm{mm}^2$
Geometrical cross-section (rear)	$26{\times}26\,\mathrm{mm}^2$	$30{\times}30\,\mathrm{mm}^2$
Crystal density	$8.28\,\mathrm{g/cm}^3$	
Radiation length	0.89 cm	
Scintillation time	80% in 25 ns	
Light yield	4.5 photoelectrons/MeV	
Light yield temperature dependance	-2%/°C	

**Table 4.1.:** The main parameters of the ECAL crystals in barrel and end-caps [21].
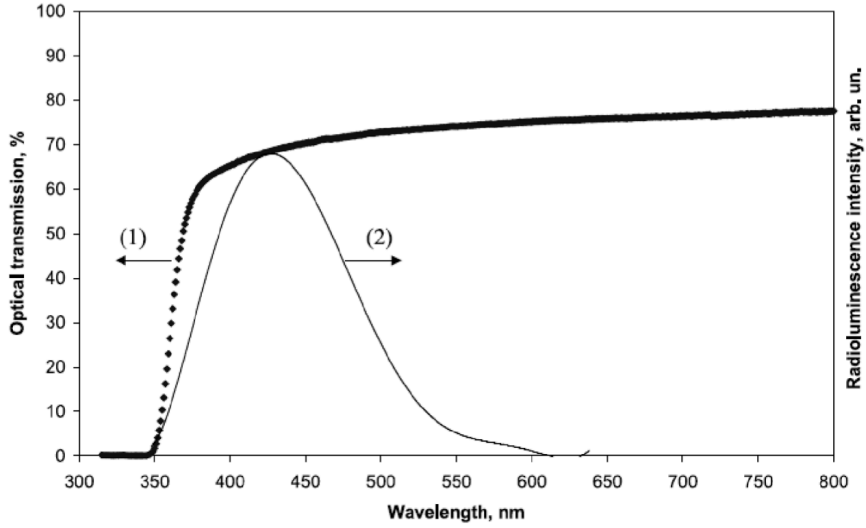
Figure 4.4.: Longitudinal optical transmission (left scale) and radioluminescence intensity (right scale) of PbWO$_4$ crystals.

crystals depend on the position in the ECAL barrel. The crystals of the end-caps have a front face cross-section of $28.62{\times}28.62\,\text{mm}^2$, a rear face cross-section of $30{\times}30\,\text{mm}^2$ and a length of $220\,\text{mm}$ corresponding to $\sim24.7\,\text{X}_0$. These properties allowed it to construct a very compact calorimeter system that could be installed inside the solenoid of CMS. Additionally, according to these parameters, an electron with an energy of $35\,\text{GeV}$ deposits 97% of its energy in a cluster of $5{\times}5$ crystals.

The light-yield of lead tungstate is proportional to the energy of the absorbed particle: ~4.5 photoelectrons are detected per MeV at a crystal temperature of 18°C. The emission spectrum of PbWO$_4$ has a broad maximum at at 420-430 nm. Figure 4.4 shows the longitudinal optical transmission and the radioluminescence spectra [36]. Since the crystal light yield changes by -2 %/°C, the crystals have to be embedded in a constant ambient temperature, that is provided by the cooling system mentioned in Section 4.1. The crystal temperature is controlled via $100\,\text{k}\Omega$ negative temperature coefficient thermistors from Betatherm, that are glued onto every tenth crystal.

In ten years of LHC operation, the crystals are expected to receive a pseudorapidity depended dose of typically 0.15-32 kGy, corresponding to an integrated luminosity of $\sim500\,\text{fb}^{-1}$. The radiation hardness of PbWO$_4$ was improved via optimized growth techniques (Czochralski and modified Bridgman-Stockbarger), by Y/Nb doping, and stoichiometric fine-tuning. Their transparency, however, is expected to degrade under irradiation. Through the formation of color centers, the self-absorption of the crystals is increased and affects the transport of light. The effects of this degradation of the optical transmission anneals at the ECAL operation temperature of 18°C due to the intrinsic
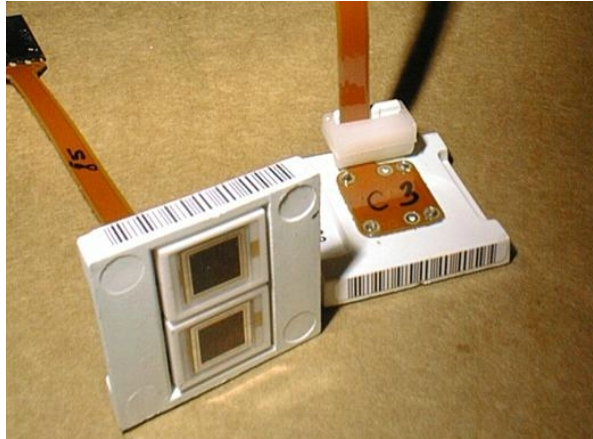
Figure 4.5.: Capsules with two APDs and Kapton cables.

properties of $PbWO_4$. The balance between the damage and the annealing results in a dose-rate dependent equilibrium. The magnitudes of the optical transmission variations are expected to vary between few percent at low luminosities in the barrel and up to tens of percent in the end-caps at high luminosity [37]. These variation have to be corrected permanently during the operation of CMS to avoid a degradation of the ECAL resolution. Therefore, laser light injected to the crystals is used to monitor the evolution of the crystal transparency. The so-called ECAL laser monitoring system is described in section 4.4.6.

4.3. Avalanche photo-diodes

The light produced in a crystal by the passage of ionizing particles is collected by two avalanche photo-diodes (APDs) in the barrel and by one vacuum photo-triode (VPT) in the end-caps [38, 39]. The configuration of the magnetic field and the expected level of radiation led to the different choices. The VTPs are single-stage photomultipliers with a metal grid anode. Due to their compact construction, they can operate in magnetic fields, as long as the angle between their axis and the magnetic field does not exceed 24°, as it is given in the ECAL end-caps. This section concentrates on a description of the APDs (Figure 4.5).

APDs have an intrinsic gain that compensates the low light-yield of the crystals and are sufficiently radiation hard to cope with the high radiation levels during the operation of LHC. It was required, that the APDs operate with a reliability of 99% during the operation period of the CMS detector, because a single faulty APD can derogate the

Parameter	Value
Sensitive area	$5{\times}5\,\mathrm{mm}^2$
Operating voltage	340-430 V
Quantum efficiency (430 nm)	$(75 \pm 2)\%$
Capacitance	$(80 \pm 2)\,\mathrm{pF}$
Serial resistance	$< 10\,\Omega$
Voltage sensitivity of the gain	$3.1 \pm 0.1\,\%/\mathrm{V}$
Temperature sensitivity of the gain	$-2.4 \pm 0.2\,\%/^\circ\mathrm{C}$
Leakage current	$< 50\,\mathrm{nA}$
Excess noise factor	2.1 ± 0.2

**Table 4.2.:** The main parameters of the avalanche photo-diodes [21].

performance of 49 other channels connected to the same HV channel. Most important, the APDs also have to be compatible with the ECAL energy resolution requirements. The APD of type S8141, developed by Hamamatsu, meets these requirements. Its main parameters are summarized in Table 4.2. It has an active area of $5{\times}5\,\mathrm{mm}^2$, a capacitance of $(80{\pm}2)\,\mathrm{pF}$ if fully depleted, a serial resistance of $<10\,\Omega$, and a leakage current of $<50\,\mathrm{nA}$. The quantum efficiency is $(75{\pm}2)\%$ at 430 nm in avalanche mode. The nominal gain of 50 requires an operating reverse bias voltage between 340 and 430 V. Because the gain changes by $3.1\%/\mathrm{V}$, the bias voltage has to be very stable to keep this contribution to the resolution at the per mille level. Additionally, the operation of the APDs requires a constant ambient temperature, due to their temperature dependance of -2.3%/°C. The excess noise factor of the APDs is $2.1{\pm}0.2$ at a gain of 50. The excess noise factor describes the statistical noise, which arises from the stochastic APD multiplication process.

Figure 4.6 shows a schematic view of the APD. Entering photons are absorbed in the p++ layer by generating electron-hole pairs. The electrons drift in the electric field through the p layer towards a p-n junction. There they are amplified by impact ionization and pass through the succeeding n-type material to the n++ electrode, where the charge is collected. V-shaped grooves in the surface of the diode reduce surface currents and improving thus the radiation hardness of the APD.

Two APDs are grouped into one capsule which is glued onto the rear face of one crystal (Figure 4.5). In addition, every tenth capsule contains a thermistor to measure the crystal and APD temperature. The capsule is connected to the detector readout using a Kapton flexible printed circuits board (PCB). The Kapton cable connects to a
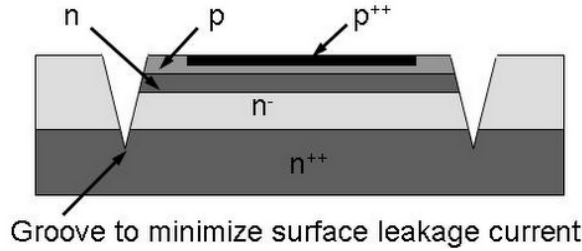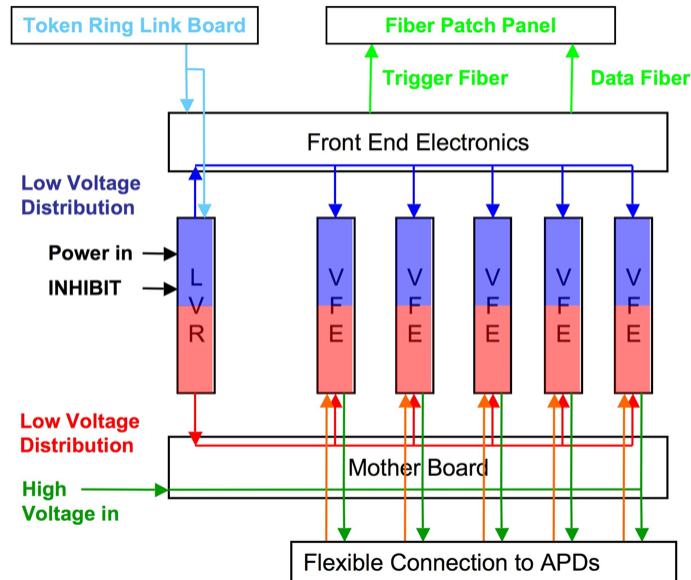
Figure 4.6.: Schematic view of the APD.
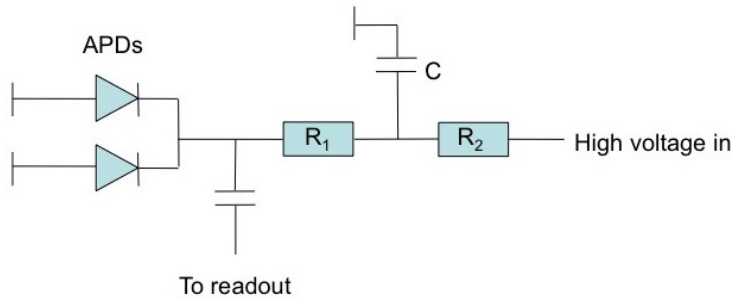
Figure 4.7.: The APD bias circuit.

PCB, the motherboard (Section 4.4.1). Among others, the motherboard contains the so called APD bias circuit (Figure 4.7). Its resistances $R_1 = R_2 = 68\,\text{k}\Omega$ limit possible short circuit currents, such that if one APD is broken, the 49 other capsules sharing the same high voltage supply are not affected. Together with the capacitor C ($10\,\text{nF}$) they compose two low-pass filters reducing the electromagnetic interference between bias voltage supply, APDs and readout electronics.

In irradiation tests with ^{60}Co, the APDs received doses of $5\,\text{kGy}$ [40]. For comparison, an irradiation dose of $0.7\,\text{kGy}$ and $2 \cdot 10^{13}\,\text{n/cm}^2$ is expected to be received by the APDs for an integrated LHC luminosity $500\,\text{fb}^{-1}$. For most of them, no change in any of their electrical properties was observed, with the exception of an increasing leakage current. According to the experiences made in these screenings, it is expected that the APDs will develop a mean leakage current of $5\,\mu\text{A}$ for a total integrated luminosity of $500\,\text{fb}^{-1}$. This results in voltage drops in the series resistances in the APD bias circuit of $\sim\!27\,\text{V}$ each, that have to be adjusted to keep the nominal APD gain of 50.

4.4. On-detector electronics

In the ECAL, a particle's energy loss is first converted into scintillation light, which then gives a photo current. The electrical signal is amplified, shaped and digitized by

Figure 4.8.: Schematic view of the trigger tower readout electronics. VFE and LVR are the Very Front End and Low Voltage Regulator card, respectively.

one ECAL readout channel. The special challenges of the ECAL readout system are the high bunch crossing rate of 40 MHz, the relatively small signals coming from the photo detectors, and the wide dynamic range of the incoming signals. Most importantly, the performance of the electronic system has to be such that it does not degrade the intrinsic ECAL resolution. Therefore, it was required to place the front-end electronics within the detector. This has the advantage of a minimized external noise, while the number of optical links to send data to the off-detector readout is reduced.

The so-called trigger tower electronics (Figure 4.8) reads and processes the data of one trigger tower (5×5 crystals) and provides all necessary services. It containes five Very Front End (VFE) cards [41], one Front End (FE) card [42], one Low Voltage Regulator (LVR) card [43, 44], two (barrel) or five (end-caps) Gigabit Optical Hybrids (GOH), and one motherboard that connects the APDs and VPTs to the readout. The trigger tower electronics uses 13 different types of application specific integrated circuits (ASICs); all of them, except the voltage regulators of the LVR card, are made in $0.25\,\mu$m CMOS technology. In total, 68 trigger towers are installed in one super-module. Due to the total unattainability of the on-detector electronics once installed in the ECAL, all electronics components were tested intensely during production and before their installation into the ECAL.
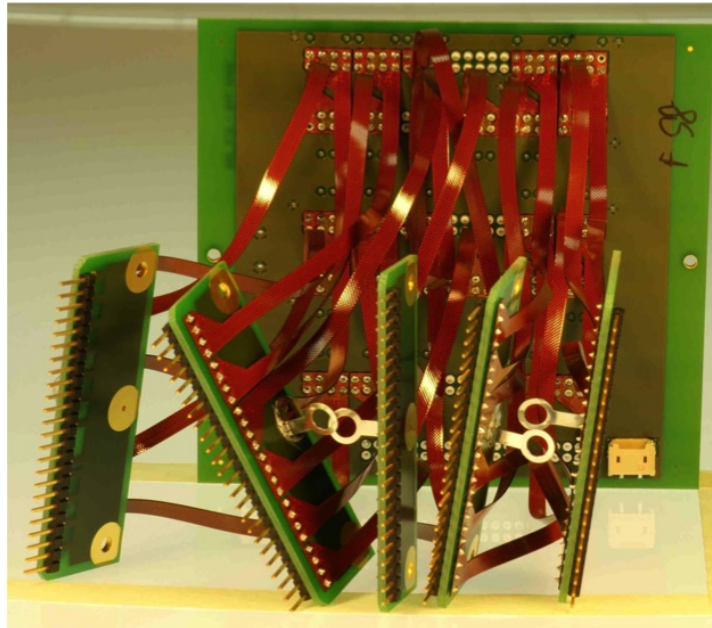
Figure 4.9.: Bottom view of ECAL barrel motherboard. The brown cables are the Kapton
cables, which connect to the small APD connectors in the front. The yellow
connector to the high voltage supply can be seen on the lower right corner of
the motherboard.

4.4.1. Motherboard

The motherboard of the ECAL barrel readout electronics has the following tasks:

- Connect the 25 APD capsules via special Kapton cables to the VFE readout chan-
  nels (see bolow for a description of the Kapton cables).

- Distribute and filter the reverse bias voltage for the APDs.

- Distribute the low voltage from the LVR card to the analog part of the five con-
  nected VFE cards.

Figure 4.9 shows the bottom layer of a motherboard. 25 Kapton cables that connect
to the APD capsules are soldered to it. For the transmission of the temperature data
taken in every tenth capsule, two or three additional Kapton cables are soldered to each
motherboard, depending on the motherboard type. The other end of the Kapton cables
are attached to small pins connectors, that plug into the APD connectors. Each two
motherboards are connected to a single high voltage channel. The HV connector is
visible on the bottom right corner of the motherboard on Figure 4.9.

Figure 4.10 shows the top layer of the motherboard. The five identical black connec-
tors are the VFE card connectors, and the connector on top is the connector for the LVR
card. The VFE connectors are through-hole connectors. The Kapton cables are soldered
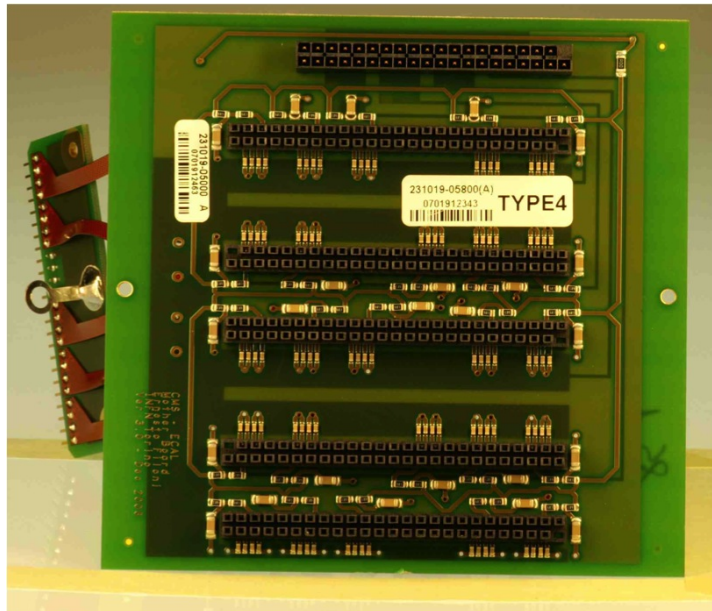
Figure 4.10.: Top view of ECAL barrel motherboard. The black connector on the top connects to the LVR card, the others to the five VFE cards. The surface mounted devices are the resistors and capacitors of the 25 APD bias circuits.
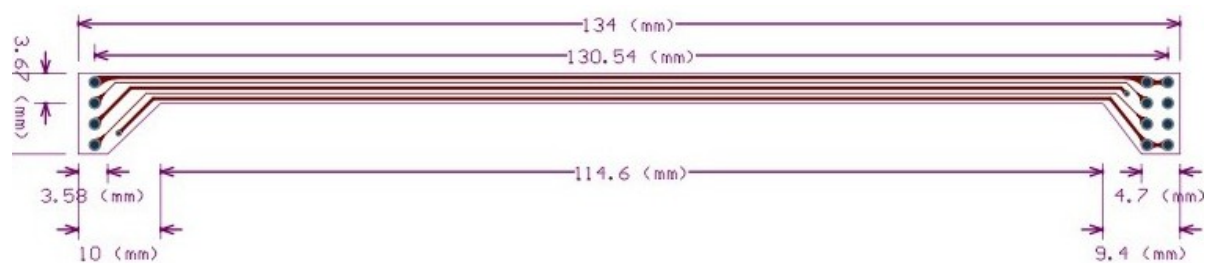
Figure 4.11.: Scheme of the Kapton cable signal layer. The three thicker lines represent the conductors to ground, the two thin ones are the anode and the cathode conductors.

Figure 4.12.: The VFE card with the five parallel readout channels.

to the pins. The low voltage from the LVR card is distributed to the VFEs through the layers of the motherboard. The beige surface mounted devices are the capacitors (10 nF) and the black ones the resistances (68 kΩ) of the 25 APD bias circuits (Figure 4.7).
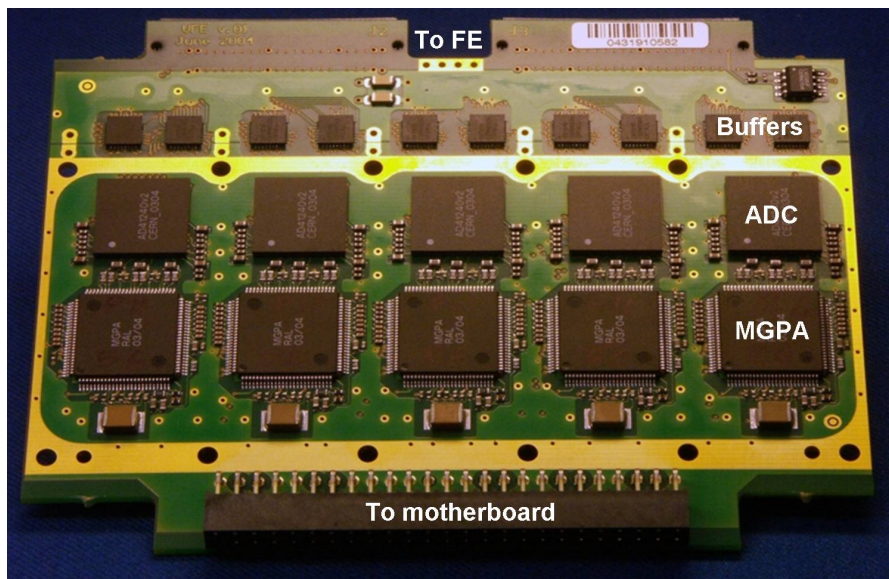
Kapton cables are flexible PCBs made of several layers, in our case a top, a signal, and a bottom layer. The signal layer (Figure 4.11) contains five conductors, three of them are connected to ground and the remaining two are connected to the anode and cathode of the APD. Their order within the Kapton is ground-anode-ground-cathode-ground. The top and bottom layer contain each a grounded mash, which screen the signal layer from parasitic electromagnetic fields.

The motherboard used in the ECAL end-caps is similar. The main differences are the use of coaxial cables instead of Kapton cables and the filter network of the high voltage that is contained on a separate card, the high voltage filter card.

4.4.2. Very front end card

The VFE card amplifies, shapes and digitizes the signals from five crystals in parallel every 25 ns (Figure 4.12). A detailed description of the VFE card and its quality tests can be found in [45]. One readout channel is composed of a Multi Gain Pre-Amplifier (MGPA) [46], followed by a custom designed Analog to Digital Converter (AD41240) [47] and two low voltage differential signal to single ended CMOS buffers (LVDS-Rx), all designed in radiation tolerant CMOS 0.25 μm technology. Figure 4.13 shows the on-detector readout chain that is explained in the following sections.
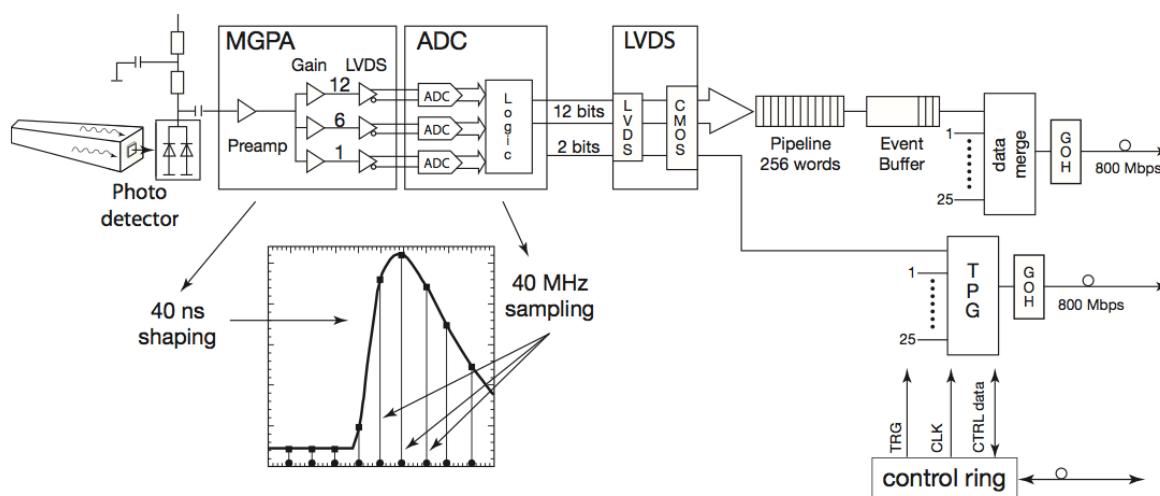
Figure 4.13.: Schematic view of the on-detector readout chain.

The MGPA comprises a low noise pre-amplifier and shaping stage, followed by three amplifiers with nominal gains of 1, 6 and 12 with a precision of $\pm 10\%$ each. The overall gain is fixed by an external resistor of $12\,\mathrm{k\Omega}$ (in the EB) with 0.1% precision, and a temperature dependance of $25\,\mathrm{ppm/^\circ C}$. The full-scale signals of the APDs and VPTs are $60\,\mathrm{pC}$ and $12.8\,\mathrm{pC}$ corresponding to energies of $\sim 1.5\,\mathrm{TeV}$ (barrel) and $1.6\text{-}3.1\,\mathrm{TeV}$ (end-caps). The shaping is performed by an CR-RC[1] network with a shaping time of $\sim 40\,\mathrm{ns}$. The noise level for gain 12 is ~ 8000 electrons for the APD configuration and ~ 4000 electrons for the VPT configuration. The non-linearity of the amplification is about $\pm 0.1\%$ of the full-scale. The three analog output signals from the MGPA are transferred to the multi-channel ADC with differential signals of $\pm 0.45\,\mathrm{V}$ using a common mode voltage of $1.25\,\mathrm{V}$.

The pedestals of the three different gains can be set individually using Digital to Analog Converters (DACs) integrated in the MGPA. The pedestal-DAC can be set to values between 0 and 100. Usually, the value that corresponded to a pedestal of about $200\,\mathrm{ADC}$ counts is programmed (Section 5.2). In addition, it is possible to inject a test charge into the input of the amplifier using a pulse generator included into the MGPA.

The ADC digitizes the three signals from the MGPA in parallel with a rate of $40\,\mathrm{MHz}$. It has 12 bits in four channels, and a effective number of bits of 10.9. Its integrated logic selects automatically the highest non saturated signal as output. The information about the chosen gain is encoded in two further bits. The low voltage differential signal (LVDS)

---

[1]C and R stand for resistance and capacitance, respectively.
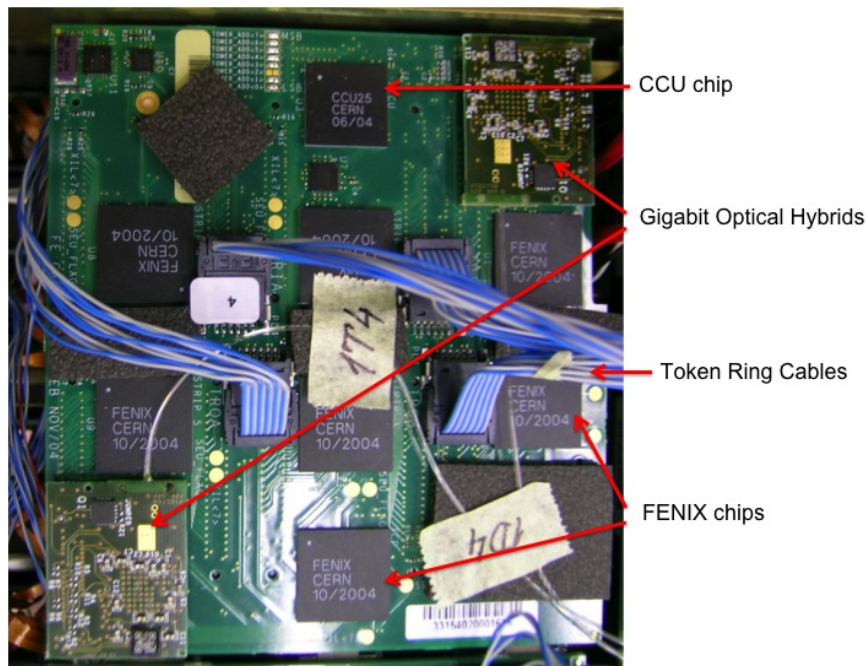
Figure 4.14.: FE card with the token ring cables and the GOHs.

output of the ADC is adapted to the CMOS single ended input of the FE strip FENIX[2] by two eight bit LVDS to single ended CMOS buffers.

Furthermore a ASICs, called Detector Control Unit (DCU) and a LVDS buffer are mounted onto each VFE card. The DCU measures and digitizes the leakage currents of the APDs with 12 bits, thus allowing a correction of the bias voltage setting (Section 4.3). In addition, the DCU measures and digitizes its own temperature, and reads the temperature sensor, mounted into every 10th capsule in the barrel.

4.4.3. Front end card and trigger tower control

The FE card plugs simultaneously into 5 VFE cards and the LVR card from the top (Figure 4.14). It contains seven FENIX ASICs. Five of them buffer the digitized data of each one VFE card during the $3\,\mu$s of the level 1 trigger latency in a pipeline and perform the trigger primitive generation (TPG in Figure 4.13). In addition, the FENIX chips estimate the sum of the energy of the five channels (strip sum in ϕ). The trigger tower energy (sum over five strip sums) is generated by the sixth FENIX. It also identifies the associated bunch crossing and sends the information to the regional off-detector Trigger Concentrator Card (TCC) every 25 ns via a 800 Mbit/s optical link, the Gigabit Optical Hybrid. In the case of the end-caps, the five strip sums are transmitted by five

---

[2]FrontEnd New Intermediate data eXtractor

GOHs. On reception of a level 1 trigger, the last FENIX on the FE card is used as event builder reading the corresponding data from the buffers and sending them via the second GOH to the off-detector Data Concentrator Card (DCC) in $\sim$7.5 μs. In addition to the FENIXs, the FE card contains a Clock and Control Unit (CCU) chip providing the interface to the token ring (see below). The CCU is provided with an ID, which is soldered as a bit pattern onto the corresponding FE card.

The trigger tower electronics is controlled by the off-detector Clock and Control System (CCS) via eight ribbons each containing eight fibers, which are connected to the eight token ring link boards of a super-module (Figure 5.4). Each token ring link board generates one redundant electrical control ring, the token ring. One super-module contains four token rings with eight, two with nine, and two with ten FE cards. One token ring consists of two separate electrical cable connections A and B, each connected to all FEs of the token ring. Figure 4.14 shows the FE card with the two in- and outputs of the token ring. By default, the CCU on every FE card uses the channel A as input and output. This can be changed separately for the input and output by sending dedicated commands to the corresponding CCU. The connections in-between the FE cards are arranged in a manner, that one broken CCU can be excluded from the token ring without affecting the remaining CCUs. Thus, the control system is partially redundant, as long as not two consecutive CCUs are broken.

The 40 MHz signal, called the LHC clock, synchronizes all functions of the trigger tower electronics with the bunch crossing rate. The clock is distributed via the token rings to a phase locked loop (PLL) on every FE card. The PLL contains a quartz that oscillates with the frequency of the clock and provides the trigger tower electronics with the clock signal. The phase between the clock and the oscillation of the quartz can be programmed into the PLL.

4.4.4. Gigabit Optical Hybrid

The GOHs comprises a PCB containing a data serializer, a laser driver chip, a laser diode and a 2 m long attached fiber pigtail (Figure 4.15). The optical links are single mode fibers operating at a wavelength of 1310 nm over a distance of $\sim$100 m. The fibers are operated at 800 Mbit/s. The fibers for the data and the trigger of one super-module are bundled separately in six ribbons, respectively.

Figure 4.15.: The gigabit optical hybrid chip with the fibre pigtail and the connector.

4.4.5. Low voltage system

The low voltage for the power supply of the trigger tower electronics is distributed through 17 low voltage distribution (LVD) blocks in the super-module (Figure 5.6). The input voltage of every block was controlled via one of 17 twisted pairs of wires, the remote sense cables. Each block serves the LVR cards of four trigger towers and the token ring link boards controlling these towers. An inhibit cable is linked from the off-detector electronics to every LVR card. Hence, when a LVR card has a short, it can be inhibited from the corresponding LVD block, such that the other trigger towers served from this block are not affected. The LVR card stabilizes the supply voltage for the VFE and FE cards, and the GOHs of one trigger tower using three regulator. The output voltage of the regulators is 2.5 V. It uses three DCU with six channels, which measure in particular:

- The first channel of every DCU is connected to one thermistor on the LVR board to monitor the temperatures near the regulators.

- The channels two to six on the first DCU measure the analog voltages of the five VFE cards in the trigger tower.

- Channel two of the second DCU monitors the supply voltage of the five DCUs on every VFE card. The channels three, four and six of the same DCU measure the voltages for the FE card. Channel five determines the digital voltages of all VFE cards.

- The channels two and six of the third DCU measure the input analog and digital voltages of the LVR card. Channel three monitors any over-current of one of the
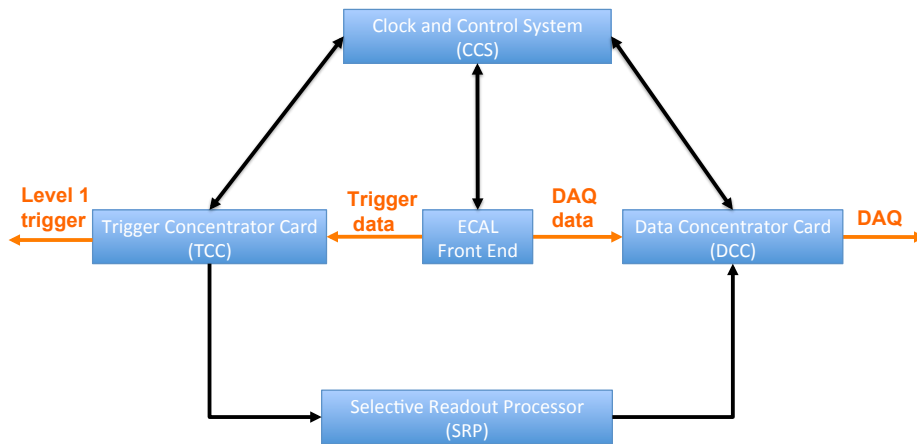
Figure 4.16.: Schematic view of the off-detector electronics.

regulators. Channel four measures the supply voltages of the GOHs and channel five the regulator inhibit level.

4.4.6. Light-injection system

A dedicated light-injection system permanently measures the dose-rate dependent evolution of the crystal transparency described in section 4.2 during the CMS operation (once per LHC beam cycle) [48]. The system injects laser light of 440 nm and 796 nm wavelength via glass fibers into each crystal. The ECAL response is normalized to a measurement of the laser pulse magnitude by silicon p-n diodes. One p-n diode per super-module is installed at the input of the laser fibers into the super-modules. The p-n diode is read by the laser monitoring electronics module (MEM) containing two FE cards. They are controlled by the token rings seven and eight.

4.5. Off-detector electronics

The off-detector electronics consists of the Trigger Concentrator Cards (TCC), the Data Concentrator Cards (DCC), the Clock and Control System (CCS), the Selective Readout Processor (SRP), and the Detector Control System (DCS) (Figure 4.16) [49].

One TCC completes the trigger primitive generation of one super-module in the barrel or one super-crystal in the end-caps. It transmits the trigger primitives to the synchronization and link board mezzanines at each bunch crossing. The TCC classifies each trigger tower according to its energy, transmits the energy to the SRP at each level 1 trigger accept signal, and stores the trigger primitives during the level 1 trigger latency.
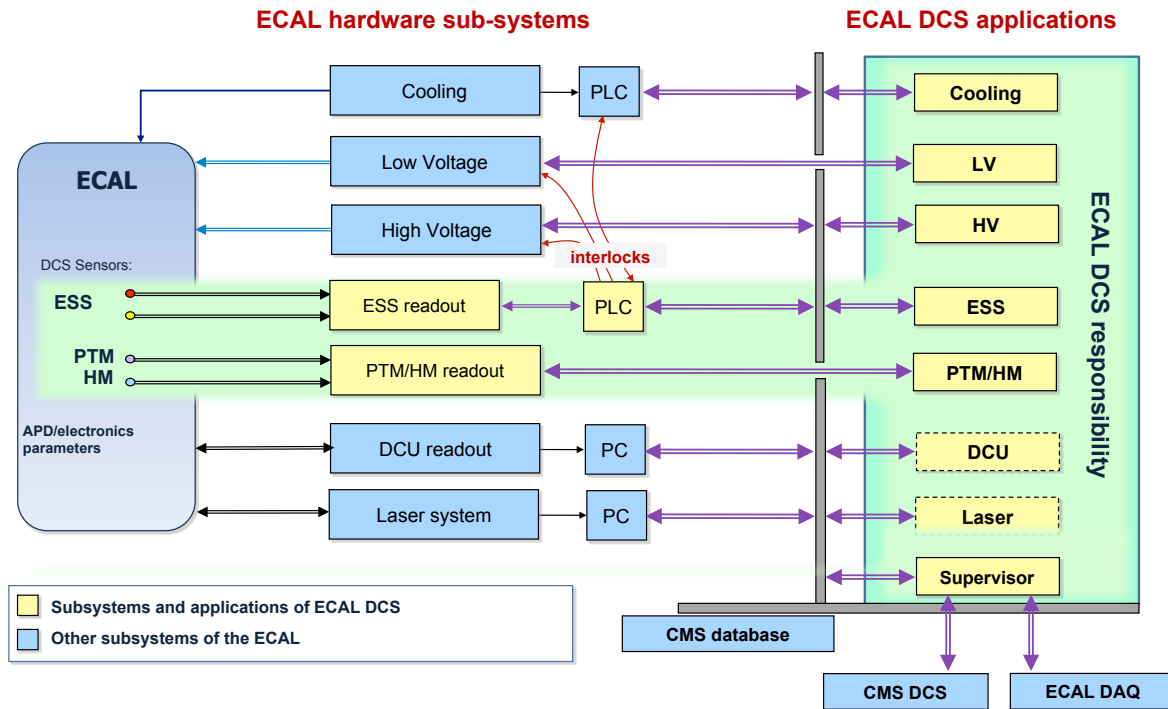
Figure 4.17.: Schematic view of the ECAL detector control system.

If a trigger is send, each DCC card receives the data of a single super-module or super-crystal and, transfers it to the CMS Data Acquisition System (DAQ). Because the total event size transferred to DAQ is restricted to a maximum average of $100\,\text{kB/s}$ (2kB per DCC), the data from the ECAL has to be reduced by a factor of ~20 (Section 3.3.5).

This reduction is achieved by zero suppression, that means data from crystals with energy lower than $\sim60\,\text{MeV}$ (barrel) and $\sim300\,\text{MeV}$ (end-caps) are neglected by the DCC. Furthermore, the SRP selects certain areas, i.e. groups of trigger towers that are read. The shape of these so-called regions of interest depend the corresponding trigger tower energies measured. Only if the cumulative energy in a region of interest is above the given threshold, the data is send to the DAQ.

The CCS provides fast and slow control functions of one super-module or one super-crystal. The fast control transmits the $40\,\text{MHz}$ clock (CLK), and the level 1 trigger information (TRG in Figure 4.13) by modulating the LHC clock signal. The slow control is used to configure the trigger tower electronics (CTRL data) via the CCUs.

The DCS consists of the ECAL Safety System (ESS), the Precision Temperature Monitoring (PTM), and the Humidity Monitoring (HM) (Figure 4.17). A detailed description can be found in [50]. The HM reads 440 humidity sensors with a precision of 5%. Therefore, the PTM monitors the crystal and photo-detector temperatures with

a precision of $< 0.01°$C. The system reads a total of 176 Betatherm $100\,k\Omega$ negative temperature coefficient thermistors. They are embedded in the aluminum grid of the ECAL and at the input and output of its cooling systems. The ESS controls the temperatures of the electronics with a precision of $< 0.1°$C. In addition, it is connected to a dedicated water leak detector and measures the water flow and temperature of the ECAL cooling system. The ESS also controls the parameterization and operation of the electronics' low voltage supplies (via the DCU measurements), the photo-detectors high voltage supplies, the cooling system, and the ECAL laser light-injection system. In case of problematic situations it is able to automatically interlock the corresponding system, to trigger predefined control actions, and to alert.

4.6. Energy resolution

For energies below $500\,$GeV, where the effect of shower leakage from the rear of the ECAL is negligible, the ECAL energy resolution is parameterized as [21]

$$(\frac{\sigma_E}{E})^2 = (\frac{S}{\sqrt{E(GeV)}})^2 + (\frac{N}{E(GeV)})^2 + C, \qquad (4.1)$$

where S is the stochastic term, N the noise and C the constant term.

The stochastic contribution arises mainly from fluctuations of the lateral shower containment, photo-statistics, and fluctuations of the energy deposits in the pre-shower detector in the end-caps. As described in Section 7.1, the energy of the electromagnetic shower is reconstructed by summing signals of a matrix of crystals centered on the crystal with the largest energy deposit. The contribution from the fluctuations in the lateral shower containment is expected to be 1.5% and 2% for the energy sum of 3×3 or 5×5 crystals, respectively. The photo-statistics contributions are estimated to be 2.1% for both barrel and end-caps. The contribution of the pre-shower detector is predicted to vary like $\sigma/E = 1/E^{0.75}$ in the end-caps [21].

The contributions to the constant term are the non-uniformities of the longitudinal light collection, inter-calibration errors (Section 5.3.1), and leakage of the electromagnetic showers from the rear side of the crystals. The non-uniformity contribution is estimated to be less than 0.3%, whereas the effect of the rear leakage is very small as test beam data with $280\,$GeV electrons showed [21].

The noise term reflects the electronics noise, digitization noise, and pile-up noise. The electronics noise depends on the amplification gain used and will be described in Chapter 5. The digitization noise is quantified by the formula $\Delta\sqrt{12}$, where $\Delta =$

1/4096 is the step size of the 12 bit ADC [51]. Pileup occurs because the shaped signals of the MGPA are extended over several LHC bunch crossings. Up to eight time samples are used for the reconstruction of the signal amplitude. If a second particle hits the crystal during the reconstruction of a pervious one, the two signals overlap. This phenomena is known as pileup of events from different bunch crossings. The contribution of pileup to the noise term is expected to be low at luminosities below $10^{33}\mathrm{cm}^{-2}\mathrm{s}^{-1}$. In addition, neutron irradiation is predicted to increase the APD leakage current leading to expected noise contributions of $30\,\mathrm{MeV}$ per channel at a luminosity of $10^{34}\mathrm{cm}^{-2}\mathrm{s}^{-1}$ [21]. The measurement of the ECAL barrel resolution with an electron beam is described in section 5.3.1.

Chapter 5.

Integration and testing of the electromagnetic calorimeter barrel

This chapter describes the integration of all detector and readout components in an ECAL super-module, and the different tests that were performed to assure the functionality. The commissioning, which completed the integration and determined the performance of the super-modules, is explained in detail. Unfortunately, an unexpected large number of hardware errors appeared during the commissioning. To classify the different errors, an analysis method based on pattern recognition was developed for this thesis and is presented. Finally, the calibrations methods and results of the super-modules with an electron beam and with cosmic muons are discussed.

5.1. Super-module integration

The super-module integration started with the mounting of the crystals including APDs, the cooling systems, and the 68 motherboards in a dedicated integration area in building 27 at CERN. The cooling system was checked for leaks with Helium and a sensitive Helium-detector, and in a one hour 15 bar test using water. The motherboard connections to the APDs and the temperature sensors were tested. In particular, every APD was set under high voltage of about 400 V and its leakage current was measured to identify shorts and other failures. When a channel drew a high leakage current ($> 200\,\mu$A) and attempts to repair it failed, it was disconnected from the high voltage supply to limit the global leakage current of the corresponding high voltage channel (Section 4.4.1). This was done by unsoldering one of the resistances R_1 or R_2 of the corresponding APD bias circuit in Figure 4.7. At this stage of assembly, the so-called bare super-modules were transported to the ECAL integration center in building 867 at CERN, for the installation

and test of the ECAL electronics [52]. The electronics installation of one super-module included the following steps:

1. Mounting of 68 trigger towers (each comprising five VFE boards, one LVR board and one FE board).

2. Installation of eight token rings together with the eight corresponding token ring link boards.

3. Mounting of 138 Gigabit Optical Hybrids and twelve Distributed Fiber Patch Panels (DFPP) .

4. Installation of 17 low voltage distribution blocks (LVD).

In addition, the temperature and humidity sensors, the water leak detector and several mechanical supports for the fixation of cables, LVD blocks, fibers, DFPPs, and connectors were integrated. The full or partial coverage of the previously installed items in every sequence of the installation demanded intensive performance tests following each installation step. In particular, steps one and three were completed by the individual testing of every trigger tower, the *single trigger tower test*. After step two, the proper working of the token ring, including the redundancy was checked. A one-week operation called commissioning completed the super-module electronics installation.

5.1.1. Integration area

The integration area was situated in building 867 at CERN, Site de Prevessin. It comprised the super-module installation and test zone (Figure 5.1), an air conditioned super-module storage area, several preparation and testing places for electronics components, a mechanical workshop and a storage space for materials and components. The super-modules were installed and tested in one of three integration stands in the installation and test zone. They were held by a mechanical support frame which could be moved with the aid of air pads on the epoxy resin covered floor. The super-modules were provided with the necessary cooling water by one of the two independent cooling water units. Each installation stand had one CAEN (SY 1527) high voltage system for the bias voltage of the APDs. Four Wiener PL500 five channel low voltage supplies powered the 17 LVD blocks of one super-module. Three channels were used as mobile LVD blocks providing the low voltage for trigger towers under test before the installation of the low voltage system. A 6U-VME based readout system was used to acquire the data of single trigger towers and entire token rings. These data were processed in a PC. The *single trigger tower test* was performed twice, once before and a second time after the
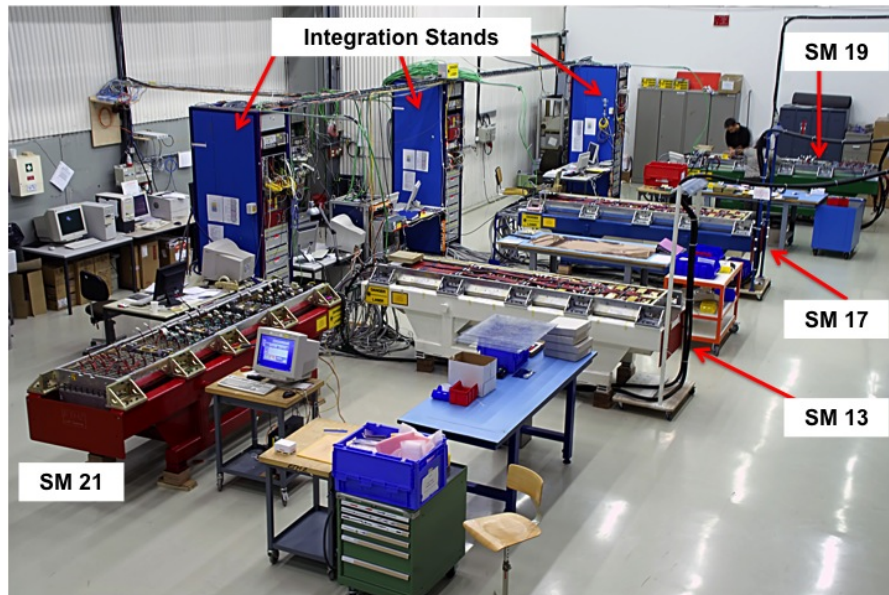
Figure 5.1.: Electronics installation and test zone with three integration stands.

installation of the token rings and the GOHs. A 532 nm pulsed laser system was used to inject light into the crystals for test purposes. The laser monitoring electronics module, integrated in the super-modules to measure the injected amount of light, was powered by a two channel linear power supply. In the integration stands, the super-modules were connected to a detector control system similar to the one used in CMS, providing safety for the operation.

5.1.2. Electronics integration

The first step of the electronics integration was the re-testing of the high voltage connections from the motherboards to the APDs and temperature sensors. Where the coverage of the cooling bars still allowed it, new channels with high leakage current were disconnected from the high voltage as described above.

The mounting of the trigger tower electronics started with the plugging of five VFEs cards and one LVR board into the motherboard and their fixation. Each of them was fixed with three screws to the cooling bars of the super-module. The FE card was plugged into the connectors on top of the six cards. All three types of cards carried a unique bar code that was scanned during the installation using a dedicated software connected to the ECAL construction database (CRYSTAL). The software program checked whether the cards were registered in the database and were accepted for installation. In addition, it associated the ID of every card with the specific location in the super-module.
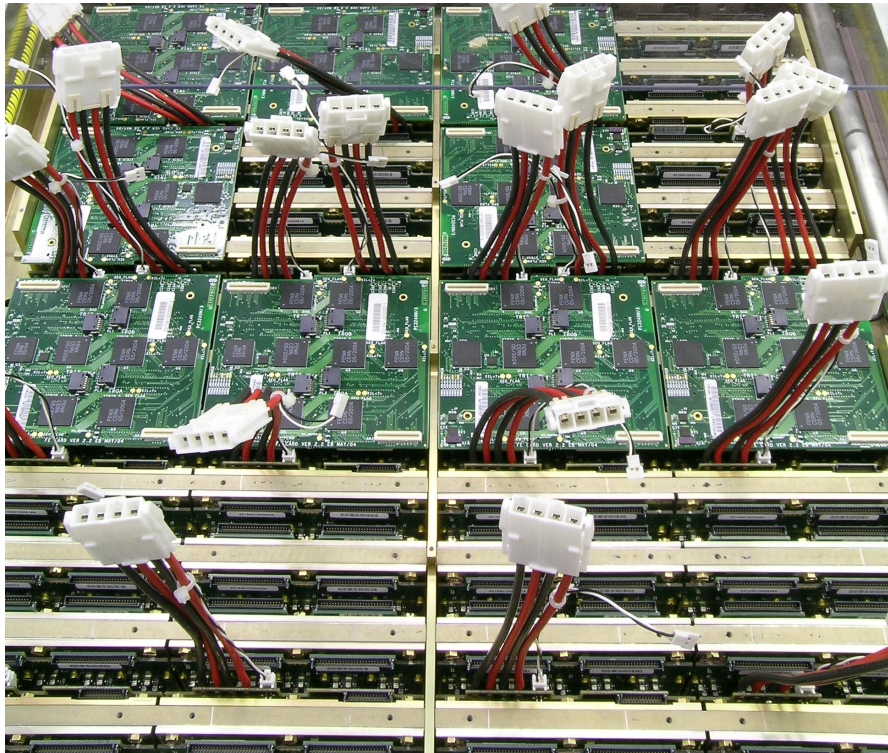
Figure 5.2.: Trigger tower installation: the VFE and LVR cards are fixed to the brass cooling
bars and the FE cards are plugged on top. The red and black cables attached to
one white connector, are each the low voltage supply cables for each one trigger
tower.

In that manner the 68 trigger towers were installed in the super-module (Figure 5.2).
Afterwards, each trigger tower was temporary connected to the power supply and to the
readout system and tested individually with the *single trigger tower test* (Section 5.1.3).

The next step was the mounting of the eight token rings including the token ring
link boards (Figures 5.3 and 5.4). Two token ring link boards were fixed to a separate
cooling bar. After a token ring was installed, it was connected to a dedicated PCI on
the installation stand via a control fiber ribbon and all its trigger towers were powered
with two or three of the mobile LVD blocks. Then, a test program verified the correct
cabling and the redundancy of the token ring by successively skipping each CCU.

Subsequently, the optical links were mounted to the super-module. Two gigabit
optical hybrids were plugged to each of the 68 FE cards (Figure 4.14). Twelve DFPP
were installed on top of the trigger towers of the modules three and four (Figure 5.5).
From each GOH the 2 m long fiber pigtail with a so called MU connector at the end
links to one of the DFPPs. The MU connector plugs to a MFS 12-way ribbon adapter
inside the DFPP. The fibers for the data and for the trigger were bundled in different
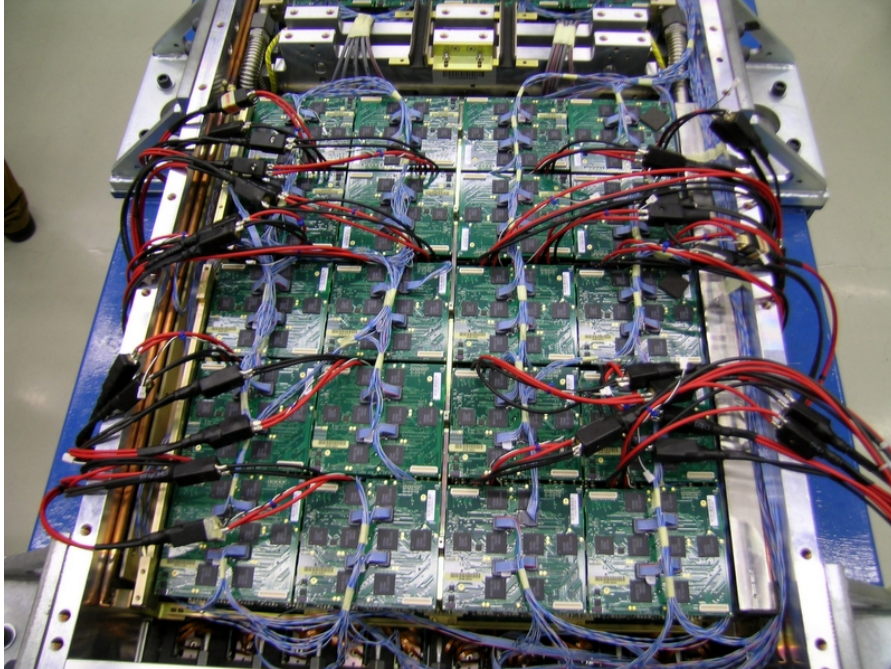
Figure 5.3.: Token rings one and two under test, each containing 10 FEs.
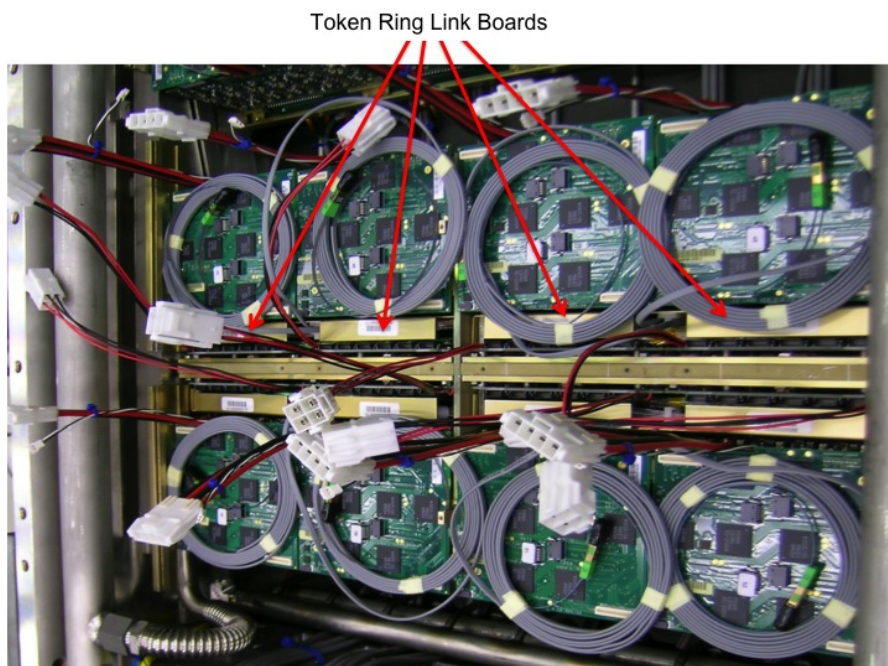
Figure 5.4.: The installed eight token ring link boards with each one optical ribbon.

Figure 5.5.: Two Distributed Fiber Patch Panels.

DFPPs. Two times five distributed fiber patch panels bundle each twelve fibers, two bundle eight data and trigger fibers, respectively. Excess lengths of 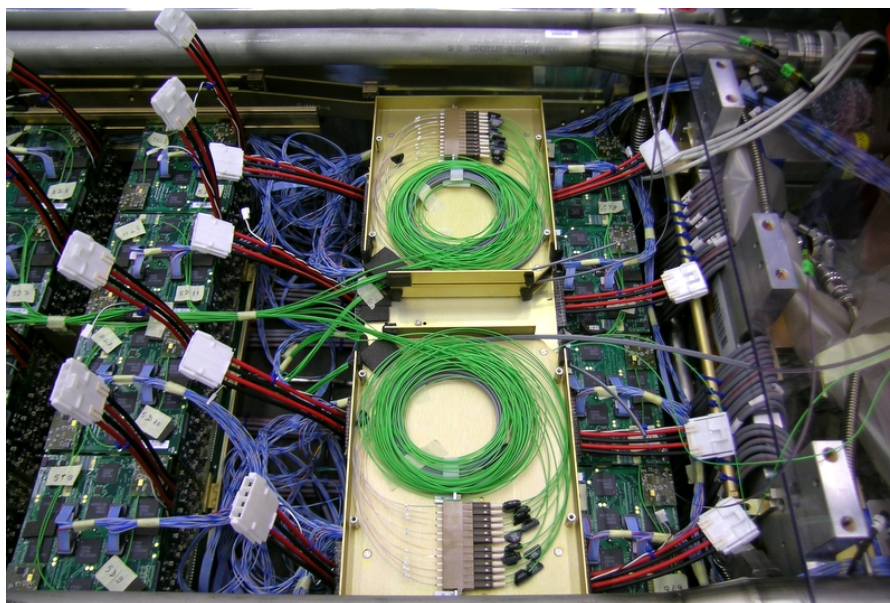the fibers were stored in the distributed fiber patch panels. From the DFPPs the ribbons routed to the inline patch panel at the super-module patch panel. There, they are plugged into a MFS to MFS adapter. The patch panel of the super-module was directly linked to the off-detector electronics. The handling of the GOHs was very delicate, because they were rather fragile and the minimal bending radius of $\sim 4\,$cm of the fibers had to be respected. Every GOH was provided with a bar code that was registered during the installation. The installation of the optical readout system was completed with a *single trigger tower test* on all trigger towers, using the final optical links.

Finally, the low voltage system was installed in the super-module (Figure 5.6). The 17 LVD blocks were mounted on the top of the distributed fiber patch panels in the modules three and four and on top of the trigger towers in modules one and two. Each block is connected to the power connector at the patch panel by four $16\,$mm^2 copper wires.

All links between the super-module's electronics and the off-detector electronics, and the cooling pipes pass through the patch panel of the super-module (Figure 5.7). It contains connectors to all systems mentioned above.
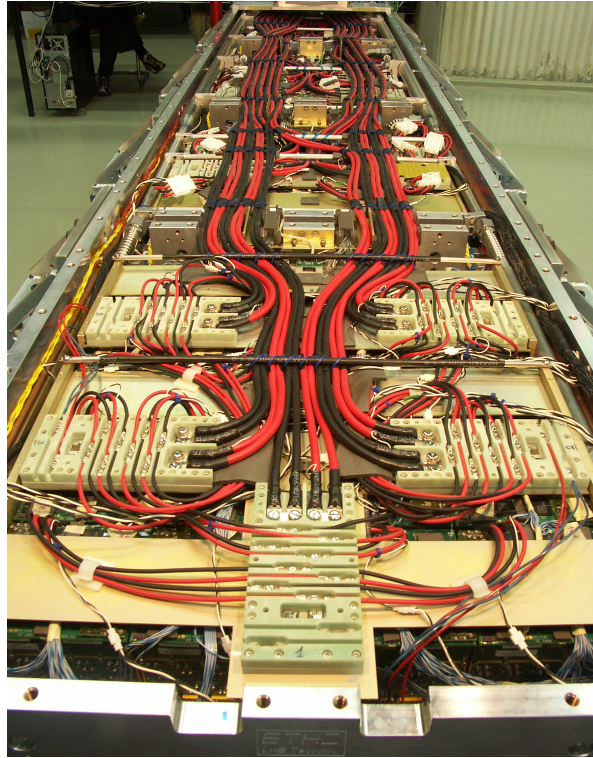
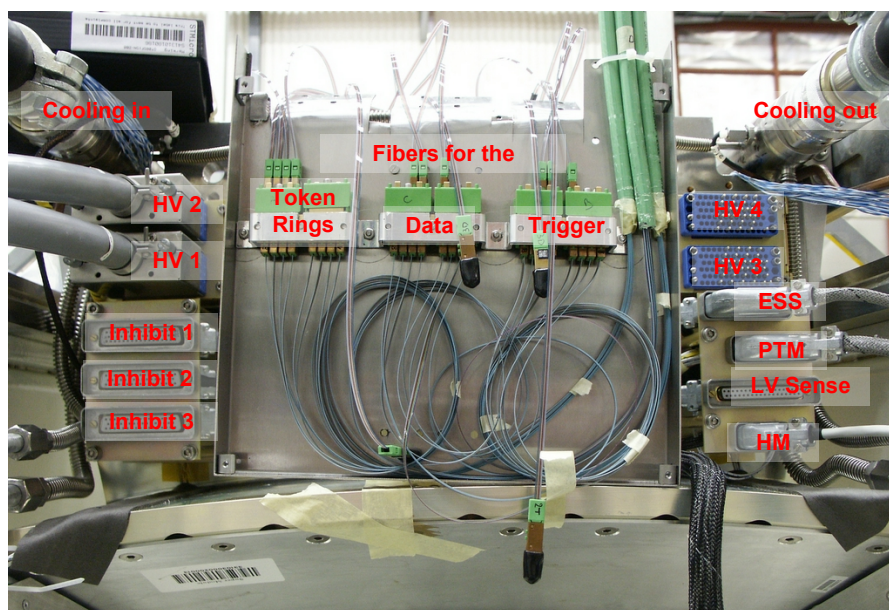**Figure 5.6.:** The completed super-module with the low voltage system on top.

Figure 5.7.: Patch panel of the super-module.

5.1.3. Trigger tower testing

The *single trigger tower tests* was performed twice on every trigger tower during the super-module integration. Once after the installation of the trigger towers and a second time after the installation of the token rings and the optical links. It scans the full functionality of all trigger tower channels and assesses their performance. The tests were controlled by a VME based readout system that provides an user-friendly interface. During these tests, the trigger towers were powered from the mobile LVD blocks and were connected optically to the PCI via two GOHs.

The test sequence was the following:

1. Verifying the communication with the CCU on the FE card. The CCU ID was read and compared with the geographical ID, indicating the location of the FE in the super-module according to a numbering scheme.

2. The I^2C[1] interfaces of the CCU were tested by checking the addresses of all sixteen connected I^2C interfaces. The read addresses had to agree with the expectations. The connected devices of the I^2C interfaces were: the seven FENIX chips and the two GOH chips and the PLL on the FE card, the fives VFE cards (carrying five MGPAs and one DCU each), and the LVR card (Section 4.4).

3. The accessibility of all important registers in the trigger tower were checked using the I^2C interfaces. In order to do so, the values of all registers were loaded, read back and compared with the settings to verify their correctness. In particular, there were 61 registers in each of the five strip FENIXs, two in each of the two GOHs, five in the PLL and five in each of the 25 MGPAs.

   The first register in every strip FENIX is the value of the pipeline delay that synchronizes the data and trigger transmission from the different trigger towers in the super-module. The remaining 60 registers divide into five groups serving one channel each: Each channel can be disabled, the gain selection in the MGPA can be enforced, the number of samples read per trigger be set (usually 10), a peak finder could be enabled, five filter of the peak finder are set, and finally three registers were used to subtract the pedestal from the pulse height and to divide it by the corresponding gain. Two registers in the GOHs set the power of the GOH laser and transmission protocol of the optical links. The five registers in each MGPAs are the following: Three set the pedestal AC values for the three gains, one enabled the pulse injection, and the last one determined the amplitude of this pulse.

---

[1]The Inter-Integrated Circuit is a commonly used serial computer bus.

4. A pedestal DAC scan was performed for every channel and every gain to find the DAC value that corresponds to a pedestal of 200 ADC counts. These values were used for the remaining tests. In particular, DAC values from 1 to 80 were set, the corresponding pedestals were measured 1000 times each and the mean and the RMS were calculated. The DAC value with a pedestal closest to 200 ADC counts was acquired and programmed in the MGPA.

5. Using the previously obtained DAC values, the pedestals of the five channels were measured 1000 times each. The measurements were divided in 100 events and the low and the high frequency noise were calculated. The low frequency noise was the RMS from the distribution of the 100 mean pedestals. The high frequency noise was calculated from the ten samples of one event. The low frequency noise was a consequence of dependences of the pedestal from other electronics like the low voltage system. Those dependences had to be avoided. Usually, the low frequency noise was very low and the total noise resulted mainly from the high frequency contributions.

6. 100 test pulses were injected using the MGPA pulse generator in every channel for each gain. Their amplitudes and RMS values were measured and had to agree with the expectations. In addition, it was checked how often every of the 14 bits of the ADCs has been "1". In that manner bits that were stuck could be found.

7. The test was performed a second time using the trigger data path. In particular, the signals were read using the trigger FENIX and the trigger GOH. However, the trigger FENIX adds the pulses from all 25 crystals of the trigger tower generating an overflow of the output. Consequently, only the crystal in the center of the trigger tower was enabled for the test of pulse shapes in the trigger data.

8. The measurements of the three DCUs integrated on every LVR card were read and compared with the expectations. The measurements of these DCU chips are described in Section 4.4.5.

9. The leakage currents and the crystal temperature were determined with the DCUs on the VFE cards.

The results of the trigger tower tests were saved in one ROOT file, named after the 5-digit run number of the test.

5.2. Commissioning

The most important test during the installation of the electronics of the ECAL barrel was the full operation of the completed super-modules during one week, called commissioning. The aims of this test, were:

- operate the super-module in running conditions similar to those at the CMS experiment,

- check the integrity of the super-module, i.e. find faulty channels, and

- perform different runs to assess the performance of all components of the super-module.

For the commissioning, the super-module was powered by the multichannel low voltage and high voltage systems of one integration stand. The cooling water was provided by the cooling units. The readout system was close to the final one to be used during operation of CMS. It included a DCC, a TCC, and a CCS. The DCC and the TCC were connected to the data and trigger fiber ribbons that transmit data and trigger primitives, respectively. The CCS was connected to the eight token rings. A PC running a dedicated test software processed the received data and compared the results with predefined limits. A summary of the results including detected problems was stored in the form of tables and histograms on a server.

The problems that were uncovered during this time were corrected, if possible. Otherwise, their character and their possible effects on the ECAL measurements were analyzed and reported.

5.2.1. Commissioning test runs

Before starting the test runs of the commissioning, the pedestal DACs in each channel and gain were set in a similar procedure as during the *single trigger tower test* to obtain uniform pedestals throughout all channels of the ECAL.

The following types of test runs were taken during the commissioning:

1. **Leakage current measurement**: During the application of high voltage on the APDs, the current for the supply of a group of 50 crystals was measured. Typically, the current was $\sim 3\,\mu\mathrm{A}$ for a functioning high voltage channel. If the current was significantly higher in one of the high voltage channels, the faulty readout channel was identified by measuring the currents of each of the 50 channels directly on the motherboard using an ampere-meter. If possible, it was disconnected from the high voltage supply (Section 5.1).

2. **Pedestal run with HV on**: High voltage was applied to the APDs to deplete them. For each channel and gain, 10×100 pedestal values were measured. The average pedestals and the RMS values were calculated. This test verified the proper setting of the pedestal DAC. The RMS represents the electronics noise.

3. **Pedestal run with HV off**: This test was identical to the one above, except that high voltage was applied to the APDs. This test identified channels, in which the APD was disconnected from readout. Without applying the reverse bias voltage, the capacitance of the APD increases. Since the electronic noise of the APDs is dependent on its capacitance, one expects an increase of the electronic noise in the channel. Consequently, if one APD was not connected to the readout electronics, the electronics noise would stay at the same level as in the *Pedestal with HV on run* (i.e. below the limits) and thus identifying the bad channel.

4. **Test pulse run**: 50 test pulses were injected in each channel for each gain. The charge of the injected pulse was chosen properly with respect to the gain. The resulting mean amplitudes and RMS values were compared with the expected values. This test allowed to verify the functionality of the MGPA and of the complete readout chain starting with the VFE card. The quality limit cuts were not very strict for this run, because the readout channels were not calibrated yet at the commissioning stage.

5. **Laser run:** 300 laser pulses (wavelength $532\,\text{nm}$) were injected into each crystal using the laser and lightmonitoring system. The mean amplitude was calculated to verify the functioning of the full readout chain including crystals, APDs and motherboards. A gain of 12 was fixed in all MGPAs for this run. The quality limit cuts of the laser run were not very tight, because of the non-calibrated supermodule.

6. **DCU run:** The output of all DCUs of the VFE and LVR cards was monitored for correctness. In particular, the DCUs measure the following quantities (see also Section 4.4 for the measurements of the different DCUs):

   – **LVR**: Input voltages from the LVD block and output voltages for the supply of the trigger towers,

   – **VFE**: Leakage current of the APDs, crystal temperature and the temperature of the DCU on the VFE.

The tests 1 to 5 verified the correct acquisition and processing of the detector information, whereas test 6 verified the readout electronics and its services. The noise measurement accomplished in the *Pedestal run with HV on* determined the performance of the

Variable	Gain 1	Gain 6	Gain 12
Pedestal mean with HV on	170-230	170-230	170-230
Pedestal RMS with HV on	< 0.9	< 1.2	< 1.65
Pedestal RMS with HV off	-	-	> 2
Test Pulse mean amplitude	> 200	> 200	> 200
Test Pulse amplitude RMS	< 20	< 20	< 20
Laser amplitude RMS	-	-	> 40% of mean amplitude

Table 5.1.: Quality criteria for the commissioning test runs. All values are given in ADC counts.

readout channels, since the electronic noise determines the noise term in the resolution of the ECAL (Section 4.6). All measured values had to agree with the criteria summarized in Table 5.1 for the tests 1 to 5, and in the Tables 5.2 and 5.3 for test 6.

Variable	APD current	APD temperature	DCU temperature
Limits	$<15\,n$A	(17-22) °C	(25-45) °C

Table 5.2.: Quality criteria of the DCU measurements of the VFE card.

Variable	inhibit voltage	LVR input	LVR output	DCU temperature
Limits	<0.1 V	(3.95-4.25) V	(2.2-2.6) V	(20-30) °C

Table 5.3.: Quality criteria of the DCU measurements of the LVR card.

5.2.2. Typical commissioning results

This section describes the results representative for commissioning test runs described in detail in the previous section. In particular, the distributions of the pedestal means, the pedestal RMS with high voltage on and off, the mean amplitudes of the tests using the MGPA test pulses and the laser pulses are discussed. All histograms show entries of all 1700 channels from one super-module. For all runs, except the *Pedestal run with HV off* run, data from the commissioning of super-module 30 were used. The *Pedestal*

run with HV off run data were taken with super-module 18. Except for the laser pulse test, all tests were performed for the three gains 1, 6, and 12. The distribution of the leakage current measurement and of the DCU runs are not discussed here, since they did not have an influence on the classification of the hardware errors discussed in the next section.

Figure 5.8, left side, displays the RMS of the pedestals taken with the *Pedestal run with HV on*. The histogram of gain 12 displays the total performance of this super-module, since the noise of $\sim$1.1 ADC counts in the highest gain determines the ECAL resolution of $\sim$40 MeV. The noise of only one channel of this super-module was above the limits for gain 6 and 12. The reason for the noise was usually a broken capacitor on the motherboard. However, apart from the slightly worse energy resolution, this channel was still usable for measurements. Another channel had a pedestal of 0 ADC counts, i.e. the readout channel was not working at all. The only reason for a dead channel was a destroyed MGPA on the VFE card.

To detect readout channels that were disconnected from the APDs, we investigated the RMS of the pedestals in each channel without applying high voltage to the APDs of the super-module (Figure 5.8, right side). The noise of the connected readout channels was expected above the limits of 1.2 and 1.65 ADC counts for the gains 6 and 12, respectively. Disconnected channel stayed below the limits, and in this particular case three disconnected channels were found. The points of failure were the Kapton cables of the motherboard. For a detailed investigation of these problems see Section 6.2.

The distributions of the mean pedestals in Figure 5.9, left side, show a wide plateau structure. The reason was that the pedestal cannot be set exactly to a value of 200 ADC counts, because changing the DAC value by one changes the measurements of the pedestal by $\sim$24 ADC counts. In this case all channels except one had a mean pedestal within the required limits 175-225 ADC counts. Another channel had a mean of 0 ADC counts for all gains because it was broken. The entry of this dead channel is not shown in the distribution, and it was already found in the *Pedestal run with HV on* run above.

The mean amplitudes of the MGPA test pulses per channel for the three gains are shown on the right side of Figure 5.9. To simplify the comparison between the amplitudes of the three different gains, the distributions were normalized to the distribution of the gain 12 test pulse run. That means, the entries of the histograms for gain 1 and gain 6 were multiplied by a factor of 12 and 2, respectively. The spread of the 1700 amplitudes around the mean value was gaussian, as expected. Here, only one channel failed the test pulse run with an amplitude of 0 ADC counts (which is not shown in the distribution). This specific dead channel was already detected with the tests above.
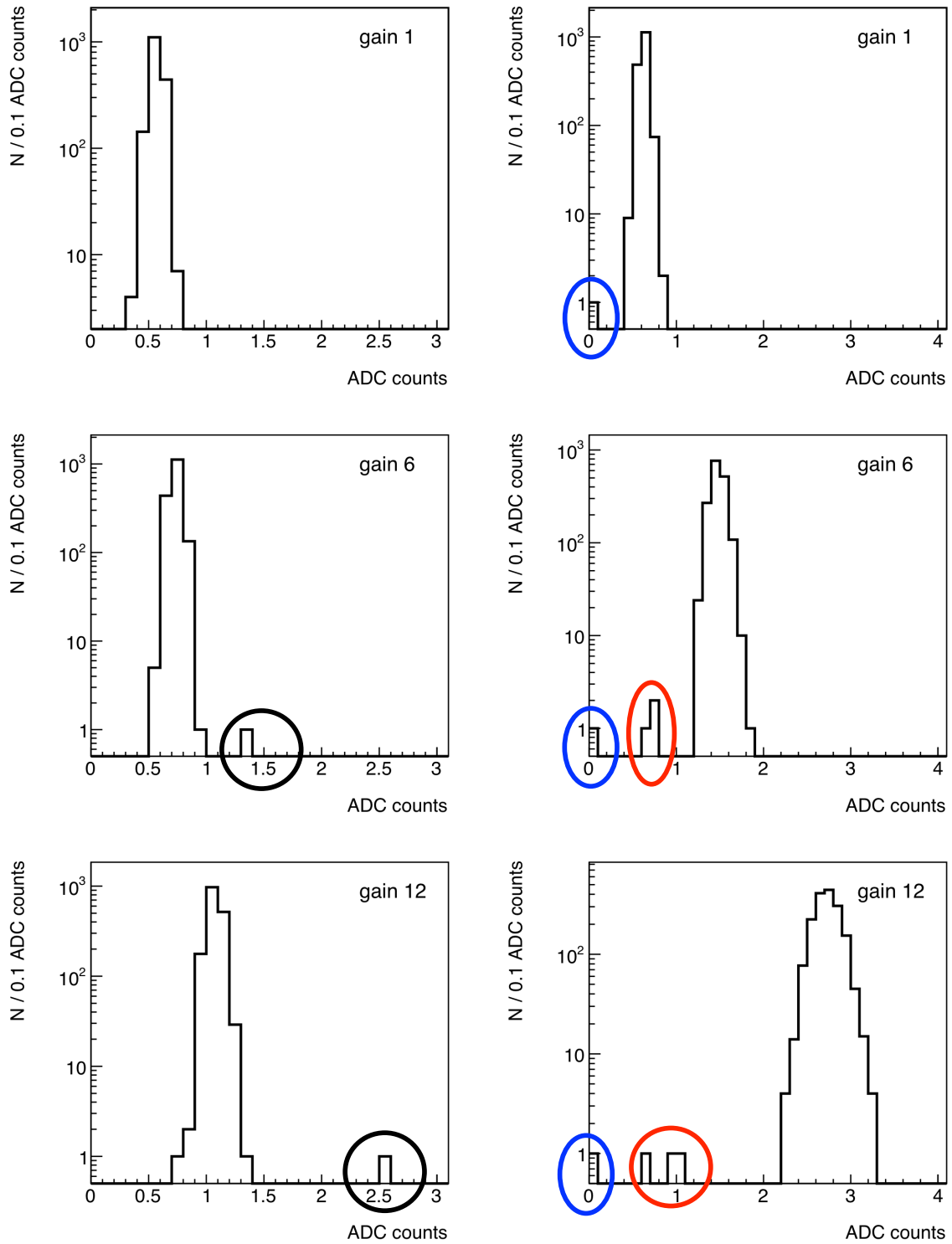
Figure 5.8.: Left side: Noise with high voltage on of super-module 30; the noisy channel is marked with the black circle. Right side: Noise with high voltage off of super-module 18; the dead channel is marked in blue, and the three disconnected channels in red.
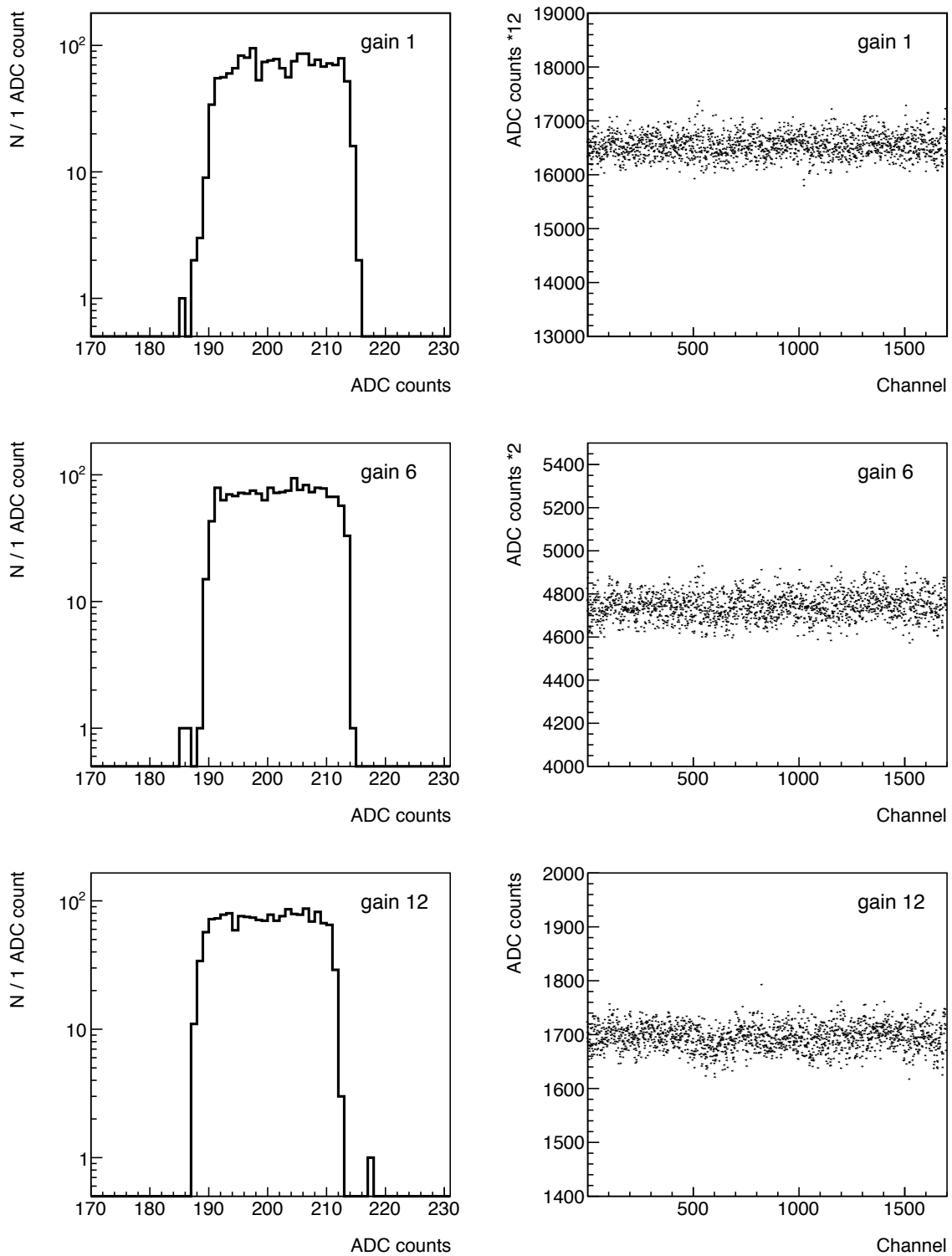
Figure 5.9.: Pedestal mean distributions (left side) and test pulse amplitudes per channel (right side) of super-module 30.
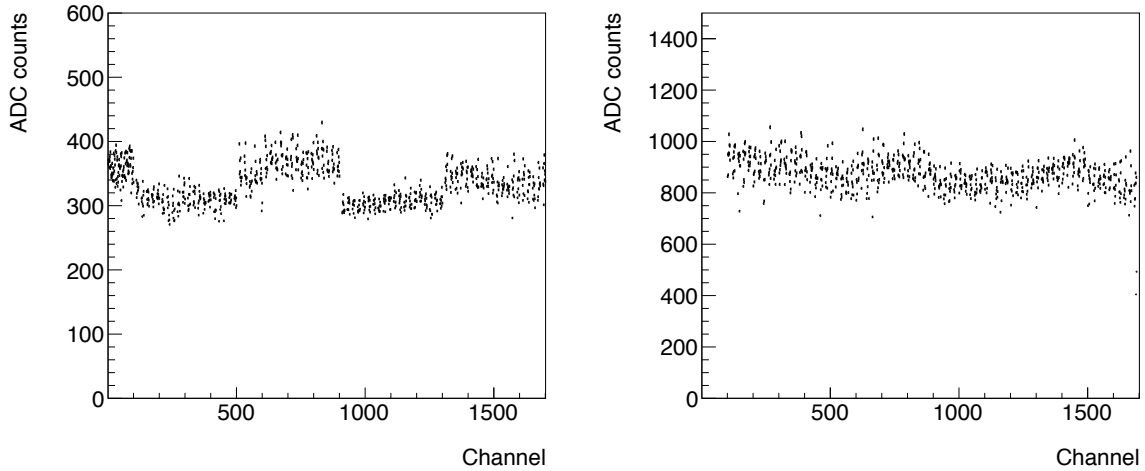
Figure 5.10.: Laser pulse amplitudes for the left and the right side of super-module 30.

Figure 5.10 displays the mean response per crystal to 300 injected laser light pulses for the two sides of one super-module. The laser light was injected via two independent fibers into the super-module, where the first fiber was connected to 900 crystals ("left side") and the second one to 800 crystals ("right side"). Since it was only possible to connect one super-module half at once, we measured two distributions of the laser pulse amplitudes. All MGPAs of the super-module were forced to run with gain 12 for the laser run. The light pulse injected in the crystals, i.e. the number of incident photons was chosen such that the signals amplified with gain 12 never saturated the full readout scale of 12 bit. The amplitudes of the left plot show a stepped profile. The steps represent the module structure of the super-module and were due to the different fiber distribution for each module. The single entries show a wide gaussian spread around the mean amplitude, since the channels were yet not inter-calibrated (Section 5.3). Here, only the dead channel, which was mentioned above, did not fulfill the required minimum amplitude of 50% of the mean amplitude.

5.2.3. Classification of the hardware errors

From November 2005 to August 2006, the super-modules numbered 0 to 26 out of 36 were integrated in the ECAL integration area. The commissioning could be completed for all these super-modules except for number 5. Due to the increasing amount of errors found during the super-module testing (Chapter 6), it became necessary to identify their origin. Thus, an analysis tool was developed in the frame of this thesis, that could identify five classes of errors that occurred repeatedly [53]. For the classification of the different errors, all data available from the test runs mentioned above were considered.

Error A: Bad APD connection

The connection of the APD to the high voltage or to the input of the MGPA was bad or lost. As a consequence, this channel failed in the *Pedestal run with high voltage off*. Additionally, the measured laser amplitude was at least 65% lower than the average amplitude measured in the run, in most cases it was 0 ADC counts. This category includes channels, where the APD had been disconnected on purpose from the high voltage supply on the motherboard level due to high leakage current.

Error B: Shorted APD

The APD anode was shorted or had a low resistance to ground. As a result, the channel drew a current of $I = U/(134\,K\Omega + R)$, where U was the bias voltage over the APD, and R was the resistance of the APD line to ground. The MGPA was often damaged in these cases. Thus, the channel failed in the *Test pulse run* and the *Pedestal run with high voltage on* showed a high noise or a pedestal of 0 ADC counts (see class **C**). In addition the laser amplitude measured in this channel was almost always 0.

Error C: MGPA dead

The MGPA and the DAC were damaged. Thus no test pulses could be injected into the channel and the pedestal could not be set to its nominal value. The channel failed in the *Test pulse run*. In most of the cases, these channels had a pedestal of 0 ADC counts or were very noisy during a *Pedestal run with high voltage on*. The laser amplitude measured in this channel was almost always 0.

Error D: Noisy

The channel showed an increased RMS in the *Pedestal with high voltage on run*.

Error E: Low laser amplitude

In these cases the channels failed only in the *Laser runs*, where they had amplitudes at least 30% below the average level. All channels that were found in that category showed a perfect behavior in the calibration. Thus, these channels can be used for physics measurement, they are not considered as a problem in the following.

To find the patterns for the classification, a binary evaluation criteria was chosen, where each channel was classified with "1" (passing) or "0" (failing) for each test run. Table 5.4 shows a summary of the patterns found for the described error classes.

Channels that showed the errors A, B or C were problematic, whereas channels with error E were considered as usable. Channels with error D can be used for measurements where the signal of the deposited energy is much higher than the noise.

Test run	Error A	Error B	Error C	Error D	Error E
Pedestal run with HV on	1	0	0	0	1
Pedestal run with HV off	0	1	1	1	1
Test Pulse run	1	1	0	1	1
Laser run	0	0	0	1	0
Leakage current measurement	1	0	1	1	1

Table 5.4.: The classification of the five errors found according to their passing ("1") and failing ("0") of a test run.

5.3. Calibration

Nine commissioned super-modules were exposed to electron test beams in 2006 to measure their response to incident particles and perform precise inter-calibration. In addition, all 36 super-modules were inter-calibrated with cosmic ray muons. For both calibrations, all super-modules were operating in their final configuration. All figures and distributions shown in this section were taken from [54, 55], if not stated otherwise.

5.3.1. Performance studies in the electron test beam

In summer 2006, two test campaigns took place at the H2 and H4 test beam areas using electrons and positrons with energies of 2-250 GeV.

As described in Section 7.1, the energy of the electromagnetic shower is reconstructed by summing the signals of a matrix of crystals centered on the crystal with the largest energy deposit. The ECAL energy resolution as a function of energy is parameterized as

$$(\frac{\sigma_E}{E})^2 = (\frac{S}{\sqrt{E(GeV)}})^2 + (\frac{N}{E(GeV)})^2 + C,$$

where S is the stochastic term, N the noise and C the constant term (Section 4.6). Data from samples taken with the electron beam in the 20-250 GeV energy range gave $S = 2.8\,\%/\sqrt{\text{GeV}}$, $N = 0.12\,\text{GeV}$ and $C = 0.3\,\%$ as shown in figure 5.11 for energy measurements in an array of 3×3 crystals. These values meet the ECAL barrel design requirements.

For incident electrons with energies above 20 GeV, as shown in Figure 5.12, the resolution of the position measurement was determined to be below 1.2 mm for both X and Y coordinates. The ECAL non-linearity was measured as a function of the beam energy in the range of 20-180 GeV and was found to be smaller than 0.2%.
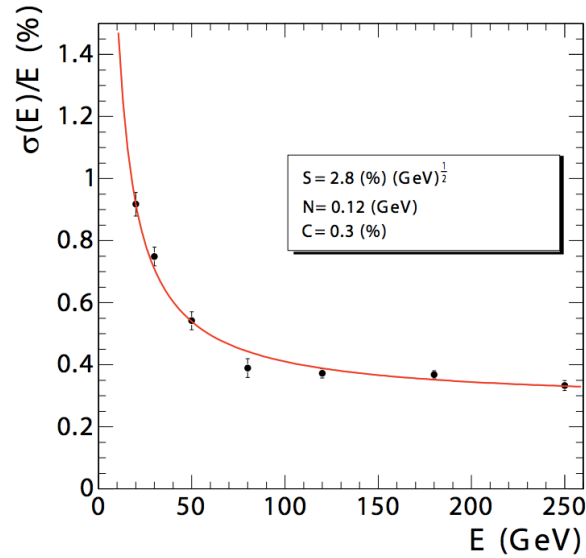
Figure 5.11.: ECAL energy resolution, $\sigma(E)/E$ as a function of electron energy as measured from a beam test for an energy measurement in an array of 3×3 crystals [21].
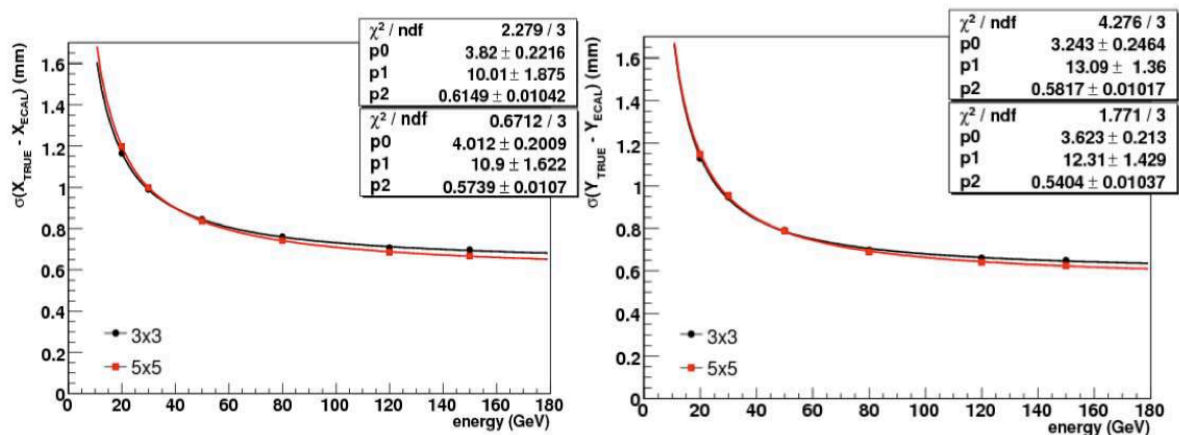
Figure 5.12.: Position resolution in the X (left side) and the Y (right side) coordinate as a function of the beam energy. S is the stochastic term, N the noise term, and C the constant term [55].

In addition, a method to correct for shower leakage out of the array used to reconstruct the electrons energy has been developed. The method only uses the distribution of energy measured within the array [56].

5.3.2. Determination of the inter-calibration constants

To correct for variations in the channel response within the ECAL barrel, inter-calibration constants have been determined for every crystal. The main origin of the variation in the channel response is the scintillation light yield of the individual crystals, which has a RMS spread of $\sim 15\%$. Other parameters that differ for the channels are for example variations in the gain and the photo detection efficiency of the APDs.

All super-modules were inter-calibrated with cosmic ray muons. Due to a lack of beam time after the completion of the super-modules, only nine super-modules were inter-calibrated with the electron beam. The response of each single crystal to an incident particle was compared to a reference signal to obtain the inter-calibration. The reference signal was either the energy of the incident electron beam or the energy of a minimum ionizing cosmic ray muon which deposited $250\,\mathrm{MeV}$ when transversing the full length of a crystal. The channels of the nine super-modules inter-calibrated with the electron beam could be equalized to 0.3%. The inter-calibration precision of the remaining 27 super-modules, inter-calibrated with cosmic muons was 1.5%.

Calibrated super-modules were ready for the installation in CMS, and were stored in a dedicated air-conditioned storage area.

5.4. Conclusions of this chapter

This chapter described the integration of the read-out electronics of the ECAL barrel and the accompanying tests. The test runs and the typical results of the super-module commissioning were discussed. Based on these test results, a simple analysis was introduced to unambiguously identify and classify hardware problems. The number of errors found during the commissioning are discussed in detail in the next chapter. The determination of the ECAL barrel energy and position resolution with electrons and cosmic muons showed that the ECAL design requirements are met.

The electronics integration of the ECAL end-caps was performed during July 2007 and July 2008 in an analogous manner. After their completion, none of the 14 648 channels in the end-caps showed an error. This excellent performance was mainly due to the experiences made in the campaign with the ECAL barrel.

Chapter 6.

Performance of the electromagnetic calorimeter barrel

From November 2005 to August 2006, 27 out of 36 super-modules were integrated and tested during the so-called first integration campaign. During the commissioning and calibration we observed a significantly increasing number of problematic channels in these super-modules. After a detailed investigation, it was found that these failures were due to the overall poor quality of the Kapton cables of the motherboards and their soldering joints. As a consequence, it was decided to re-manufacture all motherboards. The new motherboards had to be prototyped, produced, and exchanged in the already integrated 27 super-modules. Since the motherboard is the first component installed from the ECAL barrel electronics, it is covered by the readout electronics and other systems. Thus, the electronics of the completed super-modules had to be dismounted, re-integrated and re-tested in the so-called second integration campaign.

This chapter summarizes problematic channels found during the first integration campaign and their development in time. The problems found in the old motherboards and the tests introduced for the new motherboards are described in detail. Furthermore, the performance of all ECAL barrel super-modules after the second integration campaign and their performance after the installation in the CMS detector are discussed. The last section of this chapter summarizes the status of the problematic channels of the ECAL barrel and end-caps as of March 2010. The results, except those of the last section, were presented in [53].

6.1. First integration campaign

The first integration campaign was stopped in August 2006 due to the increasing number of faulty channels. In particular, disconnected photo-detectors, shorted photo-detectors

and dead MGPA chips were found. During that time, the super-modules numbered 0 to 26 were completely integrated and commissioned except for number 5. The calibration with electrons and cosmic muons was accomplished for 9 and 20 super-modules, respectively. The increase of the unusable channels in time could be determined because of time delays of usually a few months between the three different phases of the ECAL barrel integration and calibration.

- **Phase 1: Integration**
  Installation and testing of the readout electronics and commissioning of the super-module. Malfunctioning components were replaced and potential systematic failures were investigated and corrected, if possible (Chapter 5).

- **Phase 2: Calibration**
  After successful completion of the commissioning, the super-modules were transferred to the H4 test area, where every crystal, including the corresponding readout electronics was calibrated using cosmic muons or electrons from the test beam (Section 5.3). The commissioning test runs were repeated several times per day.

- **Phase 3: Good health check**
  The calibrated super-modules were re-commissioned during the first commissioning campaign to identify the reason for problems mentioned above. Since the performance of the super-modules was stable after the motherboards exchange, the good health check was not necessary during the second integration campaign. The *Good health check* then determined the status of the ECAL frequently after the insertion in CMS.

Table 6.1 summarizes the status of the 26 super-modules after the *Good health check* in August 2006. 109 channels were found with a bad APD connection, 18 with a shorted APD, 27 with a dead MGPA, and 26 were noisy. Since channels with errors of the last two categories were considered as usable, we obtained a total of 154 unusable channels in the 26 super-modules, corresponding to a fraction of problematic channels of 0.3%. This was well below our aimed fraction of below 1%, that was necessary to meet the ECAL design resolution requirements.

Nevertheless, we observed a considerable increase of the non-usable channels during the different integration phases. Figure 6.1 represents the time evolution of the errors A, B, and C. It shows the cumulative number of problematic channels nA, nB, and nC as a function of ΔT. ΔT is the time in months elapsed since the time of phase 1 (T1 = 0 months) and the time of a successive test during the phases 2 or 3. Thus, the points in time ΔT are determined by the time intervals between the different tests of a super-

| Super-module	Bad APD connection	APD shorted	MGPA dead	Noisy
0	17	1	0	1
1	1	0	0	0
2	2	0	2	1
3	3	1	0	1
4	7	1	0	0
6	5	0	0	1
7	0	0	0	0
8	1	1	0	0
9	4	0	3	0
10	1	0	0	1
11	2	2	1	5
12	2	0	3	2
13	3	1	2	1
14	4	2	1	0
15	7	1	0	1
16	3	1	1	0
17	2	1	0	6
18	4	1	1	0
19	10	1	2	4
20	8	1	1	1
21	6	1	6	0
22	7	2	3	1
23	3	0	1	0
24	4	0	0	0
25	3	0	0	0
26	0	0	0	0
All	**109**	**18**	**27**	**26**

Table 6.1.: Hardware errors of the 26 super-modules, which were integrated and commissioned during the first integration campaign.
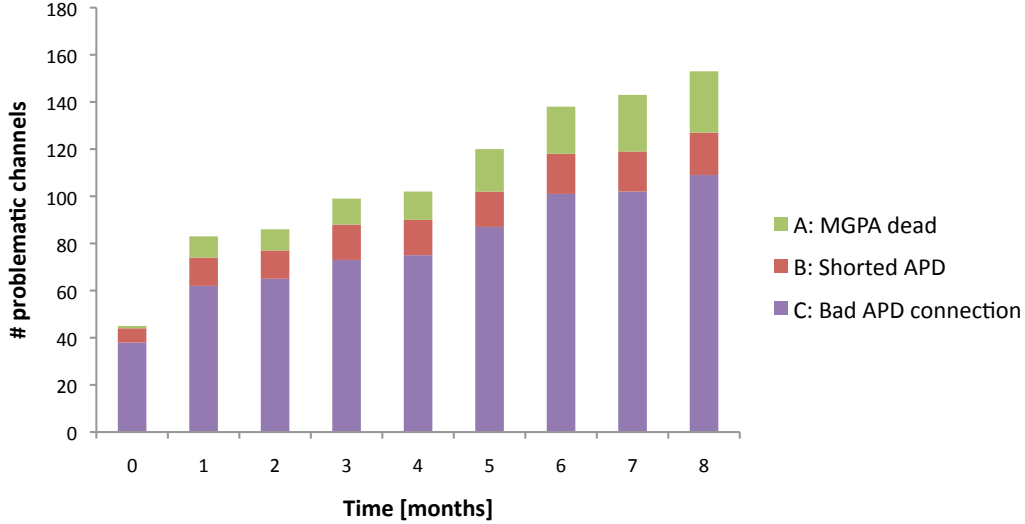
Figure 6.1.: Time evolution of the number of channels with errors A, B or C.

module. The plot shows a continuous growth for all three errors over a time period of eight months. In particular, the numbers of bad APD connections and of dead MGPAs grew from 38 to 109 and from 1 to 26, respectively. As a result, the integration campaign was stopped and the problems were investigated. The motherboard was identified as the cause of the problems. In particular, the poor quality of the Kapton cables and of the soldering joints of the cables to the PCB induced bad APD connections (error A) and shorted APDs (error B). Dead MGPA chips (errors C) were also caused by bad Kaptons, since discharges through their insulation destroyed the input of the MGPA chip (Section 4.4.1 for a detailed description of the motherboard). Section 6.2 explains the details of the observed problems.

The total number of problems was still low with respect to the aim, but the high growing rate required a prediction of the number of motherboard related errors. To gain the require knowledge, accelerated aging tests were performed on 250 motherboards from four dismantled super-modules. The aging tests included a thermal cycling and a chemical stress test, which simulated an aging of $\sim$10 years of LHC operation. The thermal cycling performed 90 thermal cycles of 4 hours each between temperatures of $-20\,^\circ$C and $+80\,^\circ$C. The chemical stress test kept the motherboards for 80 hours at an ambient temperature of $+80\,^\circ$C at a relative humidity of 80%. Before the aging, we found 22 errors out of 7 500 channels related to categories A or B. After the aging tests, this number increased to 79, corresponding to a fraction of problematic channels of 1%, which was considered as too high. This fraction, together with results of a detailed

Metallization of Kapton cable

Kapton cable
Motherboard PCB
Solder
Pin of VFE connector
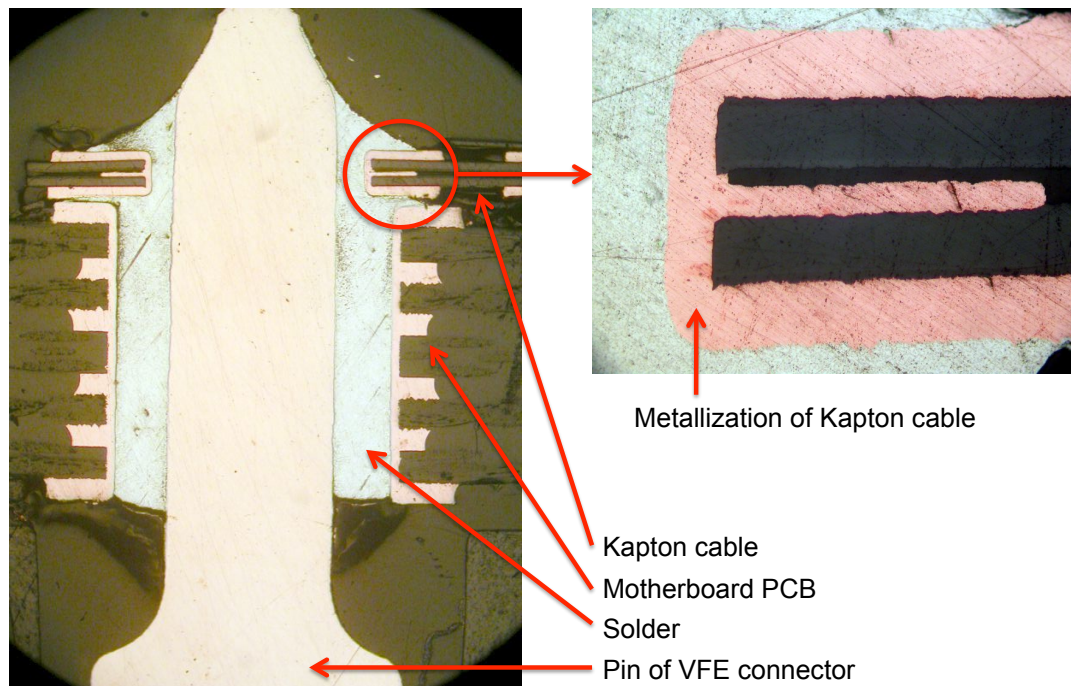
Figure 6.2.: An example of a perfect motherboard soldering joint (left side) and a perfect barrel metallization of the Kapton cable (right side) [58].

study of the motherboards problems (Section 6.2) resulted in the replacement of the motherboards.

6.2. Analysis of motherboards failures

The motherboards were investigated in detail to identify the reasons for the shorts and lost connections. The Division-Metallurgy and Metrology of the Technical Support Department of CERN and the producer of the Kapton cables for the new motherboards (GS Präzisions AG, Küssnacht, Switzerland) analyzed the old motherboards [57, 58]. Both analyses were based on metallographic cuts and microscopic inspections. The pictures shown in the following are taken from both reports. Figure 6.2, left side, shows an example of a perfect soldering joint. The microscope image shows the three layer Kapton cable on top of the motherboard PCB. The pin of the VFE connector is in the center, and the grey material is the solder. The right side of Figure 6.2 shows the metallized edge of the Kapton cable. This so-called barrel metallization assures a proper connection between the cathode strip of the Kapton and the soldering joint.

Figure 6.3 displays an example of a poor barrel metallization of the Kapton. As can be clearly seen, the cathode of the Kapton cable is not connected to the barrel
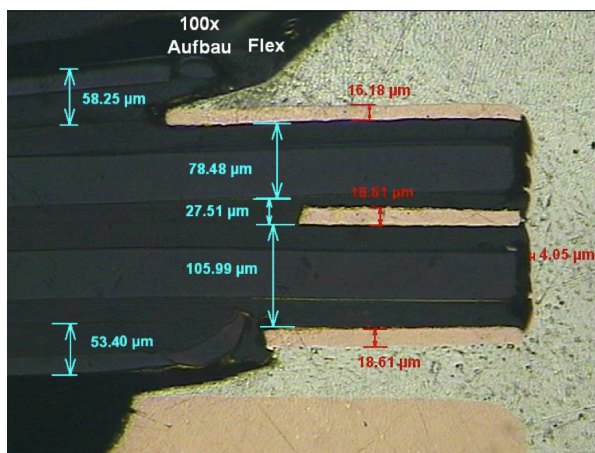
Figure 6.3.: An example of a bad barrel metallization of the Kapton cable [58].
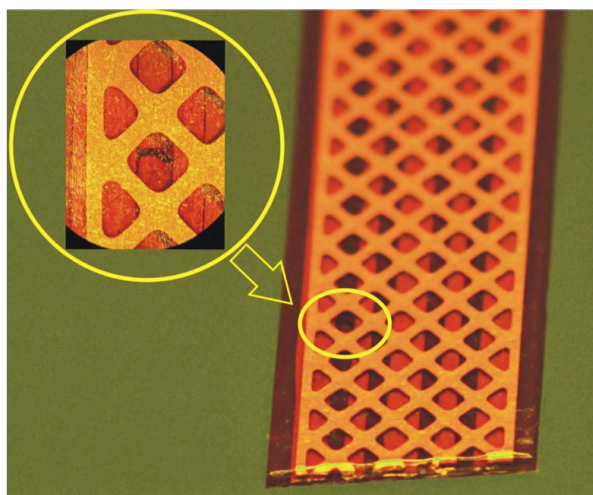
Figure 6.4.: Short between the cathode and the ground conductor within the signal layer of the Kapton cable.

metallization. In addition, the barrel metallization is in the range of 2-5 μm, which is too thin to withstand thermal or mechanical stress. Moreover, it does not meet the quality specification established by the Association Connecting Electronics Industries (IPC). A possible explanation for this failure could be poor drilling quality or insufficient cleaning of the drilled hole prior to the barrel metallization.

In conclusion, these failures found by the two teams explained the bad APD connections (error A) we found during the commissioning. This proved that there were two systematic problems in the manufacturing process. Consequently, one concluded that there were many further cases with only very weak connections between cathode and metallization. These weak connections might have broken during the LHC operation due to aging, resulting in too many unusable channels in the ECAL barrel.

Another type of hardware failures encountered were shorts. Figure 6.4 shows an example, where the cathode and the ground conductors were shorted within the signal layer of a Kapton cable. This type of failure was found to be the reason for the shorted APDs (error B), which occurred during the commissioning. These failures originated from the poor quality of the Kaptons and were also considered as a systematic problem, which might have caused an unacceptable increased number of shorts during the LHC operation.

6.3. New motherboards production and tests

In December 2006, the ECAL community decided to re-manufacture the motherboards of the ECAL barrel super-modules. Ascom Schweiz AG (Hombrechtikon, Switzerland) was chosen as manufacturer of the motherboards and GS Präzisions AG (Küssnacht, Switzerland) as supplier for the new Kapton cables. A total of 2 700 motherboards were ordered and 2 734 pieces have been delivered between February and July 2007.

In addition to a visual inspection, two quality tests were performed on the motherboards. First, a high voltage of $500\,\mathrm{V}$ was applied, and the leakage current was measured to find shorts (the operation voltage of the APDs was $\sim 380\,\mathrm{V}$). Secondly, the connectivity of all 25 channels on the motherboards was checked with a special test setup provided by our collaborators from INFN Torino. Out of the 2 734 delivered motherboards, only two pieces with a short were found. The second test showed positive results for all motherboards. We found nine motherboards with at least one mechanically broken connector and one with an insufficiently soldered connector. The first batch of 49 pre-produced motherboards underwent aging tests. These aging tests included the same thermal cycling and chemical stress test as described in Section 6.1. After the aging, the devices were retested for shorts and connectivity. The new motherboards did not show a single failure.

Four motherboards from the pre-production were also tested for their radiation hardness in the Proton Irradiation Facilities (PIF) at Paul Scherrer Institute (PSI) [59]. A proton beam with an energy of $72\,\mathrm{MeV}$ was used. The diameter of the beam spot was about $90\,\mathrm{mm}$ with uniformity of 90% inside of a circle with $50\,\mathrm{mm}$ diameter. The beam monitoring system at PIF-PSI was used to control the beam intensity and absorbed doses. During the irradiation, a high voltage of $500\,\mathrm{V}$ was applied to the motherboards. The motherboards were irradiated in two runs lasting 12 and 16 hours, respectively. The fluences were $2 \times 10^{13}\,\mathrm{protons/(s \cdot cm^2)}$ and $3 \times 10^{12}\,\mathrm{protons/(s \cdot cm^2)}$. The doses received by the motherboards in run A and B corresponded to an irradiation of 10 and 1.5 years

under the nominal LHC conditions, respectively. We did not observe any increase of leakage currents in the four motherboards after the irradiation.

6.4. Second integration campaign and installation

The second integration campaign included the dismantling of the electronics of the 27 completed super-modules from the first integration campaign and the integration of all 36 super-modules of the ECAL barrel. This campaign had to be accomplished in only six months to meet the installation time window of the ECAL barrel in the CMS detector. It lasted from February to July 2007.

Ten super-modules were calibrated with cosmic muons at the test beam area (Section 5.3). The calibration constants of the super-modules calibrated during the first integration campaign were kept. To make sure that these constants were still valid, all dismantled electronics parts were reinstalled in the same super-module and at exactly the same position.

Table 6.2 summarizes the status of the 36 super-modules at the end of the second integration campaign. The total number of non-usable channels according to the error categories A, B and C was 29 in total and 14 channels were noisy. The error rate of 0.05% was extremely low compared to the rate of 0.3% after the first integration campaign. The completed super-modules were stored in the storage area until their transport to Point 5 of the LHC ring for insertion into the CMS detector.

The 36 super-modules were installed in CMS during two campaigns in May and June/July 2007. In November 2007, the ECAL barrel was connected to all necessary services and to the off-detector trigger and data acquisition. Table 6.3 summarizes the status of the ECAL barrel after this so-called "cabling" campaign. Surprisingly, we found less errors of the categories A and B than during the integration. This observation might be explained with the slight shaking of the super-modules during the transport. Unwanted electrical connections (shorted APDs, error B) or unwanted electrical disconnections (bad APD connection, error A) might have been fixed by the moving of the connectors during the slight shaking of the hole super-module. This shaking could also explain the increase of the errors of category C. The number of errors of the categories D increased only slightly.

The installation of the two ECAL end-caps was accomplished in August 2008. The first tests showed that all 14 648 channels of the end-caps worked correctly.

Super-module	Error A	Error B	Error C	Error D
0	3	1	0	0
1	0	0	0	0
2	3	0	0	0
3	0	1	0	3
4	0	0	0	0
5	2	0	0	1
6	0	0	0	1
7	1	0	0	1
8	0	0	0	0
9	1	0	0	1
10	0	0	0	0
11	0	1	0	0
12	2	0	0	0
13	0	0	0	1
14	2	0	0	0
15	0	0	0	0
16	1	0	0	0
17	0	0	0	0
18	1	0	0	0
19	0	0	0	1
20	1	0	0	0
21	1	1	0	0
22	0	0	0	0
23	0	0	0	0
24	0	0	0	0
25	0	1	0	0
26	0	1	0	0
27	0	0	0	0
28	0	0	0	0
29	0	0	0	2
30	1	0	0	1
31	1	0	0	0
32	0	0	0	0
33	1	0	0	0
34	1	0	0	0
35	1	0	0	2
All	**23**	**6**	**0**	**14**

Table 6.2.: Hardware errors per super-module in the second integration campaign before the installation in CMS.

Super-module	Error A	Error B	Error C	Error D
All	**19**	**5**	**5**	**15**

Table 6.3.: Total number of hardware errors found in the ECAL barrel after the installation in CMS.

Variable	Gain 1	Gain 6	Gain 12
Pedestal mean with HV on		170-230	
Pedestal RMS with HV on	< 1	< 1.2	< 2
Pedestal RMS with HV off	-	-	> 2
Test Pulse mean amplitude	$> 50\%$ average amplitude		
Laser amplitude RMS	-	-	> 300

Table 6.4.: Cuts of the *Good health check* test runs for the ECAL barrel. All values are given in ADC counts.

6.5. Status in February 2010

This section summarizes the number of malfunctioning channels of the ECAL barrel and end-caps just before the start of data taking with LHC in March 2010. The data were taken in a *Good health check* and in the CMS magnetic field of $3.8\,\mathrm{T}$. The test runs were the same as during the commissioning, however the cuts applied to identify problematic channels changed due the different running conditions e.g. the strong magnetic field. Notably, the cuts for the *Pedestal run with HV on* were less strict compared to the cuts applied during the commissioning. Table 6.4 summarizes the cuts for the barrel part of the ECAL.

The cuts applied in the test runs for the end-caps are summarized in Table 6.5. They are slightly different compared to the ones applied to the barrel runs, mostly due to the use of VPTs instead of APDs as photo-detectors. In particular, VPTs have a gain of 10 compared to 50 of the APDs. Consequently, the gains of the MGPAs in the end-caps are 12 times higher than those of the barrel. As a result the channels in the end-caps have a higher noise level. In addition, VPTs do not have a leakage current. A *Pedestal run with HV off* was not performed because the test does obviously not identify bad VPT connections.

Variable	Gain 1	Gain 6	Gain 12
Pedestal mean with HV on		170-230	
Pedestal RMS with HV on	< 1	< 1.4	< 2.5
Test Pulse mean amplitude	$> 50\%$ average amplitude		
Laser amplitude RMS	-	-	> 100

Table 6.5.: Cuts of the *Good health check* test runs for the ECAL end-caps. All values are given in ADC counts.

ECAL part	Bad APD connection	Shorted APD	MGPA dead	Noisy
Barrel	**19**	**6**	**28**	**97**
End-caps	**0**	**0**	**1**	**65**

Table 6.6.: Hardware errors of the ECAL barrel in the *Good health check* from February 2010.

The corresponding histograms can be found in Appendix A. The distributions of the pedestal RMS in Figure A.2 have a mean noise in the highest gain of 1.2 and 2 ADC counts corresponding to $\sim 40\,\text{MeV}$ and $\sim 50\,\text{MeV}$ for barrel and end-caps, respectively.

The results of the tests are summarized in Table 6.6. For barrel and end-caps, the number of bad APD/VPT connections and shorted APDs stayed constant. However, the numbers of dead MGPAs and noisy channels increased significantly. A possible explanation of this behavior could be the very frequent on and off switching of the detector in the past years. This should be avoided, since the readout electronics was not designed for that purpose.

35 additional channels were off since the LVR boards powering them were broken. Three trigger towers did not send any data due to failures of the GOH chip. Five trigger towers and nine single channels had problems with the data integrity. The problems were still under investigation in May 2010. In total, the fraction of faulty channels stayed constantly at less than 0.4% over a period of one and a half year.

6.6. Conclusions of this chapter

This chapter summarized the number of malfunction channels in the ECAL barrel over the different stages of construction. The reasons to re-manufacture and change the motherboards of the ECAL barrel were described. Thereby, the classification of hardware errors described in the previous chapter was a useful tool to support the decision of the motherboard change. Using the new motherboards, the fraction of problematic channels of the ECAL barrel was extremely low almost three years after the insertion in CMS. The ECAL end-caps also exhibit an excellent performance one year after their installation.

In conclusion, the ECAL of the CMS detector is performing reliably and is ready for high precision measurements of the energies of photons and electrons during the LHC runs at $E_{CM} = 7\,\mathrm{TeV}$ in 2010 and 2011.

Chapter 7.

Electron identification

The efficient identification of isolated high-energy electrons with small or even negligible background is of highest importance for a large number of physics processes investigated at LHC. The electron selection presented in this thesis was developed for the Higgs search in the channel $H \rightarrow W^+W^- \rightarrow e^+\nu_e e^- \bar{\nu}_e$ and a Higgs mass between 160 and 170 GeV, which is discussed in detail in Chapter 9. The main purpose of this electron selection is to reduce the potential background contribution from WX events, where the W decays to an electron and a neutrino and X is either a jet or a photon, misidentified as an electron. The size of the problem can be understood from the ratio of the production cross-sections, being roughly 10^{-5} (signal-to-background ratio). The electron selection should combine a strong background reduction and a high efficiency of the electron reconstruction.

This chapter explains how electron candidates are reconstructed. Various electron selection variables are introduced and selection cuts are derived. The performance of the obtained electron selection is then compared for two different versions of the CMS analysis and software framework CMSSW [60]. Finally, the low energy electron candidates that were found in the first collision data taken with LHC in 2009 are briefly discussed.

The analysis is restricted to electrons that are found in the barrel part of the CMS ECAL. This approach simplifies the understanding of systematic errors, which are different for the barrel and end-caps, mainly due to the presence of the pre-shower detector in front the latter. In addition, the searches for the Higgs boson and the W presented in Chapters 9 and 10 rely on rather centrally produced electrons.

7.1. Reconstruction

The reconstruction and selection of electrons in CMS is based on the experiences of previous collider experiments. The main characteristics used to distinguish electrons from other particles are based on:

- A high-energy deposit in the ECAL, with a shower profile consistent with an electromagnetic shower, which distinguishes electrons and photons from hadrons and muons.

- A high momentum track pointing to the shower center of the ECAL cluster, which separates electrons from photons.

- The matching of the position and the energy/momentum measurements of the ECAL and the tracker.

- An isolation criteria, which discriminates electrons from hadronic jets, where for example a charged pion gives a track and an overlapping decay $\pi^0 \to \gamma\gamma$ leaves a deposit in the ECAL.

In the following, these criteria are used to reconstruct electrons in the barrel of the CMS detector. Detailed descriptions of the CMS electron reconstruction algorithm can be found in [61, 62, 63].

7.1.1. Electron energy measurement in the electromagnetic calorimeter

As discussed in Section 4.2, an electron entering an ECAL crystal triggers an electromagnetic shower. The amount of light in the shower is proportional to the electron's energy and is measured by photo detectors. Since the shower spreads laterally, an electron of for example 35 GeV typically deposits 97% of its energy in a matrix of 5×5 crystals [56].

Due to the relatively large amount of material in the CMS central tracker (Figure 7.18), propagating electrons emit many bremsstahlung photons before they reach the ECAL. Some of these photons convert into electron-positron pairs well before the calorimeter. Because of the CMS magnetic field of 3.8 T, which is parallel to the z-axis, the energy deposits in the ECAL crystals from these secondary particles spray in the ϕ direction from the electron's trajectory. The total electron energy can be determined by summing these energy deposits along a ϕ road. The ECAL region where this summing is performed is called a *super-cluster*.

Two different algorithms define the super-clusters in the ECAL barrel and end-caps [61]. The clustering algorithm in the ECAL barrel starts from a single crystal, called *seed crystal*, which has a local maximum energy deposit of at least 1 GeV. Subsequently, a row of 3 or 5 crystals in the η direction is build symmetrically around the seed crystal. 5 crystals are used, if the energy sum of 3 crystals is larger than 1 GeV. Additional rows of 3 or 5 crystals are added to the super-cluster in the ϕ-direction. The algorithm stops if the number of added rows reaches ten in either direction of ϕ, or the energy deposited in the row to be added is lower than 0.1 GeV.

The total super-cluster energy is obtained by summing the energy deposits of all crystals of the super-cluster. As shown in [61], this energy does not perfectly represent the energy of the incident electron, because of shower leakage through the gaps between the crystals. This loss, of typically a few percent in the ECAL barrel, is dependent on the number of crystals in the super-cluster. The loss can however be determined from the distribution of energy within the super-cluster as shown with test beams of 120 GeV [56]. After the correction, the super-cluster energy gives an accurate and almost Gaussian measurement of the original electron energy at the event vertex as shown in Figure 7.1 (left side).

Finally, the position of the super-cluster is obtained by calculating the energy weighted mean position of the crystals in the cluster.

7.1.2. Electron track reconstruction

Electrons, like all charged particles, ionize the silicon layers of the CMS tracker. The resulting signals, called hits, are combined to a single track. For electrons, the track must point towards a super-cluster. The track can also be used for the measurement of the electron's momentum, due to the bent electron trajectory in the magnetic field of CMS.

The next step of the electron reconstruction, after a super-cluster is found, is the matching of the super cluster with hits in the pixel detector. Hereby, a relatively wide window $\Delta\eta \times \Delta\phi$ is used to look for doublets or triplets of pixel hits. These hits are used as seeds for the electron track construction. The track reconstruction tries to take into account the electron's energy loss induced by bremsstrahlung in the material of the tracker. The distribution of this energy loss, however, is highly non-Gaussian due to the low electron mass. Figure 7.1 (right side) exemplifies the energy loss of electrons compared to that of the much heavier muons using a Monte Carlo detector simulation of CMS. The distributions compare the reconstructed and generated transverse momenta
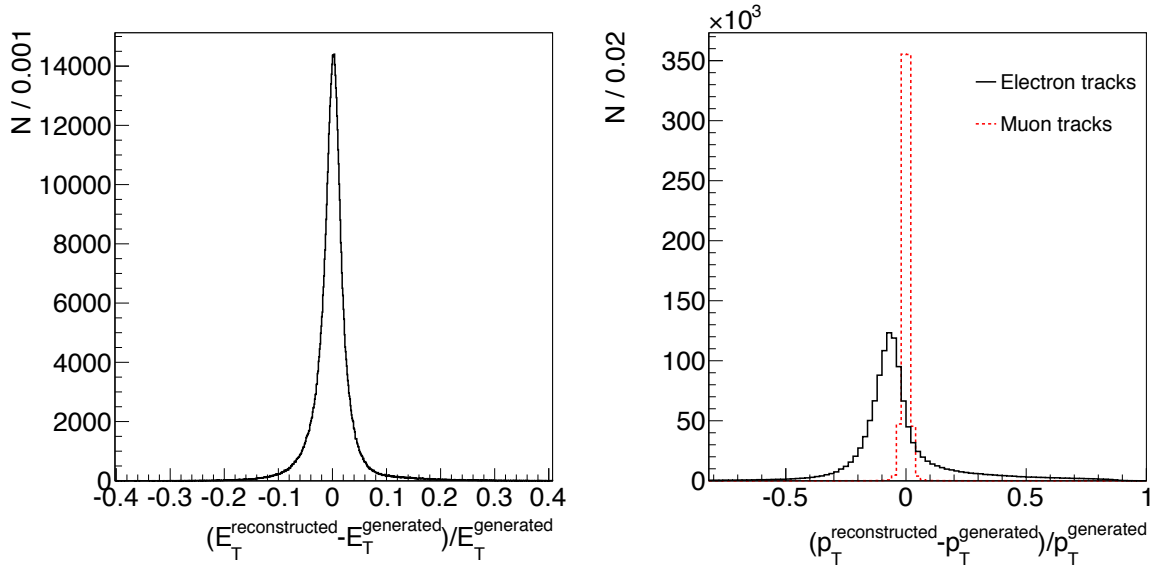
Figure 7.1.: The resolution of the electron transverse energy measurement with the ECAL (left side) and the transverse momentum reconstruction from tracks for electrons and muons (right side). The distributions are shown for electron and muons with $E_T > 20\,\text{GeV}$ and $|\eta| < 1.44$ using Monte Carlo data.

for electrons and muons. Here, the transverse momenta were reconstructed from the track. As can bee seen, the resolution in the muon case peaks at zero and has a Gaussian shape. In the electron case, the momenta are systematically underestimated and long asymmetric tails are observed.

Therefore, the electron's energy loss is modeled by a Gaussian mixture, called the Gaussian-sum filter (GSF) algorithm [64]. The usual CMS track reconstruction, however, uses a single Gaussian, the so-called Kalman filter [65]. The GSF algorithm leads to multi-component trajectory states for each measured point of the electron trajectory. In particular, the momentum measurements at the innermost (p_{in}) and outermost (p_{out}) states of the tracker are available.

7.1.3. Preselection

Electron candidates found with the reconstruction algorithm are defined as the combination of a ECAL super-cluster and an associated GSF track. To reduce the background from jets, these electron candidates are preselected using the following observables:

- The transverse energy E_T of the super-cluster defined as $E_T = E \sin\theta$, where θ is the super-cluster's angle with respect to the beam axis and E the ECAL super-cluster energy,

| Preselection cut	CMSSW 2_2_X	CMSSW 3_1_X
$E_T >$	$4\,\mathrm{GeV}$	$4\,\mathrm{GeV}$
$\Delta\eta <$	0.02	0.02
$\Delta\phi <$	0.1	0.15
$\Delta R_H <$	0.05	0.15
$H/E <$	0.1	0.1

Table 7.1.: Preselection cuts of the electron reconstruction for two different versions of CMSSW

- the ratio H/E, where H is the candidate's energy deposit in the HCAL within a cone with radius $\Delta R_H = \sqrt{(\Delta\eta)^2 + (\Delta\phi)^2}$ centered around the super-cluster position,

- $\Delta\eta = |\eta_{SC} - \eta_{track}|$, where η_{SC} is the weighed super-cluster position, and η_{track} the coordinate of the track at the point that is closest to the beam line, and

- $\Delta\phi = |\phi_{SC} - \phi_{track}|$, that is defined accordingly to $\Delta\eta$.

The H/E variable measures leakage of the candidate's energy from the back of the ECAL into the HCAL. $\Delta\eta$ and $\Delta\phi$ measure the spatial matching of track and super-cluster. Cuts on these observables of electron candidates increase the signal-to-background ratio after the electron preselection.

The cut values and the cone size of the H/E sum are summarized in Table 7.1 for the two CMSSW versions 2_2_X and 3_1_X. For both versions, the minimum transverse energy measured in the super-cluster is $4\,\mathrm{GeV}$. In addition, the cuts on $\Delta\eta$ are tighter than those on $\Delta\phi$, because the trajectory of the candidates is only deviated in ϕ direction. The comparison between the versions shows that the cut on $\Delta\phi$ is softer in the more recent version of CMSSW. The cut on H/E is tighter, since the HCAL energy is summed in a larger cone, whereas the cut value itself stayed constant.

However, as the next section will show, the signal-to-background-ratio after applying either set of preselection cuts is still too low for our purpose. In particular, roughly 1% of the jets with $E_T > 20\,\mathrm{GeV}$ are reconstructed as electron candidates. Thus, further electron selection criteria have to be applied. The next section discusses the development of electron selection cuts for the CMSSW version 2_2_X. A comparison of the obtained electron selection for both CMSSW versions follows in Section 7.3. The electron selection was for the first time presented in [66].
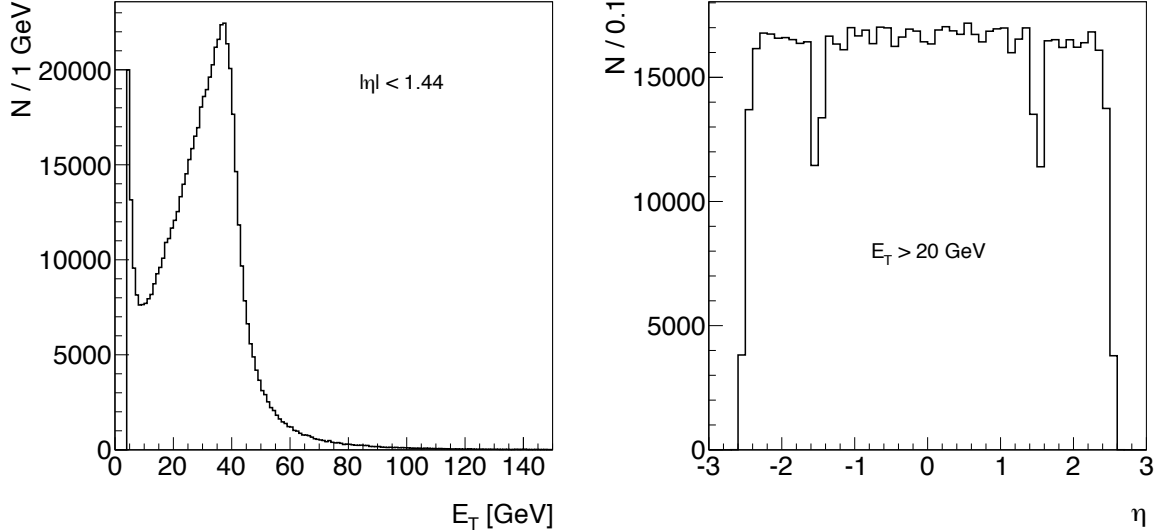
Figure 7.2.: Transverse energy (left side) and η distributions (right side) of all reconstructed electron candidates of 1.11 million $W^{\pm}X \to e^{\pm}\nu X$ events.
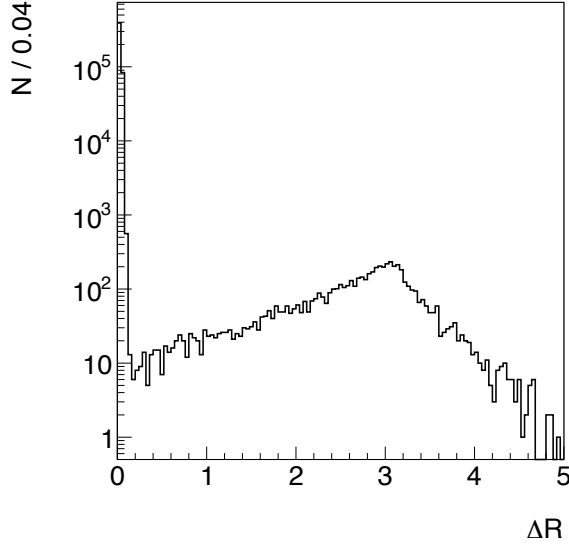
7.2. Electron selection

The electron selection criteria presented in this section, are based on Monte Carlo generated events and a CMS detector simulation using the program Geant 4 [67, 68]. In particular, a sample of 1.11 million inclusive $W^{\pm}X \to e^{\pm}\nu X$ Monte Carlo events generated with PYTHIA [69] at $E_{CM} =10\,\text{TeV}$ was used. This sample corresponds to an integrated luminosity of $0.098\,\text{fb}^{-1}$. The generated events were passed through a full detector simulation in the CMSSW version 2_2_X.

In 95% of the events, at least one reconstructed electron candidate was found. Figure 7.2 shows the E_T spectrum of all electron candidates with $|\eta| < 1.44$ and the η distribution for all candidates with E_T above 20 GeV, respectively. In addition to the Jacobian electron E_T spectrum with a peak at around 40 GeV, which can be expected from the mass of the decaying W boson, Figure 7.2 (left side) shows a peak at very low transverse momenta. As will be shown below, all these electrons can be identified to come from various backgrounds. Since we were mainly interested in high E_T electrons, the electron candidate's transverse energy E_T was required to be larger than 20 GeV and the corresponding super-cluster had to be in the ECAL barrel, e.g. $|\eta| < 1.44$.

Without additional electron selection criteria, 473k events were found with exactly one electron and about 3 000 with more than one electron within this sample of 1.11 million events. Since only one electron from a W boson decay was generated per event, the additional electrons that showed up were considered as *fake electrons*. This also

Figure 7.3.: ΔR between generated and reconstructed electron candidates with $E_T > 20\,\text{GeV}$ and $|\eta| < 1.44$.

includes real electrons from semi-leptonic decays within jets. The contributions from fake electrons, can be reduced by applying harder electron selection criteria.

To separate signal electrons and their backgrounds in a clear way, the electron candidate which corresponded to the electron coming from the W boson decay was identified using a simple geometrical matching. Figure 7.3 shows the distributions of the distance $\Delta R = \sqrt{(\Delta\phi)^2 + (\Delta\eta)^2}$ between the generated electron from the W boson decay and all reconstructed electron candidates. As the figure shows, the reconstructed electrons that match the generated one and those which do not, can clearly be distinguished using a cut at $\Delta R = 0.2$. In the following, we refer to the matched electron candidates ($\Delta R < 0.2$) as *true electrons*. The remaining reconstructed electron candidates in this sample were considered as potential electron background, in the following referred to as *fake electrons*. In total, 474 449 true and 6 197 fake electrons were found in the sample.

The E_T and η distributions of all fake electron candidates are shown in Figure 7.4. The large number of fake electrons with very low E_T is due to large cross-section of low E_T jets. In addition, an increased rate of fake electrons with pseudorapidities close to the gaps between the ECAL barrel and end-caps at $|\eta| \approx 1.5$ was observed. The position of these spikes was most likely related to the applied energy corrections for super-clusters reconstructed near the gap region. The analysis presented in the following section, however, is not sensitive to this area.
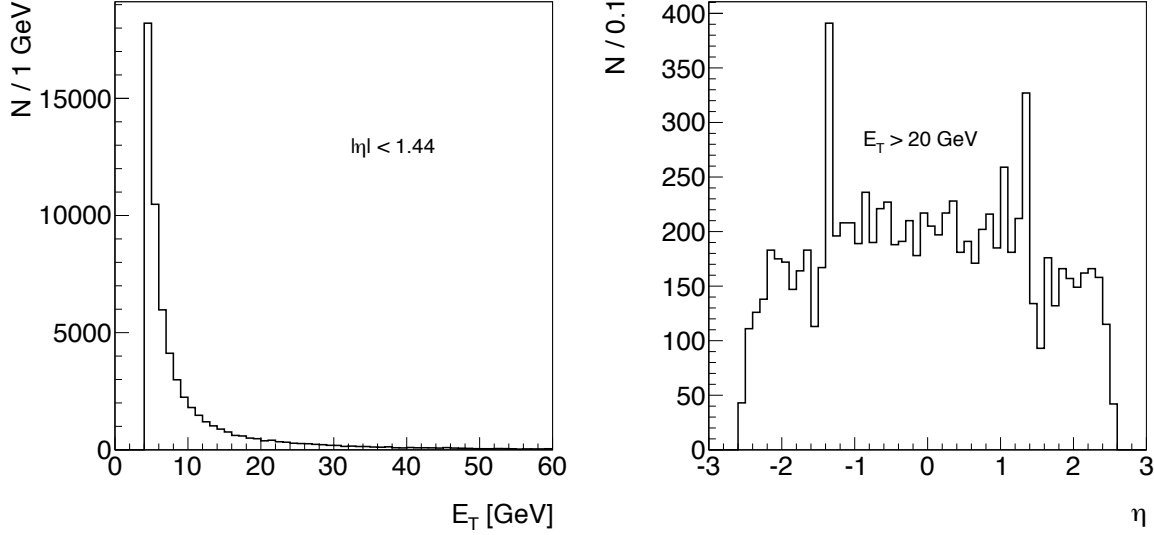
Figure 7.4.: Transverse energy (left side) and η (right side) distributions of fake electrons.

7.2.1. Selection variables

With these well defined true and fake electron candidates various experimental distributions, which are useful for an electron selection, can be studied. The most significant distributions, which allow to distinguish true and fake electrons are shown in Figures 7.5 to 7.9. Each histogram shows the normalized distributions of true and fake electrons in the $W^{\pm}X \to e^{\pm}\nu X$ events with $E_T > 20\,\text{GeV}$ and $|\eta| < 1.44$ as a solid black and dashed red line, respectively.

The electron isolation is perhaps the most important criteria. It is defined as the ratio of the sum of the transverse energies ($p_T^{Tracker}$, E_T^{ECAL}, or E_T^{HCAL}) of all well reconstructed particles (objects) within a cone of $\Delta R = 0.5$ around the electron candidate, and the candidate's super-cluster energy $E_T^{electron}$. The corresponding isolation variables for the three sub-detectors are defined as

$$
\begin{aligned}
\text{Isolation(Tracker)} &= \textstyle\sum_{\Delta R < 0.5} p_T^{Tracker} / E_T^{electron}, \\
\text{Isolation(ECAL)} &= \textstyle\sum_{\Delta R < 0.5} E_T^{ECAL} / E_T^{electron}, \text{ and} \\
\text{Isolation(HCAL)} &= \textstyle\sum_{\Delta R < 0.5} E_T^{HCAL} / E_T^{electron}.
\end{aligned}
\tag{7.1}
$$

To be counted in the sum of the tracker isolation, a well reconstructed track has to have a p_T above $1.5\,\text{GeV}$ and a distance of less than $2\,\text{mm}$ from the electron at the event vertex along the beam line. The distance cut assures, that only charged particles from the same vertex as the electron candidate are counted. For a well reconstructed object

in the ECAL and HCAL, a minimum E_T of $0.5\,\mathrm{GeV}$ is required. The HCAL isolation is a measure for the leakage of fake electrons to the hadron calorimeter and the isolation of both non isolated true electrons and fake electrons. The isolation variables are shown separately using the tracker, the ECAL and the HCAL in Figures 7.5 and 7.6.

The most powerful variable for the signal and background separation was found to be the track isolation criteria (Figure 7.5 (left side)). The isolation criteria in the electromagnetic and hadron calorimeter combined after applying the tracker isolation cut of 0.1 is shown in Figure 7.6 (right side).

Other important electron criteria are the matching between the track and the super-cluster parameters, either in η and ϕ, or in the reconstructed energy and momentum. As can be seen from Figure 7.7, the geometrical matching between the track and the super-cluster in η and ϕ are useful characteristics to discriminate electrons from background. The kinematic matching between the track momentum and the ECAL energy measurements, defined through the variables E/p and $|1/E - 1/p|$, are shown in Figure 7.8. For true electrons, in contrast to fake ones, the measured values E and p should agree within measurement errors. Accordingly, the distributions of the variables E/p and $|1/E - 1/p|$ should peak around 1 and 0, respectively. Even though the two variables contain the same information, the shape of the $|1/E - 1/p|$ can be controlled more easily once real LHC data will become available, since this distribution is very smooth for the fake electrons.

Figure 7.9 (left side) shows the sensitivity of the two cluster shape variables E_9/E_{25}, defined as the ratio of the energies deposited in 3×3 and 5×5 ECAL crystals centered around the seed of the electron's super-cluster. The variable $\sigma_{\eta\eta}$ measures the spread of the electrons electromagnetic shower in η over 5×5 crystals around the seed (Figure 7.9 (right side)). A detailed description of $\sigma_{\eta\eta}$ and the other variables can be found in [70].
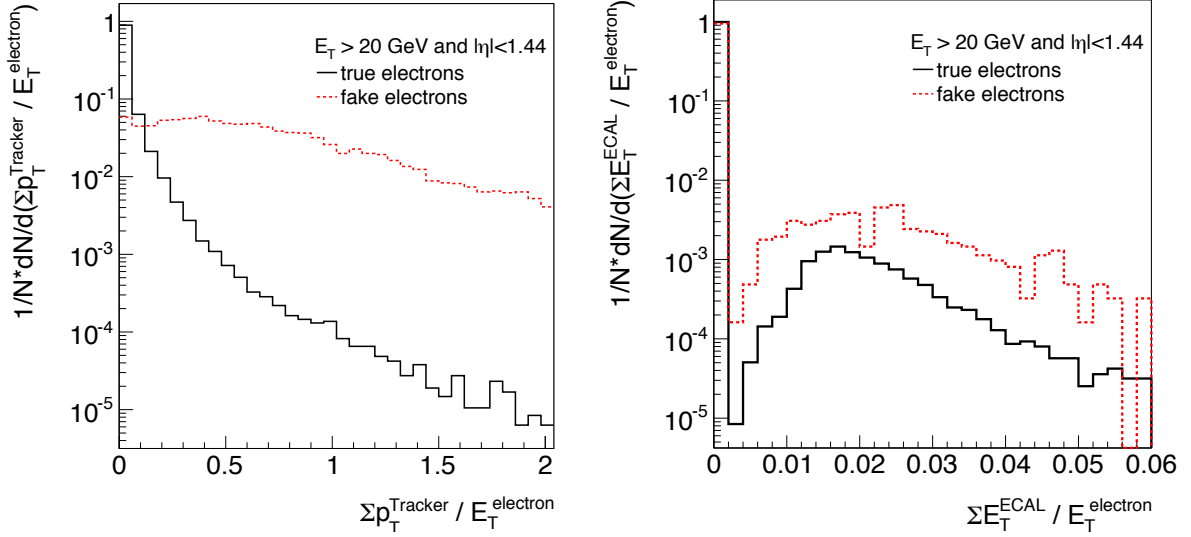
Figure 7.5.: Electron candidate isolation as measured from the tracker isolation (left side) and the ECAL (right side).
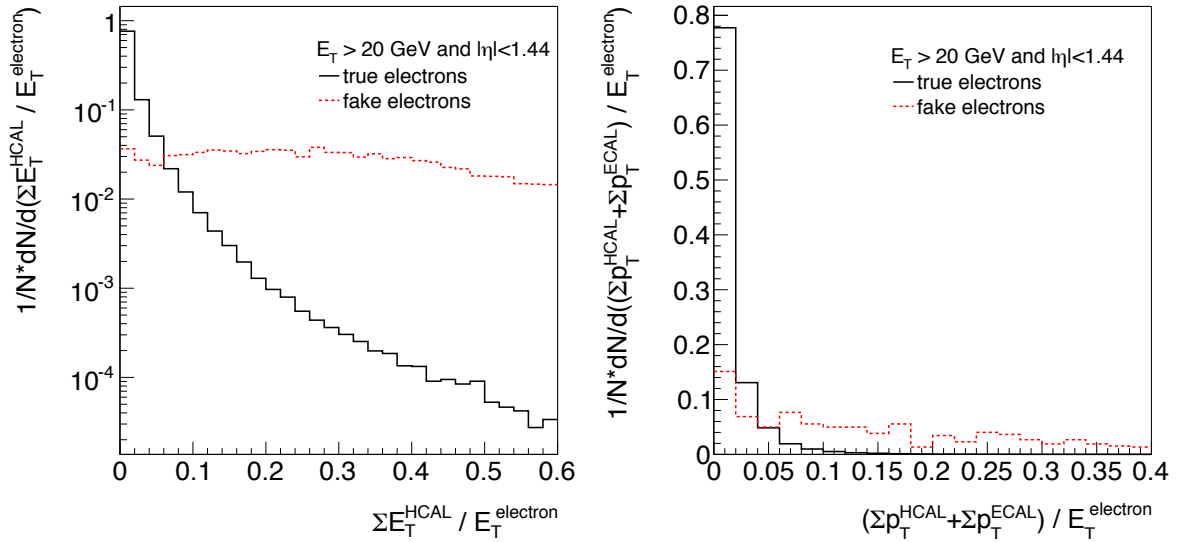

Figure 7.6.: Electron candidate isolation as measured from the HCAL (left side) and the combined ECAL plus HCAL isolation distribution, after the tracker isolation requirement of 0.1 is applied (right side).
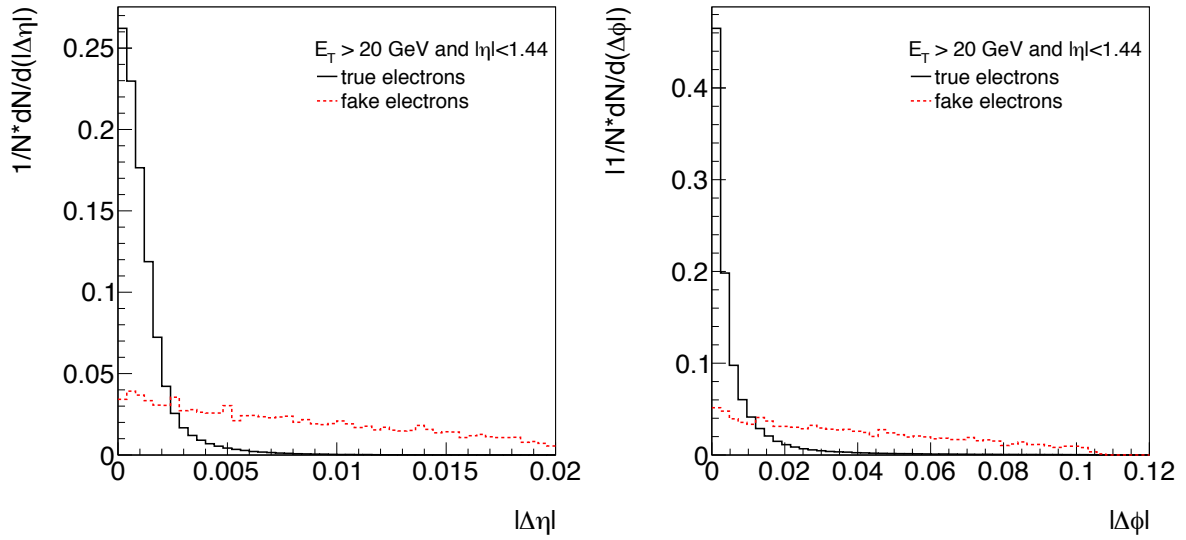
Figure 7.7.: The electron candidate track super-cluster matching for $|\Delta\eta|$ (left side) and $|\Delta\phi|$ (right side).
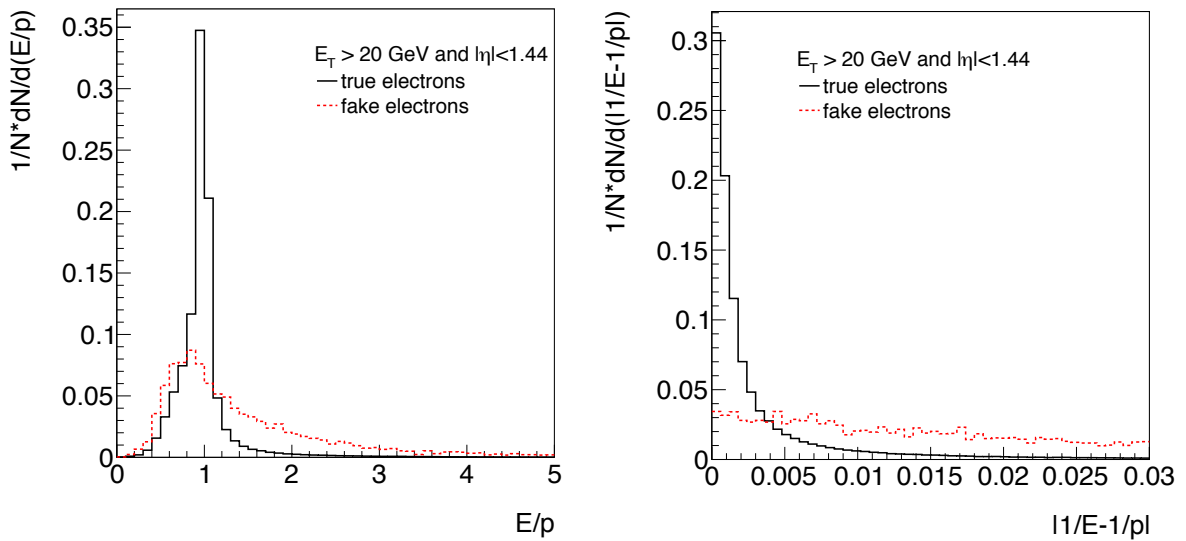
Figure 7.8.: The E/p (left side) and $|1/E - 1/p|$ (right side) distributions for the electron candidates.
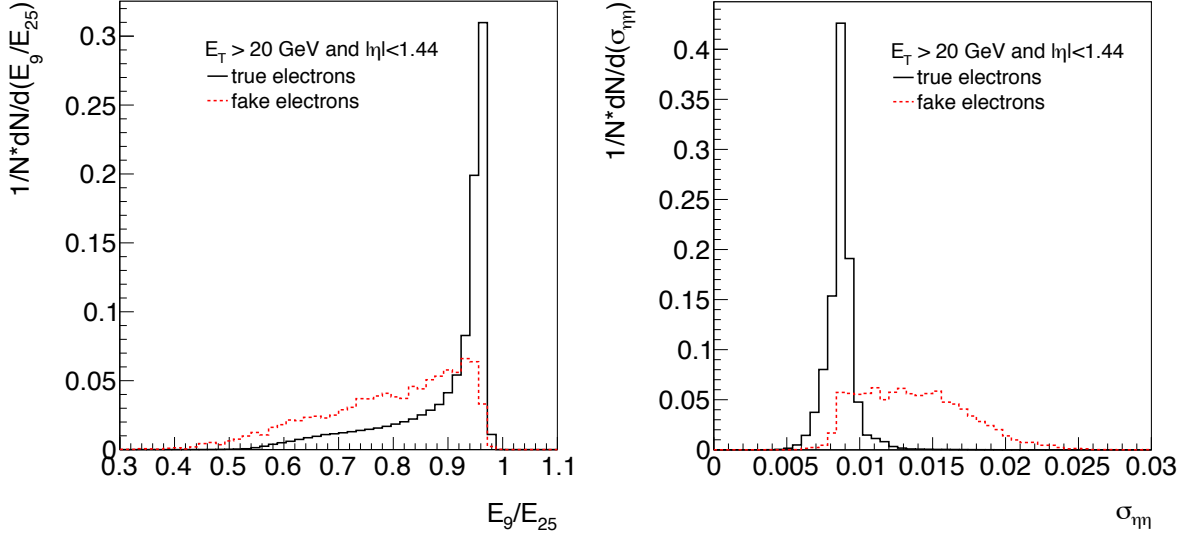
Figure 7.9.: The ECAL shower shape distributions E_9/E_{25} (left side) and $\sigma_{\eta\eta}$ (right side) for the electron candidates.

After having defined the most important electron selection criteria, their distributions of fake and true electrons were used to define the selection variables. Accordingly, it was first required that the electrons are isolated in the tracker, using $\frac{\Sigma p_T^{Tracker}}{E_T(electron)} < 0.1$. Successively, the following track super-cluster matching criteria were applied:

1. $|\Delta\eta| < 0.004$,

2. $|\Delta\phi| < 0.02$, and

3. $|1/E - 1/p| < 0.005$.

Figure 7.10 shows the HCAL isolation and $\sigma_{\eta\eta}$ distributions for the electron candidates after having applied these cuts. As can be seen, these observables have a further background reduction potential which can eventually be used as a cross check and a final proof that the selected candidates are indeed consistent with being electrons.

The application of the tracker isolation together with the first three selection cuts leaves about 350k true electrons out of the 480k reconstructed ones. From the 6 200 fake electrons, only 43 remained. The HCAL isolation cut would reduce the fakes further to 29, while it still still leaves 349k true electrons. This last cut will not be used for the analysis presented here, to be independent on information from the HCAL due to its limited resolution. In addition, the restriction on tracker and ECAL information only, provides redundancy. However, once real data become available and once the related detector systematics are understood, this isolation criteria might become an important additional selection tool.
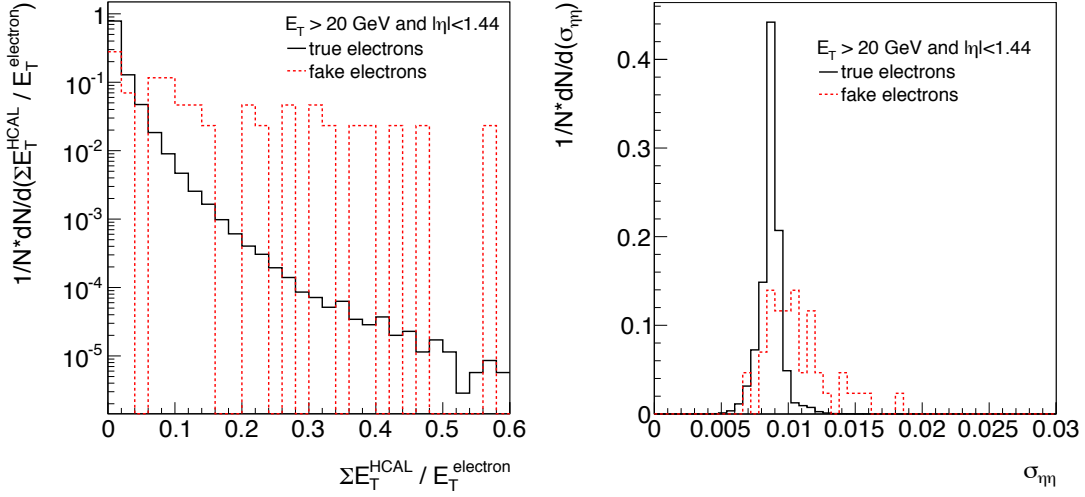
Figure 7.10.: The electron candidate distributions after all other criteria are applied: HCAL isolation (left side) and $\sigma_{\eta\eta}$ (right side).

7.2.2. Efficiency of the electron selection

To determine the corresponding electron efficiency we normalize the number of true electrons to the number of generated electrons from W boson decays with $E_T > 20\,\text{GeV}$ and $|\eta| < 1.44$ (Table 7.2). The E_T and η distributions of the generated electrons together with the reconstructed true electrons after the selection cuts are shown in Figure 7.11. About 45% of the generated electrons from W boson decays were found with E_T above $20\,\text{GeV}$ and within the barrel. The electron efficiency is defined by the ratio of all true electrons and the generated electrons with $|\eta| < 1.44$ and $E_T > 20$ GeV.

The numbers of accepted true and fake electrons after each selection cut are given in Table 7.3. Applying all cuts except the HCAL isolation, the electron efficiency was found to be $(72.5 \pm 0.1)\%$ on average. The efficiency as functions of E_T and η is shown in Figure 7.12. The η distribution is rather flat and the E_T rises from about 60% at a E_T of $20\,\text{GeV}$ to about 85% for values above $60\,\text{GeV}$. This smooth behavior, also in the gaps of the ECAL barrel, is an important advantage of this electron selection. The decrease of the efficiency in the last bin was found to be due to statistical fluctuations. The inclusion of HCAL isolation caused the average efficiency to drop to $(72.2 \pm 0.1)\%$.

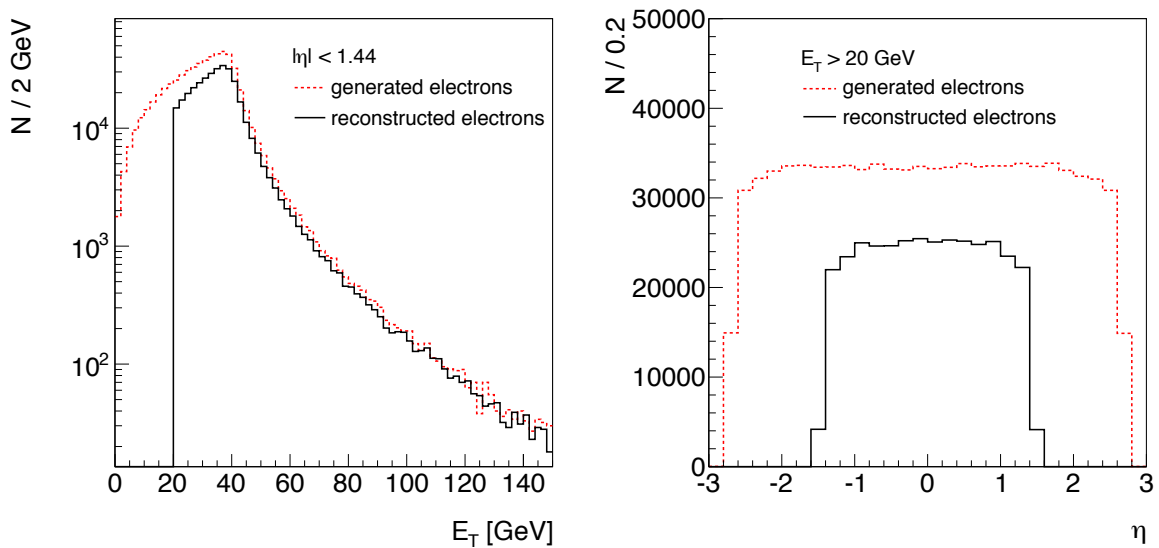| Cut	Generated electrons	Generated jets
$E_T > 20\,\mathrm{GeV}$ and $|\eta| < 1.44$	482 455	266 744

Table 7.2.: Numbers of generated electrons and jets after cuts on E_T and η in 1.1 million $W^\pm X \to e^\pm \nu X$ events.

Cut	True electrons	Fake electrons
$E_T > 20\,\mathrm{GeV}$ and $|\eta| < 1.44$	474 499 (98.4%)	6 197 (2.3×10^{-2})
$\frac{\Sigma p_T^{Tracker}}{E_T(electron)} < 0.1$	447 546 (92.8%)	533 (2.0×10^{-3})
$|\Delta\eta| < 0.004$	417 529 (86.5%)	218 (8.2×10^{-4})
$|\Delta\phi| < 0.02$	406 476 (84.3%)	103 (3.9×10^{-4})
$|1/E - 1/p| < 0.005$	349 860 (72.5 %)	43 (1.6×10^{-4})
$\Sigma p_T^{HCAL}/E_T^{electron} < 0.15$	348 507 (72.2 %)	29 (1.1×10^{-4})

Table 7.3.: Numbers of reconstructed and accepted electron candidates after various selection cuts in 1.1 million $W^\pm X \to e^\pm \nu X$ events. The efficiencies in brackets are with respect to the generated objects given in Table 7.2. The HCAL isolation cut is not used in this analysis.

7.2.3. Fake electrons

The Monte Carlo information of the W$^\pm$X was used to identify the particles (X) that were the origin of the 43 fake electrons that passed the electron selection. It was found that

Figure 7.11.: E_T (left side) and η (right side) distributions of generated electrons and true electrons that passed all electron selection cuts.
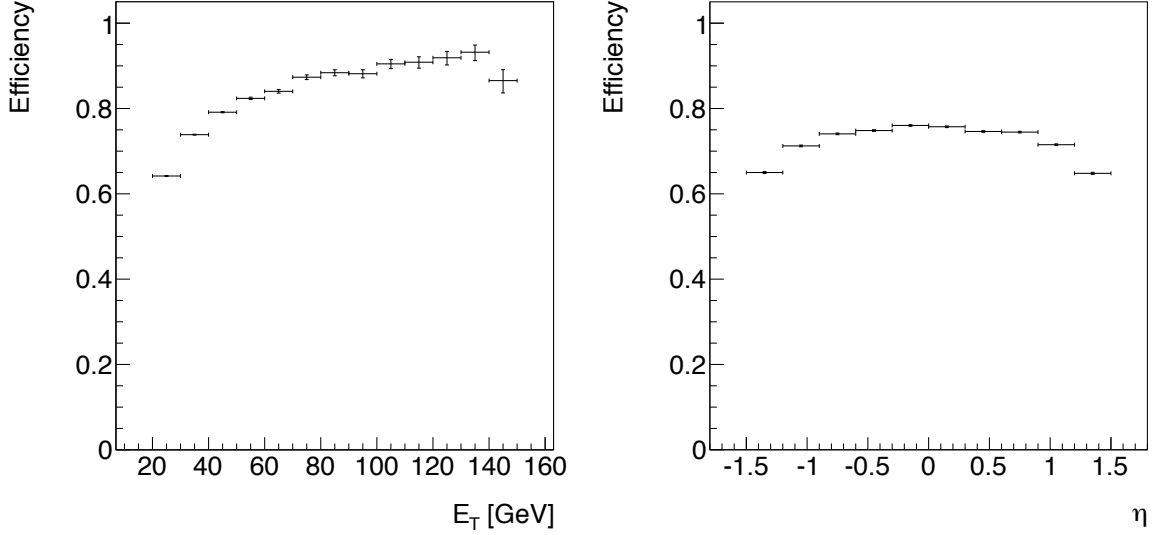
Figure 7.12.: Electron efficiency as function of E_T (left side) and η (right side) of the generated electrons.

18 of them were faked by charged pions, 12 originate from an isolated converted photon and five electron candidates were faked by charged kaons. In four cases the electron was faked by the process $\rho^\pm \to \pi^\pm + \pi^0 \to \pi^\pm + \gamma\gamma$, where the track of the charged pion and the ECAL hit of the two very close photons were combined to a fake electron. One electron was faked in the process $D^0 \to K^- + \pi^+ + \pi^0 + \pi^0 \to K^- + \pi^+ + \gamma\gamma\gamma\gamma$ in a similar manner. Finally, one fake electron was a misidentified proton, one came from the decay products of a Σ^+ baryon, and one was a real electron from the process $B^0 \to D^+ + e^- + \bar{\nu}$.

Somewhat unexpected, 31 out of the 43 fake electrons, or 73%, had the opposite charge of the $W^\pm$ boson in the event. The origin of this strong charge correlation was studied in detail and it was found that the fake electron was often associated with the leading hadron in the jet (X) appearing in the event. The charge of this hadron was strongly correlated with the original quark of the quark-gluon scattering process, which produces the WX final state (Section 10.1). Due to charge conservation this quark tended to show the opposite charge of the W boson.

In the following, the probability that a jet fakes an electron with $E_T > 20\,\text{GeV}$ and $|\eta| < 1.44$ is determined. As such a fake electron can only originate from a generated jet (for simplification isolated photons are included in this jet sample) with an energy of more than $20\,\text{GeV}$, we first identify the number of generated jets with $E_T > 20\,\text{GeV}$ and $|\eta| < 1.44$. Within the 1.11 million generated $W^\pm X \to e^\pm \nu X$ events, 266 744 generated jets could be observed using the *SisCone5* algorithm as shown in Table 7.2. The η and
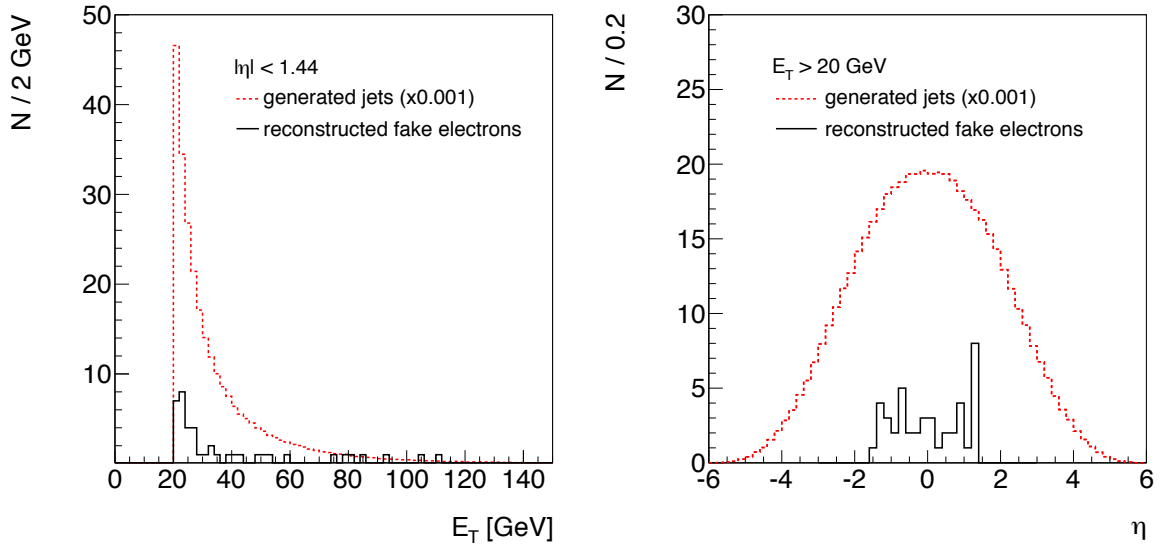
Figure 7.13.: E_T (left side) and η (right side) distributions of generated jets and fake electrons that passed all electron selection cuts. The cut on $E_T > 20\,\text{GeV}$ was required for the generated jets of both distributions.

E_T spectra of the generated jets together with the fake electron candidates that passed the selection are shown in Figure 7.13. The resulting probability that a jet fakes an electron was found to be $(1.6 \pm 0.2) \times 10^{-4}$ on average. A reduction to $(1.1 \pm 0.2) \times 10^{-4}$ could be achieved, when the HCAL isolation criteria was added to the electron selection (Table 7.3). As shown in Figure 7.14, the efficiency to find a fake electron suffered from a lack of statistics. However, this efficiency is rather flat in E_T in our region of interest (20-60 GeV, Section 9.3) and rises only smoothly in η, as can expected due to the material distribution in the tracker (Figure 7.18).

The probability that an isolated energetic photon might be identified as an electron was also investigated in detail. We used a special Monte Carlo sample of 103 122 $W^{\pm}\gamma$ events (with $E_T(\gamma) > 10\,\text{GeV}$) where 16 420 generated photons with E_T above 20 GeV and $\eta < 1.44$ were selected. 119 of these photons, or about $0.72 \pm 0.08\%$, survived all electron selection cuts, consistent with the photons occurring in the $W^{\pm}X \rightarrow e^{\pm}\nu X$ sample. In addition, we used a sample of 450 000 γ-jet events where we found a similar efficiency of a photon faking an electron of $0.59 \pm 0.02\%$.
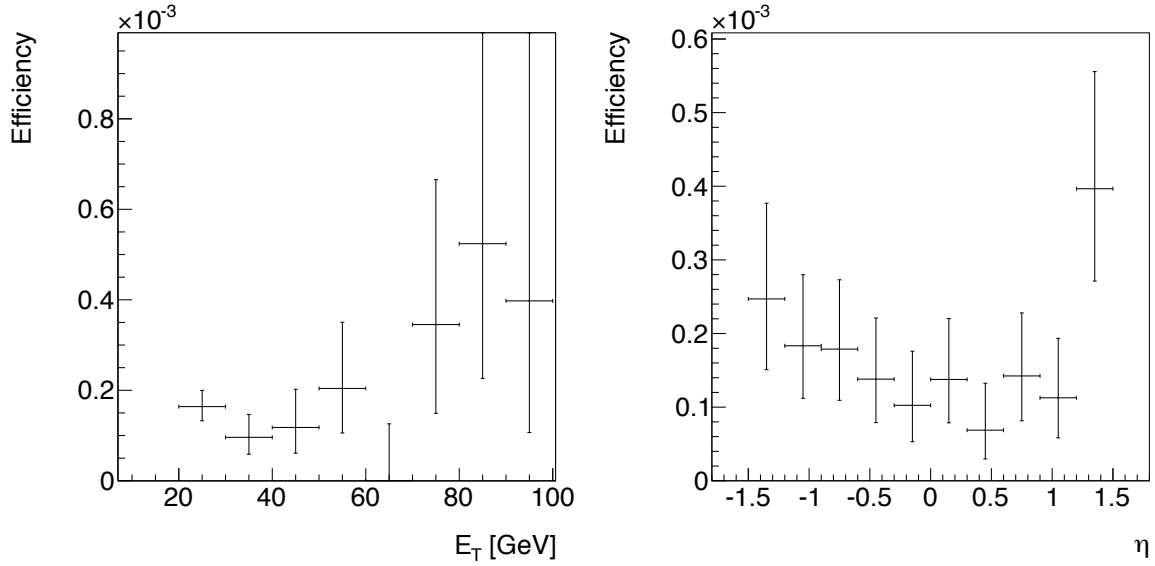
Figure 7.14.: Efficiency of a jet faking an electron as functions of E_T and η of the generated jets (left and right side).

## 7.3. Comparison of the CMS software versions 2_2_X and 3_1_X

During the writing of this thesis, the CMS analysis and software framework, CMSSW, changed several times. Especially, the update from version 2 to 3 explicitly affected the electron identification presented here. In particular, the changes included a different set of the preselection cuts, as discussed in Table 7.1, and a more realistic simulation of the CMS detector. This section compares the performance of the electron selection described in the previous section for the CMSSW versions 2_2_X and 3_1_X.

For the comparison, a similar inclusive $W^\pm X \to e^\pm \nu X$ Monte Carlo sample of 2.16 million events generated with PYTHIA at $E_{CM} = 10\,\text{TeV}$ was used. The sample was passed through a full detector simulation using CMSSW version 3_1_X. In the following, all distributions make use of this sample and of the $W^\pm X \to e^\pm \nu X$ sample from the previous sections (CMSSW 2_2_X). To simplify the comparisons between the samples, either was scaled to one million events. The distributions corresponding to CMSSW version 2_2_X and 3_1_X are shown as solid black and dashed red lines, receptively.

Figure 7.15 compares the E_T spectrum of all generated electrons from a W decay with $|\eta| < 1.44$ and the η distribution of these electrons with $E_T > 20\,\text{GeV}$ for both CMSSW versions. Figure 7.16 shows the same distributions for the generated jets. As the distributions show, the number as well as the kinematics of the generated electrons and jets were identical for both versions. The only difference between the versions found
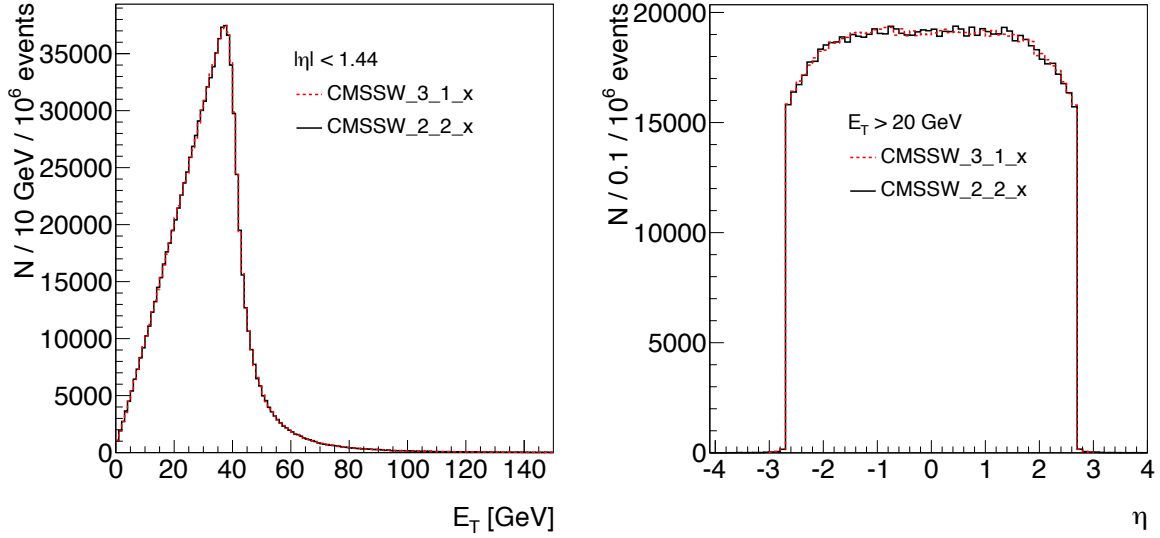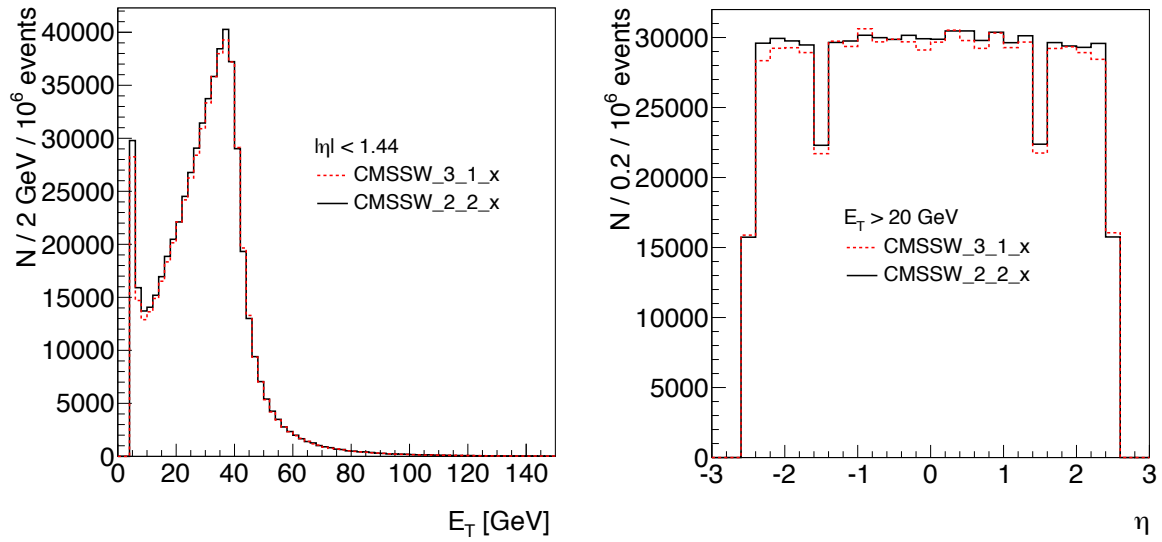
Figure 7.15.: E_T (left side) and η distributions (right side) of the generated electrons in 1 million $W^{\pm}X \to e^{\pm}\nu X$ events for CMSSW version 2_2_X and 3_1_X.
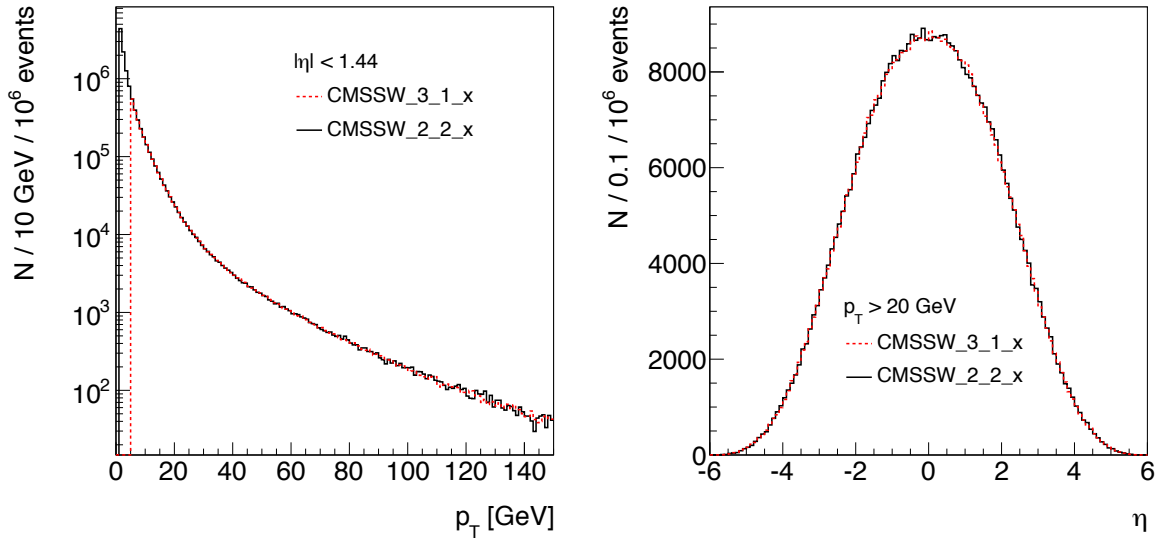

Figure 7.16.: p_T (left side) and η distributions (right side) of the generated jets in 1 million $W^{\pm}X \to e^{\pm}\nu X$ events for CMSSW version 2_2_X and 3_1_X.

in these spectra, is the minimum p_T cut-off for jets, which moved from 1 to 5 GeV in the more recent version. Since the minimum E_T of this analysis was 20 GeV, this change had no effect.

Figure 7.17 shows the E_T spectrum of all reconstructed electron candidates found for both versions with $|\eta| < 1.44$ and the η distribution for all candidates with E_T above 20 GeV, respectively. The electron selection was not applied at this point. The

Figure 7.17.: E_T (left side) and η distributions (right side) of all reconstructed electron candidates in 1 million $W^{\pm}X \to e^{\pm}\nu X$ events for CMSSW version 2_2_X and 3_1_X.
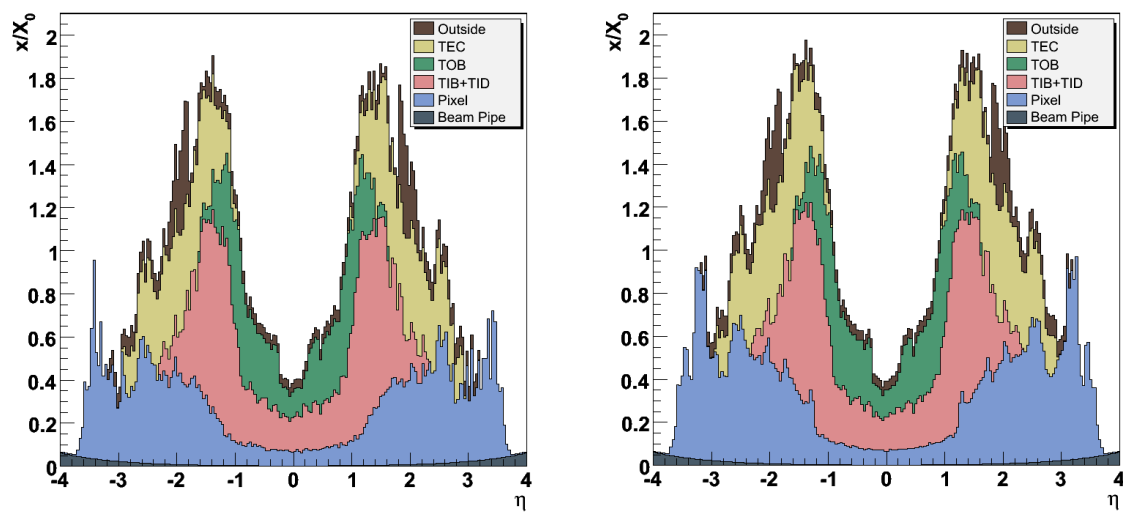
Figure 7.18.: The material budget used as a function of η for CMSSW version 2_2_X (left side) and 3_1_X (right side).

Common preselection cut	cut value
$E_T >$	$4\,\mathrm{GeV}$
$\Delta\eta <$	0.02
$\Delta\phi <$	0.1
$\Delta R_H <$	0.15
$H/E <$	0.1

Table 7.4.: Cuts of the common preselection for the two different versions of CMSSW

comparison between the two versions shows, that the reconstruction efficiency dropped slightly from 98.4% to 98.2%. Especially the η distribution shows a decrease in the forward region $|\eta| > 2$. This decrease was found to be due to the tighter preselection as shown in Table 7.1. In addition, the higher material budget simulated in the central tracker grew from CMSSW version 2_2_X to 3_1_X as shown in Figure 7.18. In particular, the material in the pixel detector was increased.

7.3.1. Effects on the selection variables

In the following, the selection variables introduced in Section 7.2.1 are compared for both CMSSW versions. Since the different preselections of the two versions complicate a proper comparison a *common preselection* was introduced. The cut variables of the common preselection were the same as for the default preselections. As cuts values, however, the tighter values out of the two versions were chosen. The cut values are summarized in Table 7.4. In particular, the tighter cut on $\Delta\phi$ from 2_2_X and the larger cone size for the H/E cut from 3_1_X were taken.

Figures 7.19 to 7.22 show the distributions of the electron selection variables of true and fake electrons with $E_T > 20\,\mathrm{GeV}$ and $|\eta| < 1.44$ for both versions. The black and the red dashed line represent the CMSSW versions 2_2_X and 3_1_X, respectively. The distributions of the true electrons are shown logarithmically on the left side of the each figure, and those of the fake electrons linearly on the right side.

The distributions show a good agreement of both versions for the true electrons. The distribution of the tracker and the HCAL isolation variable for the true electrons, however, became wider in CMSW version 3_1_X.

The comparison of the fake electrons reflects the increase of pixel material budget more clearly. In particular, the distributions of the fake electron variables have the
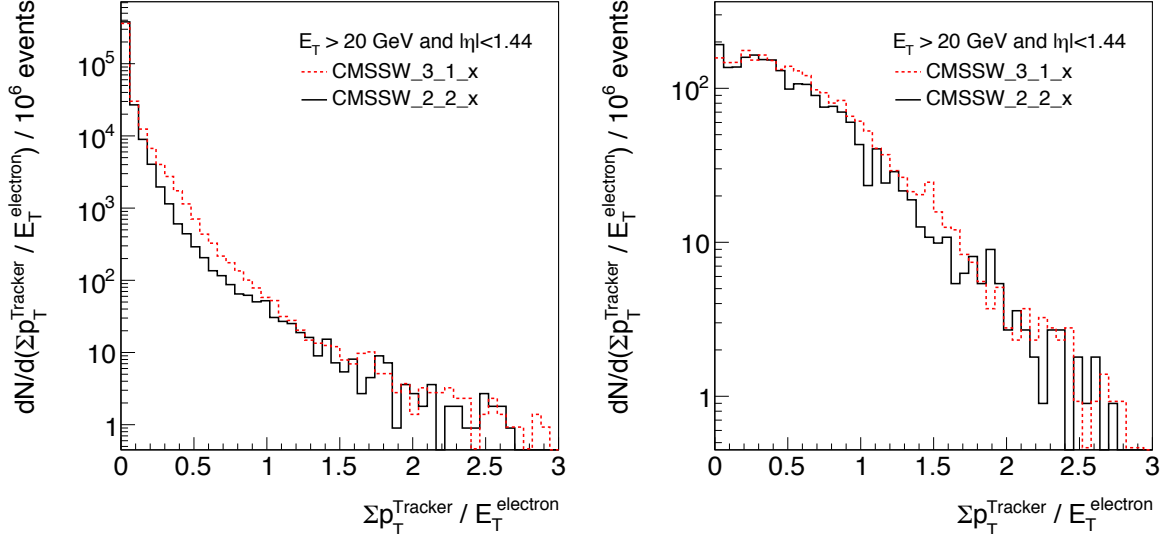
Figure 7.19.: Distributions of the tracker isolation variable for true electrons (left side) and fake electrons (right side).
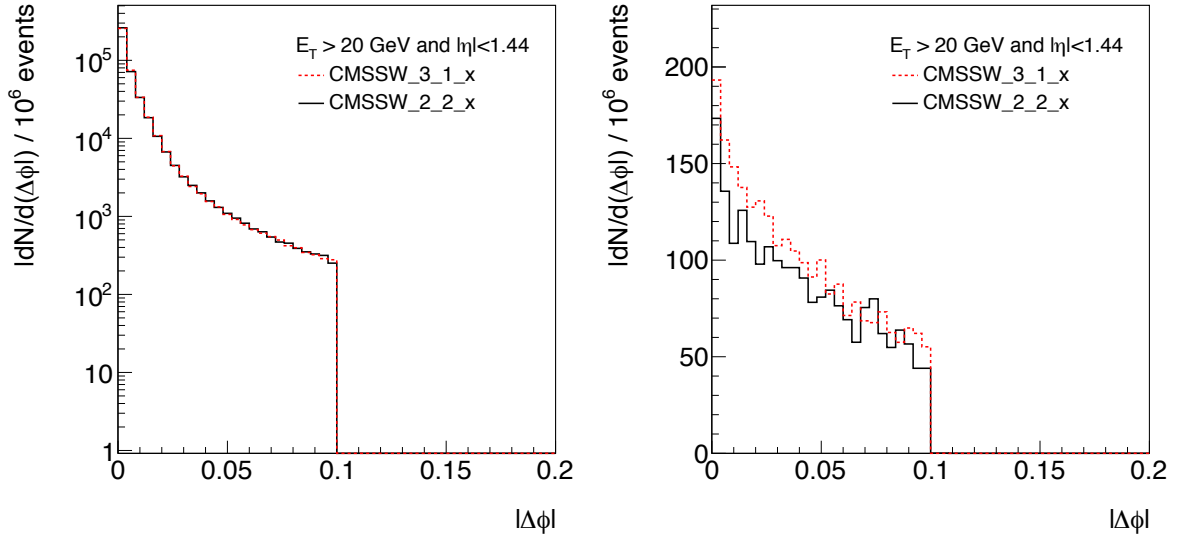
Figure 7.20.: Distributions of $\Delta\phi$ for true electrons (left side) and fake electrons (right side).

tendency to peak more around zero. The reason is, that with the increased material budget, it is more difficult for a hadron to behave like an electron due to the higher scattering probability. Thus, the preselection criteria are harder to be fulfilled by fakes. As a result, only fake electrons that fulfill the preselection criteria (peak at zero) are counted as electron candidates.
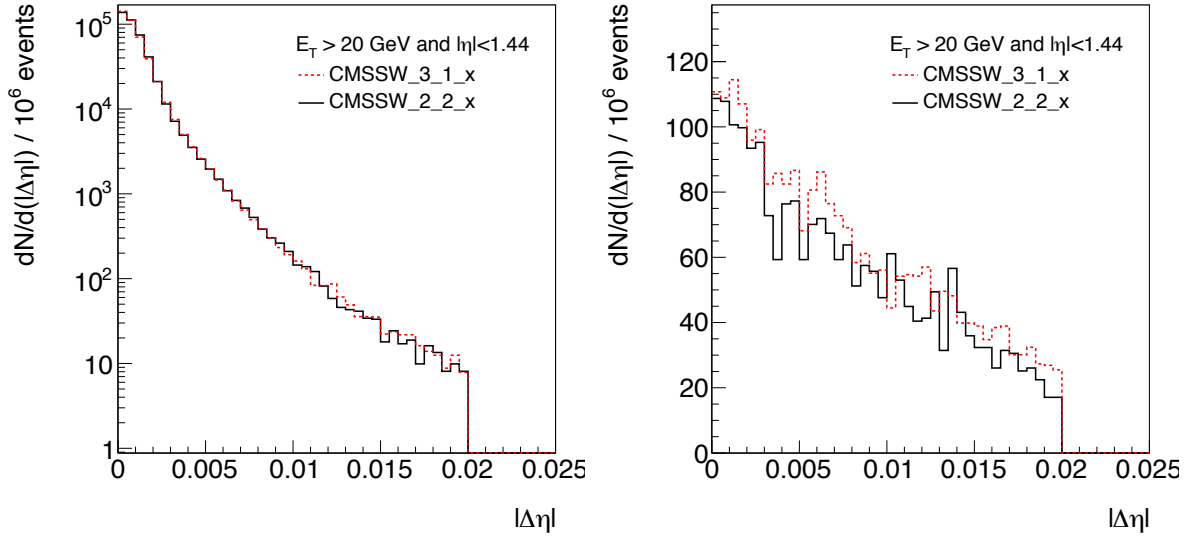
Figure 7.21.: Distributions of $\Delta\eta$ for true electrons (left side) and fake electrons (right side).
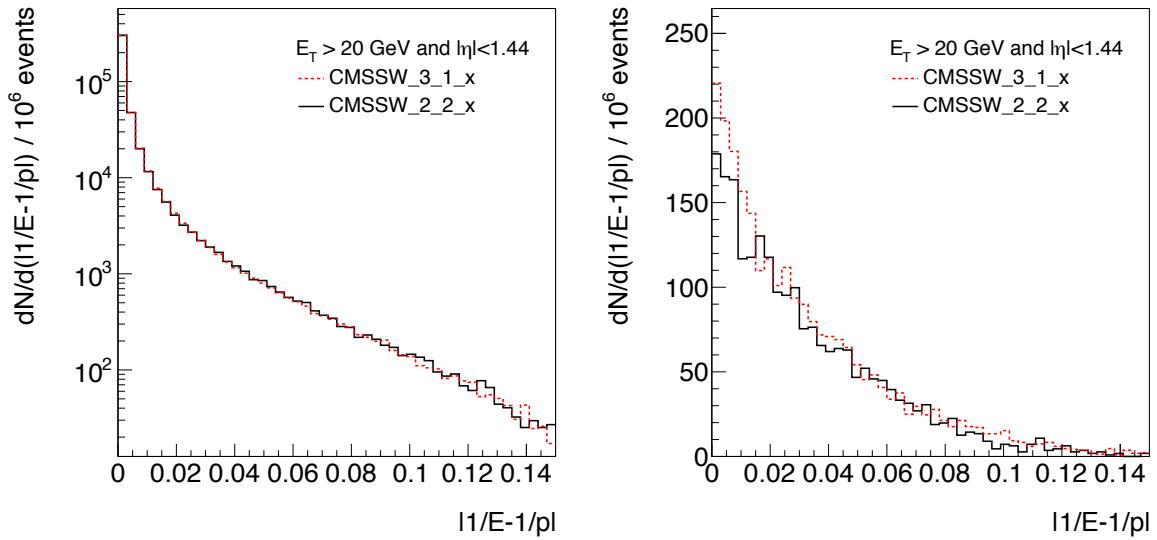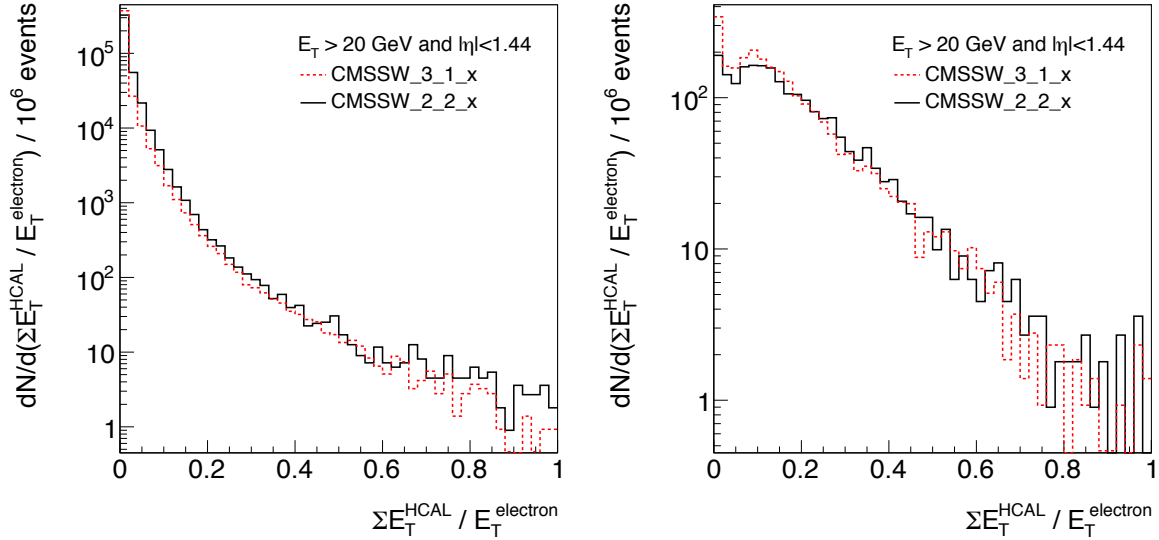

Figure 7.22.: Distributions of $|1/E - 1/p|$ for true electrons (left side) and fake electrons (right side).

Figure 7.23.: Distributions of the HCAL isolation variable for true electrons (left side) and fake electrons (right side).

7.3.2. Effects on the performance

Coming back to the default preselections of each CMSSW version, the overall electron efficiencies and fake rates are compared in the following. Table 7.5 shows the numbers of generated electrons from W decays for 10^6 $W^{\pm}X \to e^{\pm}\nu X$ events in both versions. Table 7.6 shows the efficiencies of true generated electrons surviving the various selection cuts. The efficiencies were calculated in the manner described in Section 7.2. Accordingly, the efficiency to reconstruct a true electron that passed all selection cuts except the HCAL isolation decreased from 72.5% to 70.1% going from CMSSW version 2_2_X to 3_1_X. Applying the common preselection instead of the default ones, does not change these numbers. Hence, the lower efficiency in CMSSW 3_1_X is only due to the higher material budget in the tracker simulation.

Table 7.7 shows the number of generated jets in each of the 10^6 $W^{\pm}X \to e^{\pm}\nu X$ events of both versions. The efficiencies that fake electrons coming from generated jets survive the different selection cuts are shown in Table 7.8. According to those numbers, the efficiency to reconstruct a generated jet as an electron after all selection cuts except the HCAL isolation dropped from $(1.6 \pm 0.25) \times 10^{-4}$ (2_2_X) down to $(1.1 \pm 0.16) \times 10^{-4}$ (3_1_X). Applying the common preselection gave comparable fake rates of $(1.3 \pm 0.25) \times 10^{-4}$ (2_2_X) and $(1.1 \pm 0.16) \times 10^{-4}$ (3_1_X). As a result, the lower efficiency to reconstruct a generated jet as an electron in the CMSSW version 3_1_X was due to its tighter preselection.

Generated electrons in 10^6 $W^{\pm}X \to e^{\pm}\nu X$ events	CMSSW 2_2_X	CMSSW 3_1_X
$E_T > 20\,\text{GeV}$ and $|\eta| < 1.44$	433 473	432 918

Table 7.5.: Numbers of generated electrons after cuts on E_T and η for both CMSSW versions.

| True electrons in 10^6 $W^{\pm}X \to e^{\pm}\nu X$ events	CMSSW 2_2_X	CMSSW 3_1_X
$E_T > 20\,\text{GeV}$ and $|\eta| < 1.44$	98.4%	98.2%
$\frac{\Sigma p_T^{Tracker}}{E_T(electron)} < 0.1$	92.8%	89.3%
$|\Delta\eta| < 0.004$	86.5%	83.5%
$|\Delta\phi| < 0.02$	84.3%	81.3%
$|1/E - 1/p| < 0.005$	$(72.5 \pm 0.1)\%$	$(70.3 \pm 0.1)\%$
$\Sigma p_T^{HCAL}/E_T^{electron} < 0.15$	72.2%	70.1%

Table 7.6.: Efficiencies of selecting true electron candidates after the various selection cuts. The percentages are with respect to the number of generated electrons in Table 7.5. The HCAL isolation cut is not used in this analysis.

Generated jets in 10^6 $W^{\pm}X \to e^{\pm}\nu X$ events	CMSSW 2_2_X	CMSSW 3_1_X
$p_T > 20\,\text{GeV}$ and $|\eta| < 1.44$	239 662	239 220

Table 7.7.: Numbers of generated jets after cuts on E_T and η for both CMSSW versions.

Fake electrons in 10^6 $W^{\pm}X \to e^{\pm}\nu X$ events	CMSSW 2_2_X	CMSSW 3_1_X
$E_T > 20\,\text{GeV}$ and $|\eta| < 1.44$	2.32%	1.25%
$\frac{\Sigma p_T^{Tracker}}{E_T(electron)} < 0.1$	0.2%	0.12%
$|\Delta\eta| < 0.004$	0.082%	0.046%
$|\Delta\phi| < 0.02$	0.039%	0.024%
$|1/E - 1/p| < 0.005$	$(0.016 \pm 0.0025)\%$	$(0.011 \pm 0.0016)\%$
$\Sigma p_T^{HCAL}/E_T^{electron} < 0.15$	0.011 %	0.011%

Table 7.8.: Efficiencies of selecting fake electron candidates after the various selection cuts. The percentages are with respect to the number of generated jets in Table 7.7. The HCAL isolation cut is not used in this analysis.
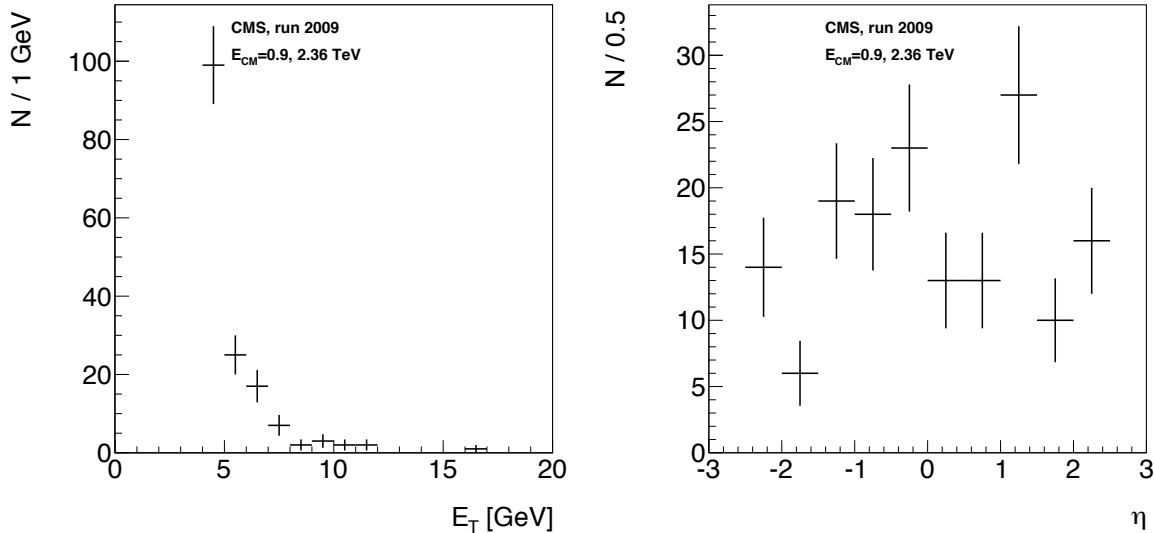
Figure 7.24.: E_T (left side) and η (right side) distributions of the electron candidates from the 2009 LHC runs.

7.4. Electrons from the 2009 LHC run

During two 2-hour runs in December 2009, CMS recorded events at center-of-mass energies of 900 GeV and at 2.36 TeV. The corresponding event rates were 11 Hz at 900 GeV and 3 Hz at 2.36 TeV.

In these two runs, the CMS data acquisition system selected 40 320 events at 900 GeV and 10 837 events at 2.36 TeV for further analysis. In these events, a total of 159 electrons candidates was found by the electron reconstruction algorithm and preselection in barrel and end-caps. The E_T and η spectra of these electrons are shown in Figure 7.24. As the distributions show, only very low-energy electron candidates were observed, except one with an energy of roughly 16 GeV. None of the electron candidates survived the electron selection criteria presented in this chapter.

7.5. Conclusions of this chapter

This chapter introduced a simple and powerful electron selection for electrons with $E_T > 20$ GeV, which were found in the barrel part of the CMS ECAL. Its performance for two different versions of the CMS analysis and software framework CMSSW was investigated. Starting from an electron preselection, the jet to electron misidentification rate was found to be about 1%. The application of the electron selection to these electron candidates, decreased this rate down to $(1.1 \pm 0.2) \times 10^{-4}$ in CMSSW version 3_1_X.

The corresponding electron identification efficiency was $(70.3 \pm 0.1)\%$ on average. For the rest of this thesis, the electron selection from CMSSW version 3_1_X is used.

In addition, the electron candidates found with the CMS detector during the 2009 run period of LHC were briefly discussed. Due to the low number of electron candidates found, and especially due to their low energies, not a single candidate was selected.

As will be shown in Chapter 9, this electron selection contributes significantly to reduction the the $W^{\pm}X \rightarrow e^{\pm}\nu X$ background in the Higgs search in the channel $H \rightarrow W^+W^- \rightarrow e^+\nu_e e^-\bar{\nu}_e$ and a mass around $165\,\mathrm{GeV}$.

Chapter 8.

Reconstruction of jets and missing transverse energy

The physics processes investigated in this thesis are based on the identification of electrons, jets and missing transverse energy. The identification of electrons was discussed in detail in the previous chapter. This chapter first introduces the reconstruction of jets with the energy measurement in calorimeter towers. Subsequently, the corrections applied to the raw jet energy are discussed. In the second part, the determination of the missing transverse energy (MET) is presented using two different methods.

8.1. Jet reconstruction

As discussed in the Section 2.5, proton-proton collisions are described by parton-parton interactions. The partons are not directly observable and manifest themselves through showering and subsequent hadronization into bunches of stable particles. In CMS, as at other collider experiments, these bunches are clustered into *jets* using different algorithms. The energy assigned to the jets, which are used for this thesis, is based on energy deposits in the CMS ECAL and HCAL. They are called *calorimeter jets*. Jets can also be reconstructed from tracks of charged particles alone, from calorimeter energy supplemented with track momenta measurements, and from individually reconstructed particles. A successful jet algorithm provides a good correspondence between the parton level and the level of the stable particles remaining after the hadronization stage.

8.1.1. Jet algorithms

All calorimeter jet algorithms start with the combination of energy deposits in the two calorimeters to *calorimeter towers*. The size of the calorimeter towers is determined by

Region	HB	HE	HF	Σ EB	Σ EE
Threshold [GeV]	0.9	1.1	1.4	0.2	0.45

Table 8.1.: Energy thresholds of the calorimeter tower reconstruction. HB, HE and HO denote the HCAL barrel, end-caps, and forward HCAL; Σ EB and Σ EE refer to the sum of the ECAL energy in the calorimeter tower for the barrel and the end-caps.

that of the HCAL cells. The HCAL cell size is $\Delta\eta \times \Delta\phi = 0.087 \times 0.087$ for $|\eta| < 1.74$ and becomes progressively larger for $1.74 < |\eta| < 1.5$. Since the size of an ECAL crystal is only 0.017×0.017, the energy deposits of a matrix of crystals has to be summed, such that the matrix matches the HCAL cell (i.e. 5×5 crystals in the ECAL barrel). To suppress noise, the energy deposits in the ECAL and HCAL have to be larger than the thresholds given in Table 8.1. The total calorimeter tower energy is then the sum of all energy deposits in the ECAL and HCAL. The center of the calorimeter tower is taken as its position within CMS.

The obtained collection of calorimeter towers is then used as input to the jet algorithm. The *iterative cone algorithm* for example, sorts the towers by their transverse energy. The calorimeter tower with the highest energy is used as seed of the jet reconstruction. As for other *cone based* jet algorithms, a cone of a certain size $R = \sqrt{\Delta\eta^2 + \Delta\phi^2}$ is formed around the seed. The cone sizes usually used in CMS are R = 0.5 and R = 0.7. The energy of other calorimeter towers is added iteratively to the jet until the total energy of the jet changes by less than 1% or the jet's position changes not more than $\Delta R = 0.01$ (stable jet). The procedure is repeated until all calorimeter towers of an events are included in stable jets. Finally, the algorithm requests a minimum jet p_T of $1\,\text{GeV}$.

However, since a p_T cut of $1\,\text{GeV}$ is applied to the energy of the seed, the *iterative cone algorithm* is not infrared and collinear safe in the terms of perturbative QCD. In particular, the variation of this p_T cut or the adding of an additional (low energy) calorimeter tower can lead to different stable cone configurations.

Therefore, the jets used for this thesis are constructed by the *Seedless Infrared-Safe Cone (SisCone)* algorithm, which was introduced in [71]. It is faster than the iterative cone algorithm, and it is infrared and collinear safe to all orders in perturbative expansion in the terms of perturbative QCD since it does not rely on seeds [72]. A description of the algorithm can be found in [73]. It is available in different cone sizes, the cone size used for this thesis is R = 0.5 (*SisCone5*).

8.1.2. Jet energy correction

The response of the combined calorimeters to the jet energy is non-linear, e.g. the energy of the reconstructed (*raw*) jets is generally not proportional to the energy of partons emerging from the hard QCD interaction, which is due to non-uniformities of the CMS calorimeters. Additionally, the fraction of the jet energy that is deposited in the ECAL (*electromagnetic fraction*) is dependent on the jet energy and shows strong fluctuations.

The different proportionalities of the ECAL and HCAL responses to the jet energy lead to the overall non-linearity of the jet energy measurements. Therefore, corrections to the raw jet energy measurement have to be applied. This *jet energy correction* is important for analyses, where jets are present. The CMS jet energy correction is a factorized multi-level jet correction, where each sub-correction is associated with different detector and physics effects [74, 75]. For the following discussions, three corrections are used exclusively.

- **Offset corrections** are applied to account for pile-up and the electronic noise in the detector. These corrections are expected to be relatively small, i.e. on average smaller than 2 GeV for single pile-up events.

- **Relative corrections (η)** adjust the non-uniformity of a given jet energy in η. The relative correction is based on the principle of transverse momentum conservation in back-to-back di-jet events: Since the incoming protons have no transverse momentum, the p_T of two back-to-back jets in the transverse plane should be balanced. Subsequently, the energy of a raw jet at a given η is corrected to a jet with the same energy in the barrel region ($|\eta| < 1.3$). Here, the energy of the central jet is assumed to be correct, since the detector is more uniform there and because it has the highest coverage of the jet transverse momentum in this region. The corresponding relative response variation is expected to be 30% for low transverse jet momenta ($\sim 30\,\text{GeV}$) and reduces progressively to 2-3% for high p_T jets ($> 100\,\text{GeV}$).

- **Absolute corrections (p_T)** are applied, since the energy response of the calorimeters to a particle level jet is smaller than unity and varies as a function of p_T. This correction is based on Monte Carlo information and controlled using γ/Z+jet events. In these events, the transverse momenta of the γ/Z and the recoiling jet balance each other. In the case of γ+jet events, the photon's p_T is expected to be measured accurately in the ECAL. In the Z+jet case, muon and electron decays of a Z are selected. The muon p_Ts are determined using the tracker and the muon chambers, and those of the electrons with the ECAL. Hence, the Z p_T can be cal-
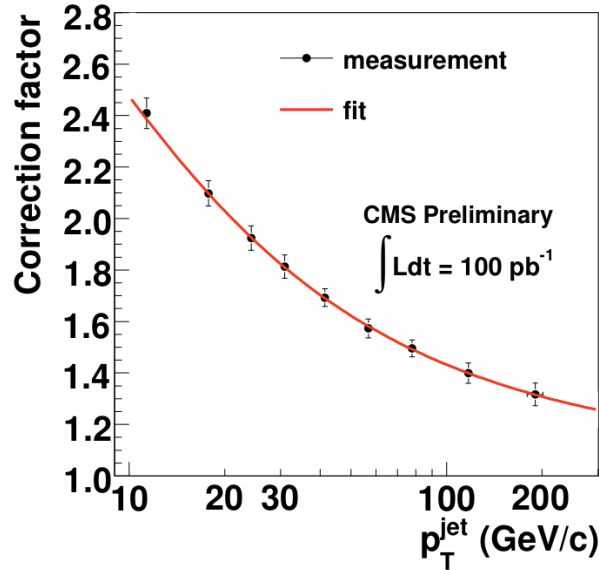
Figure 8.1.: Absolute jet energy correction as a function of the uncorrected jet p_T. The error
bars indicate the statistical uncertainty corresponding to $100\,\mathrm{pb}^{-1}$ of integrated
luminosity (Monte Carlo study performed in [75]).

culated with a high precision. Finally, making use of momentum conservation in
the transverse plane of CMS, the jet energies ($|\eta| < 1.3$) can be determined totally
independent from the calorimeter jet energy measurements. The expected absolute
correction factors are 2.5 for jets with $p_T = 10\,\mathrm{GeV}$ and decrease to almost unity
for very high jet p_Ts as shown on Figure 8.1.

Using these methods to obtain the total jet energy correction, the systematic uncertainty
on the jet energy measurements is expected to be $\sim$10% for an integrated luminosity of
$\mathcal{L} = 10\,\mathrm{pb}^{-1}$ [75].

To exemplify the effect of the total jet energy correction, jets in the $W^{\pm}X \to e^{\pm}\nu X$
Monte Carlo sample were used. Figure 8.2 (left side) shows the transverse momentum
spectra of jets found in this sample before and after the correction together with the
associated generated jets. Here, only reconstructed jets with $p_T > 10\,\mathrm{GeV}$ and $|\eta| < 2.5$
were used. As the distributions show, the transverse momentum of the corrected jets
describe the one of the generated jets much better than the uncorrected ("raw") jet
momenta, especially above $\sim 30\,\mathrm{GeV}$. The direction of the jet, however, is measured
with a high precision as Figure 8.2 (right side) shows. The distribution displays the
difference in ϕ between reconstructed raw jets ($p_T > 10\,\mathrm{GeV}$, $|\eta| < 2.5$) and the associated
generated jet. The reconstruction of the η direction of the jet is similarly good.
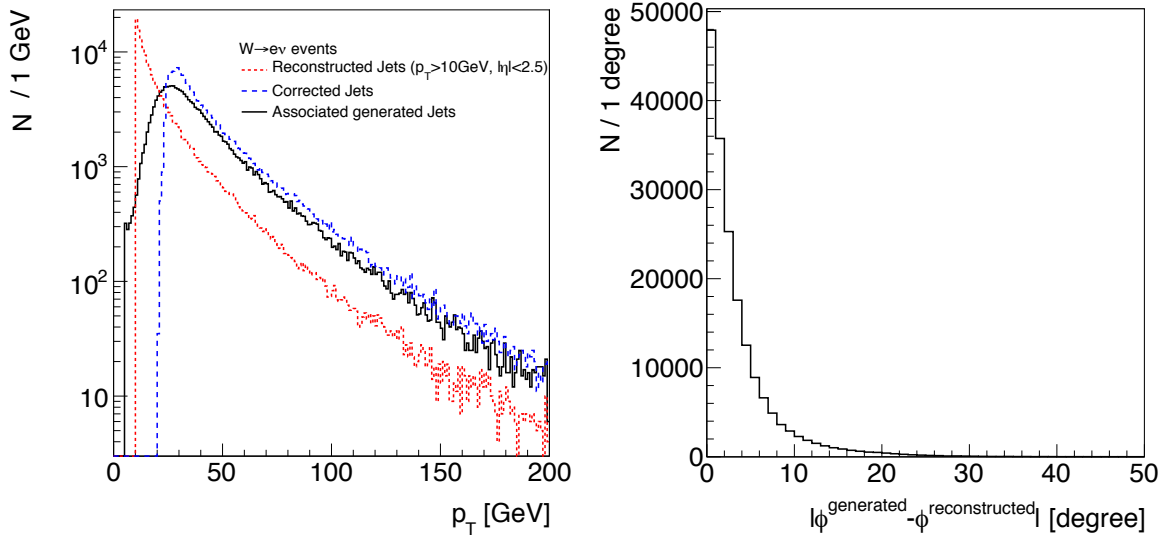
Figure 8.2.: Jets in $W^\pm X \to e^\pm \nu X$ events. Left side: the p_T spectra of jets before (*reconstructed Jets*) and after (*corrected Jets*) the application of the jet energy corrections, and the p_T of the associated generated jets. Right side: difference in the ϕ direction between the generated and reconstructed jets.

8.2. Missing transverse energy

Many interesting physics processes at high energies can be identified if the exclusively weakly interacting neutrinos are reconstructed. Prominent Standard Model processes with neutrinos are the W boson and top quark productions. In addition, there are also exclusively weakly interacting particles predicted by beyond the Standard Model theories, e.g. the *neutralino* predicted by Super-Symmetry.

Due to their nature, neutrinos and neutralinos typically escape the detector without being measured. The colliding protons, however, have no momentum component transverse to the beam. Accordingly, in processes including neutrinos, there is an imbalance of transverse momentum in the event due to momentum conservation. The large pseudo-rapidity coverage of the CMS detector allows to measure this imbalance, called missing transverse energy (MET). The MET of an event is obtained from the observed energy deposits in the detector and corresponds to the vector sum of the transverse momenta of all non-detected particles.

The analysis presented in this theses uses two methods to determine the MET:

- The **calorimeter MET** uses the vector sum of transverse energy deposits in the calorimeter towers (Section 8.1):

$$calorimeter\ MET = -\sum_n E_n(\sin\theta_n\cos\phi_n\hat{x} + \sin\theta_n\sin\phi_n\hat{y}), \qquad (8.1)$$

  where n indicates the index of the calorimeter towers, E_n denotes their energy, ϕ_n and θ_n refer to their positions, and $\hat{x}$ and $\hat{y}$ are the unit vectors of the transverse plane of CMS. As stated above, the minimum energy E_n of a calorimeter tower is $0.5\,\text{GeV}$. The maximum absolute pseudorapidity is 3.

- The **jetElectron MET** uses the vector sum of the high p_T objects, e.g. here jets and electrons.

$$jetElectron\ MET = -\sum_n E_n^{electron}(\sin\theta_n\cos\phi_n\hat{x} + \sin\theta_n\sin\phi_n\hat{y})$$
$$-\sum_m E_m^{corrected\ jet}(\sin\theta_m\cos\phi_m\hat{x} + \sin\theta_m\sin\phi_m\hat{y}), \qquad (8.2)$$

  where n and m indicate the indices of the electrons and jets, $E_n^{electron}$ and $E_m^{corrected\ jet}$ are the electron and jet energies, $\phi_{n,m}$ and $\theta_{n,m}$ refer to their positions, and $\hat{x}$ and $\hat{y}$ are the unit vectors of the transverse plane of CMS. The electrons used for the sum passed the electron selection (Section 7.2.1) including the cuts $E_T > 20\,\text{GeV}$ and $|\eta| < 1.44$. The jets are found with the *SisCone5* algorithm and are required to have a minimum $p_T^{corrected}$ of $30\,\text{GeV}$ and a maximum $|\eta|$ of 2.5.

The *calorimeter MET* is a standard algorithm, whereas the *jetElectron MET* was developed for this thesis. In addition to these methods, MET algorithms can also be based on calorimeter energy supplemented with track momenta, and on individually reconstructed particles. A detailed explanation of the MET measurements with the CMS detector can be found in [74].

8.2.1. Missing transverse energy comparison

In the following, the performances of the *calorimeter MET* and the *jetElectron MET* are compared. A good MET algorithm should describe the p_T of a high energy neutrino correctly and should also be robust against *fake* MET. Fake MET occurs in (Standard Model) events, where no neutrino is present. It is caused by any imbalance in the p_T vector sum of the detected objects in the detector. This imbalance can result from the miss-measurement of directions or energies of the objects used for the MET calculation.
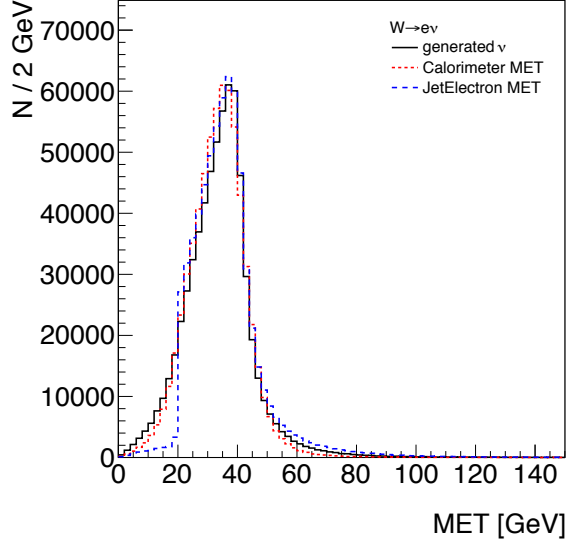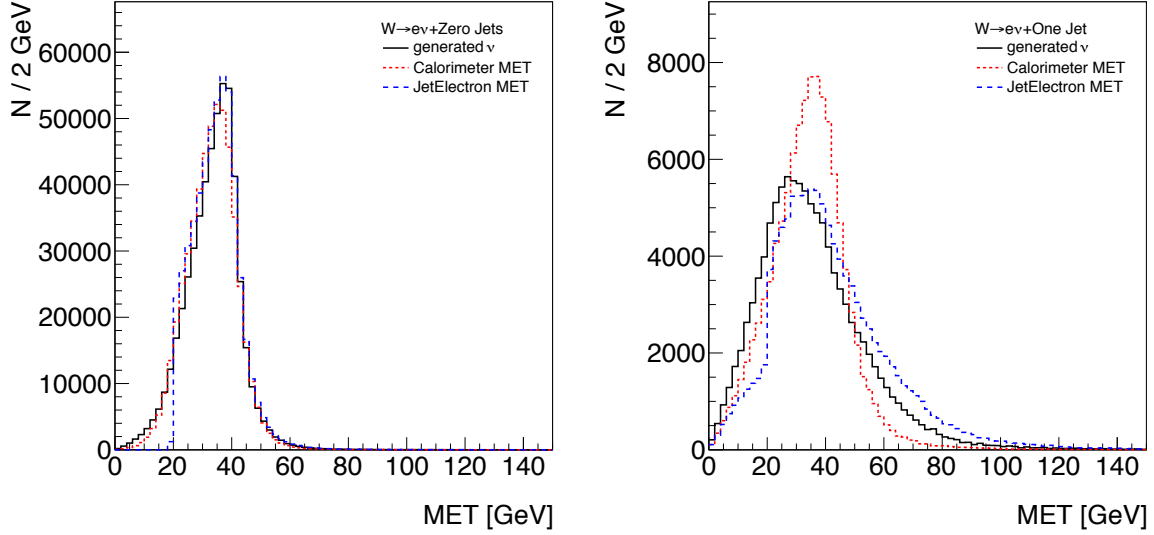
Figure 8.3.: The neutrino p_T , the *calorimeter MET*, and the *jetElectron MET* in W events, where one electron with $E_T > 20\,\text{GeV}$ and $|\eta| < 1.44$ was selected.

Furthermore, fake MET can arise from areas in the detector, where the hermeticity is not perfect and particles can escape the detector.

To study the MET description of high energy neutrinos, a sample of 2.16 million $W^{\pm}X \rightarrow e^{\pm}\nu X$ events was used. From this sample, 657k events with one selected electron with $E_T > 20\,\text{GeV}$ and $|\eta| < 1.44$ were chosen for further analysis. Figure 8.3 shows the distributions of the p_T of the generated neutrino (ν), and the MET calculated with both algorithms. The neutrino p_T spectrum shows a Jacobian shape with a peak around 40 GeV, as it is expected from a two-body decay of a particle with a mass around 80 GeV. As can be seen, both methods describe the neutrino p_T similarly precise. The *jetElectron MET*, however, shows a cut-off of at 20 GeV, which is due to the minimum E_T of the electron of 20 GeV.

To investigate the role of the jets for the MET determination further, the W events with one electron are separated into two subsamples: *W+zero jets* and *W+one jet* events. From the 657k W events with one electron, 529k were found with zero jets and 109k with exactly one jet. Here, the jet multiplicity of the W events was determined for jets with $p_T^{corrected} > 30\,\text{GeV}$ and $|\eta| < 2.5$.

Figure 8.4 shows the neutrino p_T and the METs for *W+zero jets* (left side) and *W+one jet* (right side). In the *W+zero jets* case, both MET methods describe the neutrino p_T perfectly, except for the cut-off of the *jetElectron MET* at 20 GeV, as described above. As shown on the right plot, the neutrino p_T is much wider in the *W+one jet* case. The reason for that is the higher p_T of the W boson due to the presence of a jet in
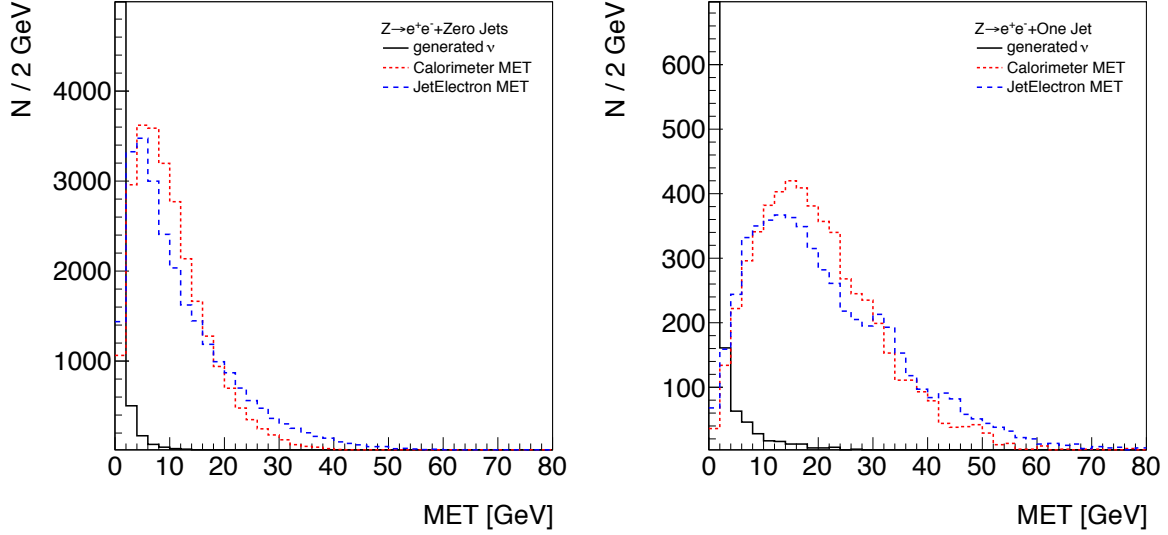
Figure 8.4.: The neutrino p_T, the *calorimeter MET*, and the *jetElectron MET* for *W+zero jets* (left side) and *W+one jet* (right side) events, where at least one electron with $E_T > 20\,\text{GeV}$ and $|\eta| < 1.44$ was selected.

these events. Thus, the neutrino gets boosted and acquires a higher momentum when it is emitted in the direction of the W momentum or vice versa. Furthermore, the shapes of two MET distributions do not match the neutrino p_T very well. In particular, the *jetElectron MET* is much wider than the neutrino p_T and has a much lower peak. This shape is due to the fact that the low energy jets are ignored by this MET algorithm. Thus, the imbalance of the p_T vector sum, which is considered as the MET, becomes larger.

An explanation for the deviation of the shape of the *calorimeter MET* for the *W+one jet* case is the insufficient energy measurement of hadronic energy in the calorimeters, discussed in Section 8.1.2. Hence, as for jets, the measurement of the *calorimeter MET* has to be corrected. The correction of the *calorimeter MET* is discussed in the next section.

To test the presented algorithms for their behavior in events where no (prompt) neutrino is present, a PYTHIA Monte Carlo sample of $Z \to e^+e^-$ events was used. Events with exactly two electrons with $E_T > 20\,\text{GeV}$ and $|\eta| < 1.44$, which passed the electron selection were selected. As before, the resulting Z events were separated into *Z+zero jets* and *Z+one jet* events. Figure 8.5 shows the neutrino p_T and the METs for *Z+zero jets* (left side) and *Z+one jet* (right side). As can be seen, the distributions of the neutrino p_T peak at zero, as expected. Nevertheless, some low p_T neutrinos could be observed. Their origins are leptonic decays of particles in the jets. Accordingly, the
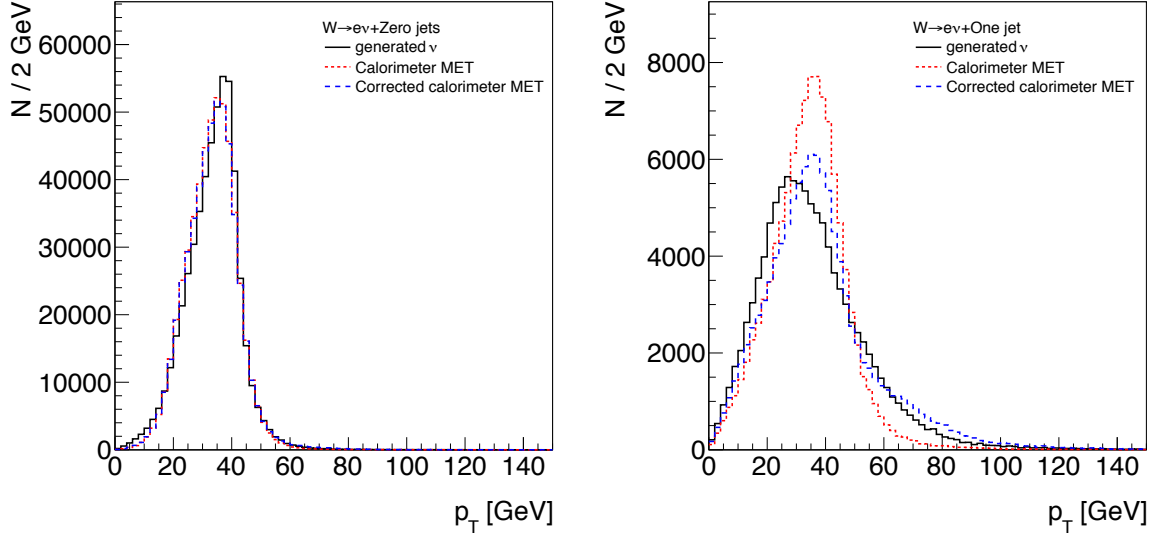
Figure 8.5.: The neutrino p_T , the *calorimeter MET*, and the *jetElectron MET* for *Z+zero jets* (left side) and *Z+one jet* (right side) events, where exactly two electrons were selected.

neutrino p_T has a tail up to $30\,\mathrm{GeV}$ in the one jet case, compared to $10\,\mathrm{GeV}$ in the zero jet case.

As Figure 8.5 shows, the distributions of the *calorimeter MET* and *jetElectron MET* are significantly above zero compared to the neutrino p_T. Both show a mean value of about $10\,\mathrm{GeV}$ for *Z+zero jets*, and $20\,\mathrm{GeV}$ for *Z+one jet*. The difference between them is the wider shape of the *jetElectron MET*, which is again due to the ignoring of low energy jets. In general, the MET in $p_T^{neutrino} \approx 0\,\mathrm{GeV}$ events is a measure for the energy and direction miss-measurements of the detected objects.

In conclusion, the *calorimeter MET* performs better for the Monte Carlo samples compared here, and is therefore used in the following. In the start up phase of the LHC, however, the *jetElectron MET* algorithm might be kept as a robust backup solution, since it relies only on high energy jets and electrons and not on the many and partial low energy deposits of the calorimeter towers.

Figure 8.6.: The neutrino p_T, the *raw*, and the *corrected calorimeter MET* for *W+zero jets* (left side) and *W+one jet* (right side) events, where at least one electron was selected.

8.2.2. Missing transverse energy corrections

The correction of the *calorimeter MET* uses the energy corrections of single jets in the events and subtracts them from the *(raw) calorimeter MET*:

$$Corrected\ calorimeter\ MET = calorimeter\ MET-$$
$$\sum_n(E_n^{corrected\ jet} - E_n^{raw\ jet})(\sin\theta_n\cos\phi_n\hat{x} + \sin\theta_n\sin\phi_n\hat{y}), \tag{8.3}$$

where n indicates the index of the jets, $E_n^{raw,\ corrected}$ denote the raw and corrected jet energies, ϕ_n and θ_n refer to the jet positions, and $\hat{x}$ and $\hat{y}$ are the unit vectors of the transverse plane of CMS. The minimum p_T^{raw} of the jets used in this sum is $20\,\mathrm{GeV}$. In addition, it is required that the electromagnetic fraction of the jets is lower than 0.9 in order not to overcorrect the MET for jets that have a high fraction of electrons and photons. The details of the *calorimeter MET* correction can be found in [76].

In the following jets, where this correction was applied are called *MET corrected jets*. The jets, where the usual jet energy corrections was applied remain denoted as *corrected jets*. To study the performance of the *corrected calorimeter MET*, the W sample is used, where events with at least one electron are selected. As before, it is divided into two subsamples with *W+zero jets* and *W+one jet* events.

Figure 8.6 shows the neutrino p_T, the *raw calorimeter MET*, and the *corrected calorimeter MET* for the zero (left side) and the one jet case (right side). In the events
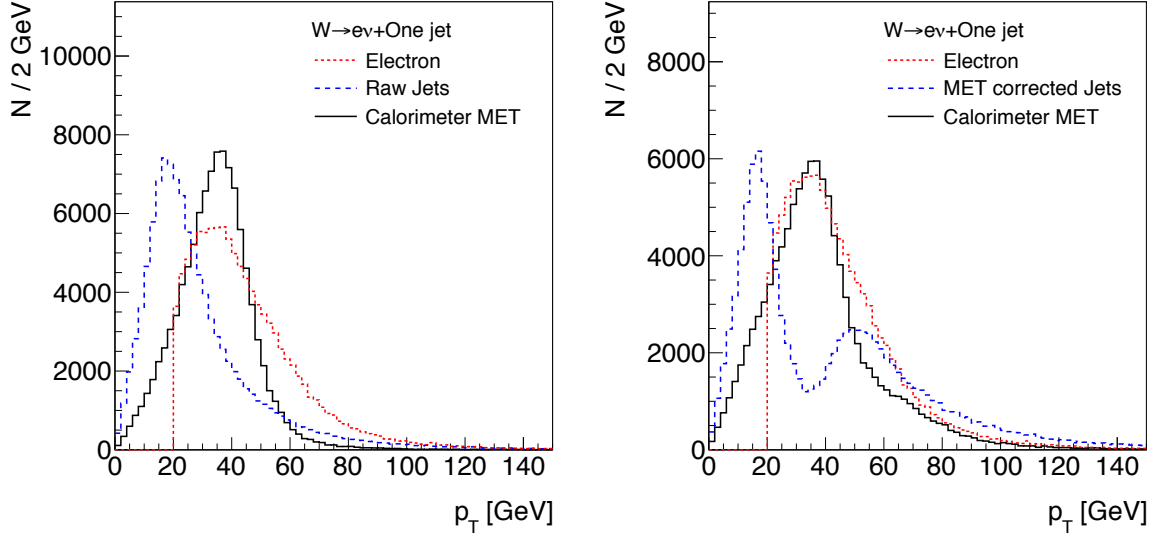
Figure 8.7.: The electron and jet components of the *uncorrected* (left side), and the *corrected calorimeter MET* (right side) for *W+one jet* events, where at least one electron was selected.

with no jets, both *calorimeter METs* are identical and match the generated neutrino p_T sufficiently good. In the *W+one jet* events, however, the agreement between the MET and the neutrino p_T improved with the correction, especially for higher values. Nevertheless, the shape of the *corrected calorimeter MET* does not describe the neutrino p_T very well. In particular, the peak is significantly shifted.

To understand this behavior better, the different components of the *raw* and the *corrected calorimeter MET* are studied in the following using *W+one jet* events. As described in the beginning of Section 8.2, the algorithm that calculates the *calorimeter MET*, uses the energy deposits in the calorimeter towers. In the case studied here, these energy deposits can originate either from electrons or from jets. These electron and jet components are considered separately in the following.

Figure 8.7 shows the contributions from the electrons and the jets to the *calorimeter MET* before (left side) and after (right side) the MET correction was applied. As expected, the p_T of the electron component does not change, since no (jet energy) correction is applied to it. The p_T spectrum of the *MET corrected jets*, however, receives a double-peaked structure through the application of the MET correction.

To understand this double structure, the jet component was further separated into high energy jets ($p_T^{corrected} > 30\,\text{GeV}$) and low energy jets. Figure 8.8 shows the p_T spectra of the high energy jets before and after the usual jet energy correction, and after applying the MET correction. As can be seen from the plot, the *MET corrected* jets
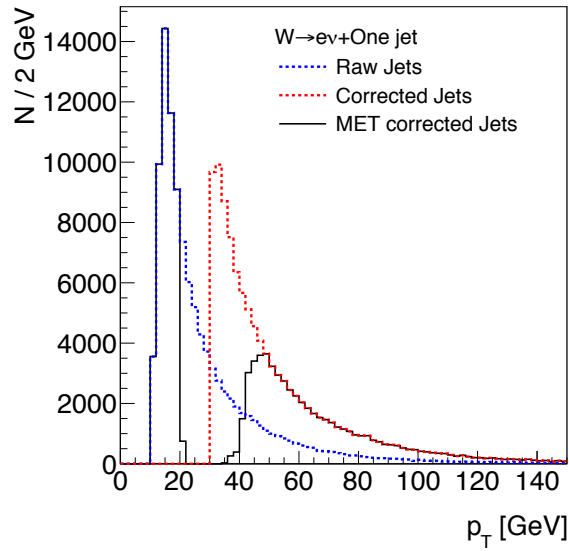
Figure 8.8.: The p_T spectra of jets before (*Raw Jets*) and after the usual jet energy correction (*Corrected Jets*), and after the *MET correction* (*MET corrected Jets*). The p_T cut-off of 20 GeV used in the *MET correction* is clearly visible.
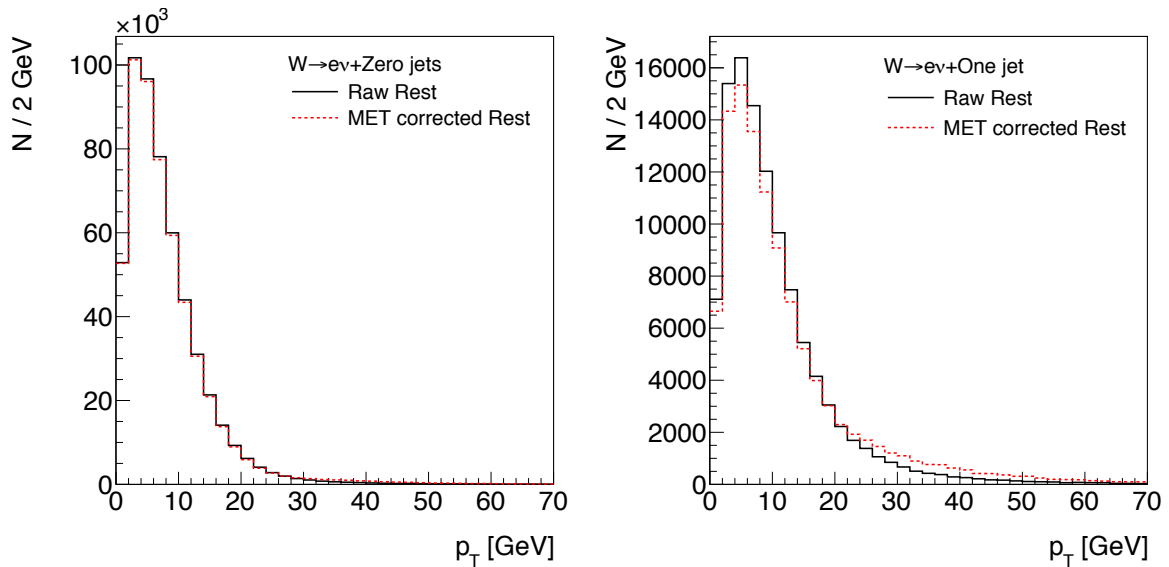
Figure 8.9.: The rest component of the *Calorimeter MET* before and after correction for *W+zero jets* (right side) events and *W+one jet* (left side) events.

agree with the raw jets below 20 GeV and with the *corrected jets* above 40 GeV. This is due to the jet p_T cut-off of 20 GeV that is used for the MET correction. This cut-off is also the reason for the double-peak structure of the whole jet component (Figure 8.7).

Finally, the effect the *MET correction* to the low energy jet component of the *calorimeter MET* was studied. Figure 8.9 shows the p_T spectra of the low energy jet component with and without correction for *W+zero jets* (left side) and *W+one jet* (right side) events. As expected, the p_T distributions of this component are not affected by the *MET correction*, since its single jet contributions have usually a p_T below 20 GeV. Comparing the *W+zero jets* and *W+one jet* cases before the correction shows their similarity: The mean values of the distributions were 8 and 10 GeV, and the RMSs 7 and 9 GeV for the zero and one jets case, respectively. That means, the "low p_T" hadronic activity in the W events is almost independent from the "high p_T" hadronic (jet) activity. However, the p_T spectrum of the low energy component has a longer tail in the *W+one jet* case. Accordingly, the *MET correction* is more effective than for the *W+zero jets* case.

8.3. Conclusions of this chapter

The reconstruction of jets and missing transverse energy in CMS was presented. The jet algorithm used in this thesis is the *Seedless Infrared-Safe Cone*. The energies of these jets are corrected to compensate for the insufficient jet energy measurements. Here, it was found that the correction gives satisfying precise energy measurements for corrected transverse jet energies above 30 GeV.

The missing transverse energy was defined with two different algorithms and compared with the generated neutrino p_T using $W^{\pm}X \to e^{\pm}\nu X$ and $Z \to e^+e^-$ events. The *jetElectron MET* algorithm was developed for this thesis and is based on high energy objects like jets and electrons only. It provides a sufficiently precise measurement of the MET, which is insensitive against miss-measurements of low energy objects in the early phase of LHC.

However, in the presented Monte Carlo studies, the *calorimeter MET* has a higher precision. The application of an additional correction to the *calorimeter MET* was found to result in an unsatisfying description of the neutrino p_T, since the jet energy corrections below 30 GeV are not used due to their imperfectness. It was concluded to use the *raw calorimeter MET* for this thesis.

Chapter 9.

# Higgs$\rightarrow$W$^+$W$^-\rightarrow$e$^+\nu$e$^-\bar{\nu}$ search

This chapter describes the search for the Higgs boson with a mass between 155 and 180 GeV at a center-of-mass energy of $E_{CM} = 10$ TeV. The discovery channel used for this search with the CMS detector is $pp \rightarrow H \rightarrow W^+W^- \rightarrow \ell^+\nu\ell^-\bar{\nu}$. The event signature is based on two high p_T electrons or muons, which are rather centrally produced and have a small opening angle. In addition, the events show a large missing transverse energy and little jet activity. The details of this analysis strategy are described in [77]. The results from these early and fast simulations were confirmed by detailed studies using full CMS detector simulations [78, 79, 80, 81].

These first studies concentrated mostly on the backgrounds from various Standard Model processes including two isolated leptons. The study presented here, however, focuses on the potential background from WX events, where the W decays to an electron and a neutrino, and X is either a jet or a photon that is misidentified as an electron. The size of the problem can be understood from ratio of the two cross-sections calculated at next to next to leading order (NNLO) [82, 83, 84].

$$\frac{\sigma(pp \rightarrow H \rightarrow W^+W^- \rightarrow e^+\nu_e e^-\bar{\nu}_e)}{\sigma(q\bar{q} \rightarrow WX \rightarrow e^{\pm}\nu X)} = \frac{0.21\,pb}{15400\,pb} = 1.4 \cdot 10^{-5}. \tag{9.1}$$

Thus, the performance of the electron selection developed in Chapter 7 has to be exploited to reduce the rate of fake electrons and to improve this ratio significantly.

This chapter starts with a general overview of the Higgs phenomenology at hadron colliders, followed by a brief description of the discovery channels of the Standard Model Higgs at the LHC. Next, the $H \rightarrow W^+W^- \rightarrow e^+\nu_e e^-\bar{\nu}_e$ signal selection according to [78] is discussed. Finally, the W+jet and Wγ background contributions to the Higgs search are quantitatively determined.

a) Gluon fusion

b) Vector boson fusion

c) Associated production

d) Higgs strahlung
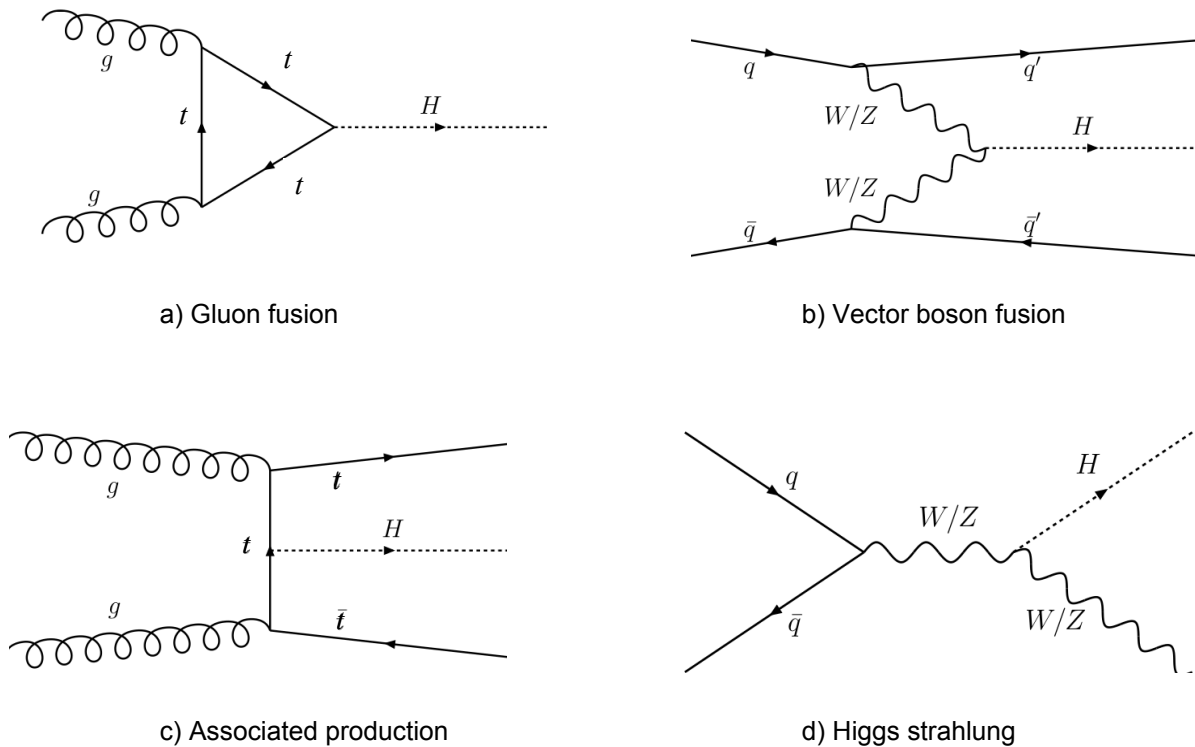
Figure 9.1.: Feynman diagrams of the Higgs production at the LHC [78].

9.1. Higgs phenomenology at hadron colliders

Chapter 2 described the necessity to introduce the Higgs boson within the theoretical framework of the Standard Model. Based on the couplings of the Higgs to the gauge bosons and fermions, theoretical predictions about the Higgs boson production and decay mechanisms can be derived.

The production processes of the Higgs boson at hadron colliders, illustrated in Figure 9.1, are:

- *Gluon fusion*
  Two incoming gluons produce the Higgs through a loop of quarks. Here, the main contribution comes from the heavy top quark (Figure 9.1(a)).

- *Vector boson fusion*
  In this production mode, two incoming quarks each radiate a W or Z boson, which then fuse to a Higgs boson (Figure 9.1(b)). In these events, two additional high energy jets at high rapidities are expected.
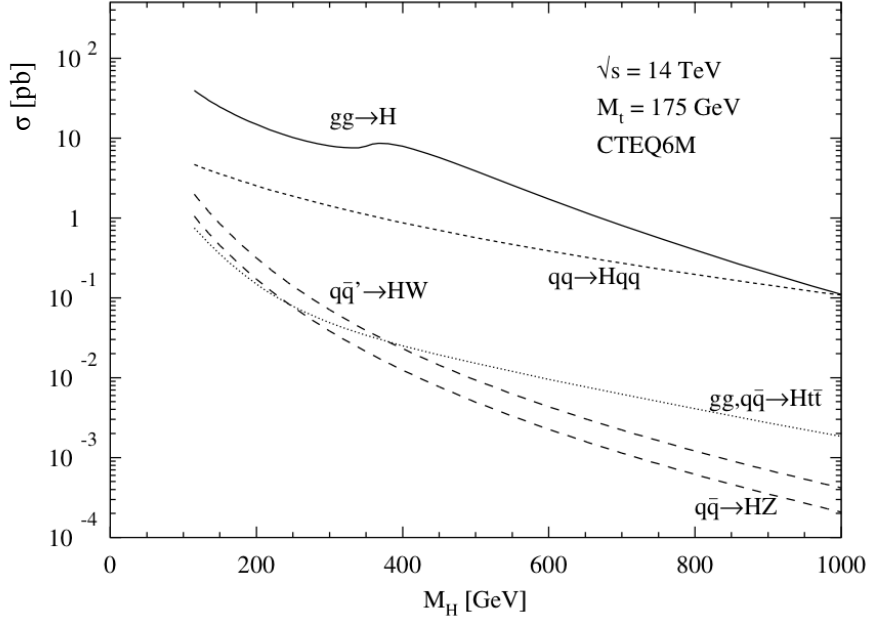
Figure 9.2.: Higgs production cross-sections at the LHC calculated at NLO [78].

- *Associated production*

  Two incoming gluons annihilate to a top-anti-top quark pair. The Higgs is then produced in association with two top-quarks (Figure 9.1(c)).

- *Higgs strahlung*

  In this process, a quark-anti-quark pair produces a W or Z boson that radiate a Higgs (Figure 9.1(d)).

The cross-sections of these processes as a function of the Higgs mass are shown in Figure 9.2 for a center-of-mass-energy of 14 TeV. As can be seen, the gluon fusion is the most important process for the Higgs production at hadron colliders. For high Higgs masses, the vector boson fusion channel has a comparable cross-section. The associated production and the Higgs strahlung have only negligible contributions.

   After its production in a proton-proton collision, the Higgs boson decays to other particles according to its couplings to them. The branching ratios of the Higgs as a function of the Higgs mass are given in Figure 9.3. As the distributions show, the decay to a bottom-anti-bottom quark pair is preferred below a Higgs mass of twice the W mass ($\sim$160 GeV). Above that threshold, the decay $H \rightarrow W^+W^-$ becomes the most important one. Its branching ratio is almost equal to unity below $\sim$180 GeV and falls down to about 60% for $m_H = 1$ TeV. The reason for the decrease is the rise of the branching ratio of the decay $H \rightarrow Z^+Z^-$ above a Higgs mass of twice the Z boson mass.
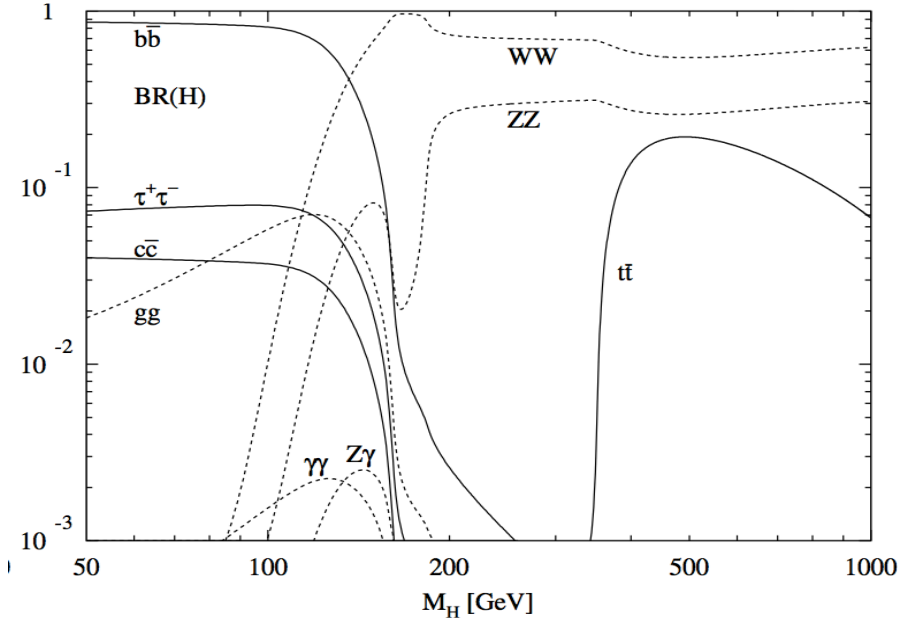
Figure 9.3.: The branching ratios of the Higgs as a function of its mass M_H [78].

Starting at $m_H = 2m_{top}$, the Higgs decay to top-anti-top quark pairs has a branching ratio of about 20%.

9.2. Higgs discovery channels

In order to discover the Higgs in a certain mass range, it is important to select not only processes with high branching ratios, but also processes, where the background contributions are controllable. In particular, decays of the Higgs that include hadronic activity are avoided in the Higgs searches at the LHC experiments. One reason is the huge QCD background in the proton-proton collisions. In addition, the determination of the flavor of the original particle forming a jet is extremely challenging. Furthermore, the jet energy measurement suffers from the limited jet energy resolution.

Subsequently, the Higgs search at hadron colliders relies on signatures that include electrons, muons, and photons, which can be measured with a much higher precision. Dependent on the Higgs mass, the following decay modes are used for the search of the Higgs boson with the CMS detector [78]. All discovery strategies, except the last one, are based on the gluon fusion production process of the Higgs.

- **$m_H <$ 140 GeV**

  Here, the decay $H \rightarrow \gamma\gamma$ is considered as the most promising discovery channel. The branching ratio of $H \rightarrow \gamma\gamma$, however, is only of the order 10^{-3}, and a discovery

requires a large integrated luminosity. The main background contributions come from jets faking photons, from continuum photon pair production, and from the process $\pi^0 \to \gamma\gamma$. The main idea of the discovery in this channel is the observation of a mass peak in the invariant mass distribution of the two photons above the background. However, since the decay width of the Higgs in this mass region is only in the order of 100 MeV, the observation relies entirely on the di-γ mass resolution of CMS.

- **155$\leq m_H \leq$180 GeV**

  The decay $H \to W^+W^- \to \ell^+\nu_\ell\ell^-\bar{\nu}_\ell$, where the leptons ℓ are either muons or electrons, is foreseen for a discovery in this region. The challenge of the Higgs discovery in this channel are the two neutrinos that escape the detector. Thus, it is impossible to reconstruct a mass peak. In addition, the backgrounds $W^+W^- \to \ell^+\nu_\ell\ell^-\bar{\nu}_\ell$ and $t\bar{t} \to W^+W^- \to \ell^+\nu_\ell\ell^-\bar{\nu}_\ell + b\bar{b}$ have to be controlled. The analysis strategy is based on the spin correlation between the charged leptons for the signal and a jet veto. It is described in detail in the next section.

- **140$< m_H <$155 GeV and 180$< m_H <$350 GeV**

  The decay $H \to ZZ^{(*)} \to \ell^+\ell^-\ell^+\ell^-$ provides a very clear signature, since the four charged leptons (electrons or muons) can be identified precisely and a narrow mass peak can be reconstructed. The main background is the $ZZ^{(*)} \to \ell^+\ell^-\ell^+\ell^-$ continuum production that can be controlled from the sidebands of the 4-lepton invariant mass distribution. However, the branching ratio is only about 0.4%. For a Higgs mass below twice the Z boson mass, the second Z of the Higgs decay is a virtual particle.

- **$m_H > 350\,GeV$**

  For higher Higgs masses, the Higgs search with the various vector boson fusion channels becomes important. The discovery strategies of these channels are similar to the ones discussed above. The main difference is the requirement of the presence of two forward jets that come from the quarks produced in the vector boson fusion [78].

Due to the different production cross-section including branching ratios of the various discovery channels, different integrated luminosities are required to discover the Higgs. Figure 9.4 shows the integrated luminosities needed for a 5σ discovery of the Higgs boson as a function of its mass at a center-of-mass energy of 14 TeV. According to the Figure, the Higgs can be discovered in the complete mass range up to a mass of about 600 GeV at the LHC, assuming some tens of fb^{-1} of integrated luminosity. Furthermore,
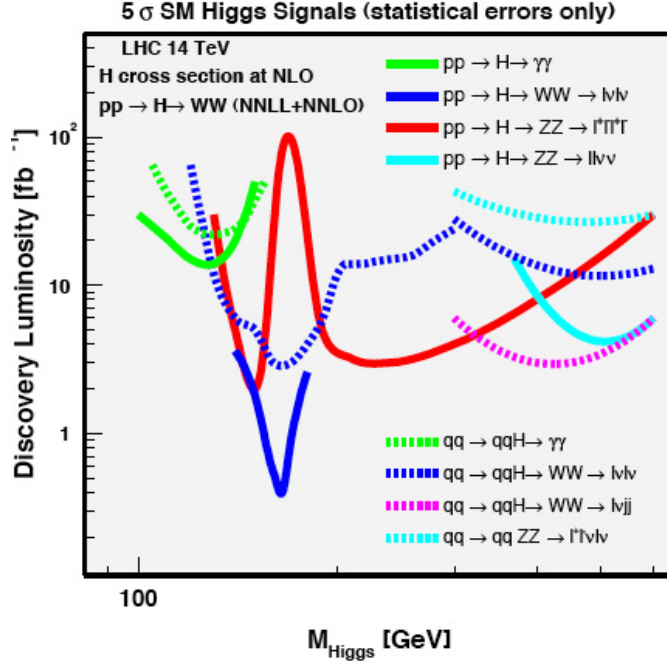
Figure 9.4.: The required luminosity to discover the Higgs as a function of its mass using various discovery channels [15].

the earliest possible discovery is for a Higgs mass around $170\,\text{GeV}$, using the decay $H \to W^+W^- \to \ell^+\nu_\ell\ell^-\bar{\nu}_\ell$, with integrated luminosities of $(0.5 \text{ - } 1)\,\text{fb}^{-1}$ at $14\,\text{TeV}$. This corresponds to roughly $(1 \text{ - } 2)\,\text{fb}^{-1}$ at a center-of-mass energy of $10\,\text{TeV}$ and $(1.5 \text{ - } 3)\,\text{fb}^{-1}$ at $E_{CM} = 7\,\text{TeV}$. In the following, the analysis strategy of this channel is described using W boson decays to electrons.

9.3. Higgs signal selection for $H \to W^+W^- \to e^+\nu e^-\bar{\nu}$

The selection of Higgs candidate events in the channel $pp \to H \to W^+W^- \to e^+\nu e^-\bar{\nu}$ with a Higgs mass between 160 and $170\,\text{GeV}$ is based on the following criteria. First, events with two isolated high p_T electron candidates that passed the electron selection are pre-selected. Thus, more "trivial" and large background contributions from $ZX \to e^+e^-X$ or $W^\pm X \to e^\pm\nu X$ events are almost entirely removed, and the events that are pre-selected are mainly consistent with W^+W^-X like events.

A second group of selection criteria provides a strong reduction of the remaining dielectron backgrounds from W^+W^-X and $t\bar{t}X$ events. The selection is based on the ideas suggested in [77] and exploit that:

- the gluon-gluon produced signal events are more central than the $q\bar{q}$ produced W^+W^- continuum events,

- the much lower jet activity in signal events compared to the $t\bar{t}$ background,

- the small opening angles between the charged leptons of signal events, which are enforced by spin correlations, and

- the electron E_T spectra show large differences for signal and background for a Higgs mass in the range of 160 to 170 GeV.

The small opening angle between the charged leptons is the most important criterion of this analysis strategy. Concerning the last point, it is important to mention, that stringent cuts on the lepton p_T spectra should not be applied too early as, assuming an excess is observed, the charged lepton p_T spectra allow it to constrain a range for the Higgs mass [85].

Figures 9.5 and 9.6 illustrate the selection ideas and motivate the cuts described below. The distributions shown in these Figures are taken from a study of the Higgs discovery in the channel $pp \rightarrow H \rightarrow W^+W^- \rightarrow \ell^+\nu\ell^-\bar{\nu}$ ($\ell^{\pm}$ = muon or electron) at $E_{CM} = 14$ TeV and for an integrated luminosity of $10\,\text{fb}^{-1}$ [81].

During the writing of the thesis, the preliminary maximal center-of-energy of the LHC was moved to $10\,\text{TeV}$[1]. Therefore, the following analysis is based on this collision energy. However, the kinematics of the Higgs and background events shown in Figures 9.5 and 9.6, does not change significantly, as it was shown in [80].

The Higgs preselection presented here is based on the ideas presented in [78]. However, like in the previous chapters, the analysis described here is limited to electrons that are found in the barrel part of the CMS detector. In particular, the subsequent cuts are required:

- **Two electrons**
  with $E_T >$ of 20 GeV and $|\eta| < 1.44$ that passed the electron selection and are oppositely charged,

- **Calorimeter MET** larger than 50 GeV, and

- **M**$_{dielectron}$ (invariant mass of the electrons) between 12 GeV and 40 GeV.

---

[1]In February 2010 the maximum center-of-energy was moved 7 TeV for the runs in 2010/2011.
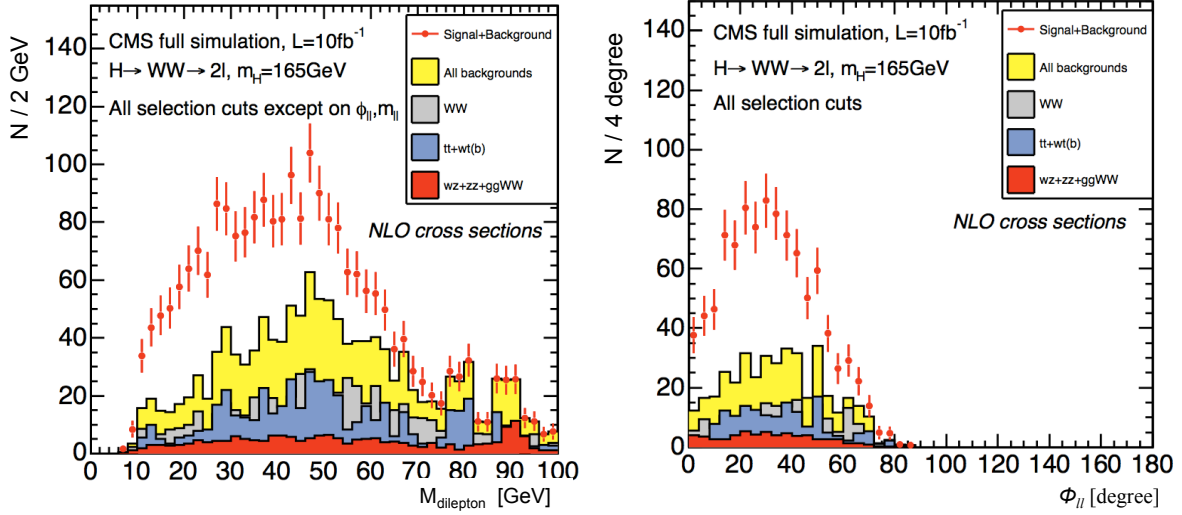
Figure 9.5.: Distributions of E_T^{hard} (left side) and E_T^{soft} (right side) for Higgs signals and several background. The plots were taken from a study at $E_{CM} = 14\,\text{TeV}$ [81].
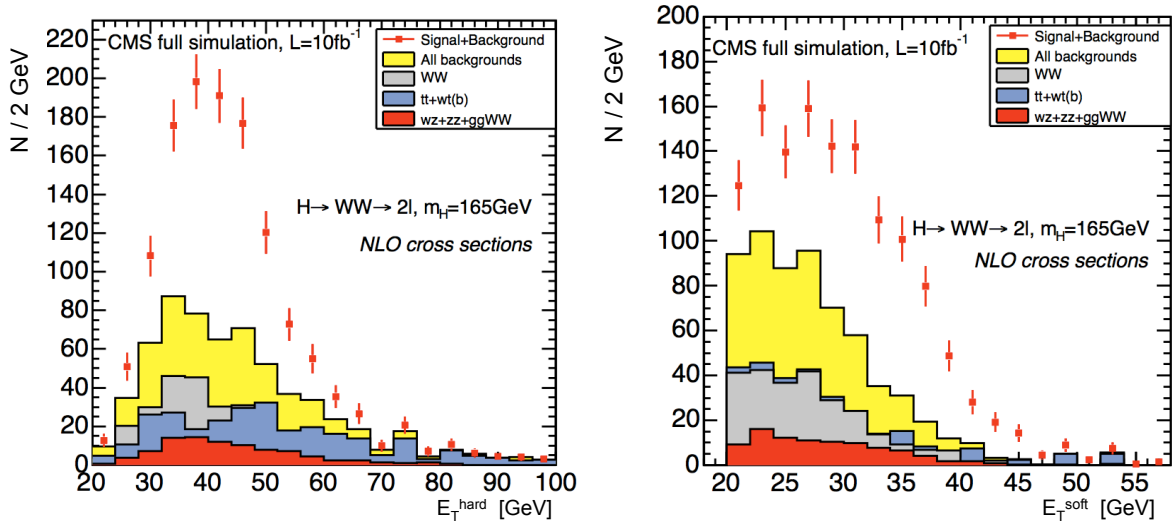
Figure 9.6.: Distributions of E_T^{hard} (left side) and E_T^{soft} (right side) for Higgs signals and several background. The plots were taken from a study at $E_{CM} = 14\,\text{TeV}$ [81].

sample	size	cross-section[pb]	filter factor
$W^{\pm}X \to e^{\pm}\nu X$	2 158 013	15 350 (NNLO)	0.738
$W^{\pm}\gamma$	103 720	35.4 (LO)	1
$H \to W^+W^- \to \ell^+\nu\ell^-\bar{\nu}$ ($m_H = 160\,\mathrm{GeV}$)	108 450	1.905 (NNLO)	1
$q\bar{q} \to W^+W^-$	960 000	75.5 (NLO)	1
$t\bar{t}$	529 750	430 (NLO+NLL)	1

Table 9.1.: Monte Carlo samples and the cross-sections used for this study. All samples were produced using the PYTHIA generator at a center-of-mass energy of 10 TeV. $\ell^{\pm}$ denotes to electrons, muons, and taus. The filter factor unequal to 1 arises from kinematic cuts applied on the generated objects (here: electrons).

The preselection leaves W^+W^-X like events and a second set of cut variables is applied to reduce the remaining background contributions.

- **Jet veto**

  Events with additional jets, reconstructed with the *SisCone5* algorithm, and with a corrected $p_T > 30\,\mathrm{GeV}$ and $|\eta| < 2.5$ are removed.

- **ϕ_{ee}**

  The opening angle of the electron pair in the plane transverse to the beam is required to be smaller than 45°.

- **p_T^{hard}**

  The p_T of the harder electron should be between 35 GeV and 55 GeV.

- **p_T^{soft}**

  The softer electron should have a p_T of more than 25 GeV.

The Monte Carlo signal and background samples, to which these cuts are applied in the following, are summarized in Table 9.1. All samples are produced using the PYHTIA Monta Carlo generator at a center-of-mass energy of 10 TeV, and were subsequently passed through a full CMS detector simulation using Geant4 in the CMSSW version 3_1_X. The $W^{\pm}X \to e^{\pm}\nu X$ cross-section was reweighted inclusively at NNLO [84]. The events of the $H \to W^+W^- \to \ell^+\nu\ell^-\bar{\nu}$ sample are reweighted with p_T dependent k-factors at NNLO [82, 83]. The $q\bar{q} \to W^+W^-$ and $t\bar{t}$ events were reweighted inclusively at NLO and NLO+NLL, respectively [86, 87].

Applying all cuts, 206 Higgs events were accepted, which corresponds to a cross-section of about 3.6 fb (Table 9.2). A similar number can be found for a Higgs mass of 170 GeV. The accepted cross-sections of remaining contributions originating from

W^+W^- and $t\bar{t}$ events after all cuts are found to be $2\,\mathrm{fb}$ and $1\,\mathrm{fb}$, respectively. The uncertainty on the total background contributions is estimated to be about $\pm 10\%$ [78, 79, 80]. The main contribution to the systematic uncertainty arise from uncertainties of the luminosity and the efficiencies of the jet and electron identification and the trigger effciency. A similar accuracy can be expected for $E_{CM} = 10\,\mathrm{TeV}$.

In contrast to former studies, the subject of this analysis is the reduction of the $W^\pm X \rightarrow e^\pm \nu X$ and the $W^\pm \gamma \rightarrow e^\pm \nu \gamma$ backgrounds with one true and one fake reconstructed electron. In particular, the aim is to reduce these contributions to the size of the systematic background uncertainty of the remaining W^+W^- and $t\bar{t}$ backgrounds, which was found to be about $\pm 0.3\,\mathrm{fb}$. Since the background $W^\pm X \rightarrow e^\pm \nu X$ has a cross-section of $15.4\,\mathrm{nb}$ at $10\,\mathrm{TeV}$ (NNLO), the achieved reduction should be of the order of 10^8. In comparison, for the reaction $W^\pm \gamma \rightarrow e^\pm \nu \gamma$, which has a cross-section of $3.5\,\mathrm{pb}$, a reduction of 10^4 is required. Since the electron from the $W^\pm$ decay has a similar p_T spectrum as the electrons from the Higgs decay, the background reductions result from a low jet (photon)-electron fake rate and from the kinematic Higgs selection criteria. Using the proposed electron selection from Section 7.2 and requiring electron pairs, the $W^\pm X \rightarrow e^\pm \nu X$ and the Wγ backgrounds were already reduced by factors of about 10^5 and 10^4, respectively (Table 9.2). As will be shown in the next section, another factor of about 10^3 can be obtained from the Higgs candidate selection.

9.4. Determination of the W$^\pm$X(γ) → e$^\pm \nu$X(γ) backgrounds

The estimation of the background contribution from WX events with one electron originating from the W$^\pm$ decay and the second being fake, faces two complications. The first problem is related to the huge $W^\pm X \rightarrow e^\pm \nu X$ cross-section of about $15.4\,\mathrm{nb}$ at $10\,\mathrm{TeV}$. Consequently, a sample of 2.16 million $W^\pm X \rightarrow e^\pm \nu X$ fully simulated Monte Carlo events corresponds to a luminosity of only $0.14\,\mathrm{fb}^{-1}$. The second problem is related to systematic modeling uncertainties of real $10\,\mathrm{TeV}$ $W^\pm X \rightarrow e^\pm \nu X$ events, which are obviously very difficult to quantify before the first high energy LHC collision data have been analyzed. Keeping these shortcomings in mind, the PYTHIA samples of 2.16 million $W^\pm X \rightarrow e^\pm \nu X$ and 103 702 $W^\pm \gamma$ events are used to estimate the probability that a true plus fake electron pair survives the various selection criteria. Table 9.2 shows the number of accepted Higgs signal events (m$_H$=160 GeV) and the number of accepted $W^\pm X \rightarrow e^\pm \nu X$ and $W^\pm \gamma$ background events.

Cut	$H \to W^+W^- \to \ell^+\nu\ell^-\bar{\nu}$	$W^\pm X \to e^\pm\nu X$	$W^\pm\gamma$
Sample size	108 450	$2.16 \cdot 10^6$	103 720
2 selected electrons			
with $E_T >$20 GeV and $|\eta| <$1.44	2 085 (37 fb)	17 (89 fb)	11 (3.7 fb)
opposite charge	2 083 (37 fb)	8 (42 fb)	3 (1.0 fb)
calorimeter MET > 50 GeV	1 317 (23 fb)	2 (11 fb)	1 (0.3 fb)
12 GeV$<$ M$_{dielectron} < 40$ GeV	1 188 (21 fb)	1 (5 fb)	0 ($<$1 fb)
jet veto	619 (11 fb)	1 (5 fb)	0 ($<$1 fb)
$\phi_{ee} < 45°$	278 (4.9 fb)	0 (< 16 fb)	0 ($<$1 fb)
35 GeV $< E_T^{hard} < 55$ GeV	265 (4.7 fb)	0 (< 16 fb)	0 ($<$1 fb)
$E_T^{soft} > 25$ GeV	206 (3.6 fb)	0 (< 16 fb)	0 ($<$1 fb)

Table 9.2.: Number of reconstructed and accepted electron pair candidates after various selection cuts and accepted cross-sections. These direct Monte Carlo results are referred to as the *Method A* results in the following.

Out of the 2.16 million generated $W^\pm X \to e^\pm\nu X$ events, 8 opposite charged electron pairs and 9 like sign pairs remain. Only two events remain after the missing transverse energy cut and zero events after the ϕ_{ee} cut. Consequently, the direct counting using this sample, called *Method A*, can only provide an upper limit of less than 3 $W^\pm X \to e^\pm\nu X$ events (at 95% confidence level), which can be transformed into a cross-section limit of about 16 fb. This limit is far too high to be useful for this analysis, when comparing it to the accepted signal cross-section of only 3.6 fb. A similar unsatisfactory result is obtained for the background from $W^\pm\gamma$ events, where again an upper limit of 3 events, corresponding to 1 fb, is obtained.

Therefore, another approach, which is based on factorization and the results from Chapter 7, is proposed. In Section 7.3 it was found that an electron, generated in the CMS barrel and with E_T of more than 20 GeV, will be reconstructed with an efficiency of 70.3%. A jet or a photon generated within the barrel and with a p_T above 20 GeV was found to be reconstructed as a fake electron with an efficiency of 1.1×10^{-4} and 0.7%, respectively.

In the following, instead of using the simulation of the CMS detector, the generated jet (or photon) 4-vector is used and combined with the one from the generated true electron in the W events. It is required that both fulfill the $E_T > 20$ GeV and $|\eta| <$

1.44 conditions[2]. The remaining events after all kinematic selection cuts are multiplied with the electron reconstruction efficiency and the jet (photon) to electron fake rate, to approximate the accepted cross-section of $W^{\pm}X \to e^{\pm}\nu X$ events. This approach to obtain higher statistic is called *Method B*. The number of accepted background events and the corresponding cross-sections obtained with *Method B* are summarized in Table 9.3. The resulting background contribution from $W^{\pm}X \to e^{\pm}\nu X$ after all cuts, was reduced to 0.3 fb.

Here, the charge cut was not applied, since obviously no charge can be assigned to a generated jet. To include the charge correlation between the true and the fake electron, we considered the 59 *fake electrons* that were found in total in the $W^{\pm}X \to e^{\pm}\nu X$ and compared their charge with the generated electron in the event. 36 of them, or 61%, had an opposite charge, which is in good agreement to what was already found in Section 7.2.3. Thus, including this charge factor, the cross-section for the accepted $W^{\pm}X$ background was (0.2 ± 0.1) fb. This value was 30% lower compared what was hoped to achieve (0.3 fb).

A treatment of the $W\gamma \to e^{\pm}\nu\gamma$ background with *Method B* leads to a negligible cross-section after cuts of about 0.004 fb, which is far below the limit set. Here, a charge factor of 0.5 was used, since in 50% of the cases the photon fakes an electron that has an opposite charge compared to the true electron.

Coming back to the reconstruction of the W events with the CMS detector simulation, a third approach to raise the statistics, called *Method C*, is introduced. The basis of this method were electron pairs ($E_T > 20$ GeV and $|\eta| < 1.44$), where the fake electron just passed the preselection of the electron reconstruction (Section 7.1.3) and the true electron was required to pass all electron selection cuts. These selected pairs are denoted as *loose-tight* pairs in the following. Electron pairs, where both electrons passed the full electron selection are called *tight-tight*. In the 2.16 million generated $W^{\pm}X \to e^{\pm}\nu X$ events, 2 448 *loose-tight* electron pairs were found, instead of the 17 *tight-tight* electron pairs obtained with *Method A*. The numbers of *loose-tight* pairs that survived the various kinematic Higgs selection cuts are given in Table 9.3. After all signal selection cuts, 5 oppositely charged *loose-tight* pairs remained. Now, the factorization approach was again assumed, e.g. that the electron selection has no influence on the kinematics of the electron-jet pairs. Then, the rule of proportion could be applied. Accordingly, the number of *tight-tight* pairs after a cut is equal to the number of *loose-tight* pairs multiplied by the factor 17/2448. This factor is the ratio of the number of *tight-tight*

---

[2]For the small number of events, where more than one generated jet was found in the barrel, the one with the higher energy was used.

Cut	Method A	Method B		Method C	
	tight-tight electron pairs	generated electron-jet pairs	efficiency corrections $\times 0.70 \times 1.1 \cdot 10^{-4}$	*loose-tight* electron pairs	scaling factor $\times 17/2448$
2 selected electrons					
with E_T >20 GeV and $|\eta|$ <1.44	17 (89 fb)	165 408	12.8 (67.2 fb)	2 448	17 (89.9 fb)
calorimeter MET> 50 GeV	3 (16 fb)	39 227	3.0 (16.0 fb)	436	3.0 (16.0 fb)
12 GeV<M$_{dielectron}$ <40 GeV	2 (10 fb)	7 455	0.6 (3.0 fb)	186	1.3 (6.8 fb)
jet veto	1 (5 fb)	7 071	0.6 (2.9 fb)	137	1.0 (5.0 fb)
ϕ_{ee} < 45°	0 (<16 fb)	3 979	0.3 (1.6 fb)	27	0.2 (1.0 fb)
35 GeV < E_T^{hard} < 55 GeV	0 (<16 fb)	1 786	0.1 (0.7 fb)	19	0.1 (0.7 fb)
E_T^{soft} > 25 GeV	0 (< 16 fb)	632	0.05 (0.2 fb)	5	0.03 (0.2 fb)

Table 9.3.: The number of events from a sample of 2.16 million $W^\pm X \to e^\pm \nu X$ events that survive the different Higgs signal selection cuts, for *Methods A, B,* and *C.*

Method A is the direct method shown in Table 9.2.

Method B: The expected event numbers and the corresponding accepted cross-sections are obtained from pairs of generated electrons and jets, which are multiplied with the true and fake electron efficiencies. The efficiency factors are 0.7 for the true electrons and $1.1 \cdot 10^{-4}$ for the fake electrons.

Method C: The event numbers and cross-sections are obtained for electron pairs, where the true electrons passed all electron selection cuts (*tight*), and the fake electrons did not (*loose*). These events are then weighted with the ratio of the 17 *tight-tight* pairs and the 2448 *loose-tight* pairs, which are obtained before the any kinematic signal selection cut is applied.

and *loose-tight* pairs before any kinematic cut was applied. Using the scaling factor of 17/2448, the $W^{\pm}X \rightarrow e^{\pm}\nu X$ background after all cuts could be estimated to be roughly 0.2$\pm$0.1 fb, which matches the result obtained with *Method B* perfectly.

As can be seen from Table 9.3, for the first few signal selection cuts, the *Methods A, B*, and *C* agree within 30%. For the subsequent cuts, where *Method A* has no more statistics, *Method C* was found to agree almost perfectly with *Method B*. In absence of larger Monte Carlo statistics, and before real $W^{\pm}X \rightarrow e^{\pm}\nu X$ data events can be studied, the background estimate from *Method B* was considered as a safer estimate, since more statistic was available.

9.5. Conclusions of this chapter

The estimation of the $W^{\pm}X(\gamma) \rightarrow e^{\pm}\nu X(\gamma)$ background contribution to the Higgs discovery channel $H \rightarrow$W$^+$W$^-\rightarrow$e$^+\nu$e$^-\bar{\nu}$ for a Higgs mass between 160 and 170 GeV was presented. Applying the electron selection criteria found in Chapter 7 and the Higgs signal selection criteria from earlier studies, reduced the background below the measurable limits due to too small Monte Carlo statistics. To increase the statistics, two independent methods based on factorization were developed. Both methods agreed perfectly and predicted a signal to background ratio after all cuts of 3.6 fb / 0.2 fb $\approx$ 18. The results of this study were summarized in [66].

In conclusion, the electron selection developed in Chapter 7 reduces the background contribution of $W^{\pm}X \rightarrow e^{\pm}\nu X$ events in the Higgs search to a level that is lower than the expected systematic errors.

Chapter 10.

# $W^{\pm} \to e^{\pm}\nu$ selection and W boson transverse momentum measurement

The production of W and Z bosons with decays to electrons or muons, are important Standard Model processes at the LHC, since they are rather simple to identify and have large production rates. Their total and differential cross-sections are one of the theoretically best understood processes and were calculated to NNLO accuracy [88].

The understanding of the kinematics of W and Z bosons is essential for the Higgs and physics beyond the Standard Model searches. For example, boson pairs decaying to leptons, are signatures for the discovery of the Higgs boson and at same time, W+jet events are potential backgrounds for the Higgs search, as discussed in the previous chapter. Furthermore, W and Z bosons could also be produced in the decays of certain heavy and exotic particles. Thus, the observation of differences between the Standard Model prediction and data could be an indication for these processes.

Another interesting application of the W and Z boson kinematics is the accurate monitoring of the proton-proton and parton-parton luminosities at the LHC as proposed in [89]. In particular, the rapidity distributions of the Z bosons and those of the charged leptons from W boson decays are very sensitive to the different parton-parton luminosities. It has been further suggested, that the production of W and Z bosons with large transverse momentum can be used to constrain the LHC gluon luminosities.

This chapter gives first an introduction of the W and Z boson physics at the LHC and explains qualitatively, how their kinematics can constrain the gluon PDFs of protons at the LHC. An almost background free selection of $W^{\pm} \to e^{\pm}\nu$ events is presented in Section 10.2 including a detailed study of the various backgrounds. Thereby, an essential selection tool is the electron selection introduced in Chapter 7. The chapter concludes in Section 10.3 with the a study of how to measure the transverse momentum spectrum of the W boson.
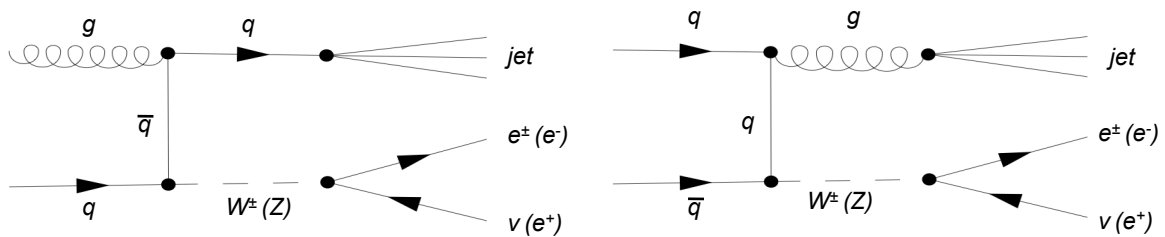
10.1. W and Z boson phenomenology at the LHC
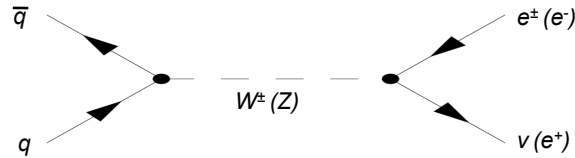
Figure 10.1.: Feynman diagram of the leading order W(Z) production and successive decay to an electron and neutrino (electron-positron pair) at the LHC.

The leading order process for the W(Z) boson production at the LHC is the annihilation of a quark-anti-quark pair as shown in Figure 10.1. Since the incoming partons have no transverse momentum, the W(Z) boson has $p_T = 0$ at leading order. Thus, to obtain W (Z) bosons with a non vanishing p_T, at least one jet is required, which balances the transverse momentum of the W boson. The jets can either be induced by a gluon or a (anti-)quark. At leading order, two different W(Z)+jet processes exist at the LHC:

1. A gluon from one incoming proton splits into a quark-anti-quark pair. Subsequently, one of them annihilates with a (anti-)quark from the other proton. The (anti-)quark that remains from the splitting undergoes hadronization and results in a jet (Figure 10.2 left side). This process is denoted as "gluon-induced" in the following.

2. An incoming (anti-)quark radiates a gluon before the annihilation to a W(Z) boson with a another (anti-) quark (Figure 10.2 right side). The radiated gluon leads to a jet as before. This process is denoted as "quark-induced" in the following.

At higher orders, more complicated processes are possible, as described in [90]. The balance of the W boson and jet transverse momenta will be exploited in Section 10.3 to determine the W p_T.

Figure 10.2.: Feynman diagrams of the leading order W(Z)+jet production with the successive decay to an electron and neutrino (electron-positron pair) at the LHC. The two processes are denoted as "gluon-induced" (left side) and "quark-induced" (right side).
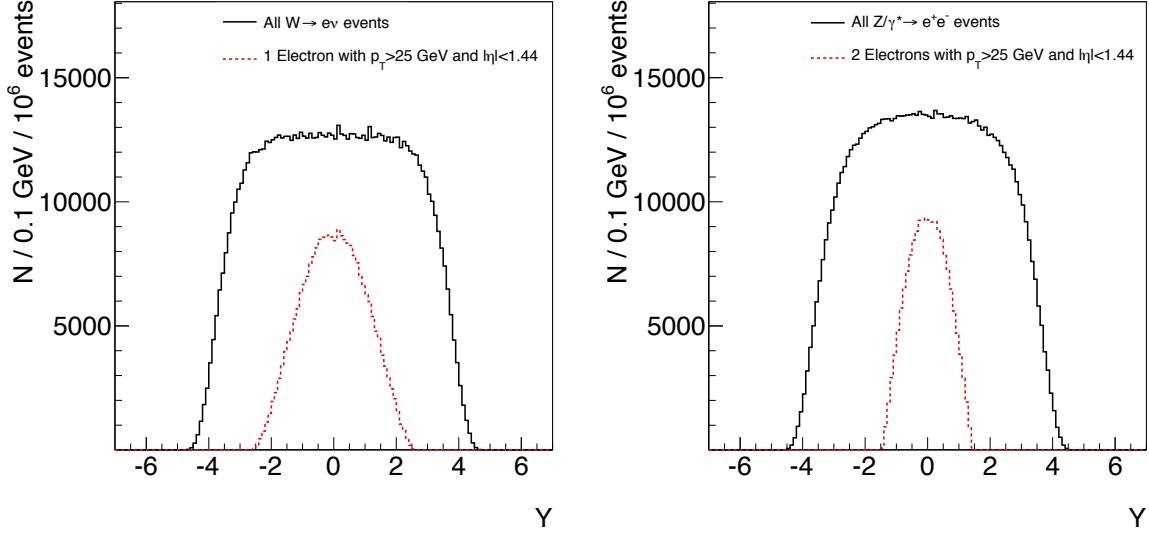
Figure 10.3.: The rapidity distributions of 10^6 $W^{\pm} \to e^{\pm}\nu$ (left side) and $Z/\gamma^* \to e^+e^-$ (right side) events and of those events, where either one or two generated electrons were found with $|\eta| < 1.44$ and $E_T > 25\,\mathrm{GeV}$.

In the following, the influence of the parton distribution functions (PDFs) on the transverse momentum distribution of the W boson is studied. The PDFs encode information about the structure of the proton, as discussed in Section 2.5. In particular, the functions parametrize the probability that a quark or gluon inside the proton carries the fraction x of the parent proton's momentum. The resonant W or Z boson production constrains the values $x_{1,2}$ of the two involved partons in the following way:

$$m_{W(Z)} = \sqrt{x_1 x_2}\, E_{CM}. \tag{10.1}$$

Then, the rapidity Y of the W (Z) boson depends on $x_{1,2}$ by

$$Y = 0.5 \ln \frac{x_1}{x_2}. \tag{10.2}$$

The black histograms in Figure 10.3 represent the rapidity distributions of 1 million generated $W^{\pm} \to e^{\pm}\nu$ events (left side) and 1 million $Z/\gamma^* \to e^+e^-$ events (right side). At $E_{CM} = 10\,\mathrm{TeV}$, the inclusive leading order cross-sections are $\sigma_{LO}(W^{\pm} \to e^{\pm}\nu) = 11.8\,\mathrm{nb}$ and $\sigma_{LO}(Z \to e^+e^-) = 1.0\,\mathrm{nb}$.

As in the chapters before, the analysis is restricted to electrons, which are found in the barrel ($\eta < 1.44$). In addition, a minimal electron E_T of 25 GeV is required as motivated in the next section. The dashed red histograms in Figure 10.3 are the distribution for those $W^{\pm} \to e^{\pm}\nu$ and $Z \to e^+e^-$ events, where one and two generated
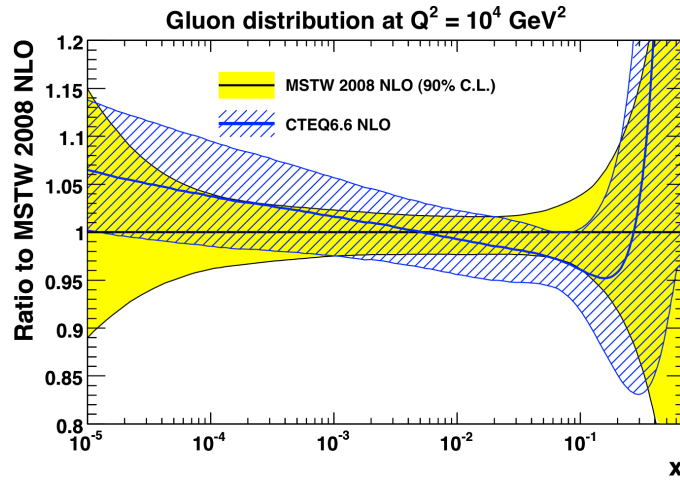
Figure 10.4.: The uncertainties of the next to leading order gluon PDFs for MSTW08 and CTEQ6.6 at $Q^2 = 10^4 \, \text{GeV}^2$.

electrons with $|\eta| < 1.44$ and $E_T > 25 \, \text{GeV}$ were found, respectively. The kinematic cuts on the electron limit the absolute W boson rapidity to a value of roughly 2. The rapidity of the Z bosons is restricted to 1.5, since its both decay products are required to be in the barrel. These values, together with Equations (10.1) and (10.2), require $x_{1,2}$ to be within the intervals [0.001, 0.06] and [0.002, 0.04] for the resonant W and Z boson production, respectively.

The accurate knowledge of the PDFs is important for the reliable prediction of the production cross-sections for the processes expected at the LHC. In particular, the gluon distribution functions are required to predict the cross-section of the Higgs, which is mainly produced by gluon fusion, as described in Section 9.1. The presently existing parton distribution functions of the proton were tuned using the results from the experiments at HERA and Tevatron. In the following, the two very commonly used and independent PDF sets MSTW08 [12] and CTEQ6 [91] are compared.

The uncertainties of the two gluon PDF sets as a function of x are shown in Figure 10.4 at next to leading order and at $Q^2 = 10^4 \, \text{GeV}^2$ [84]. The yellow band represents the systematic uncertainty of the MSTW08 distribution. The ratio of the two different PDF distributions is represented by the blue line. Accordingly, the uncertainty of both PDFs is $\pm 5\%$ between 10^{-4} and 0.1, matching the x range of the W(Z) bosons considered here. For higher and lower x values, the uncertainties become very large. Additionally, one observes that the two PDFs agree within 5% between x values of 10^{-5} and 0.2. Above $x = 0.2$, they differ strongly.

To study the influence of these PDFs on the transverse momentum of the W boson, two samples of 1 million leading order $W^{\pm} \to e^{\pm}\nu$ events, each based on one of the two
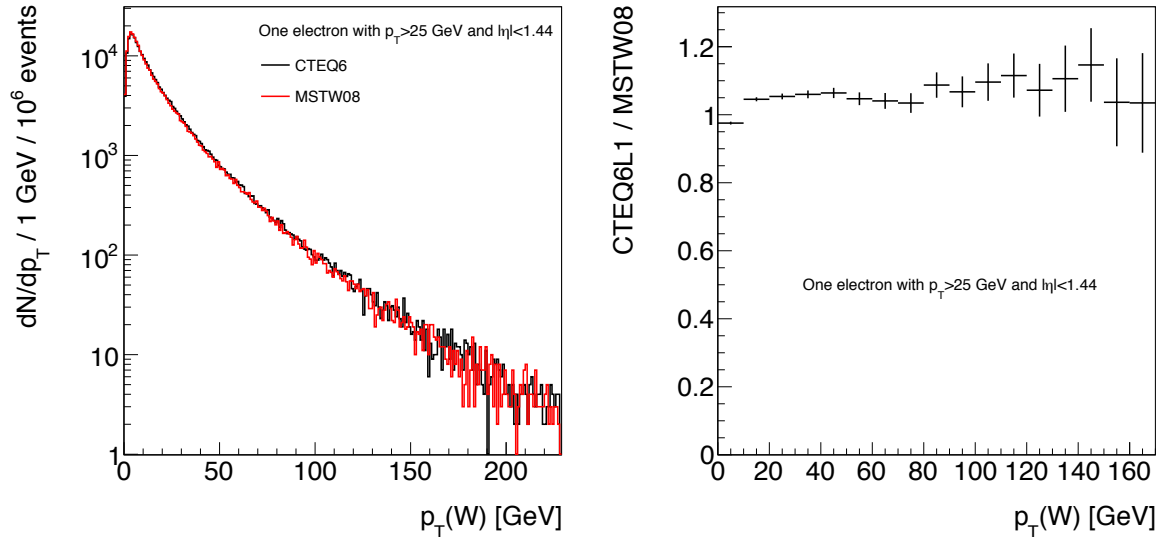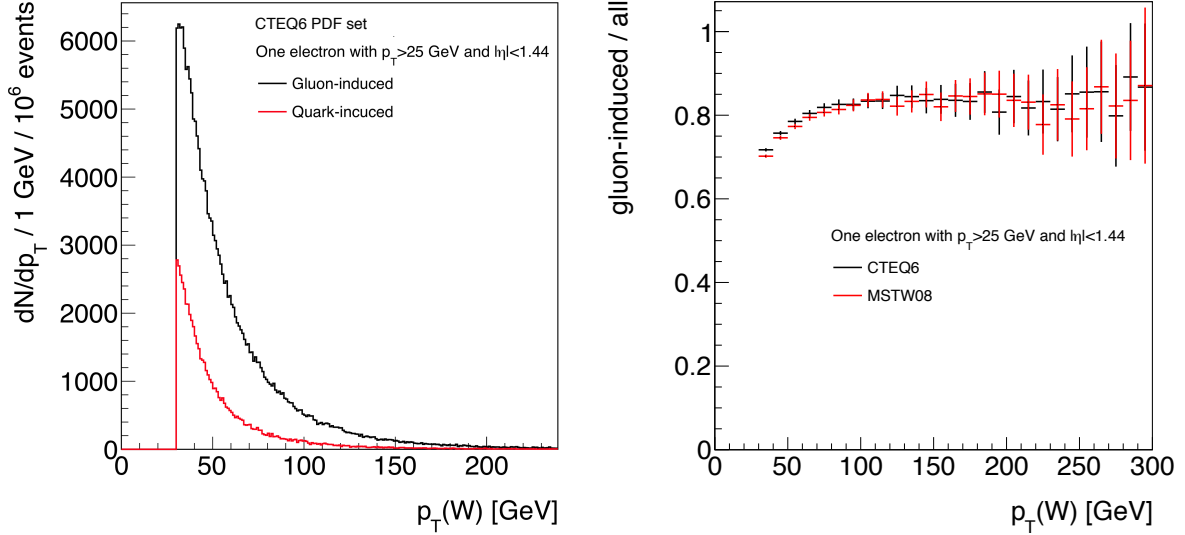
Figure 10.5.: Left side: W transverse momentum spectra predicted by the MSTW2008 and the CTEQ6 PDF sets for events with one generated electron with $E_T > 25\,\text{GeV}$ and $|\eta| < 1.44$.
Right side: Ratio of the two distributions.

PDF sets, were produced with the PYTHIA Monte Carlo generator at $E_{CM} = 10\,\text{TeV}$. The results presented in the following are also valid for Z bosons events. As before, events with exactly one generated electron with $E_T > 25\,\text{GeV}$ and $|\eta| < 1.44$ were selected. Figure 10.5 shows the W p_T spectra for the two PDF sets on the left side and their ratios on the right side. At a first look, both PDF sets predict a very similar transverse momentum spectrum (left side). The ratio, however, shows that the spectrum from the CTEQ6 PDF set is 5% below that from MSTW08 for $p_T < 10\,\text{GeV}$, 5% above it for $p_T > 10\,\text{GeV}$, and is 10% higher for p_T values above $80\,\text{GeV}$.

To investigate the origin of this difference, the gluon-induced and quark-induced W production processes shown in Figure 10.2 are considered separately for both PDF sets. For the study, special leading order PYTHIA samples of each 1 million W+jet events (with $W^{\pm} \to e^{\pm}\nu$) were generated for both PDF sets. Since the calculation of the W+jet process diverges for small W p_Ts, a minimum W p_T has to be required (here $p_T > 30\,\text{GeV}$). According to Figure 10.5, 17.6% (16.9%) of the W events are produced with a p_T higher than $30\,\text{GeV}$ for the CTEQ6 (MSTW08) PDF set. As will be shown below, this difference arises from the different composition of the PDFs sets.

Figure 10.6 (left side) shows the p_T spectra of the gluon-induced and quark-induced W bosons in the CTEQ6 sample. The corresponding spectra for the MSTW08 sample are very similar. As can be seen, the gluon-induced process is roughly a factor of 3 more

Figure 10.6.: Left side: W transverse momentum spectra of the CTEQ6 sample for the two different production processes of high p_T W-bosons with one generated electron with $E_T >$ 25 GeV and $|\eta| < 1.44$.

Right side: The fraction of W bosons produced with the gluon-induced process as a function of the W boson p_T for the CTEQ6 and the MSTW08 samples. The error bars represent the statistical errors.
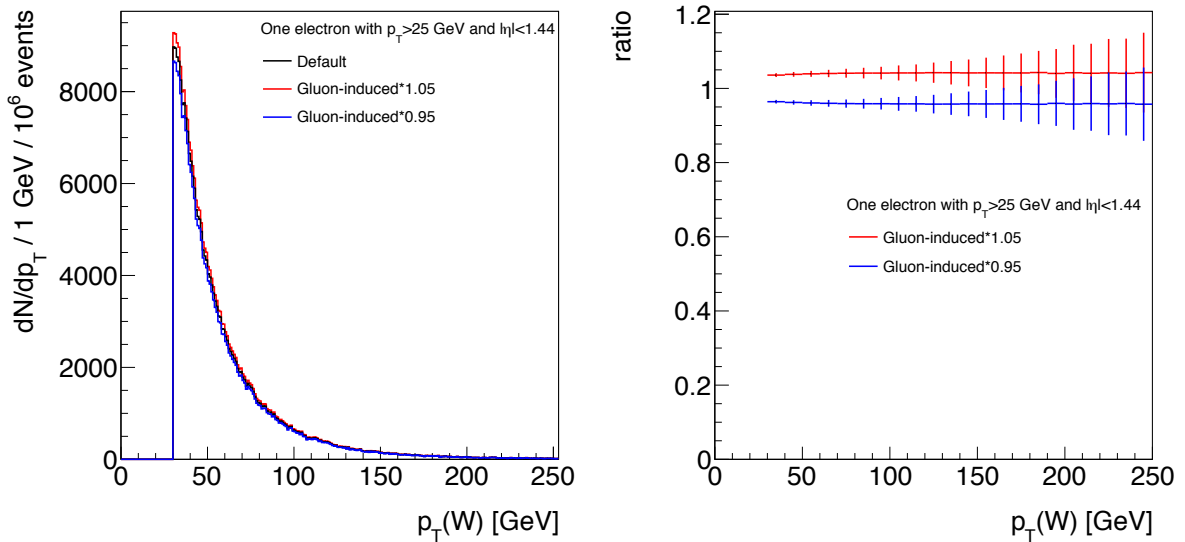
Figure 10.7.: Left side: W transverse momentum spectra for an 5% increased and 5% decreased fraction of the gluon-induced W production process with one generated electron with $E_T >$ 25 GeV and $|\eta| < 1.44$.

Right side: The ratio of the p_T spectra that were varied by $\pm$5% and the default p_T spectrum. The error bars represent the statistical errors.

frequent than the quark-induced process for this high p_T W sample. The fractions of the gluon induced processes as a function of the W boson p_T is shown in Figure 10.6 (right side) for both PDF sets. One finds, that the gluon-induced fraction increases from 70% at 30 GeV to about 85% at 130 GeV and stays at this value for higher p_Ts. Accordingly, the gluon-induced process is mainly responsible for the production of high p_T W bosons. However, this distinction between the two production processes is not possible for small W boson p_Ts due to the mentioned divergence of the calculation of the W+jet process. But, as can be understood from the extrapolation of the ratio distributions to zero, low p_T W bosons are mostly produced by the quark-induced production process.

Furthermore, differences can be observed for the gluon-induced fractions of the two PDF sets. In particular, for p_Ts below 90 GeV, the CTEQ6 PDF has a few percent higher gluon-induced fraction. This observation is in good agreement with the W p_T spectrum, which is higher for the CTEQ6 PDF, as shown in Figure 10.5. In conclusion, a variation of the gluon distribution functions changes the p_T spectrum of the W boson. Since the sum of all PDFs is constrained by the momentum of the proton, an increase of the gluon PDFs leads to a decrease of the quark PDFs and vive versa. Thus, especially the ratio of the W bosons produced at low p_T (more quark-induced) and at high p_T (more gluon-induced) can be used to constrain the PDFs.

To simulate the influence of a variation of the gluon PDF on the W boson p_T spectrum, the gluon-induced fraction of the W bosons was varied by $\pm 5\%$ using the CTEQ6 PDF set. The number of quark-induced W bosons was kept stable. Figure 10.7 (left side) shows three W p_T spectra. The black distribution denotes the case, where the fraction of gluon-induced was the default one. The red and the blue line, the cases with an increased and decreased gluon-induced fraction, respectively. As it can be expected from Figure 10.6, the increase of the gluon PDF shifts the W p_T spectrum to higher values and vice versa. The distributions in Figure 10.7 (right side) show the ratios of the p_T spectra with the increased and decreased gluon-induced fractions and the default one in red and blue, respectively. The ratios show, that a $\pm 5\%$ variation of the fraction of the gluon-induced W boson production, leads to a $\sim 4\%$ higher or lower cross-section of W bosons with $p_T > 30$ GeV. Thus, measuring the W p_T spectrum with a precision of less than 5%, constrains the gluon PDFs of the proton at the LHC. As will be shown in Section 10.3, with a integrated luminosity of 10(20) pb^{-1} at $E_{CM} = 10(7)$ TeV, this precision is achievable.

10.2. W boson selection

The selection of $W^\pm \to e^\pm \nu$ events presented in this section is performed for an integrated luminosity of $10\,\mathrm{pb}^{-1}$ at a center-of-mass energy of $10\,\mathrm{TeV}$. It uses Monte Carlo samples, which passed a full CMS detector simulation with the CMSSW version 3_1_X. The signal and backgrounds samples used here are summarized in Table 10.1. As mentioned earlier, the corresponding cross-sections for $E_{CM} = 7\,\mathrm{TeV}$ are roughly a factor of two smaller than the given ones. The important backgrounds are processes, where high E_T electron candidates can be expected. These electron candidates can either be real electrons or fake electrons, i.e. miss-identified jets or photons.

The selection of $W^\pm \to e^\pm \nu$ events is most importantly based on the clean identification of electrons. Figure 10.8 (left side) shows the E_T spectra of selected electron candidates for $W^\pm \to e^\pm \nu$, $\gamma + jet$, and QCD events, and the sum of all three together. Here, only events with exactly one electron in the barrel were accepted ($|\eta| < 1.44$). The electron candidates in the QCD and $\gamma + jet$ events were fake electrons or electrons that were produced in leptonic decays of hadrons. The rate for generated jets or photons that are identified as an electron candidate is of the order of only 10^{-4}, as shown in

Sample	Q [GeV]	Cross-section [nb]	#Events in $\mathcal{L}$=10 pb^{-1} $\cdot 10^3$
$W^\pm \to e^\pm \nu$	incl.	12×0.783	87
$W^\pm \to \tau^\pm \nu$	incl.	12	118
$t\bar{t}$	incl.	0.2	2
$Z/\gamma^* \to e^+ e^-$	> 20	2	19
QCD	30-80	109 000	1 090 000
QCD	80-170	1 900	18 400
$\gamma + jet$	30-50	26	263
$\gamma + jet$	50-80	5	46
$\gamma + jet$	80-120	0.8	8
$\gamma + jet$	120-170	0.2	2

Table 10.1.: Monte Carlo samples used for this study at $E_{CM} = 10\,\mathrm{TeV}$. All samples were produced with the leading order PYTHIA generator. Q denotes the momentum transfer of the collision reaction; "incl." refers to samples, where no cut on Q was applied. The $W^\pm \to e^\pm \nu$ cross-section was multiplied by a filter factor due to a cut of $|\eta| < 2.5$ applied to the generated electrons.
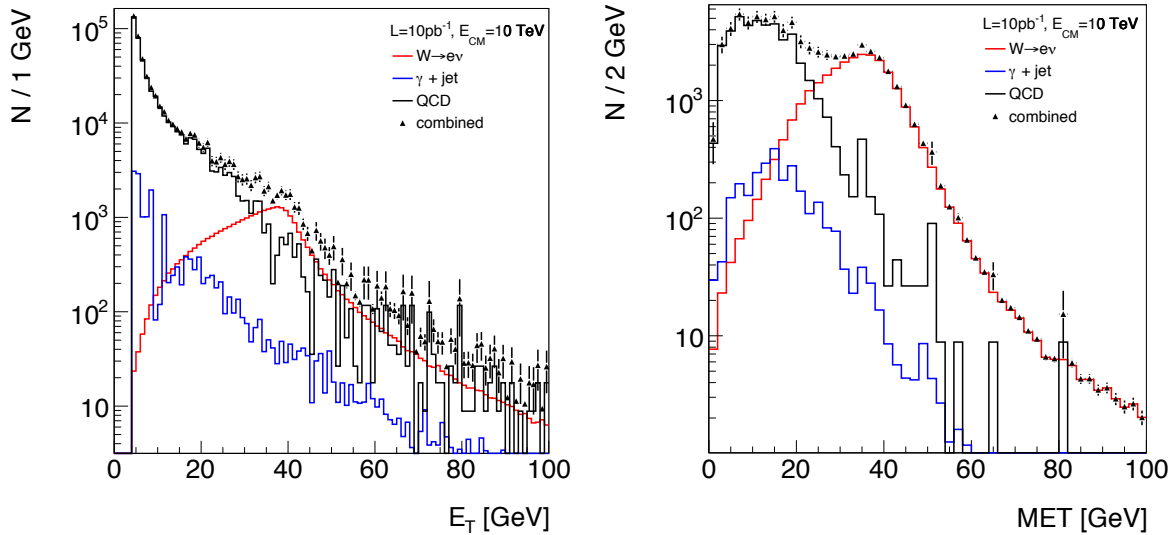
Figure 10.8.: E_T of selected electrons in the ECAL barrel (left side) and missing transverse energy spectra (right side) for the signal, two backgrounds, and all three together. For the MET spectrum, events with exactly one electron candidate with $E_T > 20 \, \text{GeV}$ and $|\eta| < 1.44$ were selected.

Section 7.2.3. The QCD background contribution is nevertheless overwhelming for low electron E_Ts. Thus, as Figure 10.8 (left side) shows, the background can already be considerably reduced by requiring a minimum electron E_T of $20 \, \text{GeV}$.

Furthermore, the missing transverse energy (MET) is an essential variable to distinguish $W^\pm \to e^\pm \nu$ signals from backgrounds. Figure 10.8 (right side) shows the *calorimeter MET* distributions of $W^\pm \to e^\pm \nu$, $\gamma + jet$ and QCD events, where exactly one electron in the barrel with $E_T > 20 \, \text{GeV}$ was found. According to the distributions, a cut of *calorimeter MET* $> 20 \, \text{GeV}$ reduces the background significantly.

Table 10.2 shows the performance of these two preselection cuts applied successively on all signal and background samples. As can be seen, the requirement of a high E_T electron and high *calorimeter MET* decreases the background contributions strongly, while keeping signal selection efficiency high. The signal to background ratio after these preselection cuts is already 3.4.

A further important variable of the W selection is the *invariant transverse mass M_T*. In contrary to for example $Z \to e^+ e^-$ events, it is not possible to reconstruct the mass of the W bosons decaying to an electron and a neutrino, since the neutrino escapes the detector. However, using the *calorimeter MET* and the E_T of the electron, one can calculate M_T. The difference between the generated W mass and generated transverse mass M_T is shown in Figure 10.9 for preselected $W^\pm \to e^\pm \nu$ events. As expected, the

Sample	1 electron in barrel with $E_T > 20\,\mathrm{GeV}$	*calorimeter MET* $> 20\,\mathrm{GeV}$
$W^\pm \to e^\pm \nu$	26 534 (30.4%)	24 477 (28.0%)
$W^\pm \to \tau^\pm \nu$	1 227 (1.0%)	885 (0.8%)
$t\bar{t}$	227 (9.4%)	199 (8.3%)
$Z/\gamma* \to e^+ e^-$	3 705 (19%)	549 (2.8%)
QCD	21 998 ($19 \cdot 10^{-4}$)	4 884 ($5.9 \cdot 10^{-4}$)
$\gamma + jet$	2 256 ($4.4 \cdot 10^{-4}$)	686 ($1.0 \cdot 10^{-4}$)

Table 10.2.: Performance of the W preselection cuts on the different samples for $\mathcal{L} = 10\,\mathrm{pb}^{-1}$. The efficiencies in brackets are calculated with respect to the figures given in Table 10.1.
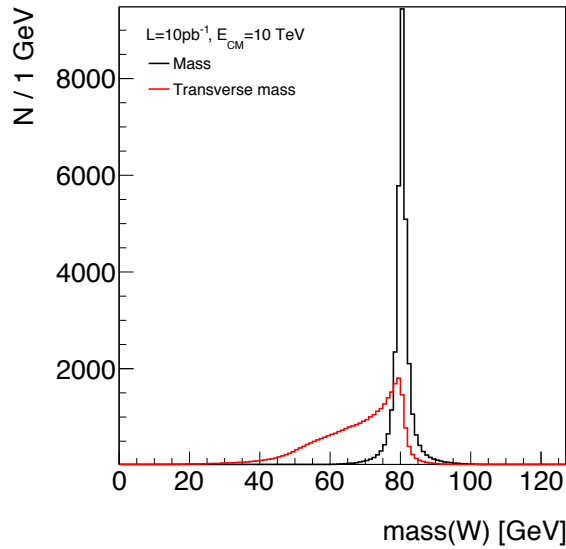
Figure 10.9.: Left Side: The generated mass and transverse mass of $W^\pm \to e^\pm \nu$ events, where one electron was generated with $E_T > 25\,\mathrm{GeV}$ and $|\eta| < 1.44$.

distribution of the distribution of the mass peaks at a value of $80\,\mathrm{GeV}$. M_T shows a Jacobian peak structure.

10.2.1. General selection cuts

In the following, events are analyzed separately for events with zero jets, one jet and more than one jet. As will be shown in this section, this separation is motivated by the higher signal to background ratio, which can be achieved. The separation represents a new approach in terms of a W boson selection at hadron colliders, which was developed
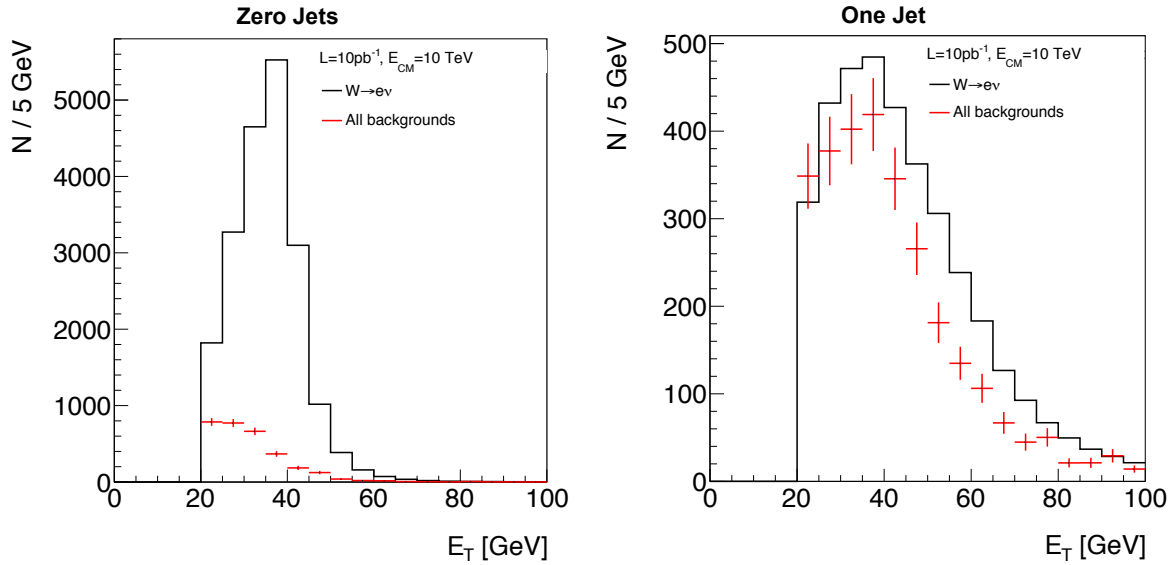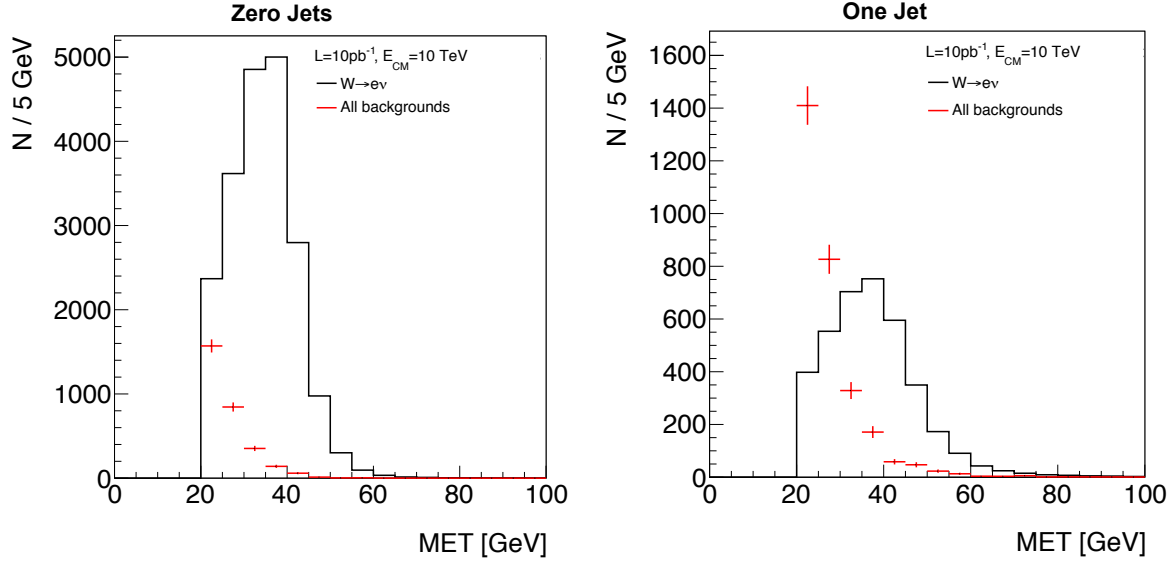
Figure 10.10.: The electron E_T for signal and the sum of all backgrounds for events, which passed the preselection and with zero jets (left side) and exactly one jet (right side). Jets were counted with $p_T > 30 \, \text{GeV}$ and $|\eta| < 2.5$.

in the frame of this thesis. Thereby, the jet multiplicity is defined for energy corrected jets found with the *SisCone5* algorithm and with a minimum p_T of $30 \, \text{GeV}$ and $|\eta| < 2.5$ (Section 8.1.1). Furthermore, only events, with exactly one electron with $E_T > 20 \, \text{GeV}$ and $|\eta| < 1.44$ and *calorimeter MET* $> 20 \, \text{GeV}$ are considered (preselection).

Figure 10.10 shows the distributions of the electron E_T for events with zero jets (left side) and one jet (right side) for the signal in black and the sum of all backgrounds in red with error bars. As the distributions show, the background contribution is already very low after the preselection for the zero jet case, whereas it is still considerable for the one jet case. The reason is, that the dominant QCD background consists mostly of di-jet events, where one of the two jets fakes an electron. The considerable E_T of the fake electron has to be balanced by the second high p_T jet. Thus, QCD events with zero jets are very rare, since the second jet has to be 'lost' in the event or has to be very forward ($|\eta| > 2.5$). The same argument is valid for $\gamma + jet$ events, where the photon fakes the electron. The electron E_T spectrum of the one jet case motivates a minimum E_T of $25 \, \text{GeV}$, which is used in the following.

The distributions of the *calorimeter MET* are shown in Figure 10.11 for events with zero jets (left side) and one jet (right side) for the signal and the sum of all backgrounds. As discussed in Section 8.2, the measurement of the *calorimeter MET* is less precise for events with high jet activity. In particular, it is more likely to measure fake MET due to the imperfect energy measurement of jets. Thus, the one jet case shows a higher

Figure 10.11.: The *calorimeter MET* for signal and the sum of all backgrounds for events, which passed the preselection for the zero jet case (left side) and the one jet case (right side). Jets were counted with $p_T > 30$ GeV and $|\eta| < 2.5$.

fake *calorimeter MET* contribution coming mostly from QCD events. According to the distributions, a minimum *calorimeter MET* of 30 GeV is required.

The transverse mass was also used as a cut variable. Figure 10.12 shows M_T for events with an electron with $E_T > 25$ GeV in the barrel and *calorimeter MET* > 30 GeV for the zero jet case (left side) and the one jet case (right side). Due to the less precise measurement of the *calorimeter MET* in the one jet case, the distribution of M_T is much wider here. According to these distributions, M_T is required to be larger than 60 GeV.

The distributions for events with more than one jet look similar to the ones with one jet shown above. Thus, for the subsequent studies, the following set of $W^{\pm} \to e^{\pm}\nu$ cuts is used for all jet cases:

- exactly one electron with $E_T > 25$ GeV and $|\eta| < 1.44$,

- *calorimeter MET* > 30 GeV, and

- $M_T > 60$ GeV.

The number of signal and background events, which were selected by these cuts are summarized in Table 10.3 for events with zero, one, and more than one jet.

For the case with zero jets, the main background contributions were either QCD events, where a jet faked an electron, or $W^{\pm} \to \tau^{\pm}\nu$ events, with the subsequent decay
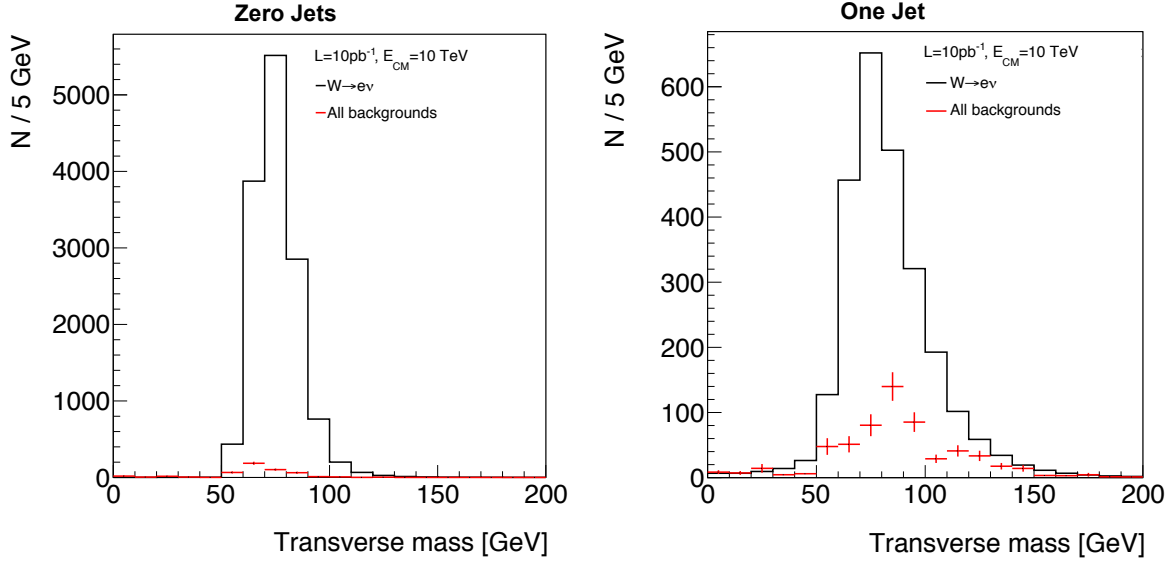
Figure 10.12.: The transverse mass for signal and the sum of all backgrounds for events with exactly one electron with $E_T > 25\,\text{GeV}$ and *calorimeter MET* $> 30\,\text{GeV}$ for the zero jet case (left side) and the one jet case (right side). Jets are counted with $E_T > 30\,\text{GeV}$ and $|\eta| < 2.5$.

Process	Zero jets	One jet	More jets
$W^{\pm} \to e^{\pm}\nu$	13 336	2 371	309
$W^{\pm} \to \tau^{\pm}\nu$	162	30	5
$t\bar{t}$	1	9	106
$Z/\gamma* \to e^+e^-$	19	56	71
QCD	159	329	260
$\gamma + jet$	35	105	41
All backgrounds	376	529	483
Signal/background	36	4.5	0.6

Table 10.3.: Performance of the W selection cuts on the different signal and background processes after the application of all cuts, and for $\mathcal{L} = 10\,\text{pb}^{-1}$ at $E_{CM} = 10\,\text{TeV}$.

$\tau^\pm \to e^\pm \nu_\tau \nu_e$. The signal to background rate for the zero jet case was found to be 36, which was considered as high enough for this analysis.

For the one jet case, the main backgrounds are QCD and $\gamma + jet$ events, where a jet or photon fake an electron. In $Z/\gamma^* \to e^+ e^-$ background events, one electron was not reconstructed as an electron candidate and was subsequently counted as a jet. The signal to background rate of 4.5 is low and can be improved by introducing a further cut variable as discussed in the next section. Due to the very low fraction of $W^\pm \to e^\pm \nu$ events with more than one jet and due to the high background rate in this case, these events are not considered in the following.

10.2.2. Selection cuts for the one jet case

To improve the $W^\pm \to e^\pm \nu$ selection in the one jet case, the kinematics of signal and background events in the transverse plane of the CMS detector were studied. Figure 10.13 shows qualitatively the difference between the kinematics of the signal and of the remaining backgrounds from QCD and $\gamma + jet$ events for the case with one jet. Here, one of the two jets in the QCD events, and the photon in $\gamma + jet$ events, was reconstructed as an electron candidate. Due to momentum conservation, the jet and the fake electron of the background events are back-to-back in the transverse plane. In the same manner, the transverse momenta of the W boson and the jet in the signal events balance each other. The difference is, however, that the W decays to an electron-neutrino pair. Thus, due to the large W boson mass, the electron and the jet are generally not back-to back for the signal.

This difference is exploited to reduce the background contribution further. Figure 10.14 shows the distributions of the angle $\Delta\phi$ between the (fake) electron and the
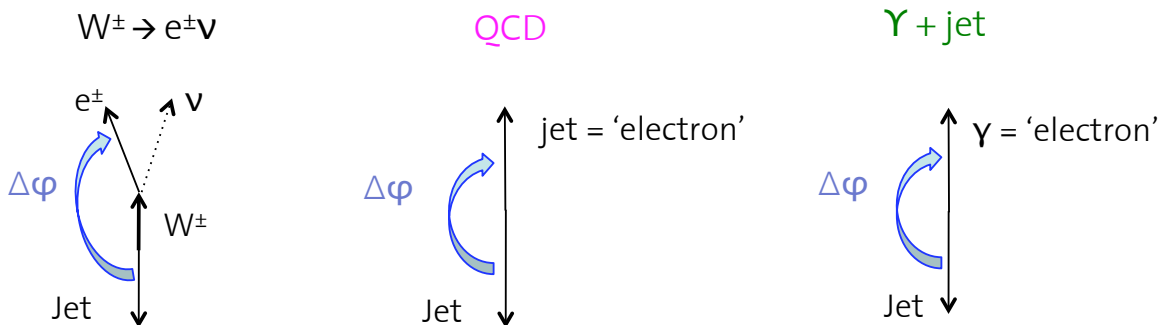
Figure 10.13.: The qualitative view of the kinematics of signal and important backgrounds in the transverse plane. $\Delta\phi$ denotes the angle between in the jet and the selected (fake) electron in the event.
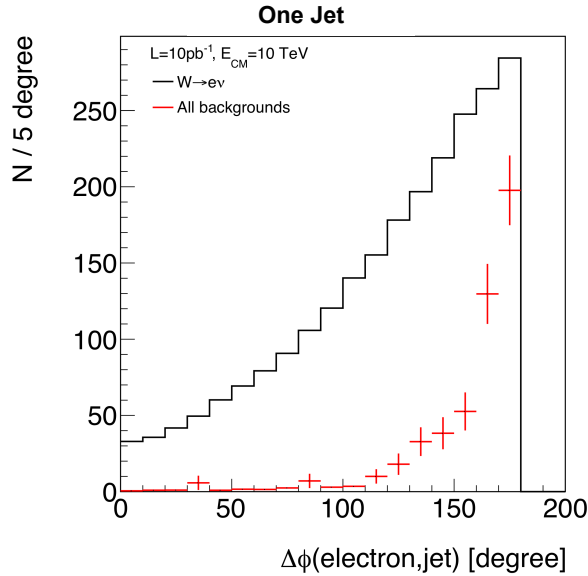
Figure 10.14.: The angle $\Delta\phi$ between the electron candidate and the jet transverse momenta for the signal and the sum of all backgrounds. Events with exactly one jet with $p_T > 30\,\text{GeV}$, one electron with $E_T > 25\,\text{GeV}$, *calorimeter MET* $> 30\,\text{GeV}$, and $M_T > 60\,\text{GeV}$ were selected.

jet transverse momenta for the signal and all background events after applying all cuts discussed before. As expected, the distribution of $\Delta\phi$ peaks at 180° for the backgrounds, while it is much smoother for the signal.

The angle $\Delta\phi$ is obviously dependent on the transverse momentum of the W boson. Due to the Lorentz boost of the W system, the transverse angle between the electron and the W boson transverse momentum vector goes to zero with an increasing W boson p_T. Accordingly, the angle between the electron and the jet goes to 180°. Figure 10.15 shows $\Delta\phi$ as a function of the jet p_T (left side) and of the electron E_T (right side) for signal and backgrounds with one jet after all cuts. As can be seen from both scatter plots, $\Delta\phi$ increases with the jet or the electron p_T. At the same time, the background fades out for high p_Ts. Thus, an electron or jet p_T dependent $\Delta\phi$ cut might improve the selection further, especially once sufficient statistics of data are available.

However, it was found that for the considered integrated luminosity of $10\,\text{pb}^{-1}$, aimed for in this analysis, a constant cut on $\Delta\phi$ is sufficient. According to the distribution in Figure 10.14, a maximum $\Delta\phi$ of 160° is required for the one jet case. Table 10.4 shows the effect of the cut on signal and the various background events with one jet. The resulting relative cut efficiency is 75% for the signal and 35% for all backgrounds. The signal to background ratio increased from 4.5 to 10. It is important to mention, that the $\Delta\phi$ cut was developed in the frame of this thesis and represents a new approach for the
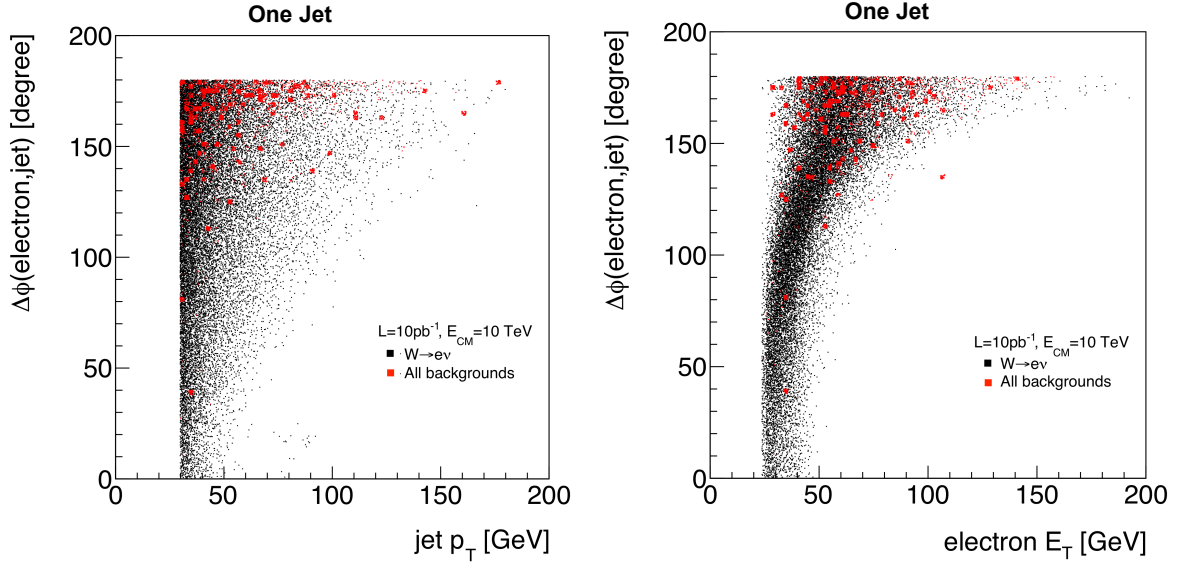
Figure 10.15.: $\Delta\phi$ as function of the jet p_T (left side) and the electron E_T (right side) for signal and the sum of all backgrounds. Events with exactly one jet with $p_T > 30\,\text{GeV}$, one electron with $E_T > 25\,\text{GeV}$, *calorimeter MET* $> 30\,\text{GeV}$, and $M_T > 60\,\text{GeV}$ were selected.

Process	Before $\Delta\phi < 160°$ cut	After $\Delta\phi < 160°$ cut
$W^{\pm} \to e^{\pm}\nu$	2 371	1822
$W^{\pm} \to \tau^{\pm}\nu$	30	24
$t\bar{t}$	9	8
$Z/\gamma* \to e^+e^-$	56	24
QCD	329	104
$\gamma + jet$	105	23
All backgrounds	529	183
Signal/background	4.5	10

Table 10.4.: Performance of the $\Delta\phi$ cut for signal and background events with one jet and for $\mathcal{L} = 10\text{pb}^{-1}$. Events with exactly one jet with $p_T > 30\,\text{GeV}$ and $|\eta| < 2.5$, one electron with $E_T > 25\,\text{GeV}$ and $|\eta| < 1.44$, *calorimeter MET* $> 30\,\text{GeV}$, and $m_T > 60\,\text{GeV}$ were selected.

selection of W boson events. The cut could only be introduced due to the separation of the events according to their jet multiplicity, which was also firstly performed in the this thesis.

10.2.3. A background determination method

Once data will be available, the different background contributions have to be determined and subtracted from the selected events. Methods to determine the most important background contributions are briefly discussed in the following. As already mentioned, the main backgrounds in the zero jet case are $W^{\pm} \to \tau^{\pm}\nu$ and QCD events. In the one jet case, QCD and $\gamma + jet$ events are the main contributions.

To correct for the $W^{\pm} \to \tau^{\pm}\nu$ background, one assumes lepton universality, e.g. the indentical branching ratios for the W decays to a τ or an electron. This assumption was confirmed by the LEP experiments. Thus, the relative background contribution of $W^{\pm} \to \tau^{\pm}\nu$ events (with $\tau^{\pm} \to e^{\pm}\nu_e\nu_\tau$) found in the Monte Carlo study can directly be used for the measurement with data. The background contributions of (1.2±0.1)% and (1.3±0.3)% in the cases with zero and one jet, respectively, can then simply be subtracted.

The contribution of the QCD and $\gamma + jet$ processes, where a fake electron is present, can be determined by enhancing the number of background events through loosening the electron selection. A similar method was already used in Section 9.4. In this particular case, the electron is not required to be isolated in the tracker. As explained in Section 7.2, the tracker isolation variable is defined as the ratio of transverse momentum sum of all well reconstructed tracks within a cone of $\Delta R = 0.5$ around the electron candidate, and the candidate's super-cluster energy $E_T^{electron}$

$$\text{Isolation(Tracker)} = \sum_{\Delta R < 0.5} p_T^{Tracker} / E_T^{electron}. \tag{10.3}$$

Figure 10.16 shows the distribution of the tracker isolation variable for electron candidates from the signal and the QCD and $\gamma + jet$ backgrounds for the zero jet case (left side) and the one jet case (right side). Here, all other electron selection and W selection cuts except the one on the tracker isolation variable were applied. As expected from Section 7.2.1, the fake electrons in the background samples are less isolated than the true signal electrons: The distribution of signal electrons peaks at zero, while that of the background electrons shows a flat shape. The dip, which is observed in the second bin of each distribution, is due to the H/E cut applied in the electron reconstruction (Section 7.1.3).

As discussed in Section 7.2, a maximal tracker isolation variable of 0.1 is required by the electron selection. Thus, with data the aim is to determine the number of background events in the first five bins of the distributions, the *signal region*, using a *data-driven*
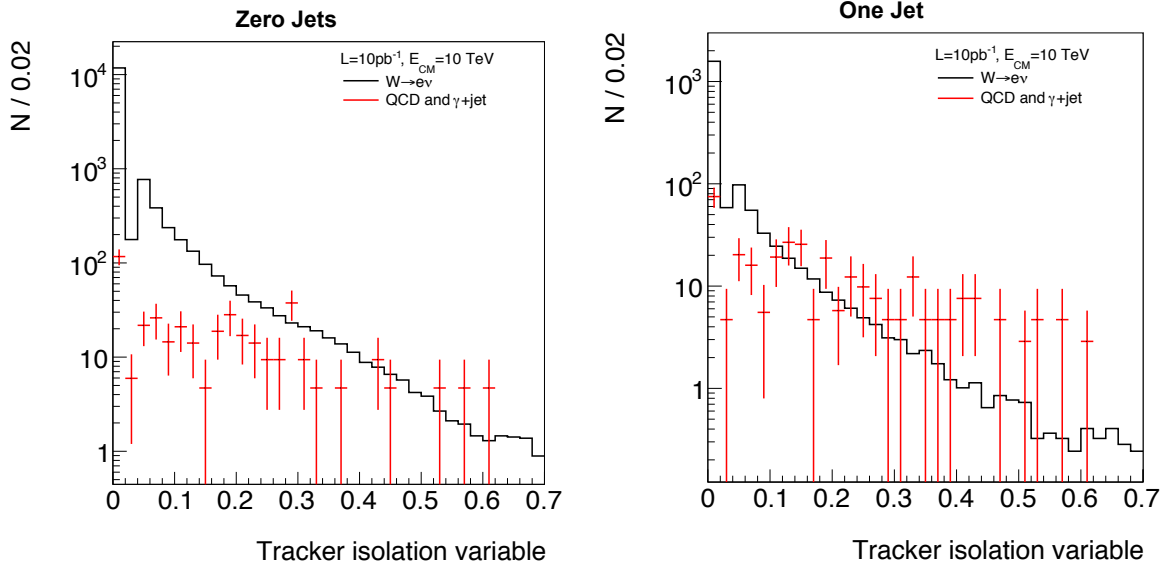
Figure 10.16.: Electron tracker isolation variable of zero (left side) and one jet events (right side), which passed all electron and W selection cuts except the tracker isolation.

method. As can be seen, the background contribution in the zero jet case is already small ($\sim 1\%$) and is therefore neglected in the following.

In the one jet case, the data-driven background determination uses the distribution of the isolation variable. In particular, the number of background events in an almost signal free background normalization region is extrapolated to the signal region. Here, the background normalization region is chosen to be $0.4 - 0.6$. 45 background events are found in that region, while the number of background events in the signal region is 122. Thus, once data are available, the number of events found in the background normalization region have to by multiplied by 122/44 to obtain the common QCD and $\gamma + jet$ background contribution.

In addition, 7 signal events were found in the background normalization region. They can either be ignored due to the low statistics, or be subtracted using Monte Carlo simulations. If these signal events are ignored, the calculated background contribution in the signal region could be considered as an upper limit.

10.2.4. On-shell W selection

In addition to the W and Z bosons, which are produced at the resonance masses of $m_W = 80.4\,\text{GeV}$ and $m_W = 91.2\,\text{GeV}$, so-called virtual W and Z bosons are observed. For this analysis, only W and Z bosons with a "on-shell" mass are considered as signal
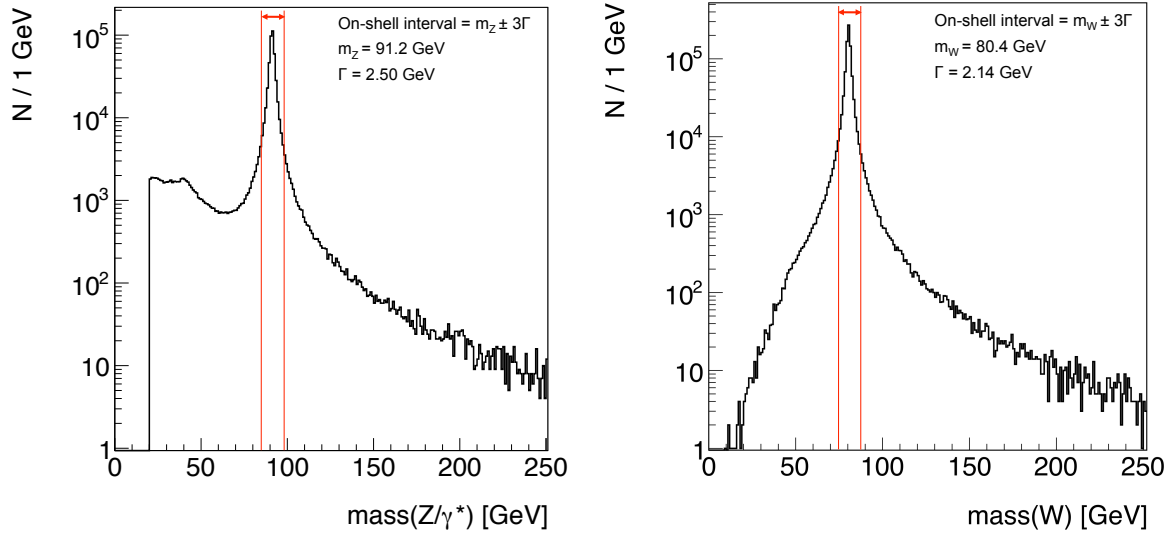
Figure 10.17.: The generated mass of $W^{\pm} \to e^{\pm}\nu$ and $Z/\gamma^{*} \to e^{+}e^{-}$ events, where one and two electrons were generated with $E_T > 25\,\mathrm{GeV}$ and $|\eta| < 1.44$, respectively. The red lines mark the on-shell W/Z bosons mass intervals.

events. A W or Z boson is here defined as on-shell, if it has a mass within the interval of $m_{W/Z} \pm 3\Gamma$, where $\Gamma_W = 2.141\,\mathrm{GeV}$ and $\Gamma_Z = 2.495\,\mathrm{GeV}$ are the decay widths of the W and Z bosons [9]. The remaining W and Z bosons, which have higher or lower masses, are called "off-shell".

Figure 10.17 shows the generated masses of $W^{\pm} \to e^{\pm}\nu$ and $Z/\gamma^{*} \to e^{+}e^{-}$ events, with one and two generated electrons with $E_T > 25\,\mathrm{GeV}$ and $|\eta| < 1.44$, respectively. In addition, the on-shell mass intervals are indicated. The comparison shows, that the mass distribution of the $Z^{(*)}$ bosons superimposes with that of γ^{*}s. Since the production cross-section of γ^{*} diverges at $0\,\mathrm{GeV}$, the Z/γ^{*} Monte Carlo sample used here requires a minimum Z/γ^{*} mass of $20\,\mathrm{GeV}$. Here, this divergence can however not be observed: the invariant distribution flattens for masses below $40\,\mathrm{GeV}$ due to the minimum electron E_T requirement. The W boson mass distribution does not show a divergent behavior, since no (charged) counterpart to the γ^{*} was observed so far.

When $Z/\gamma^{*} \to e^{+}e^{-}$ events are reconstructed in data, the invariant mass of the two electrons can also be reconstructed. One usually concentrates on on-shell Z bosons by applying a selection cut of $\pm 3\Gamma$ to the reconstructed Z boson mass (Section 10.3). Since this analysis compares the W and Z bosons in many ways, only on-shell W bosons are used in the following. However, due to the escaping neutrino, the W boson mass cannot be reconstructed, as described in Section 10.2.1. Thus, to predict and subtract the
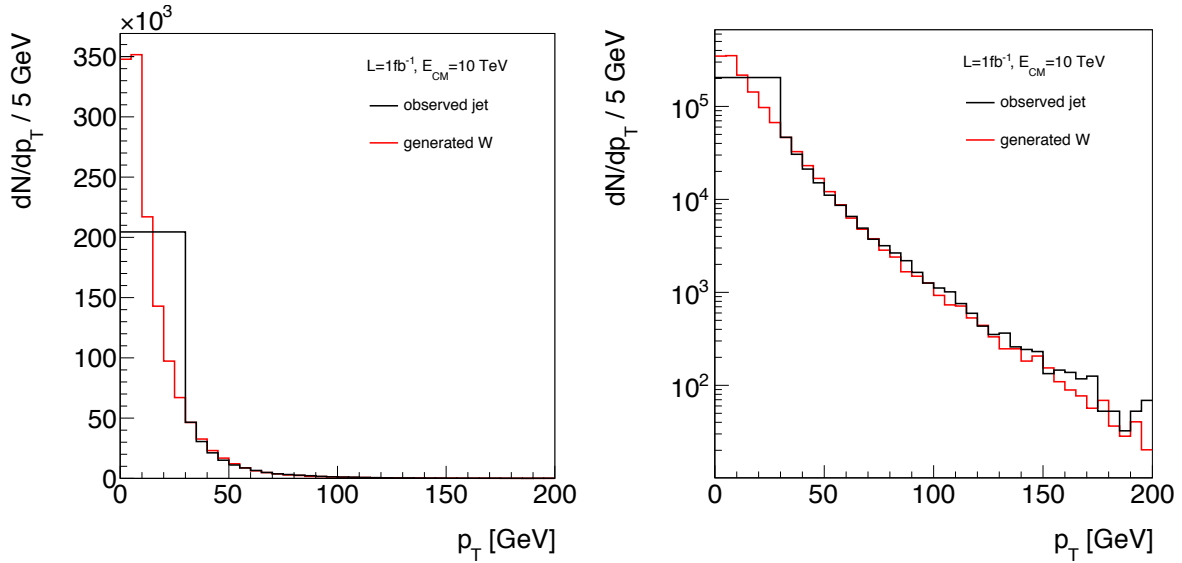
Figure 10.18.: The transverse momenta of the reconstructed jets and the generated W bosons on a linear (right side) and a logarithmic scale (left side). All $W^\pm \to e^\pm \nu$ events, which passed the W selection were used. Since no jets were reconstructed below 30 GeV, the first bin of the jet p_T distribution refers to the $W^\pm \to e^\pm \nu$ events with zero jets.

contribution of the off-shell W bosons in data, one relies on the theoretical shape of the Monte Carlo study.

Here, the remaining off-shell W boson contributions after all cuts are 8.0% in the *W+zero jets* case, and 9.1% for the *W+one jet* case. These events are subtracted from the $W^\pm \to e^\pm \nu$ events for the study in the following section.

10.3. W-boson transverse momentum

This section presents a method to measure the transverse momentum spectrum of the W boson, as motivated in Section 10.1. Since the transverse momentum of the W is not directly accessible due to the escaping neutrino, one makes use of the transverse momentum balance in $W^\pm \to e^\pm \nu$ events, where one jet is present. In particular, the p_T of the jet balances that of the W boson and approximates it. As before, only jets found with the *SisCone5* algorithm, a corrected p_T of 30 GeV, and $|\eta| < 2.5$ were counted.

Using the $W^\pm \to e^\pm \nu$ events, which were selected as described in the previous sections, the spectra of the observed jet p_T and the generated W boson p_T are compared in Figure 10.18 for large statistics ($\mathcal{L} = 1\,\text{fb}^{-1}$) at $E_{CM} = 10\,\text{TeV}$. The left and right side of the figure show the same distributions on a linear and logarithmic scale, respectively. As can be seen, the jet p_T spectrum matches the one of the W boson well above 30 GeV.
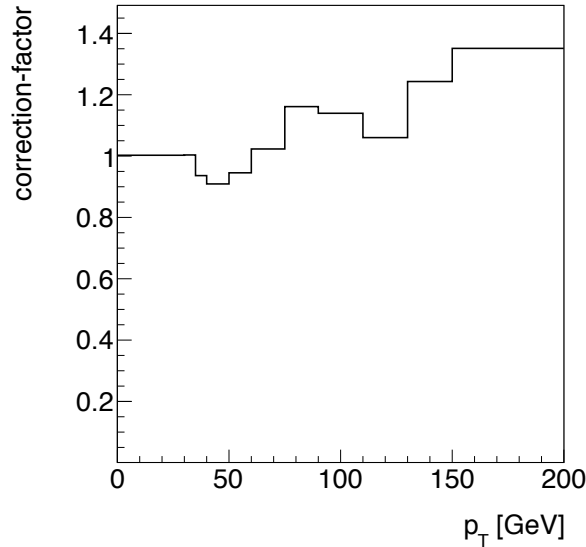
Figure 10.19.: The ratio of the jet and W boson transverse momenta distributions from Figure 10.18.

The $W^{\pm} \to e^{\pm}\nu$ events with zero jets are represented by the first bin in the jet p_T distribution (0-30 GeV) and the number of reconstructed zero jet events of 12 277 matches the number of the generated W bosons with a p_T below 30 GeV of 12 237 within 0.3%.

To compare the p_T distributions in more detail, Figure 10.19 shows the ratio of the p_T distributions of jets and W bosons from Figure 10.18. The binning was chosen such that sufficient statistics in every p_T bin up to 200 GeV is obtained. The single entries of the ratio distribution are denoted as "correction-factors" in the following. As can be seen, the transverse momenta of the jets and the W bosons do not match perfectly, since the correction-factors are generally not equal to one. The reason is the imperfect measurement of the jet p_T, as explained in Section 8.1.2.

It is important to mention, that the correction-factors presented here were produced using the full statistics of a 2.16 million $W^{\pm} \to e^{\pm}\nu$ sample, corresponding to $\mathcal{L} \approx 250 \, \mathrm{pb}^{-1}$. Once data are available, these Monte Carlo corrections-factors can be used to obtain the correct W p_T spectrum from the measured jet p_T spectrum. In particular, the single entries of the measured jet p_T spectrum will be divided by the corresponding Monte Carlo correction-factor.

In the following it is illustrated, how a measurement of the W transverse momentum spectra should look like with an integrated luminosity of $10 \, \mathrm{pb}^{-1}$ at $E_{CM} = 10 \, \mathrm{TeV}$[1]. Therefore, a pseudo-data sample of 87k $W^{\pm} \to e^{\pm}\nu$ events was used. Figure 10.20 shows the p_T spectra of the expected W bosons, e.g. from the 2.1 million $W^{\pm} \to e^{\pm}\nu$ events

---

[1] Corresponding to roughly $20 \, \mathrm{pb}^{-1}$ at $E_{CM} = 7 \, \mathrm{GeV}$.
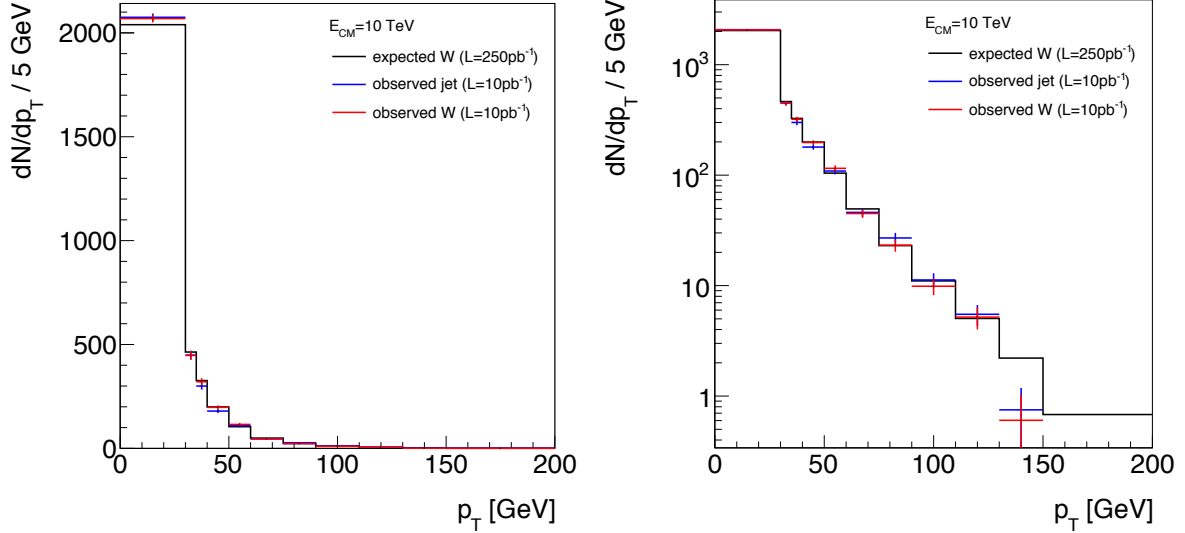
Figure 10.20.: The p_T spectrum of the expected W bosons from the 2.16 million $W^{\pm} \to e^{\pm} \nu$ sample (L=250 pb^{-1}) and the p_Ts of the observed jets and W bosons from a pseudo-data (L=10 pb^{-1}) sample on a linear (left side) and a logarithmic scale (left side). The observed W p_T spectrum is obtained from the jet p_T by the bin-wise multiplication with the correction-factors from the full statistic Monte Carlo sample shown in Figure 10.19.

sample, and those of the observed jets and observed W bosons in the pseudo-data sample. The observed W p_T spectrum is obtained from the jet p_T by the bin-wise division by the correction-factors from the large statistic Monte Carlo sample. The distributions on the left and right side of Figure 10.20 are the same on a linear and a logarithmic scale. As can be seen, the observed W p_T spectrum matches the expected one quite well. According to the distributions, measurable numbers of W bosons can be expected up to a transverse momentum of $\sim$130 GeV. For transverse momenta below 75 GeV, the statistical errors are below 5% for the considered integrated luminosity. As discussed in Section 10.1, the variation of the W p_T spectrum due to the uncertainty of the gluon PDFs is currently of the order of 5%. Thus, with only $\mathcal{L} = 10 \, \mathrm{pb}^{-1}$ at $E_{CM} = 10 \, \mathrm{TeV}$, one can start to constrain the gluon PDF with the W p_T measurement.

However, this method has an obvious dependance on the jet energy scale (JES) (Section 8.1.2). According to [75], the precision for the JES is expected to be $\pm 10\%$ for $\mathcal{L} = 10 \, \mathrm{pb}^{-1}$ at $E_{CM} = 7 \, \mathrm{TeV}$. The uncertainty of the presented W boson transverse momentum measurement is obviously similar.

But, as it was discussed in Section 8.1.2, one can determine the JES to a high precision using $Z \to e^+ e^-$ events, where an additional jet is present. In particular, the transverse momentum of the Z boson is balanced by the jet in the same way as for the W
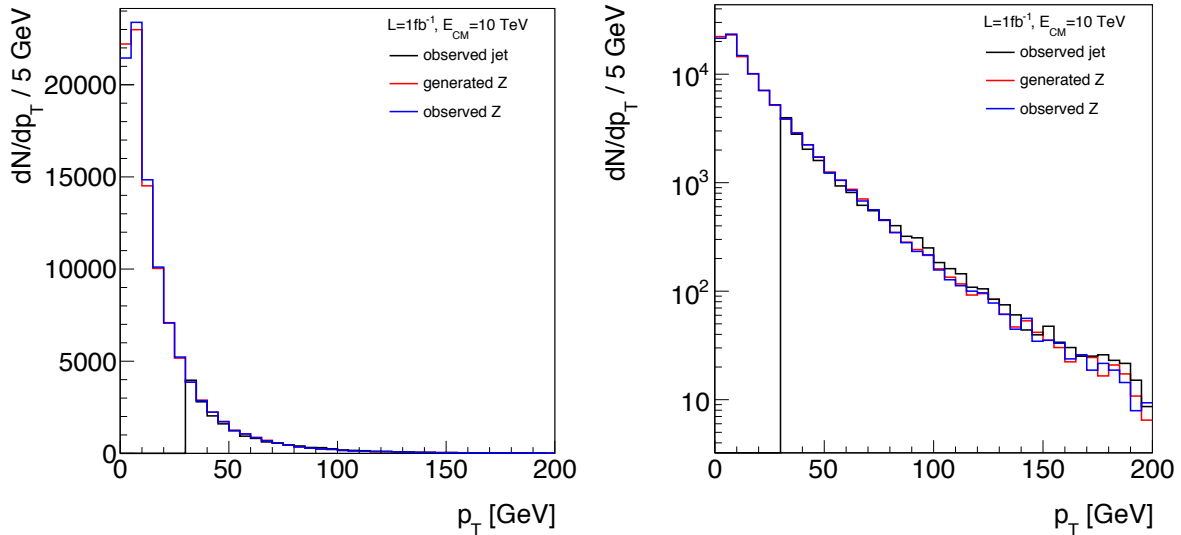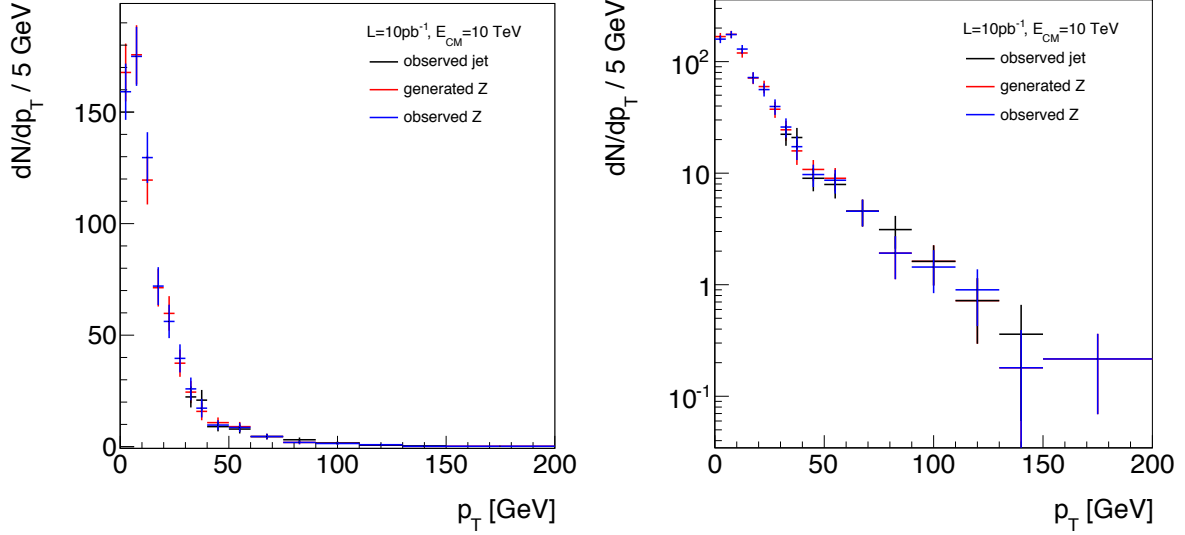
Figure 10.21.: The transverse momenta of the reconstructed jets and the generated and reconstructed Z bosons on a linear (left side) and a logarithmic scale (left side). The statistic corresponds to $\mathcal{L} = 1\,\mathrm{fb}^{-1}$ at $E_{CM} = 10\,\mathrm{TeV}$.

boson. However, the difference between Z and W bosons is, that the Z boson transverse momentum can be measured directly using the two charged electrons. Thus, the JES can be determined using the precise measurement of electron energies. This method is verified in the following. Here, $Z \rightarrow e^{+}e^{-}$ events were selected by the following criteria:

- 2 electrons that passed the electron selection with $E_T > 25\,\mathrm{GeV}$ and $|\eta| < 1.44$,

- a reconstructed Z mass within the on-shell interval: $83.8 < m_Z < 98.7\,\mathrm{GeV}$.

- For a better comparison with the $W^{\pm} \rightarrow e^{\pm}\nu$ events, events with zero or one reconstructed jet with a corrected $p_T > 30\,\mathrm{GeV}$ and $|\eta| < 2.5$ were required.

First, a high statistics $Z \rightarrow e^{+}e^{-}$ sample is used, which corresponds to an integrated luminosity of $1\,\mathrm{fb}^{-1}$ at $E_{CM} = 10\,\mathrm{TeV}$. Figure 10.21 shows the p_T spectra of the reconstructed jets, the generated and the reconstructed Z bosons on an linear (left side) and a logarithmic scale (right side). The distributions show a very good matching between the different p_T spectra. In particular, the Z p_T spectrum, which was reconstructed from the electron-positron pairs, is in excellent agreement with the generated one. In addition, as for the W bosons, the jet p_T describes the Z boson p_T well above $30\,\mathrm{GeV}$. Thus, $Z \rightarrow e^{+}e^{-}$ events can be used in data to verify the W p_T measurement using jets.

However, the leading order cross-section for the process $Z \rightarrow e^{+}e^{-}$ of $1\,\mathrm{nb}$ is roughly a factor of 10 smaller than $W^{\pm} \rightarrow e^{\pm}\nu$. To simulate, how the p_T spectra of $Z \rightarrow e^{+}e^{-}$ events might look like for $\mathcal{L} = 10\,\mathrm{pb}^{-1}$ at $E_{CM} = 10\,\mathrm{TeV}$, a pseudo-data sample of 20k

Figure 10.22.: The transverse momenta of the reconstructed jets and the generated and reconstructed Z bosons on a linear (left side) and a logarithmic scale (left side). The statistic corresponds to $\mathcal{L} = 10\,\text{pb}^{-1}$ at $E_{CM} = 10\,\text{TeV}$.

$Z \rightarrow e^{+}e^{-}$ events was used and the events were selected as above. Figure 10.22 shows the generated and reconstructed Z p_T spectra and the reconstructed jet p_T spectrum of these events. The binning was chosen accordingly to that of the W p_T measurement, and the left and right side of the figure show the distributions on a linear and a logarithmic scale, respectively.

As the figure shows, the reconstructed jet and Z boson p_T spectra matched that of the generated Z bosons, but the statistic errors were found to be rather large. Thus, with only $10\,\text{pb}^{-1}$ of integrated luminosity at $E_{CM} = 10\,\text{TeV}$, the Z p_T measurement can not be used as a tool for the high precision determination of the jet energy corrections. Nevertheless, the measurement of the Z boson p_T can prove the consistency of the assumed balance of the jet and W/Z boson transverse momenta.

10.4. Conclusions of this chapter

This chapter presented a Monte Carlo analysis of $W^{\pm} \rightarrow e^{\pm}\nu$ events for $\mathcal{L} = 10\,\text{pb}^{-1}$ at $E_{CM} = 10\,\text{TeV}$. As a new approach, the selection of these events was based on the separation into the cases, where either non or one jet was reconstructed. For simplicity, the selection of the events was identical in both cases. After the application of some simple cuts, the zero jet case was found to be quasi background free with a signal to background ratio of 36. For the case with one reconstructed jet, the different kinematics

of signal and background was exploited. Using a new cut on the angle between the electron and the jet in the transverse plane, the signal to background ratio could be increased from 4.5 to 10.

In addition, a method to measure the transverse momentum distribution of the W boson above 30 GeV was introduced. It was shown, how the measurement of the W boson p_T spectrum can be used to improve the knowledge of the gluon distribution functions. For the measurement, the balance between the transverse momenta of the W boson and the recoiling jet was used. The analysis showed, that already with $\mathcal{L} = 10\,\text{pb}^{-1}$ (or $\mathcal{L} = 20\,\text{pb}^{-1}$ at $E_{CM} = 7\,\text{TeV}$) a measurement of the transverse momentum of the W boson with sufficient statistics is possible up to $p_T = 130\,\text{GeV}$. The method represents a new approach to determine the W boson p_T with CMS. With the obtained statistics of the W p_T measurements, one starts to constrain the gluon distribution functions of the proton. The results of these studies were summarized in [92].

Chapter 11.

Conclusions and outlook

In December 2009, the first proton-proton collisions with a center-of-mass energies of 0.9 and 2.36 TeV were observed by the experiments at the LHC. The proton-proton collisions at $E_{CM} = 7$ TeV, which is the highest energy so far reached in a particle collision, were recorded in March 2010 and mark the start up of the physics research at the LHC. In the coming years, the crucial research topics are the search for the Higgs boson to complete the Standard Model and the searches for *Beyond Standard Model* physics.

Since the proton-proton collisions of the LHC produce enormous backgrounds, the search for the Higgs boson and *Beyond Standard Model* processes relies on the clean identification of electrons and the precise measurement of their kinematic properties. CMS uses a electromagnetic calorimeter made from 75 848 scintillation crystals to measure the energy of electrons and photons. This thesis described the integration, testing and performance of the readout electronics of the ECAL. In addition, an effective analysis tool based on pattern recognition was introduced to unambiguously identify and classify hardware problems found during the integration. This systematic investigation and the correction of the observed failures contributed significantly to the high rate of operational channels of over 99%, which has been stable over almost three years since the ECAL integration in Summer 2007. This reliable performance of the ECAL electronics and its low noise level of $\sim$40 MeV and $\sim$50 MeV in the barrel and end-caps, are essential for the upcoming challenges at the LHC.

Based on the measurements of the CMS ECAL and tracker, an efficient and simple electron selection was presented for isolated high-energy electron candidates in the barrel part of the ECAL. A Monte Carlo analysis of the electron selection gave a very low fake rate of $\sim$10^{-4} and a high electron efficiency of $\sim$70%. This simple and effective electron selection will be useful tool for the selection of various physics processes, which rely on the identification of electrons.

The electron selection was applied to a study of the Higgs boson search in the decay channel $Higgs \rightarrow W^+W^- \rightarrow e^+\nu e^-\bar{\nu}$ and for a mass between 155 and 180 GeV. In particular, the background process $W^\pm X \rightarrow e^\pm \nu X$, where X (jet or photon) fakes an electron, is important due to its high cross-section. However, the proposed electron selection was found to reduce this background considerably. Hereby, two different methods were introduced to determine the background in the frame of a Monte Carlo analysis. A factorization approach was used, where the kinematics of the events and the electron efficiency and fake rate were considered to be independent. Both methods agreed and predicted a signal to background ratio of 3.6 fb / 0.2 fb $\approx$ 18 for $E_{CM} = 10$ TeV. This ratio was found to be sufficiently low compared to the irreducible background processes and it proves the efficiency of the proposed electron selection.

Finally, the performance of the electron identification was exploited for the selection of inclusive $W^\pm \rightarrow e^\pm \nu$ events within the ECAL barrel. Hereby, a new approach was introduced, which separated the events according to their jet activity. In the case with zero jets, the Monte Carlo based analysis predicted about 13 000 $W^\pm \rightarrow e^\pm \nu$ events with almost no background contribution for an integrated luminosity of $10(20)$ pb^{-1} at $E_{CM} = 10(7)$ TeV. For the case with one jet, roughly 2 000 signal events were expected with a background contribution of $\sim$10%. Events with more jets were ignored due to their low signal rate and the low signal to background ratio of less than 1.

Furthermore, it was shown that the p_T of the W boson has a certain dependance on the gluon distribution functions of the proton. Since the current uncertainty on the gluon PDFs is of the order of 5%, the measurement of the W boson p_T spectrum with sufficient statistics can be used to constrain gluon PDFs at the LHC energies. To measure the transverse momentum of the W boson, a method that exploits momentum conservation in W+jet events (with $W^\pm \rightarrow e^\pm \nu$) was introduced. Hereby one relies on the precise momentum measurement of the jet recoiling the W boson. It was shown, how the crucial jet energy scale can be determined using inclusive $Z \rightarrow e^+e^-$ events. According to the presented study, one can start to improve the precision of the gluon PDFs with the presented W boson p_T measurement and an integrated luminosity of 10 pb^{-1} at $E_{CM} = 10$ TeV.

A further perspective of the presented electron analysis is most importantly the verification of the performance of the electron selection with LHC data. The next step should be the extension of the electron selection to the end-caps of the ECAL, i.e. to pseudorapitities of $1.44 < |\eta| < 2.5$. In the end-caps, however, the systematics errors are expected to be different compared to the barrel due to the presence of the ECAL pre-

shower detector. These errors and the electron efficiency and fake rate for the end-caps have to be studied in detail.

With the data that are expected to be collected during the year 2010, one can perform the measurement of the W boson p_T spectrum and compare it with the Monte Carlo predictions of this thesis. In particular, for an integrated luminosity of $20\,\mathrm{pb}^{-1}$ at $E_{CM} = 7\,\mathrm{TeV}$, the p_T spectrum of the W boson can be determined with a precision of $\sim 5\%$ and sufficient statistics up to a value of $\sim 130\,\mathrm{GeV}$. Thus, starting with this data sample, it should be possible to constrain the gluon PDFs to a precision, which is higher than the current values.

Furthermore, the presented W boson analyses have to be adapted for W bosons, which are found in the ECAL end-caps using an extended version of the electron selection. In addition, one can apply the same selection to W bosons decaying to muon-neutrino pairs to increase statistics and to cross check the results from the electron case.

Appendix A.

Good health check of February 2010

This section shows the results of the *Good Health Check* performed in February 2010 for ECAL barrel and end-caps. The errors that were found in these test runs are summarized in Section 6.5. Figure A.1 displays the distributions of the mean pedestals measured in all three gains for barrel (left side) and end-caps (right side). The distributions show the plateau shape already known from former test runs (Section 5.2). Figure A.2 shows the distributions of the pedestal RMSs for all gains for barrel (left side) and end-caps (right side). The channels with a high RMS are considered as noisy according to the limits shown in Tables 6.4 and 6.5. The distributions of the mean test pulse amplitudes for all gains for barrel (left side) and end-caps (right side) are displayed in Figure A.3. All distribution show the expected Gaussian shape. Figure A.4 shows the distributions of the laser mean amplitudes for the channels of the barrel (left side) and the end-caps (right side). The shape is not perfectly Gaussian since not all crystals were inter-calibrated, yet. The comparison of the presented results with the *Good Health Check* distributions from the 2009 data showed only minor differences.
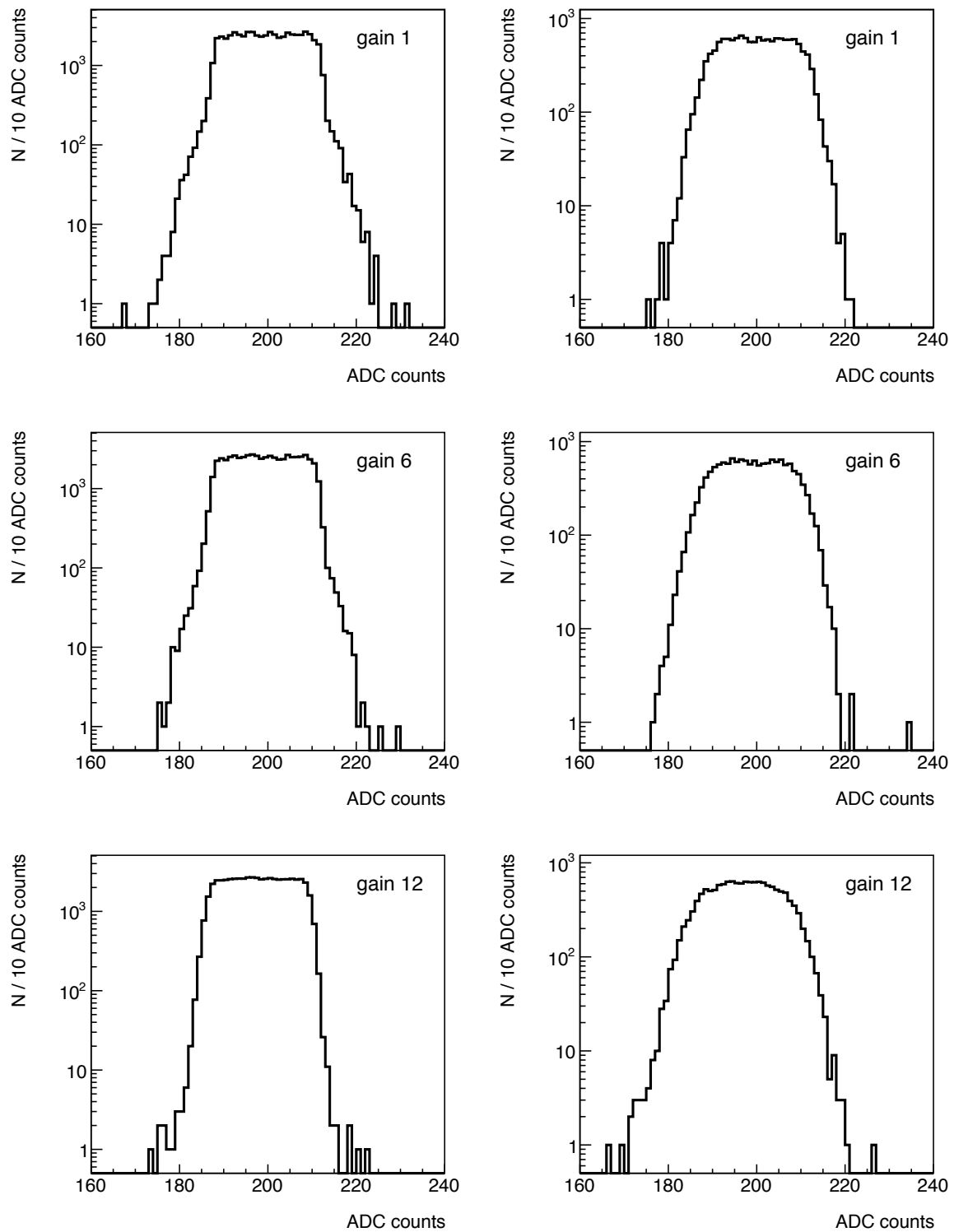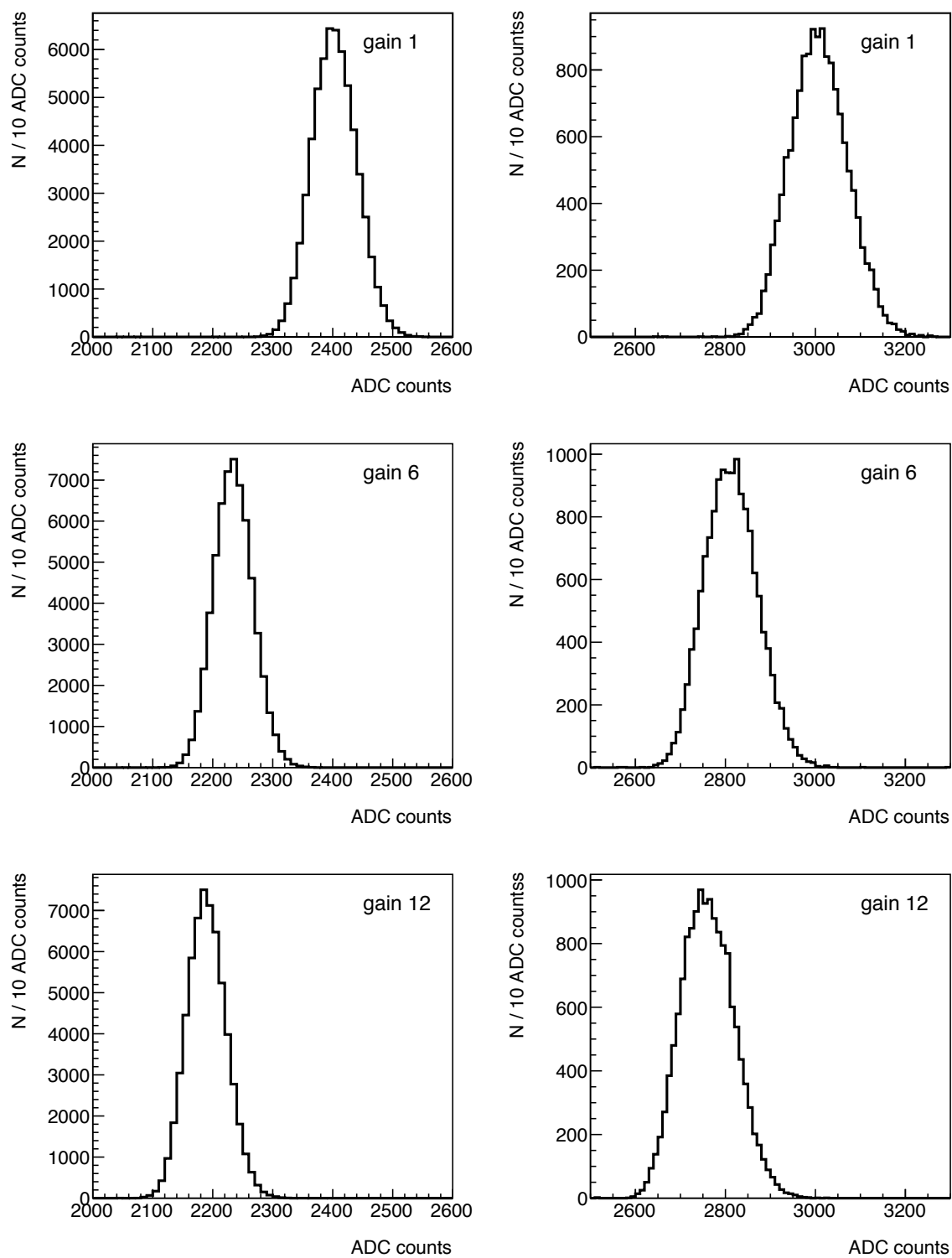
Figure A.1.: *Good health check* February 2010: Pedestal mean distributions for barrel (left side) and end-caps (right side).
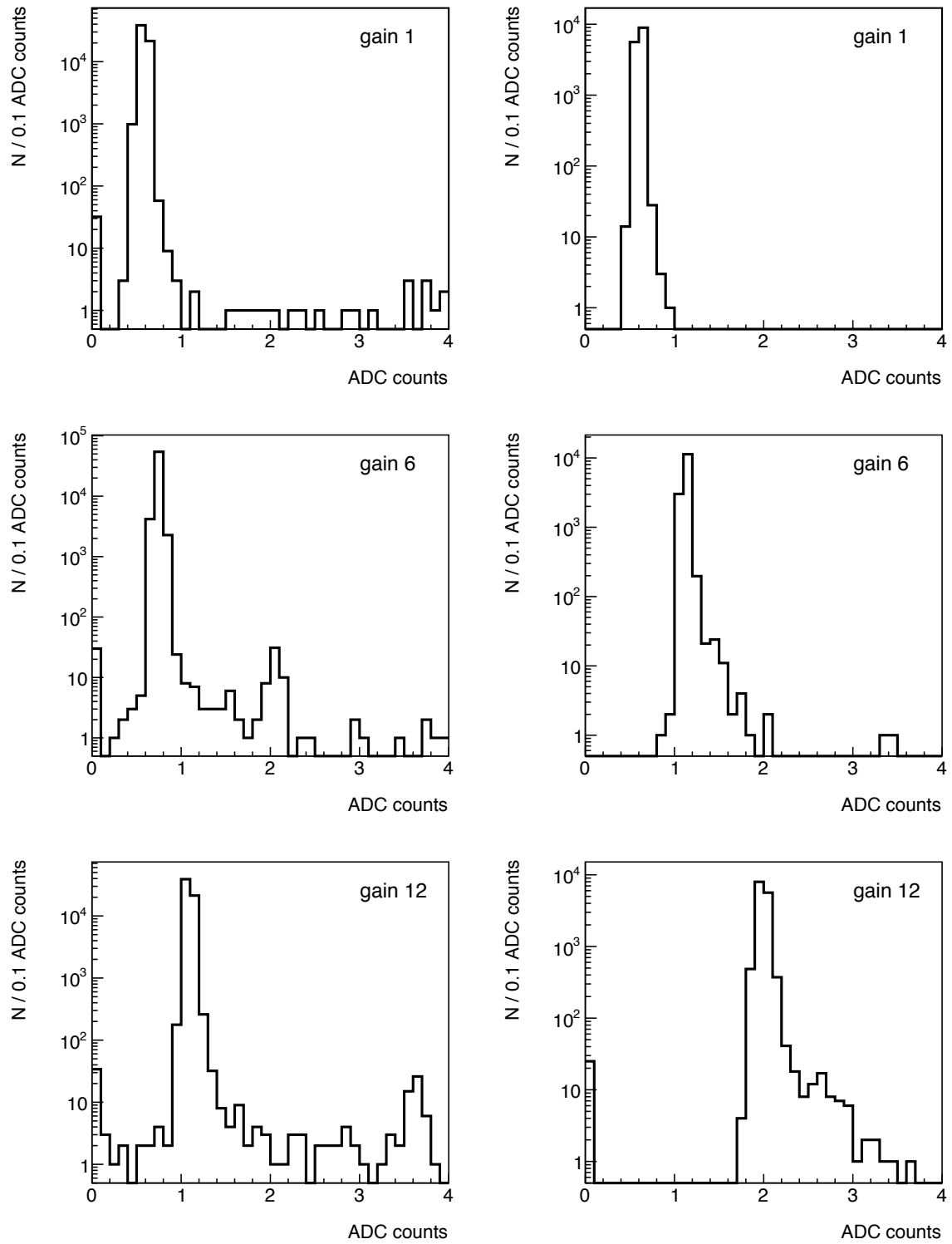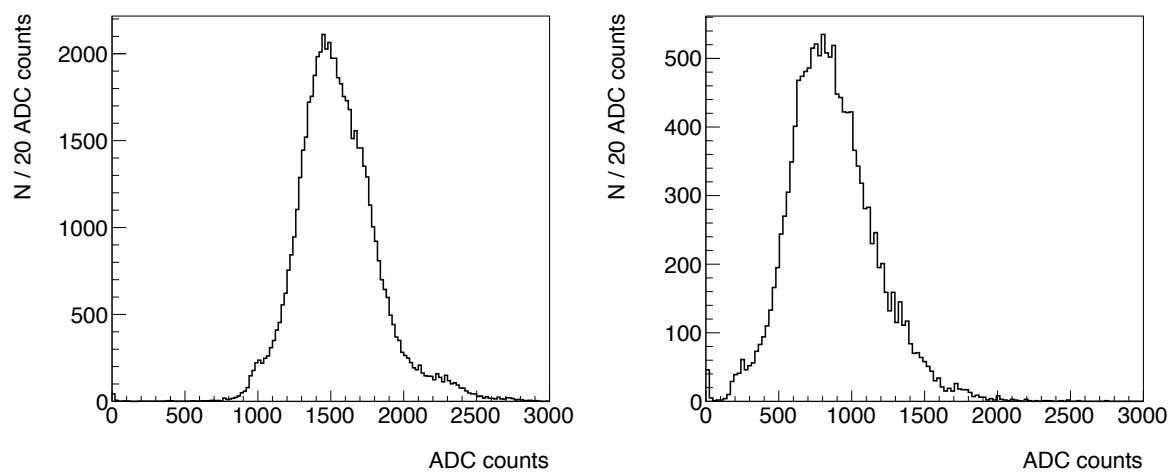
Figure A.2.: *Good health check* February 2010: Pedestal RMS distributions for barrel (left side) and end-caps (right side).

Figure A.3.: *Good health check* February 2010: Test pulse distributions for barrel (left side) and end-caps (right side).

Figure A.4.: *Good health check* February 2010: Laser pulse amplitude distributions for barrel (left side) and end-caps (right side).

Bibliography

[1] The Particle Data Group, http://pdg.lbl.gov.

[2] F. Halzen and A. Martin, *Quarks and Leptons*, John Wiley&Sons, Jan. 1984.

[3] L. M. Brown, M. Dresden, L. Hoddeson and M. Riordan, *The Rise of the Standard Model*, Cambridge University Press, 1995.

[4] M. E. Peskin and D. V. Schroeder, *An Introduction to Quantum Field Theory*, Perseus Books, 1995.

[5] S. Mele, *Measurements of the Running of the Electromagnetic Coupling at LEP*, arXiv:hep-ex/0610037 .

[6] The LEP Electroweak Working Group, *Precision Electroweak Measurements and Constraints on the Standard Model*, http://lepewwg.web.cern.ch/LEPEWWG/stanmod/summer2009/s09_ew.pdf (2009).

[7] The LEP Electroweak Working Group, http://lepewwg.web.cern.ch/LEPEWWG/.

[8] M. Goldhaber, *Helicity of Neutrinos*, Phys. Rev. **109**(1015-1017) (1958).

[9] Particle Data Group, *The Review of Particle Physics*, Physics Letters B **667** (2008).

[10] G. Dissertori, I.K. Knowles, M. Schmelling, *Quantum Chromodynamics: High energy experiments and theory*, Oxford University Press, 2003.

[11] Richard P. Feynman, Proceedings of the 3rd Topical Conference on High Energy Collision of Hadrons (1969).

[12] MSTW group, Parton distribution functions, http://projects.hepforge.org/mstwpdf/plots/plots.html .

[13] H1 and ZEUS Collaborations, *Combined Measurement and QCD Analysis of the Inclusive ep Scattering Cross Sections at HERA*, arXiv:hep-ex/0911.0884 (2009).

[14] ALEPH, DELPHI, L3, OPAL, and the LEP Working Group for Higgs Boson Searches: D. Abbaneo et al., *Search for the Standard Model Higgs Boson at LEP*, Physics Letters B **565**(61) (2003).

[15] M. Dittmar, *If the Higgs mass is … or "What might be known by 2016"*, http://physikseminar.desy.de/hamburg/seminars_in_2010/feb_9_2010/ .

[16] The Large Hadron Collider, http://lhc.cern.ch/lhc.

[17] S. Martin, *A Supersymmetry Primer*, arXiv:hep-ph/9709356 (2008).

[18] G. Arnison et al., *Experimental observation of lepton pairs of invaiant mass around 95 GeV/c2 at the CERN Sp$\bar{p}$S collider*, Physics Letters B **126**(5), 398–410 (1983).

[19] G. Arnison et al., *Experimental obervation of isolated large transverse energy electrons with associated missing energy at E=540 GeV*, Physics Letters B **122**(1), 103–116 (1983).

[20] The LHC study group, *The Large Hadron Collider, Conceptual Design*, CERN/AC (Oct. 1995).

[21] The CMS collaboration, *The CMS experiment at the CERN LHC*, JINST **3**(S08004) (2008).

[22] The ATLAS Experiment, http://atlas.ch.

[23] The Large Hadron Collider beauty experiment, http://lhcb.web.cern.ch/lhcb.

[24] A Large Ion Collider Experiment, http://aliceinfo.cern.ch.

[25] Total Cross Section, Elastic Scattering and Diffraction Dissociation at the LHC, http://totem.web.cern.ch/Totem/.

[26] LHC forward experiment, http://www.stelab.nagoya-u.ac.jp/LHCf/LHCf/index.html.

[27] The CMS collaboration, *The Compact Muon Solenoid, Technical Proposal*, CERN/LHCC **38** (1994).

[28] The Compact Muon Solenoid Experiment, http://cms.cern.ch.

[29] The CMS collaboration, *The Tracker Project, Technical Design Report*, CERN/LHCC (Apr. 1998).

[30] The CMS collaboration, *The Electromagnetic Calorimeter Project, Technical Design Report*, CERN/LHCC **33** (1997).

[31] The CMS collaboration, *The Hadron Calorimeter, Technical Design Report*, CERN/LHCC **31** (June 1997).

[32] The CMS collaboration, *The Magnet Project, Technical Design Report*, CERN/LHCC **10** (May 1997).

[33] The CMS collaboration, *The Muon Project, Technical Design Report*, CERN/LHCC **32** (Dec. 1997).

[34] The CMS collaboration, *The TriDAS Project, Technical Design Report, Volume 1: The Trigger Systems*, CERN/LHCC **38** (Dec. 2000).

[35] W. Lustermann on behalf of the CMS ECAL Collaboration, *The CMS Crystal Calorimeter*, Proceedings IEEE IMTC **2**, 1251–1256 (May 2004).

[36] P. Roldan, *Status of the PWO Crystal production for the Electromagnetic Calorimeter of CMS and of its construction*, Proceedings of 7th International Conference on Inorganic Scintillators and Industrial Applications (2003).

[37] P. Lecomte et al., *High-energy proton induced damage study of scintillation light output from PbWO4 calorimeter crystals*, Nuclear Instruments and Methods in Physics Research **A 564**, 164 (2006).

[38] J. Grahl et al., *Radiation hard avalanche photodiodes for CMS ECAL*, Nuclear Instruments and Methods in Physics Research **A 504**, 44–47 (2003).

[39] K. Bell et al., *The development of vacuum phototriodes for the CMS electromagnetic calorimeter*, Nuclear Instruments and Methods in Physics Research **A 469**, 29–46 (2001).

[40] K. Deiters et al., *Double screening tests of the CMS ECAL avalanche photodiodes*, Nuclear Instruments and Methods in Physics Research **A 543**, 549 (2005).

[41] Christina Biino et al., *The CMS ECAL Very Front End Electronics: production and tests*, CERN/LHCC **30**, 107–111 (2004).

[42] M. Hansen, *The New Readout Architecture for the CMS ECAL*, CERN/LHCC (2003).

[43] Botio Betev et al., *Low voltage supply system for the very front-end readout electronics of the CMS electromagnetic calorimeter*, CERN/LHCC **55**, 353–357 (2003).

[44] S. Dhawan et al., *CMS electromagnetic calorimeter low voltage system for the front end electronics*, Conference Record **2**, 1118–1122 (Oct. 2003).

[45] W. Hintz, *VFE Readout Electronics of the CMS Electromagnetic Calorimeter, Studies of the Performance*, Master's thesis, ETH Zurich, 2006.

[46] M. Raymond et al., *The MGPA Electromagnetic Calorimeter Readout Chip for CMS*, CERN-LHCC , 83–87 (2003).

[47] G. Minderico et al., *A CMOS low power, quad channel, 12 bit, 40 MS/s pipelined ADC for applications in particle physics calorimetry*, CERN-LHCC , 83–87 (2003).

[48] J. Rander, *The monitoring system for the CMS-ECAL*, Proceedings of Eighth International Conference on Calorimetry in High Energy Physics, Lisbon (Portugal) (June 1999).

[49] R. Alemany et al., *Overview of the ECAL off-detector electronics of the CMS experiment*, IEEE Nucl. Sci. Symp. Conf. Rec. **2**, 1053 (2004).

[50] P. Milenovic et al., *The Detector Control System for the electromagnetic calorimeter of the CMS experiment at LHC*, CMS CR-2007/059 .

[51] Werner Lustermann, *Ausleseelektronik, Trigger, Data Acquisition, and Simulation (Geant)*, http://www.ipp.phys.ethz.ch/education/lectures/hs08-empp/contents/wl_lec2a.pdf .

[52] W. Lustermann on behalf of the CMS ECAL Collaboration, *Installation and Test of the CMS Crystal Calorimeter Electronics*, CERN-2005-011 (2005).

[53] W. Hintz on behalf of the CMS ECAL Collaboration, *The CMS Electromagnetic Calorimeter detector control and monitoring system*, Nuclear Instruments and Methods in Physics Research **A 090** (2009).

[54] The CMS collaboration, *Intercalibration of the barrel electromagnetic calorimeter of the CMS experiment at start-up*, JINST **2**(P10007) (2008).

[55] R. Arcidiacono (On behalf of the CMS ECAL Group), *Studies of the CMS Electromagnetic Calorimeter performance in the electron test beam*, Journal of Physics: Conference Series **160**(012048) (2009).

[56] The CMS ECAL Group, *Energy resolution of the barrel of the CMS Electromagnetic Calorimeter*, JINST **2**(P04004) (2007).

[57] TS Division-Metallurgy and Metrology CERN/TS/MME/MM/AG, *Failure on PCB-CMS*, Unpublished, 2007.

[58] GS Präzisions AG, *Analysis Report ADP Flex for CMS*, Unpublished, 2007.

[59] B. Betev, K. Deiters and W. Hintz, *Radiation test of CMS ECAL motherboards*, Unpublished, 2008.

[60] http://cms.cern.ch/iCMS/jsp/page.jsp?mode=cms&action=url&urlkey=CMS_OFFLINE.

[61] E. Meschi et al., *Electron Reconstruction in the CMS Electromagnetic Calorimeter*, CMS Note 2001/034.

[62] W. Adam et al., *Electron Reconstruction in CMS*, CMS AN -2009/164.

[63] M. Pioppi et al., *Electron Pre-identification in the Particle Flow framework*, CMS AN 2008/032.

[64] W. Adam et al., *Reconstruction of electrons with the Gaussian-sum filter in the CMS tracker at the LHC*, J. Phys. G: Nucl. Part. Phys. **31**(N9-N20) (2005).

[65] W. Adam et al., *Track reconstruction in CMS tracker*, CMS Note 2006/41.

[66] M. Dittmar and W. Hintz, and C. Marchica, *Towards a simple, robust and clean electron selection for the $H \to W^+W^-$ search*, CMS AN-2009/134 .

[67] J. Allison et al., *Geant4 developments and applications*, Nuclear Science, IEEE Transactions on **53**(1), 270–278 (2006).

[68] S. Agostinelli et al., *Geant4-a simulation toolkit*, Nuclear Instruments and Methods in Physics Research **A 506**, 250–303 (2003).

[69] http://home.thep.lu.se/∼torbjorn/Pythia.html.

[70] M.Dittmar and A.-S. Giolo-Nicollerat, *Identifying central electrons in the CMS detector*, CMS IN-2004/036 .

[71] G.Soyez and G.Salam, *A practical Seedless Infrared-Safe Cone jet algorithm*, JHEP **05**(086) (2007).

[72] A. Bhatti et al., *Performance of the SISCone Jet Clustering Algorithm*, CMS AN-2008/002.

[73] *The SISCone Jet Algorithm*, http://projects.hepforge.org/siscone/.

[74] D. Dobur on behalf of the CMS Collaboration, *Jets and Missing Transverse Energy Reconstruction with CMS*, http://arxiv.org/abs/0904.0391v1 .

[75] A. Santocchia on behalf of the CMS Collaboration, *Jet Energy Corrections at CMS*, CMS CR -2009/314 (2009).

[76] M. Vazquez Acosta et al., *Jet and MET Performance in CMSSW_1_2_0*, CMS IN-2007/053 .

[77] M. Dittmar and H.K. Dreiner, *How to find a Higgs boson with a mass between 155 GeV-180 GeV at the LHC*, Phys. Rev. D. **55**(1) (1997).

[78] The CMS collaboration, *CMS Physics Technical Design Report*, CERN/LHCC 2006-021 **Vol II section 10.2.2**.

[79] G. Davatz, M. Dittmar and A.-S. Giolo-Nicollerat, *Standard Model Higgs Discovery Potential of CMS in the $H \to WW \to \ell\nu\ell\nu$ Channel*, CMS NOTE-2006/047.

[80] G. Bauer et al., *Search Strategy for a Standard Model Higgs Boson Decaying to Two W Bosons in the Fully Leptonic Final State at $\sqrt{s} = 10$ TeV*, CMS AN-2009/139.

[81] G. Davatz and M. Dittmar, *Standard Model Higgs Discovery Potential of CMS in the* $H \rightarrow WW \rightarrow \ell\nu\ell\nu$ *Channel*, CMS NOTE 2006/047.

[82] F. Stoeckli, Calculation of the NNLO Higgs cross section for $M_H = 160\,\text{GeV}$ at $10\,\text{TeV}$ using MC@NLO and VV2Hat,
http://wwweth.cern.ch/HWWKFactor/node9.html .

[83] C.Anastasiou, R. Boughezal and F. Petriello, *Mixed QCD-electroweak corrections to Higgs boson production in gluon fusion*, JHEP **0904**(003) (2009).

[84] A.D. Martin, W.J. Stirling, R.S. Thorne and G. Watt, *Parton distributions for the LHC*,
http://xxx.lanl.gov/pdf/0901.0002 .

[85] G. Davatz, M. Dittmar, F. Pauss, *Simulation of a Cross Section and Mass Measurement of a SM Higgs Boson in the* $H \rightarrow WW \rightarrow \ell\nu\ell\nu$ *Channel at the LHC*, Phys. Rev. D. **76** (2007).

[86] M. Cacciari et al., *Updated predictions for the total production cross sections of top and of heavier quark pairs at the Tevatron and at the LHC*, arXiv:hep-ph/0804.2800 (2008).

[87] Cross section calculated using the program MCFM, http://mcfm.fnal.gov/.

[88] C. Anastasiou et al., Phys. Rev. D. **69**(094008) (2004).

[89] M. Dittmar et al., *Towards a precise parton luminosity determination at the CERN LHC*, Phys. Rev. D. **56**(11) (1997).

[90] T. Kasprzik, *Radiative Corrections to W+Jet Production at Hadron Colliders with a Leptonic Decay of the W Boson*, PhD thesis, Universität Freiburg, 2009.

[91] The Coordinated Theoretical-Experimental Project on QCD,
http://www.phys.psu.edu/∼cteq/.

[92] M. Dittmar, W. Hintz, C. Marchica and A.Sanchez, *Towards a precise measurement of the W and Z boson* p_T *spectrum with CMS*, CMS AN-2010/282 .

Acknowledgements

Curriculum Vitae

Name	Wieland Hintz
Date of Birth	18 November 1980
Nationality	German

Education

2006-2010	**CERN, Switzerland** PhD in Particle Physics, Group of Prof. F. Pauss, ETH Zurich
2001-2006	**ETH Zurich, Switzerland** Diploma in Experimental Physics
1991-2000	**Landschulheim Schloss Ising, Germany** Abitur

Scientific Publications and Talks

2010	**Towards a precise measurement of the W and Z boson p_T spectra with CMS** M. Dittmar, W. Hintz, C. Marchica and A.Sanchez CMS AN-2010/282
2009	**Towards the transverse momentum measurement of the W boson with CMS** W. Hintz Joint Annual Meeting of ÖPG/SPS/ÖGAA
2009	**Towards a simple, robust and clean electron selection for the $H \rightarrow W^+W^-$ search** M. Dittmar, W. Hintz and C. Marchica CMS AN-2009/134
2009	**The CMS Electromagnetic Calorimeter detector control and monitoring system** W. Hintz on behalf of the CMS ECAL Collaboration Nuclear Instruments and Methods in Physics Research **A 090**
2008	**Integration and test of the CMS electromagnetic calorimeter electronics** W. Hintz Joint Annual Meeting of SPS